Acoustical Physics, Vol. 47, No. 3, 2001, pp. 243–246. Translated from Akusticheskiĭ Zhurnal, Vol. 47, No. 3, 2001, pp. 293–296.
Original Russian Text Copyright © 2001 by Andronov.

Power Flux along a Straight Crack in an Elastic Plate

I. V. Andronov
St. Petersburg State University, Ul'yanovskaya ul. 1/1, Petrodvorets, 198904 Russia
e-mail: iva@aa2628.spb.edu

Received May 12, 2000

Abstract—Propagation of the edge waves along a straight crack in an elastic plate is studied. The power fluxes associated with these waves are calculated, and the modes of vibration are considered. *© 2001 MAIK "Nauka/Interperiodica".*

The question of the existence of localized waves remains topical. The localized waves can be observed near bodies placed in waveguides (see, e.g., [1]), in periodic structures [2], and at the surface of an elastic body [3].

It is known [4] that a Rayleigh-type wave can propagate in the vicinity of an edge of a plate placed in free space. Dispersion relations for the edge waves in a plate that is in contact with an acoustic medium are studied in [5]. It was found that a straight crack with free edges can support symmetric and antisymmetric waves. The symmetric wave is possible for any parameters and any frequency, while the antisymmetric wave exists only in a limited frequency range. This paper studies the power flux carried by the symmetric and antisymmetric waves. The power flux is represented as a sum of the power E' in the acoustic medium and the power E'' of the flexural vibrations of the plate; in turn, from the latter component, the contribution E''' of the corner forces is separated.

Let (as in [5]) the mechanical system consist of an acoustic halfspace, $z < 0$, bounded by the Kirchhoff plate, $z = 0$, with a crack along the straight line $x = 0$. The symmetric and antisymmetric edge waves are described by the formulas [5]

$$e^{i\mu_0 y}V_0(x,z) = e^{i\mu_0 y}\frac{c_0}{2\pi}\int_{-\infty}^{+\infty}\frac{\sigma\mu_0^2+\lambda^2}{l(\lambda,\mu_0)}e^{i\lambda x-\sqrt{\lambda^2+\mu_0^2-k^2}z}d\lambda, \tag{1}$$

$$e^{i\mu_1 y}V_1(x,z) = e^{i\mu_1 y}\frac{c_1}{2\pi}\int_{-\infty}^{+\infty}\frac{(2-\sigma)\mu_1^2+\lambda^2}{l(\lambda,\mu_1)}e^{i\lambda x-\sqrt{\lambda^2+\mu_1^2-k^2}z}d\lambda, \tag{2}$$

where

$$l(\lambda,\mu) = ((\lambda^2+\mu^2)^2-k_0^4)\sqrt{\lambda^2+\mu^2-k^2}-\nu$$

and the wave numbers μ_0 and μ_1 are calculated from the respective dispersion relations (see Eqs. (12) and (15) in [5]). The pressure waves V_0 and V_1 are connected with the plate displacements ξ_0 and ξ_1, respectively:

$$\xi_j(x) = -\rho^{-1}\omega^{-2}\frac{dV_j(x,0)}{dz}.$$

Here, ω is the vibration frequency and ρ is the density of the acoustic medium.

The amplitudes c_0 and c_1 can be chosen, for example, to normalize the displacement amplitudes of the crack edges:

$$c_0 = \frac{\rho\omega^2}{D_2(\mu_0)+\sigma\mu_0^2D_0(\mu_0)},\quad c_1 = 2\rho\omega^2,$$

where

$$D_j(\mu) = \frac{1}{2\pi}\int_{-\infty}^{+\infty}e^{+i0\lambda}\frac{\lambda^j\sqrt{\lambda^2+\mu^2-k^2}}{l(\lambda,\mu)}d\lambda.$$

We use the formulas from [6] for the power flux and represent the power propagating in the plate in the form [7]

$$E' = \frac{1}{2\omega\rho}\mu\int_{-\infty}^{0}dz\int_{-\infty}^{+\infty}dx|V(x,z)|^2, \tag{3}$$

$$E'' = E''' + D\omega\mu\int_{-\infty}^{+\infty}dx\left(\mu^2|\xi(x)|^2+\mathrm{Re}\left(\xi^*(x)\frac{d^2\xi(x)}{dx^2}\right)\right), \tag{4}$$

$$E''' = -D\omega(1-\sigma)\mu\mathrm{Re}\left[\xi^*\frac{d\xi}{dx}\right]. \tag{5}$$

Here, D is the flexural stiffness of the plate, σ is the Poisson ratio, the asterisk means complex conjugation, and $[f]$ denotes the step in the function f at $x = 0$.

We substitute Eqs. (1) and (2) into Eqs. (3)–(5) and change the order of integration. The integral with respect to z is calculated explicitly, and the integrals

1063-7710/01/4703-0243$21.00 © 2001 MAIK "Nauka/Interperiodica"

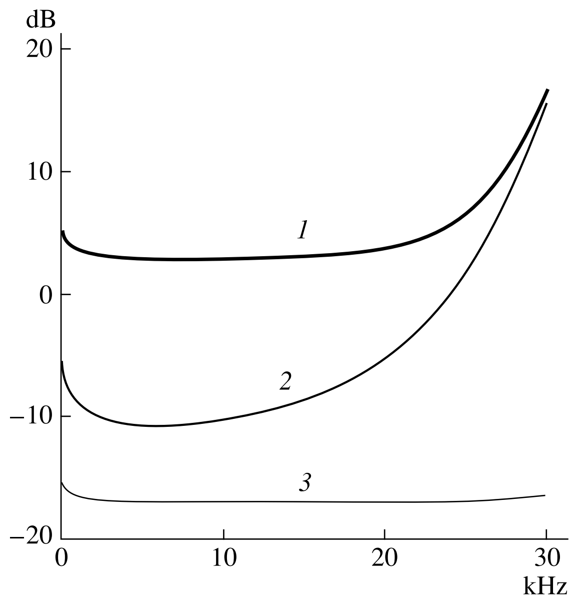

Fig. 1. Power fluxes of the edge wave for a plate in water versus frequency: (*1*) total power flux; (*2*) contribution of the acoustic vibrations; and (*3*) contribution of the corner forces.

with respect to x yield the delta-function. Finally, we obtain

$$E_0' = \frac{\mu_0|c_0|^2}{8\pi\rho\omega}\int_{-\infty}^{+\infty}\frac{(\sigma\mu_0^2+\lambda^2)^2 d\lambda}{l^2(\lambda,\mu_0)\sqrt{\lambda^2+\mu_0^2-k^2}}, \tag{6}$$

$$E_0'' = E_0''' + \frac{D\mu_0|c_0|^2}{2\pi\rho^2\omega^3} \times \int_{-\infty}^{+\infty}\frac{(\sigma\mu_0^2+\lambda^2)^2(\lambda^2+\mu_0^2-k^2)(\mu_0^2+\lambda^2)}{l^2(\lambda,\mu_0)}d\lambda, \tag{7}$$

$$E_0''' = \frac{D(1-\sigma)\mu_0|c_0|^2}{\rho^2\omega^3}(D_2(\mu_0)+\sigma\mu_0^2 D_0(\mu_0)) \tag{8}$$

for the symmetric wave and

$$E_1' = \frac{\mu_1|c_1|^2}{8\pi\rho\omega}\int_{-\infty}^{+\infty}\frac{((2-\sigma)\mu_1^2+\lambda^2)^2\lambda^2 d\lambda}{l^2(\lambda,\mu_1)\sqrt{\lambda^2+\mu_1^2-k^2}}, \tag{9}$$

$$E_1'' = E_1''' + \frac{D\mu_1|c_1|^2}{2\pi\rho^2\omega^3} \times \int_{-\infty}^{+\infty}\lambda^2\frac{((2-\sigma)\mu_1^2+\lambda^2)^2(\lambda^2+\mu_1^2-k^2)(\mu_1^2+\lambda^2)}{l^2(\lambda,\mu_1)}d\lambda, \tag{10}$$

$$E_1''' = \frac{D(1-\sigma)\mu_1|c_1|^2}{\rho^2\omega^3}(D_4(\mu_1)+(2-\sigma)\mu_1^2 D_2(\mu_1)) \tag{11}$$

for the antisymmetric wave.

The integrals in Eqs. (6), (7), (9), and (10) are real, because the wave numbers μ_0 and μ_1 are greater than k. These integrals can be reduced to a sum of residues in the same way as was done in [8] for the integrals D_j. The resulting formulas are fairly cumbersome, because all poles are of multiplicity 2.

Below, we present the results of calculations for the power fluxes and the modes of vibration. Figure 1 shows the power flux in the symmetric edge wave along a crack in a 1-cm-thick steel plate immersed in water. The power fluxes are normalized to the power flux of the edge waves in an isolated plate

$$E^0 = D\omega k_0^2\frac{\tau_0}{a_+^2}\left(\frac{a_+^2}{\sqrt{\tau_0-1}} - \frac{a_-^2}{\sqrt{\tau_0+1}} + 4(1-\sigma)(a_+\sqrt{\tau_0-1} - a_-\sqrt{\tau_0+1})\right),$$

where $a_\pm = (1-\sigma)\tau_0^2 \pm 1$ and $k_0\tau_0$ is the wave number of the edge wave in the isolated plate for which [4]

$$\tau_0 = ((1-\sigma)(3\sigma-1+2\sqrt{1-2\sigma+2\sigma^2}))^{-1/4}.$$

Figure 2 shows similar power fluxes for the plate in air. Figures 2a and 2b refer to the symmetric and antisymmetric waves, respectively. The energy characteristics are seen to change their structure at frequencies near the coincidence frequency. At lower frequencies, the major portion of the power is the power of the elastic deformation of the plate, which is almost equal to E° for the symmetric wave. At the frequencies higher than the coincidence frequency, the major contribution is given by the power flux in the adjacent acoustic medium. As the frequency increases further, the power of the elastic deformation again becomes dominant. The oscillations observed in Fig. 2a at high frequencies are related to the errors of the calculation. As was noted in [5], at high frequencies, the wave number μ_0 of the symmetric edge wave is close to the wave number κ of the flexural waves in the plate immersed in the acoustic medium. The formulas for the power flux contain the quantity $\mu_0^2 - \kappa^2$, which is calculated with an error. A similar loss in accuracy occurs near the upper critical frequency for the antisymmetric edge wave.

Figures 1 and 2 show that the contribution of the corner forces E''' exhibits no abrupt changes near the coincidence frequency nor at the critical frequencies of the antisymmetric wave. Therefore, one can assume that the modes of vibration of the plate edges remain essentially unchanged. Our calculations show that, near the crack, the dependence of the plate displacement ξ on the distance from the edge has the form of a rapidly decaying function, which is almost the same for the symmetric and antisymmetric waves. Near the critical frequencies of the antisymmetric wave, the rate of the

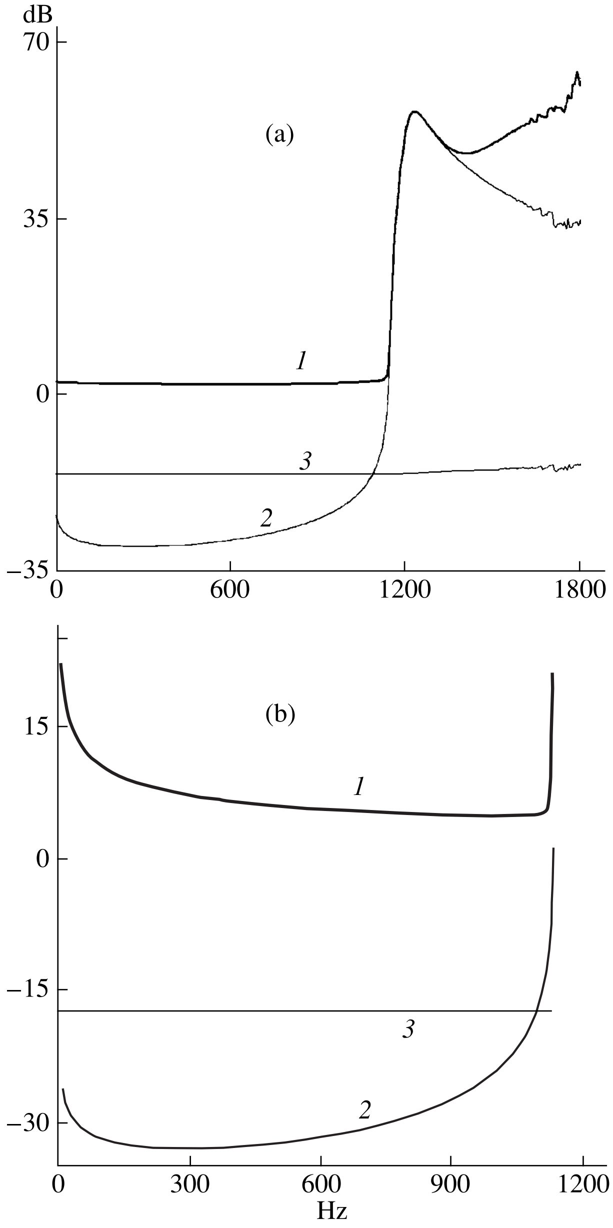

Fig. 2. Power fluxes of the (a) symmetric and (b) antisymmetric waves for a plate in air versus frequency: (*1*) total power flux; (*2*) contribution of the flexural vibrations; and (*3*) contribution of the corner forces.

decay decreases. Figure 3 shows the amplitude distributions of the antisymmetric edge wave in the vicinity of the lower critical frequency. Similar effects are observed near the upper critical frequency (see Fig. 4). These changes in the amplitude distributions cause an increase in the power flux in both the plate and the adjacent acoustic medium as the frequency approaches the critical value. It is clear that, in this situation, it becomes more difficult to excite the antisymmetric wave.

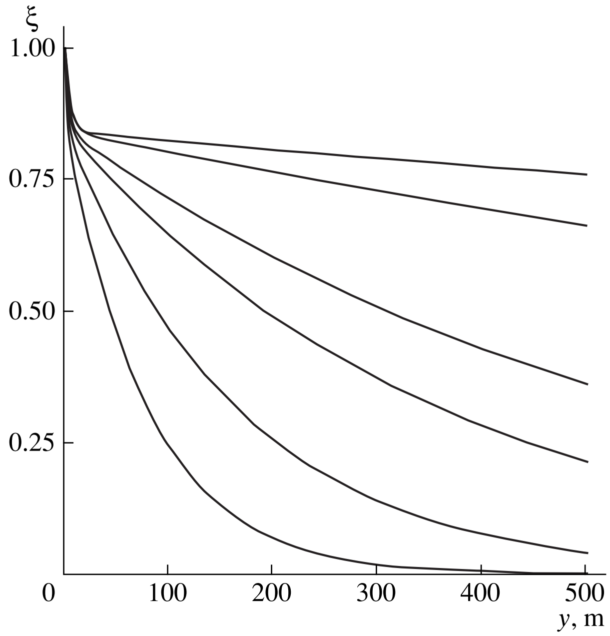

Fig. 3. Distribution of the plate displacements in the antisymmetric wave at the frequencies (from top to bottom) 0.5, 0.2, 0.1, 0.075, 0.05, and 0.045 Hz.

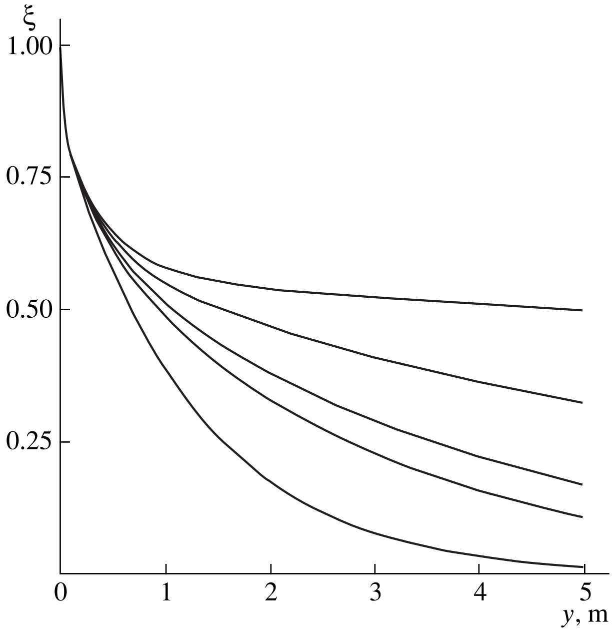

Fig. 4. Distribution of the plate displacements in the antisymmetric wave at the frequencies (from top to bottom) 1000, 1130, 1132, 1134, and 1135 Hz.

Note that, with decreasing density of the acoustic medium, the edge waves in general are not transformed to the Rayleigh waves for an isolated plate. In particular, the antisymmetric edge wave does not exist at frequencies higher than the coincidence frequency at any density; i.e., the only possible type of vibrations is the symmetric wave. At the same time, in the absence of the acoustic medium, semi-infinite plates vibrate independently.

Similar results were obtained in [9] for the Stoneley waves propagating along an elastic cylinder in the case of a decreasing density of the acoustic medium.

REFERENCES

1. C. M. Linton, P. McIver, and M. McIver, in *Proceedings of the 5th International Conference on Mathematical and Numerical Aspects of Wave Propagation* (Santigo de Compostella, Spain, 2000), p. 419.
2. R. Poter and D. V. Evans, J. Fluid Mech. **386**, 233 (1999).
3. A. S. Bonnet-Ben Dhia and L. Dahi, Boll. Geofis. Theor. Appl. **40**, 140 (1999).
4. Yu. K. Konenkov, Akust. Zh. **6**, 124 (1960) [Sov. Phys. Acoust. **6**, 122 (1960)].
5. I. V. Andronov, Akust. Zh. **45**, 445 (1999) [Acoust. Phys. **45**, 393 (1999)].
6. B. P. Belinskiĭ and D. P. Kouzov, Akust. Zh. **26**, 13 (1980) [Sov. Phys. Acoust. **26**, 8 (1980)].
7. V. A. Veshev, I. I. Klyukin, D. P. Kouzov, and V. D. Luk'yanov, Akust. Zh. **23**, 228 (1977) [Sov. Phys. Acoust. **23**, 129 (1977)].
8. D. P. Kouzov, Prikl. Mat. Mekh. **27**, 1037 (1963).
9. A. S. Bonnet-Ben Dhia and L. Dahi, in *Proceedings of the 5th International Conference on Mathematical and Numerical Aspects of Wave Propagation* (Santiago de Compostella, Spain, 2000), p. 394.

Translated by A. Khzmalyan

Acoustical Physics, Vol. 47, No. 3, 2001, pp. 247–252. Translated from Akusticheskiĭ Zhurnal, Vol. 47, No. 3, 2001, pp. 297–303.
Original Russian Text Copyright © 2001 by Balabaev, Ivina.

Acoustic Radiation of a Water-Filled Piezoelectric Cylinder near a Rigid Plane

S. M. Balabaev and N. F. Ivina
Far-Eastern State Technical Fishery University, ul. Lugovaya 52-B, Vladivostok, 690600 Russia
e-mail: omsdti@mail.primorye.ru

Received April 20, 2000

Abstract—The combined finite-element–boundary-element method is used to solve the problem on the radiation of a water-filled piezoceramic cylinder positioned near an infinite plane. For the case of a perfectly rigid plane, the frequency characteristics of the transmitting response of the piezoelectric cylinder are obtained along with the frequency characteristics of the acoustic power, the directional characteristics, and the velocity and pressure distributions over the radiating cylindrical surfaces. It is found that, when the distance between the plane and the piezoelectric cylinder is small relative to the wavelength, the frequency characteristics of the cylinder and the velocity and pressure distributions noticeably differ from those obtained for a piezoelectric cylinder in an infinite space. The effect of the antisymmetric mode, which appears at small wave distances between the cylinder and the plane, on the characteristics of a water-filled piezoelectric cylinder is considered. *© 2001 MAIK "Nauka/Interperiodica".*

A water-filled (free-flooded) piezoceramic cylinder and an array of such cylinders are known to exhibit peculiar frequency characteristics and, therefore, have been the objects of many investigations. The problems on the radiation of these systems were analyzed with the use of different models of a water-filled cylinder and with different methods [1–15]. The numerical methods and, specifically, the finite-element and the boundary-element methods [8, 9, 11–15] provide approximate solutions to such problems with an accuracy that is sufficient for practical applications. These solutions take into account the real distribution of the particle velocity and pressure at the radiating surface of a piezoelectric cylinder. The numerical methods are successfully used for solving other problems concerned with the analysis of piezoelectric transducers [16–17]. The publications cited above [1–15] consider water-filled cylinders in an unbounded liquid medium without taking into account the effect of the structural elements, the sea floor, and the like.

The purpose of this paper is the analysis of the acoustic radiation of a water-filled piezoelectric cylinder positioned near a plane, which can serve as an approximate model of the sea floor or some elements of a structure located near the cylinder.

To solve this problem, we apply the combined finite-element–boundary-element method considered earlier [12–15]. In the combined method, the forced vibrations of a finite transducer are described with allowance for the piezoelectric effect and acoustic radiation in a liquid in terms of a system of linear algebraic equations

$$\begin{aligned}(H_{uu} - \omega^2 M + i\omega C)|u_i\rangle + WS|P\rangle &= |H_{uv}\rangle, \\ \omega^2 \rho B W^T |u_i\rangle - A|P\rangle &= 0,\end{aligned} \tag{1}$$

where H_{uu} is the global transducer stiffness matrix taking into account the piezoelectric effect; M is the global mass matrix; ω is the circular frequency; C is the damping matrix taking into account the mechanical loss; S is the diagonal matrix of the area; W is the direction cosine matrix for the outer unit normal; $|H_{uv}\rangle$ is the global vector of the piezoelectric "stiffness"; $|u_i\rangle$ is the nodal displacement vector; $|P\rangle$ is the pressure vector; A and B are the global matrices of the boundary-element method; ρ is the density of the liquid; and T denotes a transposition.

The system of equations (1) relates the pressure at the surface of the piezoelectric transducer to the displacements of its nodal points. This system is complemented by two equations

$$Y = i\omega(H_{uv}^T|u_i\rangle - H_{vv}), \tag{2}$$

$$P = (4\pi)^{-1}(A_1^T|P\rangle + i\omega\rho B_1^T|v_n\rangle). \tag{3}$$

Equation (2) determines the conductivity of the piezoelectric transducer; H_{vv} is the global "dielectric" stiffness matrix (in fact, with the introduction of the boundary conditions at the electrodes and the elimination of the electric potentials of the nodes lying outside the electrodes, it is a single element). Equation (3) determines the pressure in the liquid in the near and far zones; A_1^T and B_1^T are the row matrices of the bound-

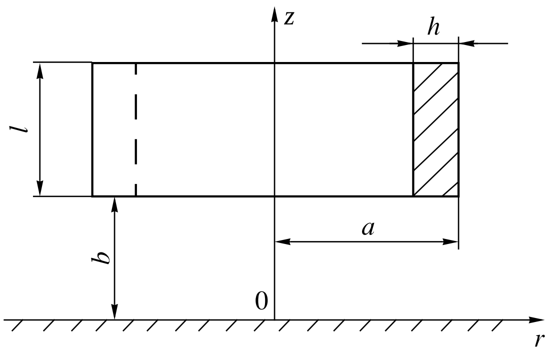

Fig. 1. Schematic representation of a cylinder near a plane.

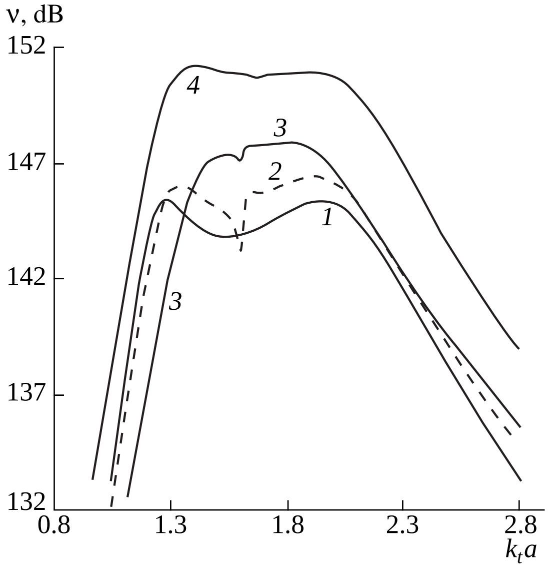

Fig. 2. Frequency characteristics of the transmitting response of a water-filled piezoelectric cylinder: l/a = (*1*) 0.8, (*2*) 0.45, (*3*) 0.45, and (*4*) 0.75; b/a = (*1*) ∞, (*2*) 0.05, (*3*) 0.2, and (*4*) 1.

ary-element method for a given point of the acoustic field, and $|v_n\rangle$ are the normal nodal velocities at the surface of the piezoelectric transducer, which are expressed through the nodal displacements $|v_n\rangle = i\omega W^T|u_i\rangle$ (the time factor is taken in the form $\exp(i\omega t)$).

The global matrices A and B of the boundary-element method are formed of the corresponding matrices determined by the integrals over the boundary element area [12]. The integrands of these element matrices involve the Green's function and its derivative with respect to the outer unit normal. In the case of a piezoelectric cylinder in an unbounded liquid medium, the Green's function is taken in its conventional form $G = \exp(-ikr)/r$, where $k = \omega/c$, c is the sound velocity in the liquid, and r is the distance between a point at the surface of the piezoelectric transducer (the source) and the point of observation. In the case of a halfspace, the Green's function can be represented in the form $G_1 = \exp(-ikr)/r + R\exp(-ikr_1)/r_1$, where r_1 is the distance between the mirror-reflected source and the observation point and R is the reflection coefficient of the infinite plane [18]. For a perfectly soft plane, we have $R = -1$, whereas, for a perfectly rigid plane, the reflection coefficient is $R = 1$ [18, 19].

We consider the acoustic radiation of a water-filled piezoelectric cylinder positioned near a perfectly rigid plane (Fig. 1) and compare it with the radiation of a piezoelectric cylinder in an unbounded medium. The geometric parameters of the problem are the height of the cylinder l, its outer radius a, the cylinder wall thickness h, and the distance to the plane b; in the following analysis, these parameters will be determined by the dimensionless ratios l/a, h/a, and b/a. We consider a sectionalized (tangentially polarized) piezoelectric cylinder consisting of 32 prisms and made of the TsTBS-3 ceramics whose parameters can be found in the handbook [20].

Before analyzing the effect of a perfectly rigid plane on the main characteristics of the water-filled cylinder, we consider its characteristics in the absence of the plane ($b/a = \infty$). For a water-filled piezoelectric cylinder in an unbounded space, we calculated the frequency characteristics of the transmitting response ν for a far-field point in the cylinder symmetry plane ($z = b + l/2$). For a cylinder located near an infinite plane, the transmitting response was determined near this plane. The response was calculated in decibels relative to the level 1 μPa/V at a distance of 1 m. Since the transmitting response is a local characteristic depending on the selected point, we also determined the integral characteristic, namely, the frequency characteristic of the dimensionless active component of the acoustic power. In addition, we calculated the directional characteristics in the vertical plane, which were normalized to the maximal pressure.

Figure 2 (curve *1*) presents the frequency characteristic of the transmitting response for a water-filled piezoelectric cylinder with the wall thickness $h/a = 0.25$ in an unbounded space. The abscissa axis represents the dimensionless frequency parameter k_ta, where k_t is the wave number of a transverse wave in the piezoceramics [12]. It is well known that the frequency characteristics of a water-filled cylinder have two peaks. The first, low-frequency, peak ($k_ta \approx 1.3$), which is usually called the volume resonance, corresponds to the resonance of the system that includes the piezoelectric cylinder, the volume of liquid inside it, and a part of the surrounding liquid. The second maximum ($k_ta \approx 1.95$) is caused by the radial resonance of the piezoelectric cylinder.

The frequency characteristic of the transmitting response shown in Fig. 2 corresponds to the optimal cylinder height $l/a = 0.8$. The optimal height is the height at which the transmitting responses at the volume resonance and at the radial resonance are approximately equal, and the nonuniformity of the frequency characteristic (the difference between the transmitting response at the resonances and between them) does not exceed 3 dB [14]. When the cylinder height is smaller than the optimal one, the response at the volume resonance is greater than at the radial resonance. When the cylinder height exceeds the optimal value, the situation is reversed. In the cited paper [14], it was noted that, for a piezoelectric cylinder with the wall thickness h/a = 0.2, the optimal height is $l/a \approx 0.95$. Hence, the optimal height of a water-filled piezoelectric cylinder essentially depends on its wall thickness. In the case under discussion, a decrease in the wall thickness by 20% leads to an increase in the optimal height by 19%. For a piezoelectric cylinder with the wall thickness h/a = 0.25, the relative radiation bandwidth at a level of –3 dB is 63%, which is 12% less than for a cylinder with the wall thickness h/a = 0.2 [14].

Figure 3 (curve *1*) shows the frequency characteristic of the dimensionless active component of the acoustic power P_a for a water-filled piezoelectric cylinder of optimal height in an unbounded space. The acoustic radiation power is proportional to the real part of the conductivity determined by Eq. (2). Figure 4 presents the directional characteristics of a water-filled piezoelectric cylinder of optimal height in the vertical plane. The first three curves are for a cylinder in an unbounded space. Curve *1* relates to the volume resonance frequency, curve *3* to the radial resonance frequency, and curve *2* to the frequency corresponding to the minimal response between these two frequencies. The directional characteristics at the volume and radial resonance frequencies account for the fact that, for a cylinder with the optimal dimensions, the acoustic power at the radial resonance is higher than at the volume resonance (Fig. 3, curve *1*). This occurs because, at the radial resonance, the main lobe of the directional characteristic (Fig. 4, curve *3*) is wider than at the volume resonance (Fig. 4, curve *1*).

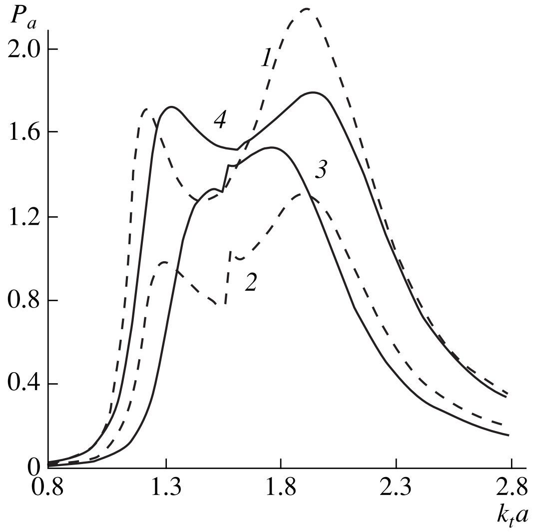

Fig. 3. Frequency characteristics of the dimensionless active component of the acoustic power of a water-filled piezoelectric cylinder. (The parameters are the same as in Fig. 2.)

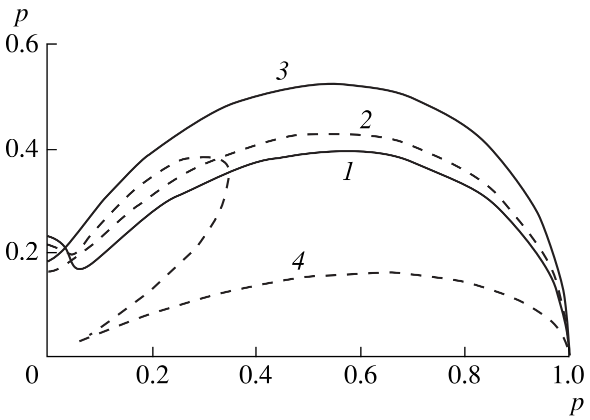

Fig. 4. Normalized directional characteristics of a water-filled piezoelectric cylinder in the vertical plane: l/a = (*1–3*) 0.8 and (*4*) 0.75; b/a = (*1–3*) ∞ and (*4*) 1; k_ta = (*1*) 1.3, (*2*) 1.55, (*3*) 1.95, and (*4*) 1.85.

Figures 5a and 6a show typical distributions of the absolute values of the dimensionless normal (radial) component of the particle velocity and the pressure at the outer and inner cylindrical surfaces of a water-filled piezoelectric cylinder of optimal height in an unbounded space. In these figures, the abscissa axis represents the ordinal number of the equidistant nodal points; the points with the numbers 7 and 20 lie in the cylinder symmetry plane. The first thirteen points lie on the outer surface, so that their numbers increase in the upward direction; the subsequent thirteen points (nos. 14–26) lie on the inner surface, their numbers increasing downwards. The distribution of the velocity and the pressure are presented for the same three frequencies as the directional characteristics of the piezoelectric cylinder in Fig. 4. From the comparison of the corresponding curves, it follows that, for a cylinder of optimal height, the absolute value of the particle velocity at the inner cylindrical surface always exceeds the corresponding value at the outer surface. When the transmitting responses at the volume and radial resonances are equal, which is possible for a water-filled piezoelectric cylinder of optimal dimensions, the absolute value of the particle velocity at the volume resonance is much greater than at the radial resonance.

The nonuniformity of the particle velocity distribution, which can be interpreted as the ratio of the absolute value of the particle velocity in the middle of the cylinder (the maximal value) to its absolute value at the cylinder end (the minimal value), is relatively small and approximately the same at the outer and inner surfaces for all frequencies. The nonuniformity of the pressure distribution is much greater, and it is maximal at the inner cylindrical surface at the volume resonance frequency. We note that most analytical models of a water-filled piezoelectric cylinder ignore the nonuniformity of the distributions of the particle velocity and pressure

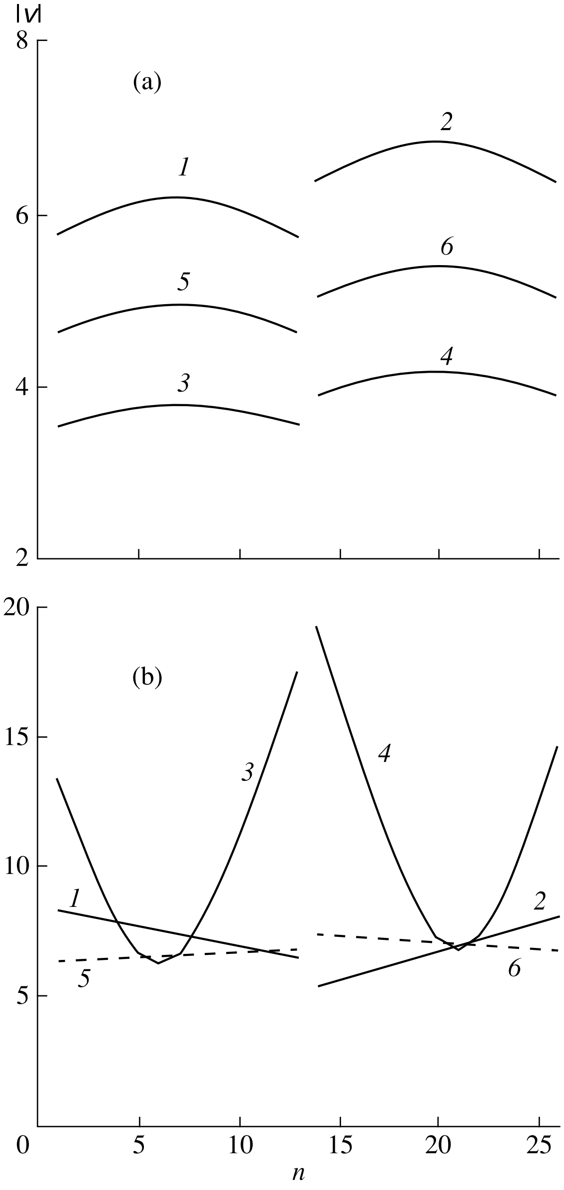

Fig. 5. Distribution of the absolute value of the dimensionless normal component of the particle velocity over the outer (n = 1–13) and inner (n = 14–26) cylindrical surfaces of a water-filled piezoelectric cylinder: (a) $l/a = 0.8$, $b/a = \infty$, k_ta = (*1*, *2*) 1.3, (*3*, *4*) 1.55, and (*5*, *6*) 1.95; (b) $l/a = 0.45$, $b/a = 0.2$, k_ta = (*1*, *2*) 1.5, (*3*, *4*) 1.6, and (*5*, *6*) 1.8.

at the cylinder surface, and, hence, the information obtained with the use of these models is incomplete. We also note that the nonuniformity of these quantities is an important factor, which limits the radiation power because of the appearance of high mechanical stresses in the piezoceramics and because of the cavitation, and this factor should be taken into account in developing water-filled hydroacoustic radiators.

The eigenfrequency spectrum of the piezoelectric cylinder can contain three different modes of oscillation in the frequency range under study: the antisymmetric mode, the symmetric mode, and the flexural mode [21]. Each of these modes can be characterized by the values of the dimensionless resonance and antiresonance frequencies, $(k_ta)_r$ and $(k_ta)_a$, and by the dynamic electromechanical coupling coefficient k. These parameters were calculated by the expressions presented in our previous paper [12]. For a piezoelectric cylinder with the wall thickness $h/a = 0.25$ and the optimal height $l/a = 0.8$, the characteristics of the first three modes are as follows: $(k_ta)_r = (k_ta)_a = 1.83$ and $k = 0.6$ for the antisymmetric mode; $(k_ta)_r = 1.91$, $(k_ta)_a = 2.38$, and $k = 0$ for the symmetric mode; $(k_ta)_r \approx (k_ta)_a = 4.14$ and $k = 0.002$ for the flexural mode. The flexural mode is only weakly excited: for a thick-walled cylinder, it is above the frequency range under study and does not affect the frequency characteristics of the water-filled cylinder. For a thin-walled cylinder, the flexural mode can approach the symmetric one, and, in this case, it will affect the frequency characteristics of the cylinder [12, 14]. The antisymmetric mode is not excited in a single piezoelectric cylinder with solid electrodes in an unbounded space (an electrically and mechanically symmetric problem). Therefore, no manifestation of this mode can be observed in the frequency characteristics, in the directional characteristic, and in the distributions of the particle velocity and pressure over the surface of the water-filled piezoelectric cylinder. If the electric or mechanical symmetry of the problem is violated, the antisymmetric mode can manifest itself and affect the characteristics of the water-filled piezoelectric cylinder. Such a situation caused by the acoustic interaction was observed in a hydroacoustic array consisting of two water-filled piezoelectric cylinders positioned at a small wave distance from each other [14]. A similar situation will take place when some metal structure elements or a rocky sea floor occur near the piezoelectric cylinder, if they can be approximately modeled by a perfectly rigid plane.

Let us consider the effect of a perfectly rigid plane located at a small wave distance from the water-filled piezoelectric cylinder on the characteristics of the latter. We note that, for the ceramics under consideration, the wavelength in liquid at the radial resonance frequency $k_ta \approx 1.9$ is $2.5a$. Figures 2 and 3 present the frequency characteristics of the transmitting response and those of the dimensionless active component of the acoustic power for the relative distance between the piezoelectric cylinder and the plane, b/a, increasing from 0.05 to 1. The curves in Figs. 2 and 3 correspond to the cylinder heights close to optimal, i.e., to an approximate equality of the responses at the volume and radial resonances. When the distance between the plane and the piezoelectric cylinder is small, the optimal cylinder height is approximately equal to half the optimal height of a water-filled piezoelectric cylinder in an unbounded space. As the distance b/a increases, the optimal height also increases, and, for $b/a \geq 1$, it is practically equal to the optimal height of the cylinder in the absence of the plane.

With the increase in b/a from 1 to 2.5, the transmitting response increases approximately by a factor of two (by 6 dB); with a further increase in b/a, the response begins to decrease. The frequency characteristic of the active component of the acoustic power is practically insensitive to the presence of the plane for $b/a \geq 2.5$ ($l/a = 0.8$). The directional characteristics depend only weakly on the presence of the plane for b/a within 0.05–0.2: the main lobe slightly narrows. With a further increase in b/a, the main lobe of the directional characteristic considerably narrows and an additional maximum is formed (Fig. 4, curve *4*).

In the case of small wave distances between the piezoelectric cylinder and the plane, the velocity and pressure distributions noticeably differ from the corresponding distributions in the absence of the plane—Figs. 5 and 6; in addition, they exhibit some changes with the frequency variation at fixed geometric dimensions. The presence of the plane violates the symmetry in the distribution of the aforementioned quantities with respect to the cylinder symmetry plane. The asymmetry is most pronounced for the pressure at the inner cylindrical surface.

When the wave distance b/a is small, the frequency characteristics are affected by the antisymmetric mode, which can be seen from curves *2–4* in Figs. 2 and 3 at $k_t a \approx 1.6$. The manifestation of the antisymmetric mode in a symmetric cylinder is explained by the acoustic interaction between the cylinder and the plane at a small wave distance between them. For a piezoelectric cylinder with the dimensions $h/a = 0.25$ and $l/a = 0.45$, the parameters characterizing the natural oscillations are as follows: $(k_t a)_r = (k_t a)_a = 1.68$ and $k = 0$ for the antisymmetric mode; $(k_t a)_r = 1.92$, $(k_t a)_a = 2.39$, and $k = 0.6$ for the symmetric mode. The flexural mode falls outside the frequency range under study. The antisymmetric mode is characterized by an antiphase distribution of the normal particle velocity at the cylindrical surfaces. Therefore, the absolute value of the particle velocity has a minimum approximately in the middle of the cylinder and reaches relatively large values at the cylinder ends (Fig. 5, curves *3*, *4*). With such a distribution of the particle velocity over the cylindrical surfaces, large mechanical stresses will occur in the piezoceramics near the cylinder symmetry plane, which may cause fracturing of the piezoelectric cylinder.

Hence, in designing water-filled piezoelectric cylinders, it is necessary to avoid the situation when the antisymmetric mode falls within the operating frequency range. This can be accomplished in the following three ways. One has to use isolated piezoelectric cylinders positioned at a distance greater than the wavelength from other elements of the structure. Another possibility is to use several thin-walled cylinders of a small (not optimal) height for building a cylinder of optimal height so that the individual cylinders are connected by acoustic decoupling elements (this problem requires special investigation). The third possibility is to use thick-walled cylinders with a small optimal height. In this case, the frequency of the antisymmetric mode will be much lower than the frequency of the symmetric mode [21] and the antisymmetric mode will not affect the characteristics of the water-filled radiator. However, a thick-walled piezoelectric cylinder has a smaller relative radiation bandwidth, as compared to a thin-walled cylinder. Therefore, in every practical realization of water-filled hydroacoustic radiators, one has to make a compromise between the acoustic power and the radiation frequency band.

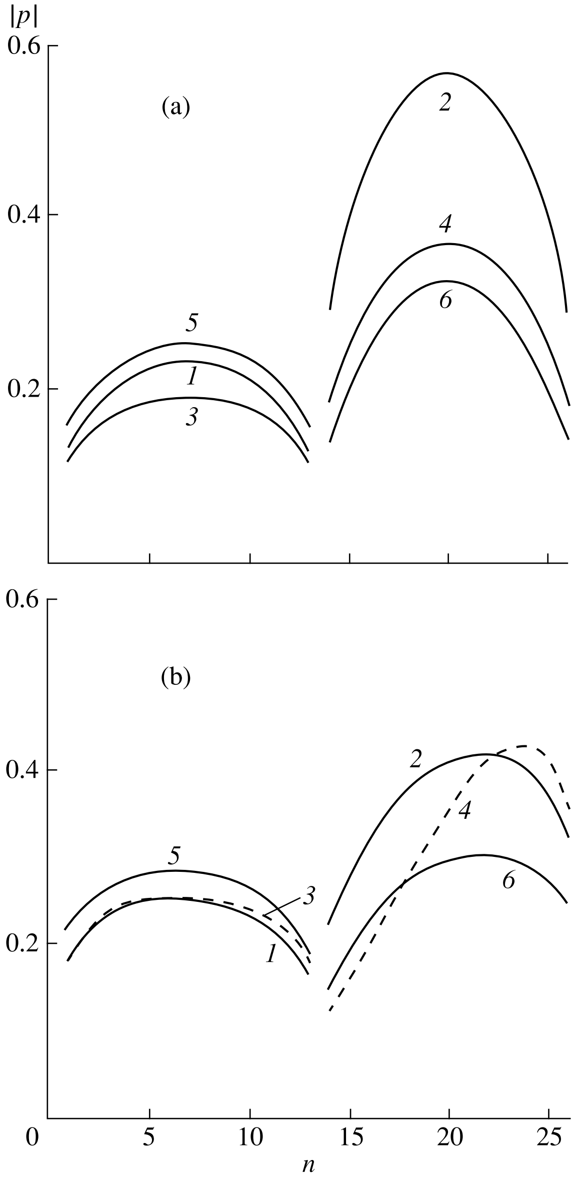

Fig. 6. Distribution of the absolute value of the dimensionless pressure over the outer (n = 1–13) and inner (n = 14–26) cylindrical surfaces of a water-filled piezoelectric cylinder. (The parameters are the same as in Fig. 5.)

REFERENCES

1. V. G. Basovskiĭ and I. V. Vovk, Akust. Zh. **44**, 581 (1998) [Acoust. Phys. **44**, 497 (1998)].
2. I. V. Vovk, Akust. Zh. **38**, 427 (1992) [Sov. Phys. Acoust. **38**, 234 (1992)].
3. I. V. Vovk and V. T. Grinchenko, Akust. Zh. **37**, 259 (1991) [Sov. Phys. Acoust. **37**, 130 (1991)].
4. V. E. Glazanov, Akust. Zh. **35**, 801 (1989) [Sov. Phys. Acoust. **35**, 467 (1989)].
5. I. L. Rubanov and G. M. Sverdlin, Akust. Zh. **36**, 1071 (1990) [Sov. Phys. Acoust. **36**, 598 (1990)].
6. T. M. Tomilina, Akust. Zh. **35**, 122 (1989) [Sov. Phys. Acoust. **35**, 73 (1989)].
7. E. L. Shenderov, *Emission and Scattering of Sound* (Sudostroenie, Leningrad, 1989).
8. R. R. Smith, J. T. Hunt, and D. Barach, J. Acoust. Soc. Am. **54**, 1277 (1973).
9. J. T. Hunt, M. R. Knittel, and D. Barach, J. Acoust. Soc. Am. **55**, 269 (1974).
10. P. H. Rogers, J. Acoust. Soc. Am. **80**, 13 (1986).
11. R. Bossut and J.-N. Decarpigny, J. Acoust. Soc. Am. **86**, 1234 (1989).
12. S. M. Balabaev and N. F. Ivina, Akust. Zh. **42**, 172 (1996) [Acoust. Phys. **42**, 149 (1996)].
13. S. M. Balabaev and N. F. Ivina, *Computer Simulation of Vibrations and Radiation from Finite Bodies: The Finite-Element and Boundary-Element Methods* (Dal'nauka, Vladivostok, 1996), p. 213.
14. S. M. Balabaev, Akust. Zh. **44**, 5 (1998) [Acoust. Phys. **44**, 1 (1998)].
15. S. M. Balabaev and N. F. Ivina, Akust. Zh. **45**, 293 (1999) [Acoust. Phys. **45**, 253 (1999)].
16. J.-C. Debus, B. Dubus, and J. Coutte, J. Acoust. Soc. Am. **103**, 3336 (1998).
17. D. Ekeom, B. Dubus, and C. Granger, J. Acoust. Soc. Am. **104**, 2779 (1998).
18. A. F. Seybert and T. W. Wu, J. Acoust. Soc. Am. **85**, 19 (1989).
19. E. L. Shenderov, *Wave Problems in Underwater Acoustics* (Sudostroenie, Leningrad, 1972), p. 352.
20. *Piezoceramic Transducers*, Ed. by S. I. Pugachev (Sudostroenie, Leningrad, 1984), p. 256.
21. S. M. Balabaev, N. F. Ivina, and K. N. Shishlov, Akust. Zh. **46**, 702 (2000) [Acoust. Phys. **46**, 616 (2000)].

Translated by E. Golyamina

Acoustical Physics, Vol. 47, No. 3, 2001, pp. 253–261. Translated from Akusticheskiĭ Zhurnal, Vol. 47, No. 3, 2001, pp. 304–312.
Original Russian Text Copyright © 2001 by Bokov, Ionov.

Exact and Asymptotic Solutions for the Field of a Point Source in a Transversely Isotropic Medium

P. M. Bokov and A. M. Ionov

Moscow State Engineering Physics Institute (Technical University),
Kashirskoe sh. 31, Moscow, 115409 Russia
e-mail: aionov@hotmail.com

Received June 19, 2000

Abstract—Exact and asymptotic solutions are obtained for the acoustic field generated by an isotropic pulsed point source in an infinite transversely isotropic elastic medium. The exact solution for the displacement field is obtained in the form of a double integral over the horizontal slowness and the frequency by using the method of integral transforms. The calculation of the integral over the horizontal slowness by the method of stationary phase reduces the exact solution to an asymptotic solution that is convenient for numerical calculations. Formulas are given for calculating the spreading factors and the wave fronts of quasi-longitudinal *qP*-waves and quasi-transverse *qSV*-waves. With the formulas obtained, the displacement field of a point source is investigated for a particular transversely isotropic medium. *© 2001 MAIK "Nauka/Interperiodica".*

INTRODUCTION

In simulating seismic wave propagation in problems of seismology and exploration geophysics, investigators usually restrict their calculations to the model of an isotropic geological medium. Many eruptive rocks and certain carbonates and sandstones do not demonstrate directional properties and behave as isotropic elastic bodies. However, mountain masses, clay deposits, and many other geological formations often represent layered structures whose elastic properties depend on the direction. This fact (the anisotropy) essentially complicates the analysis of seismic wave propagation, especially in the case of an arbitrary anisotropy [1–3]. The only exception is represented by transversely isotropic media in which the elastic moduli in the plane perpendicular to the symmetry axis are identical but may differ in the general case from the modulus in the direction of the symmetry axis. As investigations show, many sedimentary rocks are transversely isotropic [4–7]. There is an additional argument in favor of making allowance for the medium anisotropy: in reference to deformations, a stack of thin parallel sheets, where each sheet is isotropic and characterized by its own elastic properties different from those of other layers, behaves as if it were a transversely isotropic medium. To model such a system by a set of thin isotropic layers, one may need to consider tens or even hundreds of layers.

The literature on the problem of seismic wave simulation in anisotropic media is quite extensive [8–11]. Nevertheless, there is no loss of interest in modeling and interpreting the seismic wave fields in anisotropic media. In particular, many investigators have considered the problem on the Green's function of a point source in an infinite elastic medium with arbitrary anisotropy. Various approaches and different representations for the Green's function are given in papers [8, 10, 11]. Generally, this problem is solved using integral transforms, which allow the solution to be found for arbitrary medium anisotropy and point source type. Then, the resulting exact integral representations can be calculated asymptotically by the method of stationary phase.

Nevertheless, in our opinion, the results obtained for the waves generated by a point source in an anisotropic medium are still inadequately elaborated for particular elastic media characterized by anisotropy of some special type. This paper considers the radiation of a point source of an explosion type in an infinite transversely isotropic medium. To solve this problem, we use the method of integral transforms with the horizontal slowness as a transform parameter. Our main goal consists in the derivation of the exact and asymptotic solutions to the considered problem in a form convenient for further numerical calculations.

EXACT SOLUTION TO THE PROBLEM ON THE RADIATION OF A POINT SOURCE IN A TRANSVERSELY ISOTROPIC MEDIUM

As is well known, the wave equation for the displacement field u_i generated by a point source located at the origin of coordinates in an elastic medium with an arbitrary anisotropy has, in the Cartesian reference system, the following form [8, 12]:

$$\rho\frac{\partial^2 u_i}{\partial t^2} - C_{ijkl}u_{k,\,jl} = -M_{ij}(t)\nabla_j\delta(\mathbf{r}), \qquad (1)$$

where C_{ijkl} are the elastic moduli of the anisotropic medium, $M_{ij}(t)$ is the tensor of the source seismic moment, $\delta(\mathbf{r})$ is the delta-function, and ∇ is the gradient operator. For an isotropic point source, we have $M_{ij}(t) = M_s(t)\delta_{ij}$ and the right-hand side of Eq. (1) is reduced to $-M_s(t)\nabla_i\delta(\mathbf{r})$.

In the cylindrically symmetric case, the Hooke law for a transversely isotropic medium with the vertical symmetry axes (VTI) can be represented as follows [1, 7]:

$$\begin{gathered}\sigma_{rr} = (\lambda_\parallel + 2\mu_\parallel)\varepsilon_{rr} + \lambda_\parallel\varepsilon_{\vartheta\vartheta} + \lambda_\perp\varepsilon_{zz};\\ \sigma_{\vartheta\vartheta} = \lambda_\parallel\varepsilon_{rr} + (\lambda_\parallel + 2\mu_\parallel)\varepsilon_{\vartheta\vartheta} + \lambda_\perp\varepsilon_{zz};\\ \sigma_{zz} = \lambda_\perp\varepsilon_{rr} + \lambda_\perp\varepsilon_{\vartheta\vartheta} + (\lambda_\perp + 2\mu_\perp)\varepsilon_{zz};\\ \sigma_{r\vartheta} = 2\mu_\parallel\varepsilon_{r\vartheta};\quad \sigma_{\vartheta z} = 2\mu_*\varepsilon_{\vartheta z};\quad \sigma_{zr} = 2\mu_*\varepsilon_{zr},\end{gathered}\tag{2}$$

where σ_{ik} is the stress tensor, ε_{ik} is the deformation tensor, $\lambda_\perp$ and $\mu_\perp$ are the Lamé coefficients along the symmetry axis (the z axis), $\lambda_\parallel$ and $\mu_\parallel$ are the Lamé coefficients in the plane perpendicular to the symmetry axis, and μ_* is the shear modulus independent of other elastic constants. The components of the strain tensor are expressed in terms of the displacement components:

$$\begin{gathered}\varepsilon_{rr} = \frac{\partial u_r}{\partial r};\quad \varepsilon_{\vartheta\vartheta} = \frac{u_r}{r};\quad \varepsilon_{zz} = \frac{\partial u_z}{\partial z};\\ \varepsilon_{r\vartheta} = 0;\quad \varepsilon_{\vartheta z} = 0;\quad \varepsilon_{zr} = \frac{1}{2}\left(\frac{\partial u_z}{\partial r} + \frac{\partial u_r}{\partial z}\right).\end{gathered}\tag{3}$$

In the cylindrical coordinates, equations of motion (1) for wave motions polarized in the vertical plane take the form

$$\begin{gathered}\rho\frac{\partial^2 u_r}{\partial t^2} = \frac{\partial\sigma_{rr}}{\partial r} + \frac{\partial\sigma_{zr}}{\partial z} + \frac{\sigma_{rr} - \sigma_{\vartheta\vartheta}}{r} - M_s(t)\frac{\partial}{\partial r}\left(\frac{\delta(r)}{2\pi r}\delta(z)\right);\\ \rho\frac{\partial^2 u_z}{\partial t^2} = \frac{\partial\sigma_{zr}}{\partial r} + \frac{\partial\sigma_{zz}}{\partial z} + \frac{\sigma_{zr}}{r} - M_s(t)\frac{\partial}{\partial z}\left(\frac{\delta(r)}{2\pi r}\delta(z)\right).\end{gathered}\tag{4}$$

In the case of a transversely isotropic medium, Eqs. (4) for the displacements u_r and u_z, together with Eqs. (2) and (3), form the system of equations equivalent to Eq. (1) of the theory of elasticity. A convenient way of solving the problem under consideration is to introduce the scalar ϕ and vector ψ potentials that are related to the displacements according to the relationships

$$u_r = \frac{\partial\phi}{\partial r} + \frac{\partial^2\psi}{\partial r\partial z};\quad u_z = \frac{\partial\phi}{\partial z} - \Delta_r\psi,\tag{5}$$

where $\Delta_r = \frac{1}{r}\frac{\partial}{\partial r}\left(r\frac{\partial}{\partial r}\right)$ is the radial part of the Laplace operator $\Delta = \Delta_r + \partial^2/\partial z^2$ in the cylindrical coordinates.

Using Eqs. (5) to introduce the displacement potentials in the equations of motion (4) and taking into account Eqs. (2) and (3), we obtain the system of linked equations for the potentials:

$$\begin{gathered}\frac{\partial^2}{\partial t^2}\left(\phi + \frac{\partial\psi}{\partial z}\right) = \alpha_\parallel^2\Delta_r\phi + \alpha_*^2\frac{\partial^2\phi}{\partial z^2} + (\alpha_\parallel^2 - \alpha_*^2 + \beta_*^2)\\ \times\Delta_r\left(\frac{\partial\psi}{\partial z}\right) + \beta_*^2\frac{\partial^2}{\partial z^2}\left(\frac{\partial\psi}{\partial z}\right) - \frac{M_s(t)}{\rho}\frac{\delta(r)}{2\pi r}\delta(z);\\ \frac{\partial^2}{\partial t^2}\left(\frac{\partial\phi}{\partial z} - \Delta_r\psi\right) = \beta_*^2\Delta_r\left[2\frac{\partial\phi}{\partial z} + \frac{\partial^2\psi}{\partial z^2} - \Delta_r\psi\right]\\ + (\alpha_*^2 - 2\beta_*^2)\Delta\left(\frac{\partial\phi}{\partial z}\right) + (\alpha_\perp^2 - \alpha_*^2 + 2\beta_*^2)\\ \times\frac{\partial^2}{\partial z^2}\left(\frac{\partial\psi}{\partial z} - \Delta_r\psi\right) - \frac{M_s(t)}{\rho}\frac{\delta(r)}{2\pi r}\delta'(z),\end{gathered}\tag{6}$$

where operator $\partial/\partial r$ is omitted in the first equation. In what follows, we will assume that seismic moment $M_s(t)$ is related to the seismic source function (the potential of the elastic displacements of the source) $\Psi_s(t)$ according to the relationship $M_s(t) = 4\pi\rho\alpha_0^2\Psi_s(t)$, where α_0 is the normalizing constant with the velocity dimension.

In Eqs. (6), we introduced additional constants with the dimensions of velocity:

$$\begin{gathered}\alpha_\parallel^2 = (\lambda_\parallel + 2\mu_\parallel)/\rho;\quad \alpha_\perp^2 = (\lambda_\perp + 2\mu_\perp)/\rho;\\ \alpha_*^2 = (\lambda_\perp + 2\mu_*)/\rho;\quad \beta_*^2 = \mu_*/\rho,\end{gathered}\tag{7}$$

where $\alpha_\perp$ is the velocity of the longitudinal wave along the symmetry axis, $\alpha_\parallel$ is the velocity of the longitudinal wave in the plane perpendicular to the symmetry axis, and β_* is the velocity of the transverse wave in any of these mutually orthogonal directions. It is common practice to express these four independent constants through four independent constants $\alpha_\perp$, ε, δ, and f [13]. The relationship between the parameter sets ($\alpha_\perp$, $\alpha_\parallel$, α_*, β_*) and ($\alpha_\perp$, ε, δ, f) is given in the Appendix.

As can easily be seen, only four independent constants appear in Eqs. (6), although the Hooke law (Eqs. (2)) includes five independent constants. The reason for this is that we consider only the waves polarized in the vertical plane (the r, z plane) and omit the *SH*-waves polarized in the azimuth direction.

System (6) is the system of linked equations for the potentials. It is well known that fundamental solutions to the wave equation in a transversely isotropic medium are represented as quasi-longitudinal *qP*- and quasi-transverse *qS*-waves [1]. In the general case, the wave motion in an anisotropic medium does not allow splitting into purely longitudinal and transverse waves, excluding some special directions.

To solve system (6), we apply the Fourier transform with respect to both the z coordinate and the time t and the Fourier–Bessel transform with respect to the r coordinate; i.e, we apply the transform $(t, z, r) \longrightarrow (\omega, k_z, k_r)$, where the Fourier–Bessel transform with respect to the r coordinate is defined as

$$f(k_r) = \int_0^{+\infty} rdr\, f(r) J_0(k_r r)$$
$$\Leftrightarrow f(r) = \int_0^{+\infty} k_r dk_r\, f(k_r) J_0(k_r r),$$

where $J_0(x)$ is the zero-order Bessel function. Changing the variables according to the rules $k_r = \omega p$ and $k_z = a\omega$, where p is treated as the horizontal component of the slowness vector [12], we obtain the system of linear equations for the potential transforms $\bar{\phi}$ and $\bar{\psi}$:

$$\begin{cases} \omega^2[1 - \alpha_\parallel^2 p^2 - \alpha_*^2 a^2]\bar{\phi} \\ - i\omega^3 a[1 - (\alpha_\parallel^2 - \alpha_*^2 + \beta_*^2)p^2 - \beta_*^2 a^2]\bar{\psi} = \dfrac{M_s(\omega)}{2\pi\rho} \\ - i\omega^3 a[1 - \alpha_*^2 p^2 - \alpha_\perp^2 a^2]\bar{\phi} + \omega^4 p^2 \\ \times [1 - \beta_*^2 p^2 - (\alpha_\perp^2 - \alpha_*^2 + \beta_*^2)a^2]\bar{\psi} = -i\omega a\dfrac{M_s(\omega)}{2\pi\rho}. \end{cases} \quad (8)$$

The solution to system (8) has the following form:

$$\bar{\phi} = \frac{M_s(\omega)}{2\pi\rho\omega^2}\frac{(p^2 + a^2)\lfloor 1 - \beta_*^2(p^2 + a^2)\rfloor - (\alpha_\perp^2 + \alpha_\parallel^2 - 2\alpha_*^2)p^2 a^2}{\Delta(a, p)};$$
$$\bar{\psi} = \frac{iM_s(\omega)}{2\pi\rho\omega^3}\frac{a\lfloor(\alpha_\parallel^2 - \alpha_*^2)p^2 + (\alpha_*^2 - \alpha_\perp^2)a^2\rfloor}{\Delta(a, p)}, \quad (9)$$

where $\Delta(a, p)$ is the determinant of system (8),

$$\Delta(a, p) = p^2[1 - \alpha_\parallel^2 p^2 - \alpha_*^2 a^2]$$
$$\times [1 - \beta_*^2 p^2 - (\alpha_\perp^2 - \alpha_*^2 + \beta_*^2)a^2]$$
$$+ a^2[1 - \alpha_*^2 p^2 - \alpha_\perp^2 a^2][1 - \beta_*^2 a^2 - (\alpha_\parallel^2 - \alpha_*^2 + \beta_*^2)p^2].$$

It can easily be shown that expressions (9) for the potentials are rearranged to the corresponding expressions for an isotropic medium when $\alpha_\parallel = \alpha_\perp = \alpha$ and $\beta_* = \beta$.

Now, we proceed to the wave field calculation for the transversely isotropic medium. The determinant $\Delta(a, p)$ is a bicubic polynomial (a sixth-degree polynomial) in a:

$$\Delta(a, p) = \alpha_\perp^2\beta_*^2(a^2 - a_1^2)(a^2 - a_2^2)(a^2 - a_3^2).$$

This polynomial can be represented in another form. Changing the variable $a^2 = c^{-2} - p^2$ and performing simple rearrangements, we obtain

$$\Delta(a, p) = \Phi(p)(p^2 + a^2)[1 - c_1^2(p)(p^2 + a^2)]$$
$$\times [1 - c_2^2(p)(p^2 + a^2)], \quad (10)$$

where $c_1(p)$ and $c_2(p)$ are the roots of the biquadratic dispersion equation

$$\Phi(p)c^4 - 2\alpha_\perp\beta_* Q(p)c^2 + \alpha_\perp^2\beta_*^2 = 0. \quad (11)$$

The coefficients in the biquadratic equation (11) are the functions of the horizontal slowness p and are given by the formulas

$$\Phi(p) = 1 + (\alpha_\perp^2 - \alpha_\parallel^2)p^2 + [(\alpha_*^2 - \alpha_\parallel^2)(\alpha_\perp^2 - \beta_*^2)$$
$$+ (\alpha_*^2 - \alpha_\perp^2)(\alpha_*^2 - \beta_*^2)]p^4,$$
$$Q(p) = (\alpha_\perp^2 + \beta_*^2 - [(\alpha_\perp^2 - \alpha_*^2)(\alpha_*^2 - 2\beta_*^2)$$
$$+ (\alpha_\parallel^2 - \alpha_*^2)\alpha_\perp^2]p^2)/(2\alpha_\perp\beta_*).$$

Taking into account expression (10) for the determinant, solutions (9) for the potentials can be represented in the form

$$\bar{\phi} = \frac{M_s(\omega)}{2\pi\rho\omega^2 c_1^2(p)c_2^2(p)}\frac{(p^2 + a^2)\lfloor 1 - \beta_*^2(p^2 + a^2)\rfloor - (\alpha_\perp^2 + \alpha_\parallel^2 - 2\alpha_*^2)p^2 a^2}{\Phi(p)(a^2 + p^2)[a^2 - (c_1^{-2}(p) - p^2)][a^2 - (c_2^{-2}(p) - p^2)]};$$
$$\bar{\psi} = \frac{iM_s(\omega)}{2\pi\rho\omega^3 c_1^2(p)c_2^2(p)}\frac{a\lfloor(\alpha_\parallel^2 - \alpha_*^2)p^2 + (\alpha_*^2 - \alpha_\perp^2)a^2\rfloor}{\Phi(p)(a^2 + p^2)[a^2 - (c_1^{-2}(p) - p^2)][a^2 - (c_2^{-2}(p) - p^2)]}. \quad (12)$$

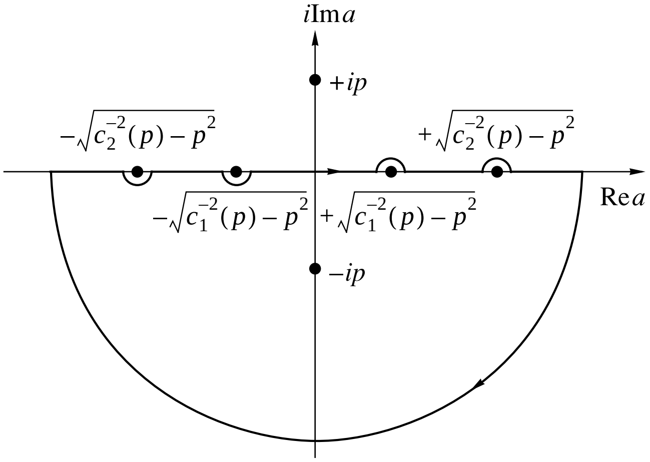

Fig. 1. Integration path and the rule of tracing around the poles for $z > 0$.

To calculate the displacement potentials, we carry out the inverse Fourier transform with respect to the variable $k_z = \omega a$ and apply the residue theorem. As can easily be seen, the right-hand sides of Eqs. (12) have simple poles at the points $a_{1,2} = \pm ip$, $a_{3,4} = \pm\sqrt{c_1^{-2}(p)-p^2}$, and $a_{5,6} = \pm\sqrt{c_2^{-2}(p)-p^2}$. Figure 1 shows the positions of these poles under the assumption that $a_{3,4}$ and $a_{5,6}$ are real. Taking into account that $a = \mathrm{Re}a + i\mathrm{Im}a$ and $\omega \ge 0$ and using the Jordan lemma, we obtain that the integration path should be closed in the lower half-plane for $z > 0$ and in the upper half-plane for $z < 0$. To correctly trace around the poles located on the real axis, one can use the limiting absorption principle [14], which shifts the poles away from the axis so that only waves outgoing from the source to infinity appear in the solution; i.e., this principle ensures the correct asymptotic behavior of the solution. As can easily be seen, the poles $a_1 = -ip$, $a_3 = +\sqrt{c_1^{-2}(p)-p^2}$, and $a_5 = +\sqrt{c_2^{-2}(p)-p^2}$ are encircled by the path for $z > 0$, and the poles $a_2 = +ip$, $a_4 = -\sqrt{c_1^{-2}(p)-p^2}$, and $a_6 = -\sqrt{c_2^{-2}(p)-p^2}$ are encircled by the path for $z < 0$. Performing the corresponding calculations and applying the inverse Fourier–Bessel transform with respect to the horizontal slowness p, we obtain the following result:

$$\phi(\omega, r, z) = -i\omega\Psi_s(\omega)\alpha_0^2\int_0^\infty \frac{pdp}{\Phi(p)}J_0(\omega pr)$$

$$\times\Bigg\{ip^3(\alpha_\perp^2+\alpha_\parallel^2-2\alpha_*^2)\exp(-\omega p|z|)$$

$$+\frac{1-\beta_*^2/c_1^2(p)-(\alpha_\perp^2+\alpha_\parallel^2-2\alpha_*^2)(1-c_1^2(p)p^2)p^2}{\sqrt{c_1^{-2}(p)-p^2}(c_2^2(p)-c_1^2(p))}$$

$$\times\exp(-i\omega\sqrt{c_1^{-2}(p)-p^2}|z|)$$

$$+\frac{1-\beta_*^2/c_2^2(p)-(\alpha_\perp^2+\alpha_\parallel^2-2\alpha_*^2)(1-c_2^2(p)p^2)p^2}{\sqrt{c_2^{-2}(p)-p^2}(c_1^2(p)-c_2^2(p))}$$

$$\times\exp(-i\omega\sqrt{c_2^{-2}(p)-p^2}|z|)\Bigg\}, \tag{13}$$

$$\psi(\omega, r, z) = \Psi_s(\omega)\alpha_0^2\mathrm{sgn}(z)\int_0^\infty\frac{pdp}{\Phi(p)}J_0(\omega pr)$$

$$\times\Bigg\{p^2(\alpha_\perp^2+\alpha_\parallel^2-2\alpha_*^2)\exp(-\omega p|z|)$$

$$+\frac{(\alpha_\perp^2+\alpha_\parallel^2-2\alpha_*^2)p^2+(\alpha_*^2-\alpha_\perp^2)/c_1^2(p)}{(c_2^2(p)/c_1^2(p)-1)}$$

$$\times\exp(-i\omega\sqrt{c_1^{-2}(p)-p^2}|z|)$$

$$+\frac{(\alpha_\perp^2+\alpha_\parallel^2-2\alpha_*^2)p^2+(\alpha_*^2-\alpha_\perp^2)/c_2^2(p)}{(c_1^2(p)/c_2^2(p)-1)}$$

$$\times\exp(-i\omega\sqrt{c_2^{-2}(p)-p^2}|z|)\Bigg\}.$$

One can see from relationships (13) that the potential ϕ is a symmetric function of z and the potential ψ is an antisymmetric function of z, which follows from the symmetry of the initial system of equations (6). In the limiting case of an isotropic medium, Eqs. (13) yield the well-known solution [12, 15]

$$\phi(\omega, r, z) = i\omega\Psi_s(\omega)\int_0^\infty\frac{pdp}{\sqrt{\alpha^{-2}-p^2}}J_0(\omega pr)$$

$$\times\exp(-i\omega\sqrt{\alpha^{-2}-p^2}|z|)$$

$$= \frac{\Psi_s(\omega)}{\sqrt{r^2+z^2}}\exp(-i\omega\sqrt{r^2+z^2}/\alpha); \quad \psi(\omega, r, z) = 0.$$

Substituting the above solutions for potentials (13) into Eqs. (5) and taking into account the fact that $\Delta_r J_0(\omega pr) = -\omega^2p^2J_0(\omega pr)$ and $\partial J_0(\omega pr)/\partial r = -\omega pJ_1(\omega pr)$, we obtain the solution to the problem on the wave generation by an explosion-type point source in an elastic transversely isotropic infinite medium in terms of the displacement components:

$$\begin{aligned} u_r(\omega, r, z) &= i\omega^2\Psi_s(\omega)\alpha_0^2\int_0^\infty \frac{p^2dp}{\Phi(p)}\frac{J_1(\omega pr)}{(c_2^2(p)-c_1^2(p))} \\ &\times\left\{\frac{1+(\alpha_\perp^2-\alpha_*^2)p^2+(\alpha_*^2-\alpha_\perp^2-\beta_*^2)/c_1^2(p)}{\zeta_1(p)}\right. \\ &\times\exp(-i\omega\zeta_1(p)|z|) \\ &-\frac{1+(\alpha_\perp^2-\alpha_*^2)p^2+(\alpha_*^2-\alpha_\perp^2-\beta_*^2)/c_2^2(p)}{\zeta_2(p)} \\ &\left.\times\exp(-i\omega\zeta_2(p)|z|)\right\}; \end{aligned} \tag{14}$$

$$\begin{aligned} u_z(\omega, r, z) &= -\omega^2\Psi_s(\omega)\alpha_0^2\operatorname{sgn}(z)\int_0^\infty \frac{pdp}{\Phi(p)} \\ &\times\frac{J_0(\omega pr)}{(c_2^2(p)-c_1^2(p))}\{[1-\beta_*^2/c_1^2(p)-(\alpha_\parallel^2-\alpha_*^2)p^2] \\ &\times\exp(-i\omega\zeta_1(p)|z|)-[1-\beta_*^2/c_2^2(p)-(\alpha_\parallel^2-\alpha_*^2)p^2] \\ &\times\exp(-i\omega\zeta_2(p)|z|)\}, \end{aligned}$$

where $\zeta_{1,2}(p) = \sqrt{c_{1,2}^{-2}(p)-p^2}$ are the vertical components of slowness. One can see that the inhomogeneous wave proportional to $(\alpha_\perp^2 + \alpha_\parallel^2 - 2\alpha_*^2)\exp(-\omega p|z|)$ appearing in solution (13) for the potentials disappears in solutions (14) for the displacement components. Expressions (14) contain both the quasi-longitudinal *qP*-wave and the quasi-transverse *qSV*-wave. Note that the problem under consideration can be solved without invoking the potentials. Namely, as follows from solution (14), the problem can be solved by using the Fourier–Bessel transform of the zeroth and first orders for the vertical and horizontal velocity components.

ASYMPTOTIC SOLUTION: THE METHOD OF STATIONARY PHASE

Further rearrangements of solutions (14) can be accomplished using the method of stationary phase to calculate asymptotically the integrals with respect to the horizontal slowness *p*. With this purpose in mind, we transform the integral with respect to the horizontal slowness *p* over the semi-infinite interval (0, +∞) into the integral over the whole real axis (–∞, +∞) by using the fact that the integrand is an even function [12]. Assuming the argument in the Hankel functions to be large $\omega pr \gg 1$ (which is identical to the condition $\lambda \ll r$, where λ is the wavelength of the radiated signal), we replace the Hankel functions in the expression for the displacement components with their asymptotic series expansions for large arguments:

$$H_0^{(2)}(\omega pr) \longrightarrow \frac{\exp(-i\omega pr+i\pi/4)}{\sqrt{2\pi\omega pr}},$$

$$H_1^{(2)}(\omega pr) \longrightarrow \frac{i\exp(-i\omega pr+i\pi/4)}{\sqrt{2\pi\omega pr}},$$

where $H_\nu^{(1)}(\omega pr)$ and $H_\nu^{(2)}(\omega pr)$ are the first- and second-kind Hankel functions of order ν. The stationary points are determined as the positions of the phase extrema in the exponential terms of solutions (14), $\exp[-i\omega(pr + \zeta_{1,2}(p)|z|]$, and satisfy the equation $d\zeta_{1,2}(p)/dp = -r/|z|$. Carrying out the differentiation, we find that the stationary points $p_{qP}(|z|/r)$ and $p_{qS}(|z|/r)$ are determined as the solutions of the following implicit equations:

$$p-\frac{1}{2}\frac{d}{dp}\left(\frac{1}{c_{1,2}^2(p)}\right) = \zeta_{1,2}(p)\frac{r}{|z|}. \tag{15}$$

Expanding the phases of exponents in the Taylor series near the stationary points $p_{qP}(|z|/r)$ and $p_{qS}(|z|/r)$ and calculating the integrals of the resulting exponents, we obtain

$$\begin{aligned} &\int_{-\infty}^{+\infty} dp\exp(-i\omega\zeta_{1,2}(p)|z|+pr) \longrightarrow \sqrt{\frac{2\pi}{\omega|z|}} \\ &\times\left|\frac{d^2}{dp^2}\zeta_{1,2}(p_{qP(S)})\right|^{-1/2}\exp\Big(-i\omega(\zeta_{1,2}(p_{qP(S)})|z| \\ &+p_{qP(S)}r)-i\frac{\pi}{4}\operatorname{sgn}\left(\frac{d^2}{dp^2}\zeta_{1,2}(p_{qP(S)})\right)\Big). \end{aligned} \tag{16}$$

Taking into account Eq. (16) and replacing the argument of the factors multiplying the exponents in the considered integrals with the stationary points, we obtain the final expression for the displacement components:

$$\begin{aligned} u_r &= \frac{\omega\Psi_s(\omega)\alpha_0^2}{2\alpha_\perp\beta_*\sqrt{|z|r}}\left\{\frac{p_{qP}^{3/2}}{\zeta_1(p_{qP})}\right. \\ &\times\frac{[1+(\alpha_\perp^2-\alpha_*^2)p_{qP}^2+(\alpha_*^2-\alpha_\perp^2-\beta_*^2)/c_1^2(p_{qP})]}{\sqrt{Q^2(p_{qP})-4\Phi(p_{qP})}} \\ &\times\left|\frac{d^2\zeta_1(p_{qP})}{dp^2}\right|^{-1/2}\exp\left(i\frac{\pi}{4}\left[1-\operatorname{sgn}\left(\frac{d^2\zeta_1(p_{qP})}{dp^2}\right)\right]\right) \\ &\times\exp(-i\omega(\zeta_1(p_{qP})|z|+p_{qP}r))-\frac{p_{qS}^{3/2}}{\zeta_2(p_{qS})} \end{aligned}$$

$$
\begin{aligned}
&\times \frac{[1 + (\alpha_\perp^2 - \alpha_*^2)p_{qS}^2 + (\alpha_*^2 - \alpha_\perp^2 - \beta_*^2)/c_2^2(p_{qS})]}{\sqrt{Q^2(p_{qS}) - 4\Phi(p_{qS})}} \\
&\times \left|\frac{d^2\zeta_2(p_{qS})}{dp^2}\right|^{-1/2} \exp\left(i\frac{\pi}{4}\left[1 - \operatorname{sgn}\left(\frac{d^2\zeta_2(p_{qS})}{dp^2}\right)\right]\right) \\
&\times \exp(-i\omega(\zeta_2(p_{qS})|z| + p_{qS}r)); \\
u_z &= \frac{\omega\Psi_s(\omega)\alpha_0^2\operatorname{sgn}(z)}{2\alpha_\perp\beta_*\sqrt{|z|r}} \qquad (17) \\
&\times \left\{ p_{qP}^{1/2}\frac{[1 - (\alpha_\parallel^2 - \alpha_*^2)p_{qP}^2 - \beta_*^2/c_1^2(p_{qP})]}{\sqrt{Q^2(p_{qP}) - 4\Phi(p_{qP})}} \right. \\
&\times \left|\frac{d^2\zeta_1(p_{qP})}{dp^2}\right|^{-1/2} \exp\left(i\frac{\pi}{4}\left[1 - \operatorname{sgn}\left(\frac{d^2\zeta_1(p_{qP})}{dp^2}\right)\right]\right) \\
&\times \exp(-i\omega(\zeta_1(p_{qP})|z| + p_{qP}r)) - p_{qS}^{1/2} \\
&\times \frac{[1 - (\alpha_\parallel^2 - \alpha_*^2)p_{qS}^2 - \beta_*^2/c_2^2(p_{qS})]}{\sqrt{Q^2(p_{qS}) - 4\Phi(p_{qS})}}\left|\frac{d^2\zeta_2(p_{qS})}{dp^2}\right|^{-1/2} \\
&\times \exp\left(i\frac{\pi}{4}\left[1 - \operatorname{sgn}\left(\frac{d^2\zeta_2(p_{qS})}{dp^2}\right)\right]\right) \\
&\times \exp(-i\omega(\zeta_2(p_{qS})|z| + p_{qS}r)).
\end{aligned}
$$

In deriving Eqs (17), we used the expression

$$c_1^2(p) - c_2^2(p) = 2\alpha_\perp\beta_*\sqrt{Q^2(p) - 4\Phi(p)}/\Phi(p),$$

which follows from dispersion equation (11).

If the second derivatives of $\zeta_{1,2}(p)$ with respect to the slowness are negative, solutions (17) can easily be represented in the time domain:

$$
\begin{aligned}
u_r(t, r, z) &= \frac{\dot{\Psi}_s(t - (\zeta_1(p_{qP})|z| + p_{qP}r))}{\alpha_\perp R_{qP}^r} \\
&+ \frac{\dot{\Psi}_s(t - (\zeta_2(p_{qS})|z| + p_{qS}r))}{\beta_* R_{qS}^r}; \\
u_z(t, r, z) &= \left[\frac{\dot{\Psi}_s(t - (\zeta_1(p_{qP})|z| + p_{qP}r))}{\alpha_\perp R_{qP}^z}\right. \qquad (18) \\
&\left. + \frac{\dot{\Psi}_s(t - (\zeta_2(p_{qS})|z| + p_{qS}r))}{\beta_* R_{qS}^z}\right]\operatorname{sgn}(z).
\end{aligned}
$$

The effective spreading factors (without separation of the angular factors) $R_{qP(S)}^{r,z}$ in Eq. (18) are

$$
\begin{aligned}
(R_{qP}^r)^{-1} &= \frac{\alpha_\perp^2}{2\beta_*\sqrt{|z|r}}\frac{p_{qP}^{3/2}}{\zeta_1(p_{qP})}\frac{[1 + (\alpha_\perp^2 - \alpha_*^2)p_{qP}^2 + (\alpha_*^2 - \alpha_\perp^2 - \beta_*^2)/c_1^2(p_{qP})]}{\sqrt{Q^2(p_{qP}) - 4\Phi(p_{qP})}}\left|\frac{d^2\zeta_1(p_{qP})}{dp^2}\right|^{-1/2}, \\
(R_{qS}^r)^{-1} &= -\frac{\alpha_\perp}{2\sqrt{|z|r}}\frac{p_{qS}^{3/2}}{\zeta_2(p_{qS})}\frac{[1 + (\alpha_\perp^2 - \alpha_*^2)p_{qS}^2 + (\alpha_*^2 - \alpha_\perp^2 - \beta_*^2)/c_2^2(p_{qS})]}{\sqrt{Q^2(p_{qS}) - 4\Phi(p_{qS})}}\left|\frac{d^2\zeta_2(p_{qS})}{dp^2}\right|^{-1/2}, \\
(R_{qP}^z)^{-1} &= \frac{\alpha_\perp^2}{2\beta_*\sqrt{|z|r}}p_{qP}^{1/2}\frac{[1 - (\alpha_\parallel^2 - \alpha_*^2)p_{qP}^2 - \beta_*^2/c_1^2(p_{qP})]}{\sqrt{Q^2(p_{qP}) - 4\Phi(p_{qP})}}\left|\frac{d^2\zeta_1(p_{qP})}{dp^2}\right|^{-1/2}, \qquad (19) \\
(R_{qS}^z)^{-1} &= -\frac{\alpha_\perp}{2\sqrt{|z|r}}p_{qS}^{1/2}\frac{[1 - (\alpha_\parallel^2 - \alpha_*^2)p_{qS}^2 - \beta_*^2/c_2^2(p_{qS})]}{\sqrt{Q^2(p_{qS}) - 4\Phi(p_{qS})}}\left|\frac{d^2\zeta_2(p_{qS})}{dp^2}\right|^{-1/2}.
\end{aligned}
$$

In Eqs. (19), it is assumed that the amplitude of the elastic displacement potential is normalized so as to satisfy the equality $\alpha_0 = \alpha_\perp$.

Explicit expressions for the displacement field can be obtained for waves propagating along the directions $r = 0$ and $z = 0$. For a wave propagating along the z axis, we have $r = 0$ and $p = 0$. To eliminate the apparent singularity in Eqs. (17) at $r = 0$, we expand Eq. (15) for the stationary point in a series for $r \longrightarrow 0$ ($p \longrightarrow 0$). Taking into account the fact that $c_1(p = 0) = \alpha_\perp$, $c_2(p = 0) = \beta_*$, and $dc_{1,2}^{-2}/dp|_{p=0} = 0$, we obtain

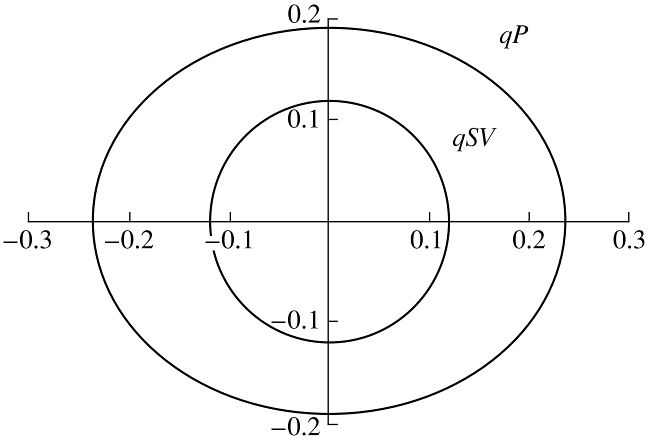

Fig. 2. Wave fronts for the quasi-longitudinal *qP*-wave and the quasi-transverse *qSV*-wave at $C = 0.05$.

$$\delta p_{qP} = \frac{1}{\alpha_\perp}\frac{r}{|z|}\left(1-\frac{1}{2}\frac{d^2}{dp^2}\left(\frac{1}{c_1^2}\right)\Bigg|_{p=0}\right)^{-1},$$

$$\delta p_{qS} = \frac{1}{\beta_*}\frac{r}{|z|}\left(1-\frac{1}{2}\frac{d^2}{dp^2}\left(\frac{1}{c_2^2}\right)\Bigg|_{p=0}\right)^{-1}.$$

Taking into account the above consideration and the fact that $\Phi(p = 0) = 1$, we arrive at the final result:

$$u_r = 0;$$
$$u_z = \frac{\dot{\Psi}_s(t-|z|/\alpha_\perp)}{\alpha_\perp z}\left(1-\frac{1}{2}\frac{d^2}{dp^2}\left(\frac{1}{c_1^2(p)}\right)\Bigg|_{p=0}\right)^{-1}. \qquad (20)$$

For a wave propagating along the r axis ($z = 0$), the solution to Eqs. (15) is $p_{qP} = 1/\alpha_\parallel$ and $p_{qS} = 1/\beta_*$. In this case, we must eliminate the singularities appearing in the factors $\zeta_1(p_{qP})$, $\zeta_2(p_{qS})$, $d^2\zeta_1(p_{qP})/dp^2$, and $d^2\zeta_2(p_{qS})/dp^2$. Performing the corresponding transformations, we obtain

$$u_r = \frac{\alpha_\perp^2\dot{\Psi}_s(t-r/\alpha_\perp)}{\alpha_\parallel^3 r\Phi(p=1/\alpha_\parallel)}\left|1-\frac{1}{2}\alpha_\parallel\frac{d}{dp}\left(\frac{1}{c_1^2(p)}\right)\Bigg|_{p=1/\alpha_\parallel}\right|^{-1/2}; \qquad (21)$$
$$u_z = 0.$$

As follows from Eqs. (20) and (21), only longitudinal waves propagate in the vertical and horizontal directions.

WAVE FRONT EQUATION FOR *qP*- AND *qSV*-WAVES: RESULTS OF CALCULATIONS FOR THE DISPLACEMENT FIELD

Let us derive the equations describing the wave fronts (the surfaces of equal phase) for the quasi-longitudinal *qP*-waves and the quasi-transverse *qSV*-waves. From solutions (17), it follows that the wave front equation for both *qP*- and *qSV*-waves can be found as the solution to the implicit system

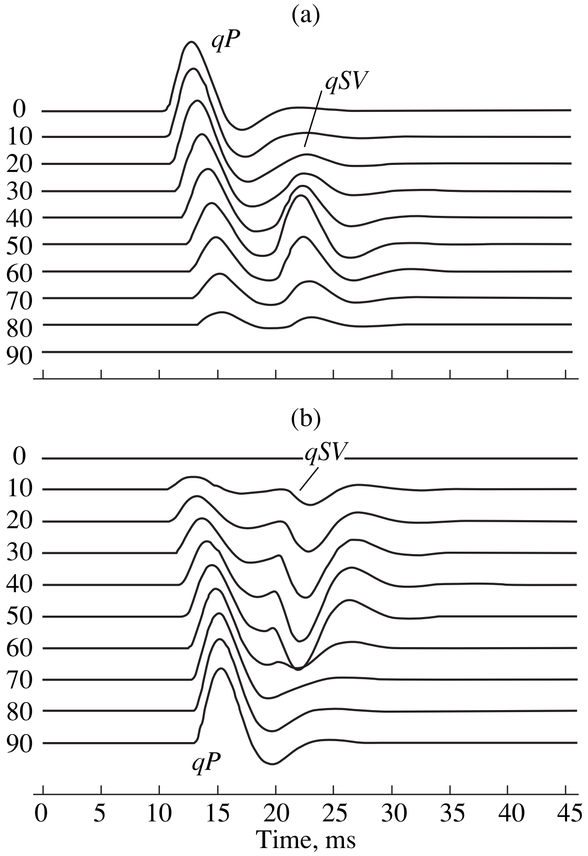

Fig. 3. (a) Vertical and (b) horizontal displacement components in the Bakken shale transversely isotropic medium for the distance $r = 50$ m.

$$\begin{cases}\zeta_{1,2}(p)|z| + pr = C\\ p-\dfrac{1}{2}\dfrac{d}{dp}\left(\dfrac{1}{c_{1,2}^2(p)}\right) = \zeta_{1,2}(p)\dfrac{r}{|z|},\end{cases} \qquad (22)$$

where C is an arbitrary constant. One would solve system (22) by determining the quantities $p_{qP}(|z|/r)$ and $p_{qS}(|z|/r)$ from the second equation and substituting the resulting expressions into the first equation. However, this method is inconvenient, because the functions $p_{qP}(|z|/r)$ and $p_{qS}(|z|/r)$ cannot be determined in an explicit form. A more efficient approach consists in solving the first equation for $|z|$ and substituting the result in the second equation. Then, we obtain an equivalent system that is more convenient for calculations:

$$\begin{cases}\left[\dfrac{1}{c_{1,2}^2(p)}-\dfrac{1}{2}p\dfrac{d}{dp}\left(\dfrac{1}{c_{1,2}^2(p)}\right)\right]r/C = p-\dfrac{1}{2}\dfrac{d}{dp}\left(\dfrac{1}{c_{1,2}^2(p)}\right)\\ |z| = C\dfrac{1-pr/C}{\zeta_{1,2}(p)}.\end{cases} \qquad (23)$$

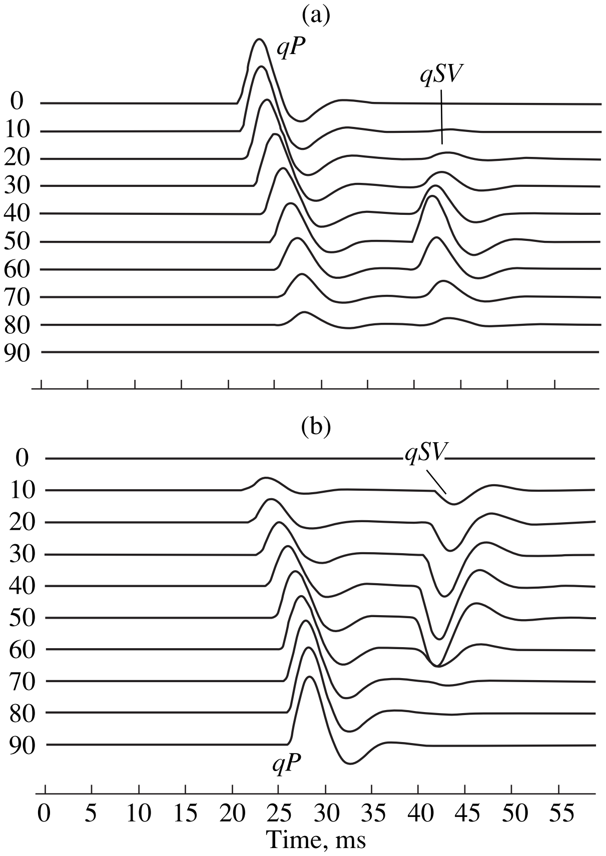

Fig. 4. (a) Vertical and (b) horizontal displacement components in the Bakken shale transversely isotropic medium for the distance r = 100 m.

The first equation of system (23) is solved using a numerical procedure to determine $p_{qP}(r/C)$ and $p_{qS}(r/C)$, which are then substituted into the second equation to determine z. Using system (23), one can easily find the edge points of the wave fronts of qP- and qS-waves. For $r = 0$ ($p_{qP} = 0$ and $p_{qS} = 0$), we find $|z^{qP}_{\max}| = \alpha_\perp C$ and $|z^{qS}_{\max}| = \beta_* C$. For $z = 0$ ($p_{qP} = 1/\alpha_\parallel$ and $p_{qS} = 1/\beta_*$), we obtain $|r^{qP}_{\max}| = \alpha_\parallel C$ and $|r^{qS}_{\max}| = \beta_* C$. Figure 2 shows the calculated wave fronts for a “Bakken shale” transversely isotropic medium with the parameters $\alpha_\perp = 3.85$ km/s, $\varepsilon = 0.26$, $\delta = 0.15$, and $f = 0.61$ [4]. For this medium, the behavior of the front of the quasi-longitudinal wave resembles an ellipsoid of revolution and the front of the quasi-transverse wave resembles an oblate sphere.

Figures 3 and 4 show results calculated from Eqs. (17), (20), and (21) for the vertical and horizontal displacement components in the same medium (Bakken shale) for the distances r = 50 and 100 m. The ten paths shown in the figures correspond to different directions, from 0° (the vertical direction) to 90° (the horizontal direction) at a step of 10°. As Figs. 3 and 4 show, only longitudinal waves propagate in the horizontal and vertical directions. The maximal velocity of the quasi-transverse wave occurs in the direction near 45°, because the calculations show that the maximum occurs just in this direction. Figure 3 illustrates the formation of quasi-longitudinal and quasi-transverse waves. At longer distances (Fig. 4), these waves are split in the time of arrival and are easily visualized separately. In the calculations, we used the seismic source function (the velocity potential $\dot\Psi_s(t) = d\Psi_s(t)/dt$) in the form of the Berlage impulse often used for geophysical simulations:

$$\dot\Psi_s = \frac{(1+B^2)^2}{B} 2\pi^2 f_0^2 \Psi_\infty t \exp(-\Omega t) \sin(2\pi f_0 t)\Theta(t)$$

with frequency f_0 = 100 Hz and B = 0.7. Here, $B = \Omega/(2\pi f_0)$, $\Psi_\infty = \int_0^{+\infty} \dot\Psi_s(t)dt$ is the static value of the elastic displacement potential and $\Theta(t)$ is the Heaviside step function.

SUMMARY

In this paper, we obtained the exact and asymptotic solutions for the acoustic field generated by an isotropic pulsed point source in an infinite transversely isotropic elastic medium. The exact solution for the displacement field is obtained in the form of a double integral over the horizontal slowness and the frequency by using the method of integral transforms. We used the Fourier transform for both time and the vertical coordinate and the Fourier–Bessel transform for the radial coordinate. The calculation of the inverse Fourier transform with respect to the vertical slowness by using the residual theorem reduces the double integral to the linear one.

The calculation of the integral with respect to the horizontal slowness by the method of stationary phase reduces the exact solution to an asymptotic solution convenient for numerical calculations. We derived the formulas for calculating the spreading factors and the wave fronts of quasi-longitudinal qP- and quasi-transverse qSV-waves generated by an isotropic pulsed point source in an infinite transversely isotropic elastic medium. The wave fronts are described by a system of implicit equations.

APPENDIX

Five independent parameters are required to exhaustively describe the elastic properties of a transversely isotropic medium. Thomsen [16] was the first to suggest the parameters V_{P0}, V_{S0}, ε, δ, and γ, where V_{P0} and V_{S0} are the velocities of longitudinal and transverse waves propagating along the symmetry axis and ε, δ, and γ are the dimensionless parameters describing the deviations of the parameters of the anisotropic medium from those of an isotropic medium. The expressions relating these parameters to the elastic moduli of the medium can be found, for example, in [5, 13]. Here, we present only the relationships between them and the parameters used in this paper:

$$V_{P0} = \alpha_{\perp}, \quad V_{S0} = \beta_{*}, \quad \varepsilon = \frac{1}{2}\left(\frac{\alpha_{\parallel}^2}{\alpha_{\perp}^2} - 1\right),$$

$$\delta = \frac{(\alpha_{*}^2 - \beta_{*}^2)^2 - (\alpha_{\perp}^2 - \beta_{*}^2)^2}{2\alpha_{\perp}^2(\alpha_{\perp}^2 - \beta_{*}^2)},$$

$$\gamma = \frac{\beta_{\parallel}^2 - \beta_{*}^2}{2\beta_{*}^2}, \quad f = 1 - \beta_{*}^2/\alpha_{\perp}^2.$$

The parameters $\alpha_{\parallel}$, α_{*}, and β_{*} used in this paper and the parameter $\beta_{\parallel}$ characterizing the velocity of transverse *SH* waves polarized in the azimuthal direction can be expressed through the constants ε, δ, f, and γ:

$$\beta_{*}^2 = \alpha_{\perp}^2(1 - f), \quad \alpha_{\parallel}^2 = \alpha_{\perp}^2(1 + 2\varepsilon),$$

$$\alpha_{*}^2 = \alpha_{\perp}^2(1 - f + \sqrt{2f\delta + f^2}),$$

$$\beta_{\parallel}^2 = \alpha_{\perp}^2(1 - f)(1 + 2\gamma).$$

REFERENCES

1. J. E. White, *Underground Sound. Application of Seismic Waves* (Elsevier, Amsterdam, 1983).
2. G. I. Petrashen’, *Propagation of Waves in Anisotropic Elastic Media* (Nauka, Leningrad, 1984).
3. I. Tsvankin, Geophysics **62**, 1292 (1997).
4. S. Ryan-Grigor, Geophysics **62**, 1359 (1997).
5. C. M. Sayers, Geophysics **60**, 1933 (1995).
6. T. Alkhalifah, Geophysics **62**, 1839 (1997).
7. R. Sheriff and L. Geldart, *Exploration Seismology* (Cambridge Univ. Press, Cambridge, 1982; Mir, Moscow, 1987).
8. I. D. Tsvankin and E. M. Chesnokov, J. Geophys. Res. B **95**, 11317 (1990).
9. I. D. Tsvankin and E. M. Chesnokov, Geophys. J. Int. **101**, 497 (1990).
10. A. V. Bakulin and L. G. Tyurikov, Akust. Zh. **42**, 741 (1996) [Acoust. Phys. **42**, 651 (1996)].
11. A. S. Vshivtsev, A. V. Tatarintsev, and E. M. Chesnokov, Fiz. Zemli, No. 9, 80 (1994).
12. K. Aki and P. G. Richards, *Quantitative Seismology. Theory and Methods* (Freeman, San Francisco, 1980; Mir, Moscow, 1983).
13. I. Tsvankin, Geophysics **61**, 467 (1996).
14. V. S. Vladimirov, *Equations of Mathematical Physics* (Dekker, New York, 1971; 4rd ed., Nauka, Moscow, 1981).
15. L. M. Brekhovskikh, *Waves in Layered Media* (2nd ed., Nauka, Moscow, 1973; Academic, New York, 1980).
16. L. Thomsen, Geophysics **51**, 1954 (1986).

Translated by A. Vinogradov

Acoustical Physics, Vol. 47, No. 3, 2001, pp. 262–267. Translated from Akusticheskiĭ Zhurnal, Vol. 47, No. 3, 2001, pp. 313–319.
Original Russian Text Copyright © 2001 by Borodina, Petukhov.

Space–Frequency Interference Structure of Acoustic Fields in Oceanic Waveguides

E. L. Borodina and Yu. V. Petukhov

Institute of Applied Physics, Russian Academy of Sciences,
ul. Ul'yanova 46, Nizhni Novgorod, 603600 Russia
e-mail: petukhov@hydro.appl.sci-nnov.ru

Received June 13, 2000

Abstract—Laws manifesting themselves in the formation of the space–frequency distribution of the intensity of the acoustic field generated by a point source of wide-band radiation are considered. Most attention is concentrated on the study of the effect of diffraction focusing on the formation of the interference structure of the acoustic field. *© 2001 MAIK "Nauka/Interperiodica".*

A space–frequency interference structure is formed in the course of the propagation of acoustic waves in oceanic waveguides. This structure is characterized by the presence of the lines of the maximal values of the field intensity $J(f, r)$ in the f–r plane, where f is the radiation frequency and r is the horizontal distance [1–6]. From the condition of the interference of the modes with the numbers l and m, it is possible to determine the equation for the corresponding interference lines $r_{l,m}(f)$. This equation has the form [5, 7–10]

$$r_{l,m} = pR_{l,m} \quad (p = 1, 2, \ldots). \tag{1}$$

Here, the quantity

$$R_{l,m} = 2\pi/|k_l - k_m| \tag{2}$$

corresponds to the period of interference of the modes under consideration with the horizontal wave numbers k_l determined from the dispersion equation for each specific waveguide.

Each interference line given by Eq. (1) has a certain inclination angle with the tangent $\beta_{l,m}$ determined by the expression following from Eq. (1) [5]:

$$\beta_{l,m} = \frac{r_{l,m}}{\omega}\Big/\frac{dr_{l,m}}{d\omega} = -\frac{v_l}{c_l}\frac{1 - c_l/c_m}{1 - v_l/v_m}, \tag{3}$$

where c_l and v_l are the corresponding values of the phase and group velocities of modes,

$$c_l = \omega/k_l, \quad v_l = d\omega/dk_l, \tag{4}$$

and $\omega = 2\pi f$ is the cyclic frequency.

At certain conditions that were considered in detail earlier [1, 5, 6, 11], we can ignore the dependence $\beta_{l,m}$ on the mode numbers and on the radiation frequency in Eq. (3). This provides an opportunity to treat the quantity $\beta_{l,m}$ approximately as an invariant that has a certain value $\beta_{l,m} \approx \beta$ characteristic of a fixed group of modes in a corresponding oceanic waveguide [1, 6, 7, 11].

The major laws manifesting themselves in the formation of a space–frequency interference structure of acoustic fields in deep- and shallow-water oceanic waveguides were investigated quite extensively in the papers cited above [1–11]. However, insufficient attention was given to the study of the possible effect of the diffraction focusing of acoustic beams on the behavior of $J(f, r)$. The manifestation of this effect in oceanic waveguides was considered exhaustively only for the case of their excitation by a source of tone radiation [12–15].

This is precisely the reason why the purpose of this study is the investigation of the effect of diffraction focusing on the formation of the space–frequency interference structure of acoustic fields in multimode oceanic waveguides.

As is well known (see [12–15]), in the case of a fixed radiation frequency, the diffraction focusing of the field is most pronounced within certain intervals of horizontal distances

$$mR_{\min} \le r \le mR_{\max} \quad (m = 1, 2, \ldots). \tag{5}$$

If we consider only the well predictable (and, therefore, being of most interest) large-scale interference structure formed by the neighboring pairs of interfering modes, the expressions for the minimal $R_{\min}$ and the maximal $R_{\max}$ periods of such a focusing will have the form [12–15]

$$\begin{aligned} R_{\min} &= \min\{R_g(l, l+1; l+1, l+2)\}, \\ R_{\max} &= \max\{R_g(l, l+1; l+1, l+2)\}. \end{aligned} \tag{6}$$

Here, the quantity

$$R_g(l, l+1; l+1, l+2) = \frac{R_{l,l+1}R_{l+1,l+2}}{|R_{l,l+1} - R_{l+1,l+2}|} \tag{7}$$

corresponds to the period of the rearrangement of the interference structure of the field formed by the neighboring pairs of interfering modes with the periods of interference $R_{l,\,l+1}$ and $R_{l+1,\,l+2}$ (see Eq. (2)).

It is quite natural that the smaller the value of the difference

$$\Delta R = R_{\max} - R_{\min} \tag{8}$$

of the corresponding maximal and minimal periods (Eqs. (6)) (i.e., $\Delta R/R_{\min} \ll 1$), the more pronounced the diffraction focusing of the tonal radiation with the spatial period $R_{\max}$ in a plane-layered oceanic waveguide. However, even in the case of a large difference between the values of $R_{\max}$ and $R_{\min}$ (Eqs. (6)) when the value of the corresponding ratio is comparable to unity, $\Delta R/R_{\min} \approx 1$, the diffraction focusing can be noticeable for certain groups of modes carrying the major part of energy with relatively small changes in the value of $R_g(l,\, l+1;\, l+1,\, l+2)$. In this case, the greater the number of modes $L_m = l_b - l_s$ in each such group $l_s \le l \le l_b$, the more noticeable the diffraction focusing of the acoustic field in the corresponding intervals of horizontal distances:

$$mR_s \le r \le mR_b, \tag{9}$$

where

$$\begin{gathered} R_s = \min\{R_g(l, l+1;\, l+1, l+2)\}, \\ R_b = \max\{R_g(l, l+1;\, l+1, l+2)\}, \\ (l_s \le l \le l_b), \end{gathered} \tag{10}$$

and l_s and l_b correspond to the boundary values of the mode numbers characterizing a specific group.

From the aforesaid (see expressions (5)–(10)), it follows that, in plane-layered oceanic waveguides, the characteristic features caused by the effect of diffraction focusing can be observed in the formation of the space–frequency distribution of the intensity $J(f, r)$ of the acoustic field excited by a point source of wideband acoustic radiation. Namely, the interference lines (Eq. (1)) for the corresponding mode groups concentrate in the f–r plane in certain intervals of horizontal distances (see conditions (5) or (9)). As a result, in the f–r plane, the interference lines $r_{l,\,m}$ (of the first order) form other (probably wider) interference structures $r_g(l, m)$ (of the second order) characteristic of each waveguide and these structures are also associated with the maximal values of the intensity of the acoustic field.

The width of the newly formed interference structures $r_g(l, m)$ depends on the number of modes L_m effectively forming the corresponding zones of the diffraction focusing of the acoustic field at each frequency and on the range of variation characterizing the tangent of the inclination angle $\beta_{l,\,m}$ of the first-order interference lines $r_{l,\,m}$ (Eq. (1)) for these modes.

In this connection, it is of interest to obtain the approximate analytical dependences of $\beta_{l,\,l+1}$ and $R_{\max}$ on the frequency of radiation for any simple model of an oceanic waveguide in order to compare the inclinations of the interference lines of the first order $r_{l,\,l+1}$ with the inclinations

$$\alpha_{l,\,l+1} = \frac{R_g}{\omega}\Big/\frac{dR_g}{d\omega} \approx \frac{R_{\max}}{\omega}\Big/\frac{dR_{\max}}{d\omega} \tag{11}$$

of the interference lines of the second order $r_g(l, l+1) = mR_g(l, l+1;\, l+1, l+2)$. Moreover, this would provide an opportunity to evaluate the positions of the spatial regions of the diffraction focusing of the acoustic field.

To do this, we consider the three simplest models of waveguides, namely: an isovelocity waveguide with a perfectly rigid bottom

$$n^2(z) = n_1^2(z) = 1 \quad (0 \le z \le H_1), \tag{12}$$

a subsurface waveguide

$$\begin{gathered} n^2(z) = n_2^2(z) = 1 + \varepsilon/\cosh^2(z/H_2) \\ (0 \le z \le \infty), \end{gathered} \tag{13}$$

and a parabolic waveguide

$$n^2(z) = n_3^2(z) = 1 - (z/H_3)^2 \quad (-\infty < z < \infty). \tag{14}$$

Here, $n(z)$ is the dependence of the refraction index of the acoustic waves on the depth z; H_1, H_2, and H_3 are the characteristic vertical scales of inhomogeneity of the corresponding waveguides; and $\varepsilon \ll 1$ is the parameter characterizing the maximal change in the refraction index in a subsurface waveguide (Eq. (13)).

For such models (Eqs. (12)–(14)), the analytical dependences for horizontal wave numbers are known [16]:

$$\begin{gathered} k_l = k\sqrt{1 - x_l}, \\ x_l = \begin{cases} \left(\dfrac{\pi(l - 1/2)}{kH_1}\right)^2, & n(z) = n_1(z) \\[2ex] \dfrac{2(l - 1/2)}{kH_3}, & n(z) = n_3(z), \end{cases} \end{gathered} \tag{15}$$

$$k_l = k\sqrt{1 + \varepsilon}\sqrt{1 + (\gamma - x_l)^2}, \quad n(z) = n_2(z), \tag{16}$$

where in Eq. (16)

$$\begin{gathered} x_l = \frac{2l - 1/2}{kH_2\sqrt{1 + \varepsilon}}, \\ \gamma = \sqrt{\varepsilon + (2k\sqrt{1 + \varepsilon}H_2)^{-2}}. \end{gathered} \tag{17}$$

Here, $k = \omega/c$, c is the minimal value of sound velocity, $x_l \le 1$ in Eq. (15), and $x_l \le \gamma$ in Eq. (16).

In considering the case of the multimode propagation, which is of major interest ($kH_1 \gg 1$, $\sqrt{\varepsilon}\, kH_2 \gg 1$, $kH_3 \gg 1$), we restrict our consideration to the modes of low numbers with the corresponding small grazing angles ($x_l \ll 1$). The introduction of this restriction is determined by the fact that the quantity $\beta_{l,\,m}$ (Eq. (3)) is an invariant in the asymptotic sense. Namely, as it is demonstrated in [5] and follows from the results presented in [6, 7, 11], this quantity does not depend on the radiation frequency and on the mode numbers only within the range of variation of ω that noticeably exceeds the critical frequencies ω_l of the corresponding modes, where the corresponding asymptotic dependences $k_l(\omega)$ are valid at $\omega_l/\omega \longrightarrow 0$. Naturally, the same restriction ($\omega_l/\omega \ll 1$) is retained in the case of the determination of the value of $\alpha_{l,\,l+1}$ (Eq. (11)).

Then, proceeding from Eq. (3) and using the approximate dependences that follow from Eqs. (15) and (16) and are obtained by expanding them in a series to the terms of the second order of smallness in x_l, we obtain

$$\beta_{l,\,l+1} = \begin{cases} 1-(\pi/kH_1)^2(l^2+1/4), & n(z) = n_1(z) \\ 1-8kH_2\sqrt{\varepsilon(1+\varepsilon)^3}(l+1), & n(z) = n_2(z) \\ 1+4kH_3l, & n(z) = n_3(z). \end{cases} \tag{18}$$

As follows from Eq. (18), within the framework of the waveguide models under consideration (Eqs. (12)–(14)), the quantity $\beta_{l,\,l+1}$ takes a definite value $\beta_{l,\,l+1} = \beta \approx 1$, which almost does not depend on the radiation frequency and the mode number in the multimode propagation conditions $kH_1 \gg 1$, only in the case of an isovelocity waveguide for modes with relatively small numbers. In this case, it is appropriate to consider the invariant $\beta_{l,\,l+1} = \beta$ of the space–frequency interference structure of the acoustic field. However, in the case of a subsurface and a parabolic waveguide (Eqs. (13) and (14)), which allow a refraction focusing of acoustic fields (see [16]), the quantity $\beta_{l,\,l+1}$ depends linearly on the radiation frequency and the mode number, and, therefore there is no sense in discussing any invariant for the interference lines of the first order in these situations. The latter conclusion means that the statement put forward by Grachev [11] about the existence of the corresponding invariant β in a parabolic waveguide where its inverse value is taken equal to zero ($\beta^{-1} = 0$, see [11]) is wrong.

Now let us proceed to the determination of the tangent of the inclination angle $\alpha_{l,\,l+1}$ of the second-order interference lines. To do this, we first find with the necessary precision the approximate dependences for the periods of interference of neighboring modes in the waveguides under consideration (Eqs. (12)–(14)):

$$n(z) = n_1(z){:}\ R_{l,\,l+1} \approx \frac{D_1/l}{1+\dfrac{\pi}{4kD_1}(4l^2+1)}, \tag{19}$$

$$D_1 = \frac{2}{\pi}kH_1^2;$$

$$n(z) = n_2(z){:}\ R_{l,\,l+1}$$

$$\approx \frac{\pi H_2\sqrt{(1+\varepsilon)/\varepsilon}}{1-\dfrac{2l+5/2}{\sqrt{\varepsilon(1+\varepsilon)^3}kH_2}-\dfrac{6l^2+15l+5}{(1+\varepsilon)^3(kH_2)^2}}; \tag{20}$$

$$n(z) = n_3(z){:}\ R_{l,\,l+1} \approx \frac{2\pi H_3}{1+\dfrac{l}{kH_3}+\dfrac{3l^2+1/4}{2(kH_3)^2}}. \tag{21}$$

Substituting Eqs. (19), (20), and (21) into Eq. (7), we obtain the approximate dependences for the spatial periods of the rearrangement of the interference structure formed by the neighboring pairs of modes:

$$n(z) = n_1(z){:}\ R_g(l, l+1; l+1, l+2)$$

$$\approx D_1\Big/\left[1+\frac{\pi}{4kD_1}(12l^2+12l+5)\right]; \tag{22}$$

$$n(z) = n_2(z){:}\ R_g(l, l+1; l+1, l+2)$$

$$\approx D_2\Big/\left[1+\sqrt{\varepsilon(1+\varepsilon)}\frac{\pi H_2}{D_2}\left(3l+\frac{21}{4}\right)\right], \tag{23}$$

$$D_2 = \frac{\pi}{2}kH_2^2(1+\varepsilon)^2;$$

$$n(z) = n_3(z){:}\ R_g(l, l+1; l+1, l+2)$$

$$\approx D_3\Big/\left[1+3\pi\frac{H_3}{D_3}(2l+1)\right], \quad D_3 = 2\pi kH_3^2. \tag{24}$$

Using Eqs. (22)–(24), we obtain from Eq. (11) that the tangent of the inclination angle of the second-order interference lines has the same value in all waveguides under consideration, and this value is approximately equal to unity. Thus, for $\omega_l/\omega \ll 1$, the quantity $\alpha_{l,\,l+1}$ is a real (in comparison with $\beta_{l,\,l+1}$) invariant of the spatial–frequency interference structure of the field in waveguides with a monotonic variation of the spatial period of interference of neighboring modes with their number (see Eqs. (19)–(21)).

It is natural that the analogous value $\alpha_{l,\,l+1} \approx 1$ is obtained when the expressions for the maximal spatial period of the diffraction focusing, which follow from Eqs. (22)–(24), are substituted into Eq. (11):

$$R_{\max} \approx \begin{cases} D_1, & n(z) = n_1(z) \\ D_2, & n(z) = n_2(z) \\ D_3, & n(z) = n_3(z). \end{cases} \tag{25}$$

The last observation provides an opportunity to generalize the statement on the invariance of the quantity $\alpha_{l,\,l+1}$ for a wide class of waveguides with monotonic dependences of $R_{l,\,l+1}$ on l and also to correct it for the waveguides with nonmonotonic dependences of $R_{l,\,l+1}$ with the corresponding extreme values $R_{l,\,l+1} = R_c$ at certain $l = l_c$. Indeed, assuming that, in the case of the multimode propagation of acoustic waves, the conditions of the applicability of the WKB approximation for the mode representation of the field in oceanic waveguides are satisfied, we can use the expressions for $R_{\max}$ obtained in [14] for the determination of the quantity $\alpha_{l,\,l+1}$ (Eq. (11)):

$$R_{\max} \approx \begin{cases} \dfrac{k}{2\pi}\max\left\{D_l^3/\left|\dfrac{dD_l}{d\xi_l}\right|\right\}, & \dfrac{dD_l}{d\xi_l} \neq 0 \\[2ex] \dfrac{k^2}{4\pi^2}\left\{D_l^4/\left|\dfrac{d^2D_l}{d\xi_l^2}\right|\right\}\Bigg|_{\xi_l = \xi_c}, & \dfrac{dD_l}{d\xi_l}\Bigg|_{\xi_l = \xi_c} = 0. \end{cases} \qquad (26)$$

Here, $D_l(\xi_l) \approx R_{l,\,l+1}$ is the dependence of the cycle length of the corresponding Brillouin rays on the ray parameter $\xi_l = k_l/k$ and $\xi_l = \xi_c$ is the value of this parameter corresponding to the mode with the number $l = l_c$ at which the extreme of the function $D_l(\xi_l)$ is attained. Then, we find from Eqs. (11) and (26) that, in oceanic waveguides with a monotonic dependence of the cycle length of the Brillouin rays on the ray parameter, the quantity $\alpha_{l,\,l+1} \approx 1$ is an invariant, whereas in oceanic waveguides with the corresponding nonmonotonic dependence $D_l(\xi_l)$, the value of $\alpha_{l,\,l+1}$ can vary within a given range $1/2 \le \alpha_{l,\,l+1} \le 1$ for $\omega_l/\omega \ll 1$.

Thus, for all really possible models of oceanic waveguides, the tangent of the inclination angle of the second-order interference lines in the case $\omega_l/\omega \ll 1$ varies in a much narrower range of values, $1/2 \le \alpha_{l,\,l+1} \le 1$, than the tangent of the inclination angle of the first-order interference lines, $-\infty < \beta_{l,\,l+1} < \infty$. This is just the reason why the quantity $\alpha_{l,\,l+1}$ rather than the quantity $\beta_{l,\,l+1}$ should be treated as an invariant of the space–frequency interference structure of acoustic fields in oceanic wavequides in the frequency range noticeably higher than the critical frequencies of the corresponding modes.

In the final part of this paper, we quantitatively illustrate the manifestation of the effect of the diffraction focusing on the formation of the space–frequency interference structure of the acoustic field by using the simplest model of an oceanic waveguide. In order to complement the results obtained by Petukhov [14] and to provide their "succession," we also use here a model in the form of an isovelocity water layer of thickness H with the sound velocity c and the density ρ, which overlies a liquid halfspace with the corresponding acoustic characteristics c_b and ρ_b.

The numerical calculations of the dependence of the spatial period characterizing the rearrangement of the interference structure of the neighboring pairs of modes R_g on their number l and on the space–frequency distribution of the intensity of acoustic field $J_0(f, r) = rJ(f, r)$ normalized to the geometric spread were conducted in the frequency range $290 \le f \le 300$ Hz for the same values of acoustic parameters as those used by Petukhov [14]: $H = 300$ m, $c = 1.45$ km/s, $\rho = 1 \times 10^3$ kg/m^3, $c_b = 1.7$ km/s, and $\rho_b = 1.6\,\rho$.

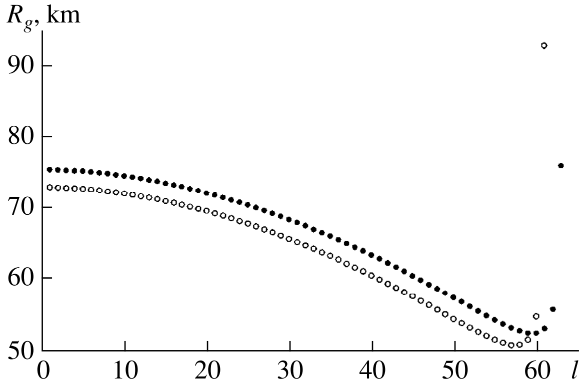

Fig. 1. Spatial period of the rearrangement of the interference structure of neighboring pairs of modes R_g (Eq. (7)) versus the mode number l at f = (○○○) 290 and (●●●) 300 Hz.

As follows from the dependences of R_g on l given in Fig. 1, the diffraction focusing of the acoustic field in its first zone ($m = 1$) must manifest itself most noticeably in the distance interval $59 \le r \le 76$ km. This is confirmed by the distributions $J_0(f, r)$ calculated for the same depths of the source z_s and the receiver z and shown in Figs. 2 and 3 in a brightness form with the dynamical range 15 dB. It is necessary to note the following laws. First, the number of the most intense interference lines of the second order in the first zone of the diffraction focusing at $z_s = 4.5$ (Fig. 2) and 9 m (Fig. 3) is completely determined by the corresponding beam structure of the spatial (in depth and horizontal distance) distribution of the intensity of the acoustic field, which was studied by Petukhov [14] (see Figs. 2, 3 there). Second, the position of the most intense interference line of the second order in the f–r plane, which manifests itself most noticeably at $z_s = 9$ m (see Fig. 3), is described by the equation $r = R_{\max} \approx D_1$ (see Eq. (25)).

It is also of interest to compare the behavior of the dependences of the quantities $\beta_{l,\,l+1}$ (Eq. (3)) and $\alpha_{l,\,l+1}$ (Eq. (11)) on l, which are given in Fig. 4. As one can see (from Fig. 4), the tangent of the inclination angle $\beta_{l,\,l+1}$ of the first-order interference lines varies in a much smaller range of values than the analogous value $\alpha_{l,\,l+1}$ for the second-order interference lines. However, at $l \longrightarrow 1$, both these quantities tend to the same value slightly exceeding unity. Here, it is necessary to note that the asymptotic behavior $\alpha_{l,\,l+1} \longrightarrow \beta_{l,\,l+1}$ at $l \longrightarrow 1$ occurs only in an isovelocity waveguide with a homogeneous bottom. The latter is also true for analogous models of waveguides with a perfectly rigid or perfectly soft bottom, where, at $l \longrightarrow 1$, the quantities

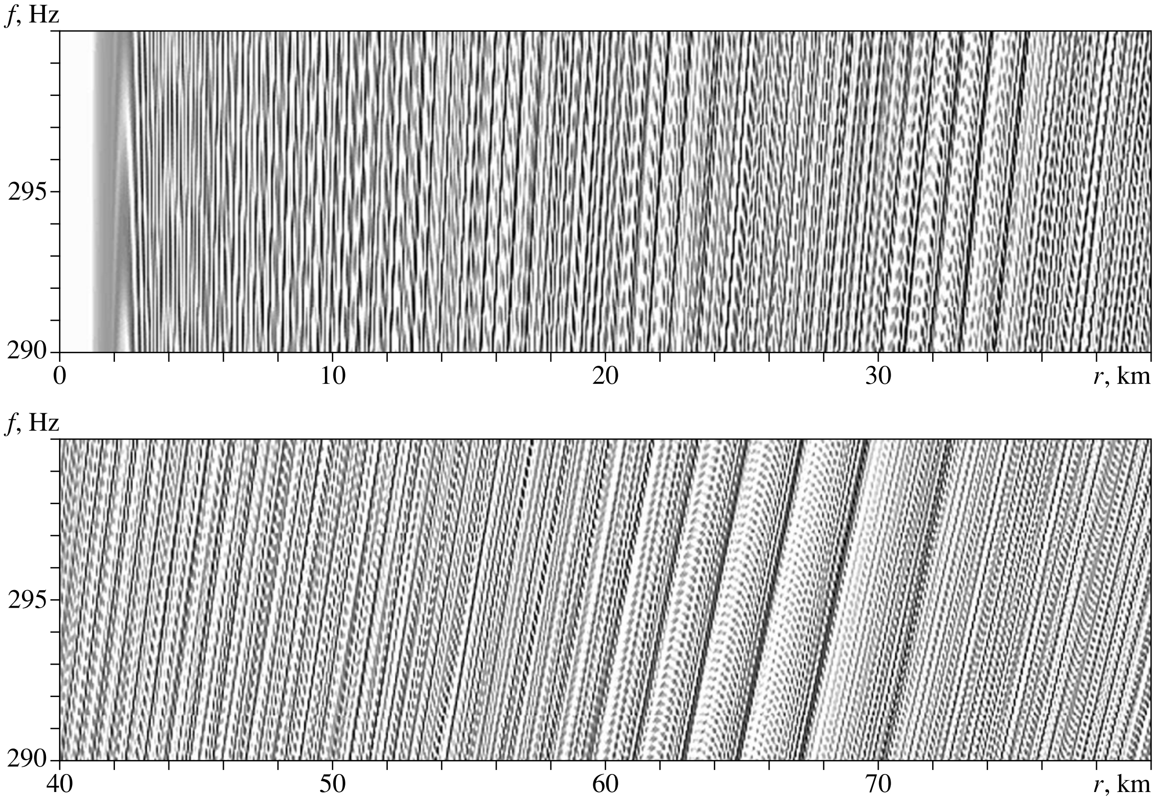

Fig. 2. Space–frequency distribution of the normalized intensity of the acoustic field J_0 (r, z) at $z_s = z = 4.5$ m.

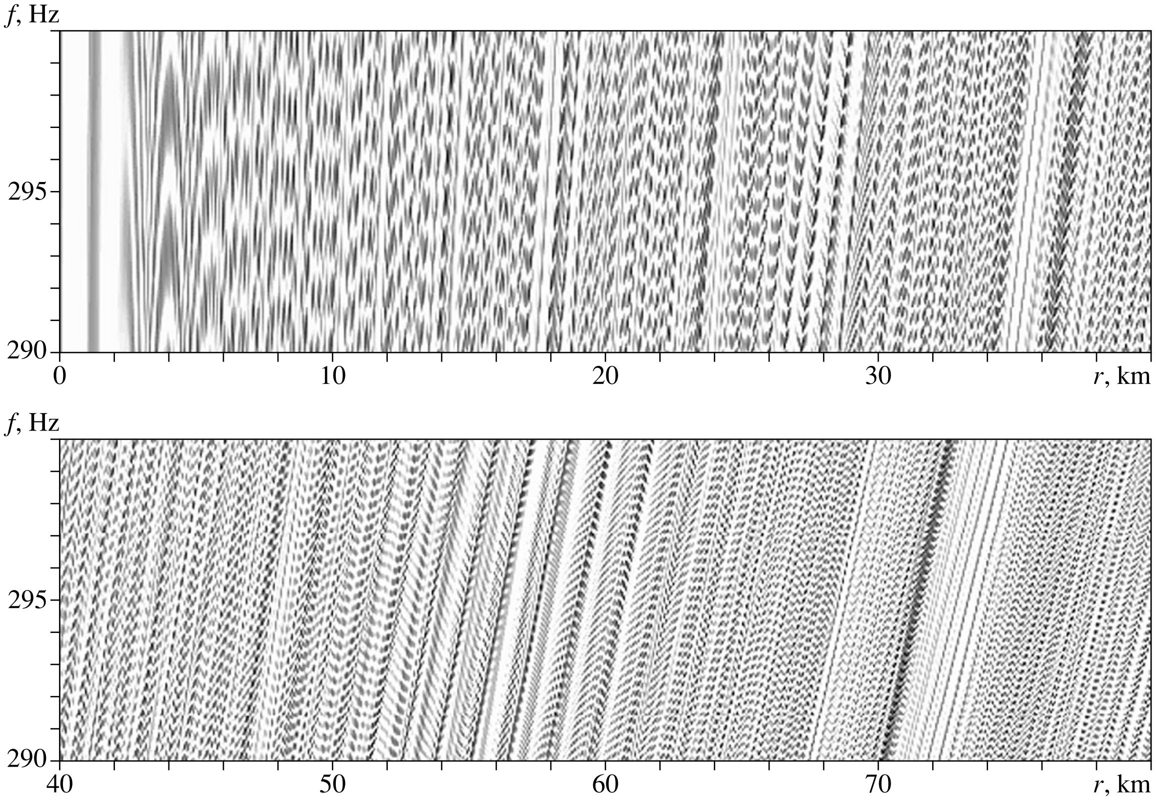

Fig. 3. Space–frequency distribution of the normalized intensity of the acoustic field J_0 (r, z) at $z_s = z = 9$ m.

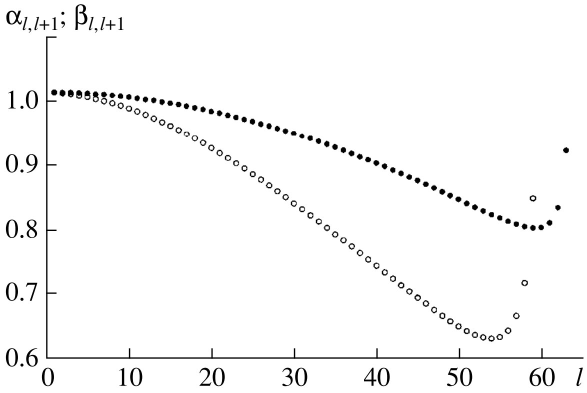

Fig. 4. Tangents of the inclination angles of the (●●●) first-order $\beta_{l,\,l+1}$ and (○○○) second-order $\alpha_{l,\,l+1}$ interference lines versus the mode number l at $f = 300$ Hz.

$\beta_{l,\,l+1}$ and $\alpha_{l,\,l+1}$ also take the same value, but this value is now slightly less than unity.

ACKNOWLEDGMENTS

This work was supported by the Russian Foundation for Basic Research, project no. 00-05-64604.

REFERENCES

1. N. E. Mal’tsev and S. D. Chuprov, Dokl. Akad. Nauk SSSR **275** (2), 475 (1981) [Sov. Phys. Dokl., No. 2 (1981)].
2. V. A. Baranov and V. S. Grigor’ev, Akust. Zh. **28**, 588 (1982) [Sov. Phys. Acoust. **28**, 349 (1982)].
3. I. G. Malkina and V. P. Shevtsov, Akust. Zh. **35**, 870 (1989) [Sov. Phys. Acoust. **35**, 506 (1989)].
4. I. G. Malkina and V. P. Shevtsov, Akust. Zh. **36**, 319 (1990) [Sov. Phys. Acoust. **36**, 173 (1990)].
5. V. N. Lobanov and Yu. V. Petukhov, Akust. Zh. **39**, 1093 (1993) [Acoust. Phys. **39**, 574 (1993)].
6. W. A. Kuperman and G. L. D’Spain, J. Acoust. Soc. Am. **106**, 2454 (1999).
7. G. K. Ivanova, Akust. Zh. **30**, 490 (1984) [Sov. Phys. Acoust. **30**, 293 (1984)].
8. K. J. Stevens and D. E. Weston, J. Sound Vibr. **21**, 57 (1972).
9. R. T. Bachman and G. T. Kay, J. Acoust. Soc. Am. **74**, 576 (1983).
10. W. Soares-Filho and M. L. Vianna, J. Acoust. Soc. Am. **79**, 76 (1986).
11. G. A. Grachev, Akust. Zh. **39**, 67 (1993) [Acoust. Phys. **39**, 33 (1993)].
12. D. I. Abrosimov and Yu. V. Petukhov, Akust. Zh. **46**, 5 (2000) [Acoust. Phys. **46**, 1 (2000)].
13. D. I. Abrosimov and Yu. V. Petukhov, Akust. Zh. **46**, 149 (2000) [Acoust. Phys. **46**, 113 (2000)].
14. Yu. V. Petukhov, Akust. Zh. **46**, 384 (2000) [Acoust. Phys. **46**, 327 (2000)].
15. Yu. V. Petukhov, Akust. Zh. **42**, 688 (1996) [Acoust. Phys. **42**, 606 (1996)].
16. L. M. Brekhovskikh, *Waves in Layered Media* (2nd ed., Nauka, Moscow, 1973; Academic, New York, 1960).

Translated by M. Lyamshev

Acoustical Physics, Vol. 47, No. 3, 2001, pp. 268–276. Translated from Akusticheskiĭ Zhurnal, Vol. 47, No. 3, 2001, pp. 320–329.
Original Russian Text Copyright © 2001 by Galkin, Shvachko.

Features of the Sound Field Structure in a Two-Channel Oceanic Waveguide

O. P. Galkin and L. V. Shvachko
Andreev Acoustics Institute, Russian Academy of Sciences, ul. Shvernika 4, Moscow, 117036 Russia
e-mail: bvp@akin.ru

Received June 20, 2000

Abstract—The results of experimental studies of the energy and angular structure of a sound field in the region of the Iberian Basin in the northeastern Atlantic are discussed. The experiments are carried out in a two-channel waveguide whose axes are located at depths of approximately 450 and 2000 m. A continuous pseudonoise signal in the frequency range 2.5–4.0 kHz is emitted. The signals are received by the omnidirectional hydrophones and, simultaneously, by a 10-m-long vertical array, which allows one to realize a narrow beam reception (~2.5°) in the vertical plane. The source and the receiver are located in a 500-m-thick layer within the upper sound channel. The field characteristics are measured in the course of a continuous change of distance from 1 to 65 km. The comparison of the experimental data with calculations shows that the sound field structure formed by the lower channel is much closer to the theoretical results than the structure formed by the upper channel. In the upper sound channel, the shadow zone manifests itself only slightly and the first convergence zone begins approximately 7–11 km nearer to the source than predicted by the calculations. The corresponding angular sound field structure is fairly pronounced in the vertical plane and bears no evidence of the random behavior that is peculiar to the fields scattered by the inhomogeneities. *© 2001 MAIK "Nauka/Interperiodica".*

One of the key problems in studying sound fields in the ocean is the determination of the correspondence between experimental data and the computational model [1–3]. The solution of this problem is necessary not only for developing an adequate waveguide model and increasing the reliability of hydroacoustic predictions, but also for successfully solving the tomography problems. The long-standing investigations carried out in various regions of the ocean have shown that, even in the stable conditions of a single-axis underwater sound channel of the tropical type, when the basic experimental and calculated dependences agree well, noticeable differences are observed in the fine structure of the sound field. First of all, this refers to the locations of the convergence and shadow zones and, especially, to the angular and temporal structure of the sound field [4–8].

The situation is much more complicated in the case of a biaxial underwater sound channel that occurs in many regions of the ocean. For example, such a channel is observed in the region of the Bermudas, off the eastern coast of North America, in the southern part of the Norway Sea, in the Iberian Basin off the Portugal coast, and in some other regions of the Atlantic ocean. In the first two regions, a two-channel system with the upper channel axis at a depth of 200–250 m is formed due to the appearance of an additional maximum in the sound velocity profile $C(z)$ at a depth of ~400–450 m, which is caused by the sloping front of the Gulf Stream. In the Iberian Basin, the upper minimum of $C(z)$ at a depth of ~450–500 m is caused by the warm Mediterranean waters of higher salinity penetrating into the Atlantic through the Gibraltar Strait and forming a deep-water sound velocity maximum at a depth of ~1200 m. As they were carried out in different years, the experimental studies of the sound velocity structure in these regions have shown that the extent of the agreement between the experimental data and the calculated field characteristics is much lower than for a single-axis underwater sound channel of the tropical type [1, 2, 7]. Note that these calculations were performed in the ray approximation, because the main body of the experimental data on the angular, temporal, energy, and correlation structure of the sound field was obtained for the signals in the frequency range 1–5 kHz. Such an approach is well justified, since, even for the maximal relative sound velocity gradients $\left(a = \frac{1}{C}\frac{\partial C}{\partial z}\right)$ that occur in the open ocean and for the above-mentioned frequencies (f), the validity conditions $\left(\frac{Ca}{2\pi f} \ll 1\right)$ of the ray theory are satisfied. The correspondence of ray and wave calculations for such situations was repeatedly verified (see, e.g., [3]). Moreover, the ray calculations allow one to easily obtain all the above-mentioned parameters of the field structure. Using other methods for solving the wave equation makes the problem of the determination of the angular spectrum of the arriving signals almost insolvable, especially if the frequency band of the signals in use exceeds two octaves.

1063-7710/01/4703-0268$21.00 © 2001 MAIK "Nauka/Interperiodica"

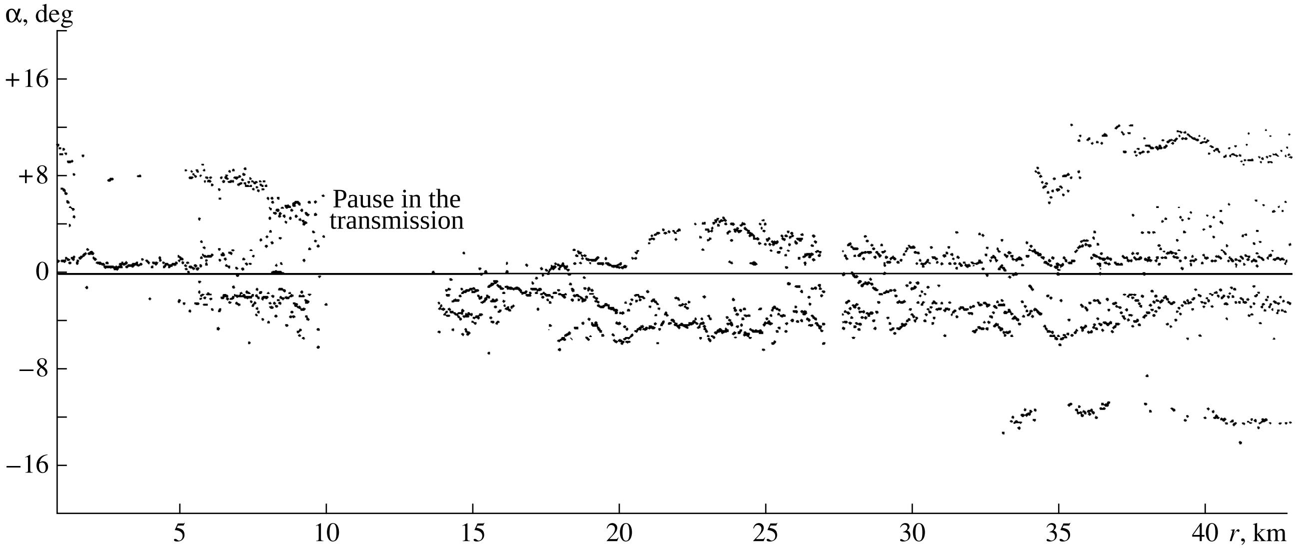

Fig. 1. Dependence of the arrival angles α on the distance *r*: +α corresponds to the signals arriving from above; –α corresponds to the signals arriving from below.

Let us consider the results of studying the energy structure and the angular spectrum of the sound field, which were obtained under conditions of the biaxial channel in the Iberian Basin of the Atlantic Ocean. By the angular spectrum we mean the dependence of the intensity of the received signals on the grazing angle in the vertical plane. The experiments were carried out in 1989 and 1991. The investigations (1989) have shown that the field structure formed by the signals propagating in the lower channel (with the axis at a depth of ~2000 m) agrees well with the computational model. The field structure in the upper channel with the axis at a depth of ~500 m noticeably differs from the results of calculations. According to theoretical views, the first convergence zone formed by the rays of the upper channel, with the source and receiver located at depths from 180 to 200 m, must begin at distances 28–30 km; at smaller distances (from 28 to 7 km), a geometric shadow zone must be formed. Figure 1 shows the experimental angular structure of the sound field, i.e., the dependence of the angular spectrum on the distance, α(*r*). From Fig. 1, one can see that the signals characterized by the arrival angles $\alpha \cong \pm 5°$ and propagating in the upper channel are recorded almost in the whole range of the distances *r* presented in this plot.

The results of the experiments of 1989 served as the basis for the detailed investigations of the features of sound propagation in the biaxial channel in the same region in December 1991, during the expedition with the research vessels *Akademik Nikolai Andreev* and *Akademik Boris Konstantinov* of the Andreev Acoustics Institute. The acoustic track was between the Ampere seamount and the Josephine seamount at the sea depth ~4800 m. The variability of the sound velocity profiles $C(z)$ measured down to a depth of 2300 m during 1.5 days in the test region is shown in Fig. 2a. The sound velocity profile $C(z)$ at which the sound field structure was studied and the ray pattern for the transmission depth 180 m are presented in Fig. 2b. It can be seen that the upper channel axis was at a depth of 450–500 m and the axis of the lower channel was at a depth of ~2000 m. As follows from the ray pattern, at this depth of the sound source, the sound field at the reception depths from 100 to 1200 m is determined by two groups of rays: the first group is completely within the upper sound channel and the second group spans the total waveguide depth. In this connection, it was necessary to determine the contribution of each group of rays to the sound field formation.

The experiment was carried out by a technique tested in many previous oceanic expeditions [2, 7]. A transmitting (almost omnidirectional) system was towed with a speed of about 6–7 k at a depth of ~180 m along a track from 1 to ~135 km long; i.e., the track covered the distances corresponding to the two convergence zones formed by rays spanning the total thickness of the waveguide. The signals were received by both the omnidirectional hydrophones located in the upper oceanic layer (from 160 to 500 m) and the 40-m-long vertical array with its center at a depth of $H_r \cong 186$ m. The signal reception was realized in the drifting mode of the receiving ship. The array allowed one to study the angular spectrum of the arriving signals in the vertical plane in the angular range ±23° in a broad frequency band. Because the source generated a continuous pseudonoise signal in the range of relatively high frequencies (2.5–4.0 kHz), the central part of the 10-m receiving array was used to form the array beam in the vertical plane. For the mean frequency of the range used ($f_{av} \cong 3.2$ kHz), the angular width of the main lobe was $\alpha_{0.7} \sim 2.4°$ (at the level 0.7). Note that the structure of the array was such that the angle of its deviation from

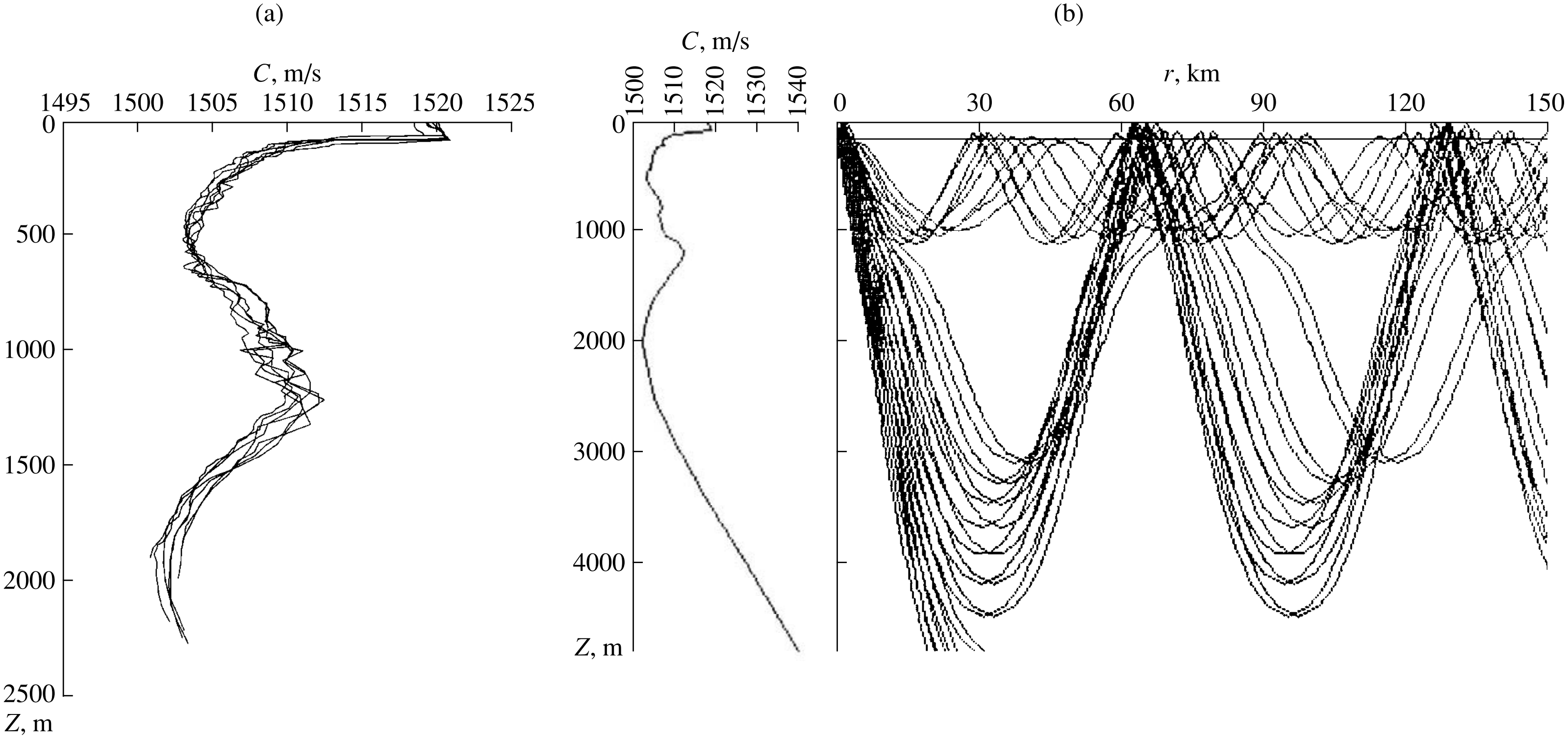

Fig. 2. (a) Variability of sound velocity profiles $C(z)$ over 1.5 days in the test region; (b) sound velocity profile $C(z)$ recorded during the experiments (at the left) and the ray pattern for the depth of radiation 180 m (at the right).

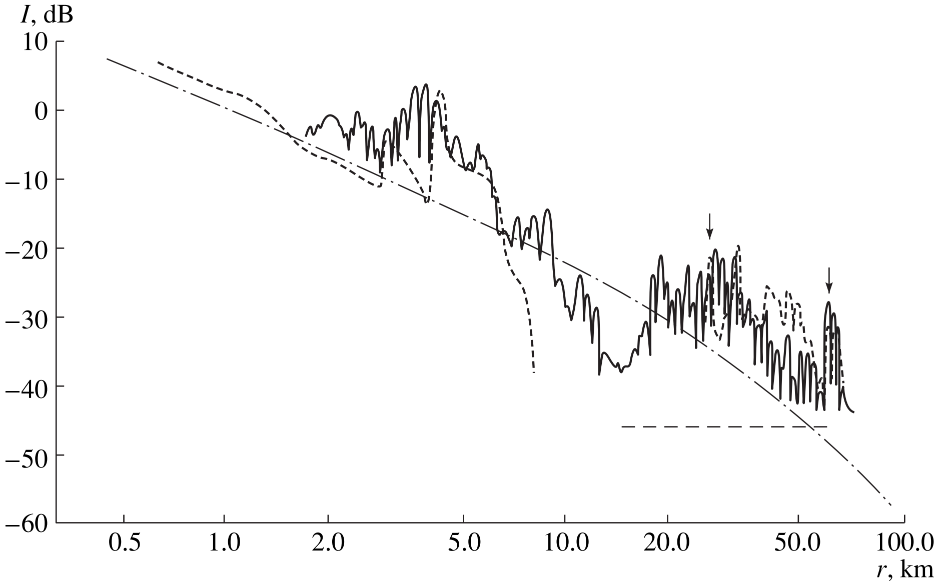

Fig. 3. Variation of the signal intensity $I(r)$ with distance in the case of the omnidirectional reception ($H_r \cong 186$ m) for a transmission depth of 180 m: experiment (the solid line) and calculation (the dotted line); the vertical arrows show the calculated positions of the beginnings of the first convergence zones formed by the signals propagating in the upper and lower channels.

the vertical line was less than 1°–1.5° at the maximal speed of the ship drift (~1.5–2.0 k). In processing the obtained data, some corrections (if necessary) were introduced, since the sloping angle of the array was determined with the use of specially developed precession inclinometers. In addition, the deviation of the array in the direction toward the source could be estimated from the difference in the arrival angles of two signals, one of which was reflected from the bottom and the other was reflected both from the bottom and the ocean surface. The problems of array deviations from the vertical line were considered in previous publications (see, e.g., [1, 8]). The distance between the transmission and reception points (but not between ships) was measured with a high accuracy with the use of a hydroacoustic system of the distance measurement [9]. To this end, in the system of unified time that was deployed aboard both ships, the continuous pseudonoise signal at certain times was mixed with short pulses of high intensity. Having determined the angles of the signal arrivals in the vertical plane and the propagation times of the pulses over respective rays at the receiving ship and using data on the sound velocity profile, the distance to the source was calculated.

It is the measurements of the energy and angular characteristics of the sound field at the initial part of the track (up to ~65 km) that holds specific interest. This part corresponds to the first shadow and first convergence zones for the signals propagating through the deep-water (lower) channel. At these distances (up to ~62 km), the best agreement was obtained between the experimental field structure and the results of calculations for the sound field formed by the upper channel. That is the reason why we will consider the results of the sound field studies only for the 65-km-long initial part of the track.

Figure 3 shows the results of measuring the energy structure of the field with the signal reception at a depth of $H_r \cong 186$ m with the use of an omnidirectional hydrophone (the central hydrophone of the vertical array). The sound field level at $r = 1$ km is taken as 0 dB for the spherical decay law of the sound intensity. The dot-and-dash line corresponds to the calculated values of the sound field variation with distance in the case of the spherical decay law with allowance for the sound attenuation in water that is equal to $\beta = 0.2$ dB/km for $f_{av} \cong$ 3.2 kHz. The experimental data are represented by the solid line and the results of calculation by the dotted line. The vertical arrows in the plot indicate the locations of the beginnings of the calculated convergence zones for the rays that do not leave the upper channel (~28 km) and for the rays spanning both the upper and the deep-water (~61 km) channels. As the experiment shows, the signals in the near zone were observed farther from the source than predicted by the calculations. The signal intensity noticeably decreases only starting from distances of ~9 km. In this case, the minimal signal level with the transmission anomaly $A \cong -(10\text{–}12)$ dB was recorded at distances of 13–14.5 km, which corresponds to the middle of the shadow zone for the rays trapped by the upper channel. According to the ray pattern in Fig. 2b, the first convergence zone in the upper channel at the reception depth (186 m) must begin at a distance of ~27–28 km. It should be noted that the whole set of the sound velocity profiles $C(z)$ presented in Fig. 1a, which characterizes the temporal variability of the medium within a time far exceeding the duration of the experiment, does not allow one to "shift" this calculated beginning of the zone. In spite of the ray pattern, the increase in the field intensity $I(r)$ began in the experiment from the distance $r \sim 16$ km; at the distance $r \cong 18$–19 km, the transmission anomaly was reached the value $A = +(6–9)$ dB. As the distance further increased, the intensity $I(r)$ was little changed on average, but it exhibited oscillations with the peak-to-peak amplitude reaching $\Delta I_{\max} \sim 10$–15 dB. The signal intensity at the distance corresponding to the calculated beginning of the convergence zone for the rays in the upper channel ($r \cong 27$–28 km) was not exceptional by its character against the high total sound field level ($A \cong +15$ dB). At distances exceeding 40 km, the field level began to decrease and reached the average values of the transmission anomaly $A_{\mathrm{av}} \cong +7$ dB. Such a value of the transmission anomaly was retained up to the distance $r \cong 59$ km. This distance is close to the calculated end of the shadow zone (~62 km) for signals propagating through the deep-water channel. At a distance of ~60 km, the first convergence zone began for the same rays. In this case, the sound field level increased up to $A \cong +20$ dB.

Thus, in contrast to the calculations, the total track in the experiment was almost completely insonified by the water signals up to the first convergence zone corresponding to the deep-water channel. The maximal discrepancy between the experimental and calculated structures was observed at distances from 7 to 28 km, where, according to the calculation, the first shadow zone for signals propagating only in the upper channel must be located.

For a more detailed study of the sound field in the upper channel, the energy characteristics of the received signals were investigated not only at a depth of 186 m, but at other depths within a 500-m-thick subsurface layer. Figure 4 shows the sound intensity $I(r)$ measured with omnidirectional reception at depths H_{r} equal to 166, 186, 206, and 500 m, at distances from 9 to 65 km. These distances correspond to the first shadow and first convergence zones for the signals propagating in the deep-water channel. At the depths 166, 186, and 206 m, the measurements were carried out using the upper, central, and lower hydrophones of the vertical array, the data in Fig. 4b corresponding to the dependence $I(r)$ presented in Fig. 3. The measurements at a depth of $H_{\mathrm{r}} \cong 500$ m were carried out with the use of the omnidirectional hydrophone. The experimental data are shown by the solid curves, and the results of calculations for the depths 186 and 500 m, by the dotted curves. As can be seen from these dependences $I(r)$, the general character of variations of the sound field structure with distance is identical for all depths of reception. For all depths, beginning from a distance of 9–11 km, a noticeable decrease in the signal intensity is observed, which corresponds to the end of the near insonified zone. At a depth of 186 m, such a decrease begins 2.0–2.5 km farther from the source than predicted by the calculation (see Fig. 3). At a depth of 500 m, these differences are insignificant (Fig. 4d). In the middle of the region with the reduced intensity, which was observed at all depths at the distance $r \sim 15$ km, the transmission anomaly increased with depth, from $A = -(13–10)$ dB in the layer where the vertical array was located (166–206 m) to the value $A = -(5–4)$ dB at a depth of 500 m. Then, starting from $r \cong 16$ km, an increase in the signal intensity was observed, which resulted in the formation of the first convergence zone for rays of the upper channel. Already at a distance of 17–18 km, the transmission anomaly increased up to $A = +(4–7)$ dB in the entire range of depths studied. At greater distances, the values of the anomaly continued to increase reaching 10–15 dB. As the distance increased up to the beginning of the convergence zone determined by the signals propagating in the lower channel ($r \sim 60$ km), the anomaly gradually decreased, being positive. Thus, under the real oceanic conditions, the distance from the source to the beginning of the first convergence zone in the upper channel proved to be shorter almost by 7–11 km than the distance predicted by the calculations (23–28 km) for all depths of reception. It should also be noted that the experimental dependences of the intensity on distance, $I(r)$, are in rather poor agreement with the corresponding calculations (see the dotted curves in Figs. 4b, 4d).

As is seen from the plots, the first convergence zone determined by the rays propagating through the deep-water channel begins at distances from 57 to 61 km, depending on the reception depth. The maximal value of the transmission anomaly weakly depends on the reception depth and varies from +20 to +18 dB as the depth increases. From comparing the experimental data for the beginning of the first convergence zone with the calculated values (the latter are marked by the vertical arrows in Fig. 4), we see that the discrepancies between them are much less than for the rays of the upper channel. The boundary of the beginning of the convergence zone in the experiment was nearer to the source only by 1.0–1.5 km than predicted by the calculation. Such a discrepancy between the calculated boundary of the zone and the experimental data obtained in real conditions was multiply observed in various regions of the ocean [1, 2, 7] and is common for the signals propagating in the deep-water channel.

The investigations of the angular spectra of the received signals were carried out with the use of scanning by the beam of a 10-m array in the angular range ±23°, the width of the main lobe being ~2.4°. The angular spectra of arriving signals were measured under a continuous variation of the distance from 1 to 65 km. This allowed one to obtain a detailed dependence of the arrival angles in the vertical plane on the distance, $\alpha(r)$, along the total acoustic track. The level ratio of the signals arriving at the point of reception at different angles allowed one to analyze the energy characteristics of the spectra. The dependence $\alpha(r)$ measured in the experiment was almost identical to that presented in Fig. 1, which was obtained in 1989 in the same region at almost the same depths of the corresponding points. In both cases, the signals with the

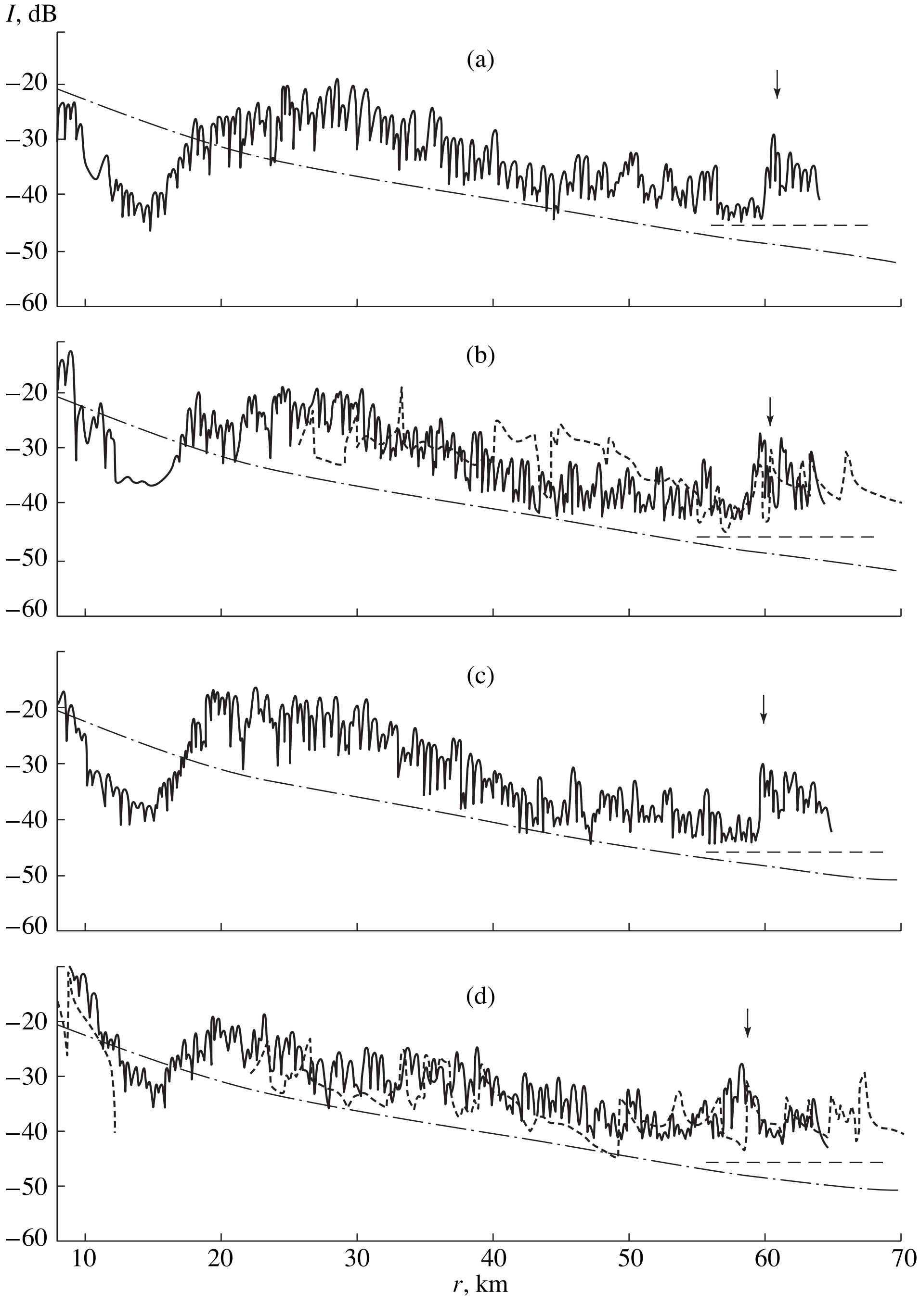

Fig. 4. Variation of the signal intensity $I(r)$ with distance in the case of the omnidirectional reception for a transmission depth of 180 m and the depth of reception $H_r \cong$ (a) 166, (b) 186, (c) 206, and (d) 500 m.

arrival angles $\alpha \cong \pm 5°$ insonified almost the whole shadow zone for the water rays of the deep-water channel, including (what is very important) the shadow zone for the water rays of the upper channel, which, according to the calculations, was located at distances from ~7 to ~28 km. The similar behavior of the experimental dependences $\alpha(r)$ obtained in the same region with an interval of about two years points to the relative stability of the sound field structure and its main characteristics, including those differing from the theoretical predictions.

It should be emphasized that, in both experiments (1989 and 1991), the shadow zone at distances from ~15 to ~28 km corresponding to the initial region of the intensity increase for the received signals was insonified not by randomly penetrating signals with unstable characteristics but by signals with a rather high intensity and with stable values of the arrival angles. In addi-

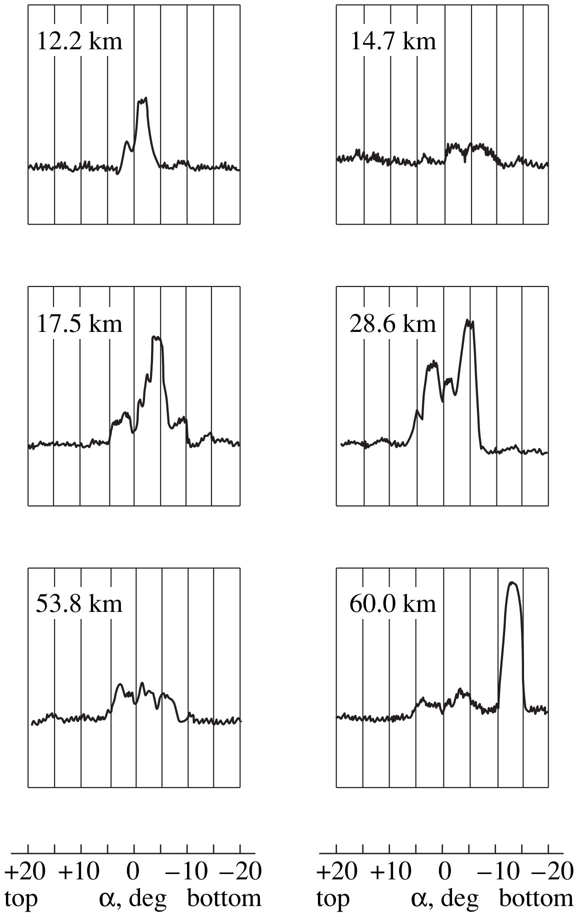

Fig. 5. Angular spectra of the received signals recorded on different parts of the track under test.

tion, the phase front of the received signals was close to a plane one (more exactly, the radius of curvature was large compared to the array size) within the total length of the vertical array or its major part. As a result, the array response only slightly differed from the response to a plane wave. All this means that the distances corresponding to the calculated position of the shadow zone are insonified by the signals arriving over a regular ray structure. If we take into account that, in the energy structure of the total field, i.e., the field recorded with the use of omnidirectional hydrophones, an almost synchronous rise of the intensity is observed at the same distances for all reception depths (see Fig. 4), we can state that the regular ray structure spans the entire range of depths (from ~160 to 500 m). It should be noted once again that these discrepancies between the experiment and the calculations cannot be corrected by allowing for the variability of the hydrological conditions, which was observed during the experiment (see Fig. 2a).

We dwell on the characteristics of the angular spectra of the received signals in more detail. Figure 5 presents some realizations of the angular field structure recorded at several distances along the track (12.2, 14.7, 17.5, 28.6, 53.8, and 60.0 km), these distances corresponding to the regions where the sound field considerably varies. Note that the angular spectra presented in Fig. 5 were recorded, except for two of them corresponding to the distances 17.5 and 28.6 km (below they will be considered in detail), with the same amplification of the receiving system, which was taken as 0 dB. The rotation angles α of the main array lobe in the vertical plane are plotted on the abscissa axis, and the received signal level is plotted on the ordinate axis. The angular spectrum at a distance of 12.2 km corresponds to the very end of the near insonified zone, which was located in the experiment beyond its calculated position (see the dotted curve in Fig. 3). At the angle $\alpha \cong -2.5°$, the signal arrived with the clearly defined front, as witnessed by the width of the array response, which almost coincides with the response to a plane wave ($\alpha_{0.7} \cong -2.4°$). In the experiment, the minimal sound field level was recorded at a distance of 14.7 km. On the noise background, one can see the signals with a low intensity in the region of shallow angles α, although these distances correspond to the zone of the geometric shadow. The angular spectrum at the distance $r = 17.5$ km refers to the beginning of the first convergence zone for rays of the upper channel (see Fig. 4). The angular spectrum is mainly determined by a well-defined intense signal arriving at the point of reception from below, at an angle of about 5°. For comparing with other spectra, the signal amplitude must be increased by 4 dB, since the amplification ratio of the receiving channel of the equipment was changed. The distance 28.6 km corresponds to the calculated beginning of the first convergence zone of the upper channel. However, the angular spectrum presented in Fig. 5 is a multiray one, which is specific for the middle of the convergence zone rather than for its beginning. Note that the signals received at a distance of 28.6 km were the most intense ones of those presented in Fig. 5. To perform the comparison, their amplitudes must be increased by 12 dB. The angular spectrum recorded at the distance $r = 53.8$ km refers to the part of the track with a relatively low level of the sound field intensity, immediately before the beginning of the first convergence zone for rays propagating through the deep-water channel (see Fig. 4). The last plot in Fig. 5 refers to the very beginning of the first convergence zone for the lower channel. At a distance of 53.8 km, the angular spectrum is formed by several groups of rays by which the signals propagate within the upper channel with the arrival angles $\alpha \sim \pm 5°$. At the distance $r = 60.0$ km, the main contribution to the sound field is made by the signal arriving from below, at the angle $\alpha \cong -12°$, which is characteristic of the beginning of the convergence zone. The other signals, which propagate only through the upper channel, are much weaker at this distance. It should also be noted that the energy characteristics of the signals in the angular spectra (Fig. 5) agree well with the level of the total sound field in the case of

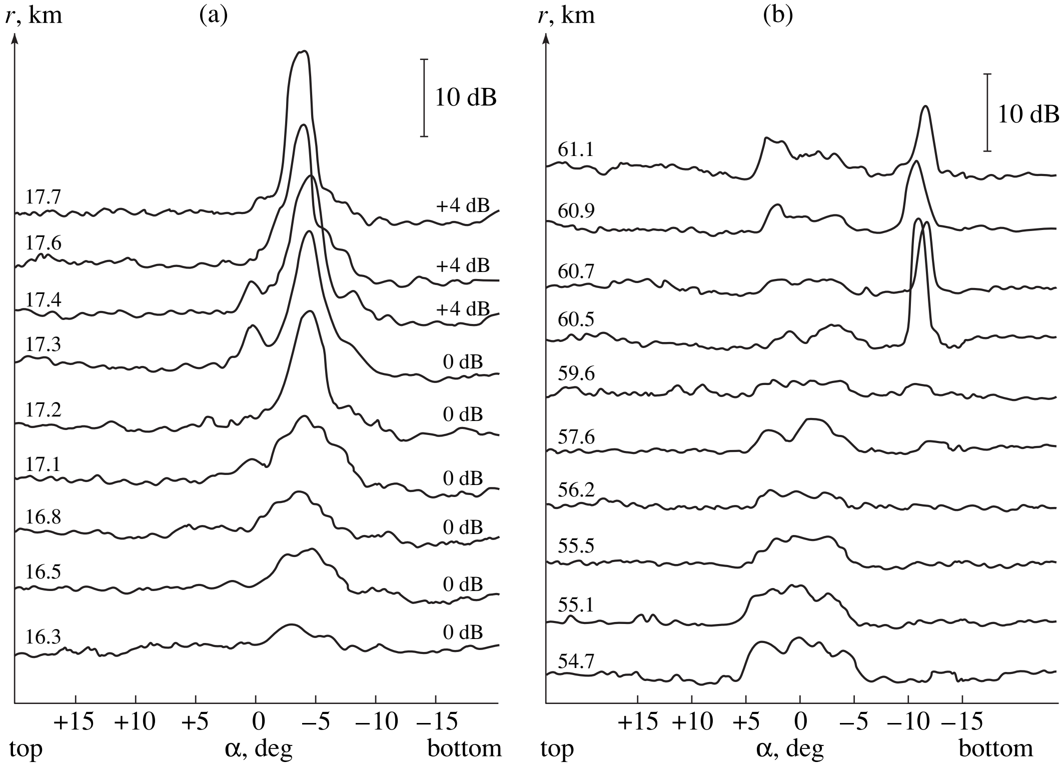

Fig. 6. Variations of the angular spectra of the received signals at the entrance to the first convergence zone (a) for the signals propagating in the upper channel only and (b) for the signals propagating in both the upper and the lower channels.

omnidirectional reception, $I(r)$, for a depth of 186 m (see Fig. 4b).

For some sound field regions that are of special interest, e.g., at the entrances to the convergence zones, we investigated in detail not only the individual angular spectra but the process of their variation as well. For this purpose, we analyzed the realizations of the angular spectra that were sequentially recorded as the distance varied. Consider two examples of such variations of the spectra for two parts of the track, which correspond to the distances from ~16 to ~18 km and from ~55 to ~61 km.

The analysis of the angular structure of the field showed that, starting from the distances of 13–14 km where the minimal values of the signal intensity were recorded for the total field (with omnidirectional reception), the angular spectra of the received signals begin to vary, which is related to the appearance of groups of rays indicating the approach to the convergence zone for the upper channel. These changes in the angular field structure can be observed in Fig. 6a where the sequence of the angular spectra of the signals recorded at distances from 16.3 to 17.7 km is presented. The signal arrival angles α in degrees are represented by the abscissa axis. On the left side of this figure, the distance from the sound source to the center of the receiving array located at a depth of 186 m is indicated for every realization. On the right side, the amplification ratios (in decibels) of the receiving channel are indicated. According to these coefficients, the signal levels at the distances 17.4 and 17.7 km must be increased by 4 dB to be compared with the signals recorded at smaller distances. From these angular spectra, it is seen that, beginning from a distance of 16.3 km (the first realization from below), the amplitude of the signal arriving from below at the angle ~2°–3° slowly increases; beginning from the distance $r = 17.2$ km, this increase is much accelerated. Such a rapid increase of the signal level points to the fact that the signal enters into the convergence zone, which starts with a caustic. The last angular spectrum in Fig. 6a (for $r = 17.7$ km) corresponds to the distance where the signal amplitude was maximal for $\alpha \cong (3°–4°)$. Simultaneously, the maximal increase in the signal intensity was observed in the total field under the omnidirectional reception (see Figs. 3, 4b). Note that, at distances from 16.3 to 17.2 km, the front of the received signal differed from the plane one, or it is possible that it was not completely formed, which is evidenced by the broader angular response of the array, as compared to the response to a plane wave. At greater distances (over 18 km) up to $r \sim 60$ km, i.e., at distances corresponding to the shadow zone for rays of the lower channel, the almost single-ray angular spectrum is transformed into a multiray one (see Fig. 5 for $r = 28.6$ and $r = 53.8$ km). In this case, the arrival angles α are close to the shallow grazing angles determined by the difference between the sound velocity at the reception depth and the maximal sound velocity $C(z)$ at a depth of ~1200 m.

The second example of the angular spectrum variations with distance is presented in Fig. 6b, which exhibits ten realizations of a rather large sequence of the spectra recorded at distances corresponding to the end of the shadow zone and the very beginning of the convergence zone for the signals propagating through the lower channel. In this figure, the same parameters are plotted along the axes as in Fig. 6a. Only the data on the amplification ratio for the receiving channel is absent (to the right of the angular spectra), since it remains constant during this time interval. As can be seen, all angular spectra contain the signals that arrived through the upper channel with grazing angles ~±5°. However, at distances exceeding 59.6 km (the last four angular spectra), the spectrum rapidly changes, because the signals propagating through the lower channel (see Fig. 2) enter into the convergence zone. The beginning of the zone corresponding to a caustic for signals arriving at the point of reception from below (in Fig. 6b, at the angle $\alpha \cong -10°$) was recorded at a distance of 60.5 km, which is 1.5 km smaller than the calculated distance corresponding to the beginning of the convergence zone (62 km). As noted above, such a discrepancy between the experimental data and the calculations is common for the signals propagating in the deep-water channel even in the stable (in a hydrological sense) regions of the ocean.

Thus, the results of the experimental studies of the energy characteristics of the sound field under omnidirectional reception and its angular and energy structure under directional (in the vertical plane) reception in a two-channel waveguide with a source located within the upper channel show that

(i) the sound field structure determined by the rays arriving through the lower channel agrees well with the results of calculations performed for a conventional model of the waveguide; the presence of the upper channel in the two-channel oceanic waveguide practically does not affect the results; the discrepancy between the experimental and the calculated locations of the shadow and convergence zones (for example, the distance corresponding to the beginning of the first convergence zone proves to be shorter by ~ 1.5 km, as compared to the calculation) in many real cases is not of fundamental importance; however, the so-called fine structure of the field (the angular, temporal, and energy structure) at every specific distance can greatly differ from the calculated one, especially at the beginning and end of a zone;

(ii) in real ocean conditions, the angular spectra and the energy field structure formed by the rays of the upper channel noticeably differ from the calculating ones; the experiments show an almost complete insonification of the whole tested track by the signals propagating over water rays; the first shadow zone for the rays trapped by the upper channel, or, more exactly, the region with the low intensity of the received signals, is much smaller in the experiment, as compared to the calculations (for example, the length of such a region at a source depth of 180 m and with the reception depths H_r from 180 to 500 m was ~8–4 km, depending on H_r, whereas its calculated length was ~22–13 km); it is necessary to note that the major part of the shadow zone ($r > 16$ km) was insonified not by random water signals with unstable characteristics (for example, the signals scattered by the inhomogeneities of the water column), but by the ray structure with almost fully developed plane fronts; in the experiments, the beginning of the first convergence zone for the rays of the upper channel was shifted by about 7–11 km (depending on H_r) toward the source relative to the position obtained from the calculations.

ACKNOWLEDGMENTS

This work was supported by the Russian Foundation for the Basic Research, project no. 00-02-17694.

REFERENCES

1. O. P. Galkin, L. V. Shvachko, and E. A. Kharchenko, Vopr. Sudostr., Ser. Akust., No. 11, 80 (1978).
2. O. P. Galkin, L. V. Shvachko, E. A. Kharchenko, *et al.*, in *Problems of the Ocean Acoustics* (Nauka, Moscow, 1984), pp. 118–133.
3. K. P. Bongiovanni, W. L. Siegmann, and D. S. Ko, J. Acoust. Soc. Am. **100**, 3033 (1996).
4. J. Gerrebout, in *Proceedings of Conference* (Saclantcen, 1971).
5. A. N. Guthrie, R. M. Fitzgerald, D. A. Nutile, and J. D. Shaffer, J. Acoust. Soc. Am. **56**, 58 (1974).
6. O. P. Galkin, E. A. Kharchenko, and L. V. Shvachko, in *Proceedings of IX All-Union Acoustical Conference* (Moscow, 1977), Sec. D, pp. 1–4.
7. O. P. Galkin and L. V. Shvachko, Akust. Zh. **44**, 192 (1998) [Acoust. Phys. **44**, 153 (1998)].
8. O. P. Galkin, E. A. Kharchenko, and L. V. Shvachko, Akust. Zh. **46**, 325 (2000) [Acoust. Phys. **46**, 274 (2000)].
9. A. E. Vedeneev, O. P. Galkin, I. S. Rogozhkin, and L. M. Filippov, Vopr. Sudostr., Ser. Akust., No. 15, 122 (1982).

Translated by Yu. Lysanov

Acoustical Physics, Vol. 47, No. 3, 2001, pp. 277–281. Translated from Akusticheskiĭ Zhurnal, Vol. 47, No. 3, 2001, pp. 330–335.
Original Russian Text Copyright © 2001 by Grigor'ev, Katsnel'son, Petnikov.

Determination of the Absorbing and Scattering Properties of the Sea Floor in a Shallow Water Environment by the Spectra of Wide-Band Signals

V. A. Grigor'ev*, B. G. Katsnel'son*, and V. G. Petnikov**
**Voronezh State University, Universitetskaya pl. 1, Voronezh, 394693 Russia*
***General Physics Institute, Russian Academy of Sciences,*
ul. Vavilova 38, Moscow, 117942 Russia
e-mail: petnikov@kapella.gpi.ru

Received December 29, 1999

Abstract—Sound propagation in a shallow sea is considered within the framework of the two-component model of the sea floor. The porosity and the coefficients of absorption and volume scattering are treated as the parameters characterizing the sea floor. These parameters are determined on the basis of the comparison between the experimental and theoretical frequency spectra of a signal received from a wide-band source. A conclusion is made about the relative contributions of different mechanisms of losses (absorption or scattering) in the sea floor at different sound frequencies. © *2001 MAIK "Nauka/Interperiodica".*

The decisive role of the sea floor in the formation of the sound field of a point source (or a distributed source) in a shallow water environment is well known. This fact allows one to connect the characteristics of the sea floor with the observed parameters of acoustic signals propagating in a shallow sea and to determine (which is very important) these characteristics by comparing measured and calculated acoustic data with the use of the quantitative comparison test. The characteristics of the sea floor that correspond to the best agreement between the calculations and the experiment are taken as true under the condition of the adequacy of the selected model of the shallow-water waveguide. In this case, it is possible to use various arrays describing the sound field as initial data, e.g., the spatial dependence of the signal intensity as a function of distance to the source in the water layer or the horizontal interference structure of the sound field, the depth dependence of the intensity or the vertical interference structure [1], and the interference structure in the frequency domain when wide-band signals are used [2–7]. On the whole, such a technique, together with other similar methods used for evaluating the parameters of the inhomogeneities of the underwater sound channel, has been called acoustic tomography based on the medium-matched signal processing [1]. We note that this technique provides an opportunity to determine the average acoustic characteristics of the upper sediment layer along the propagation path in a shallow sea.

An example of utilization of a similar technique is given by Jensen and Kuperman [5] (see also [4, 7]) who, in the framework of the model of a homogeneous liquid sea bottom, determined the frequency dependence of the coefficient $\alpha(f)$ connected with the imaginary part of the wave number in the bottom k_1:

$$k_1 = \frac{2\pi f}{c_1}\left(1 + \frac{\alpha}{2}\right), \tag{1}$$

where c_1 is the sound velocity in the bottom.[1] It was assumed in this case that the coefficient α determined by the loss of the sound energy in the sea floor depends on the frequency in a phenomenological way:

$$\alpha = \alpha_0 (f/f_0)^b, \tag{2}$$

where f_0 is a certain normalizing frequency and the parameters α_0 and b are determined on the basis of the comparison of the experimental and calculated interference structures of the sound field in the near-bottom sound channel in the frequency domain.

This study is a continuation of our previous paper [5]. Here, we try to derive a physically more adequate dependence $\alpha(f)$ that is based on the assumptions concerning the floor structure and the role of different mechanisms of sound absorption. The parameters determining the frequency dependence are also to be refined by comparing the calculated sound field in the water layer with the experimental data.

Our approach is based on the following model of a shallow sea. A water layer with the density ρ and the sound velocity profile $c(z)$ lies on a halfspace filled with sediments (Fig. 1). These sediments are a two-component medium, i.e., water plus mineral particles. The main parameter that will be used to characterize the

---

[1] Note that, in these notation, the coefficient of sound absorption in the bottom is equal to $\beta = 2\,\mathrm{Im}\,k_1$.

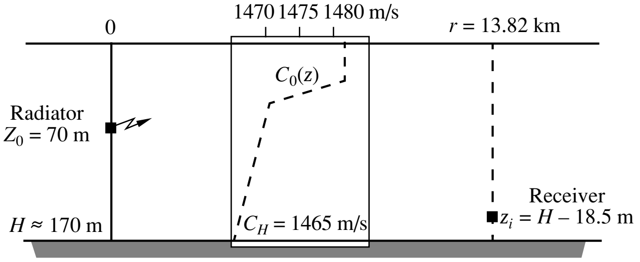

Fig. 1. Model of a shallow-water waveguide and the experimental conditions.

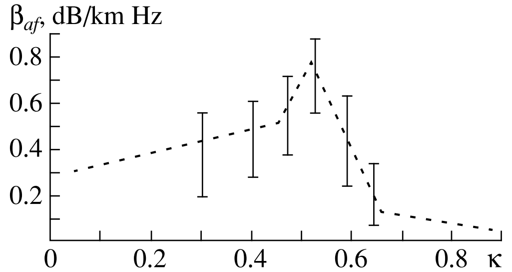

Fig. 2. Coefficient of sound absorption divided by frequency as a function of porosity for different regions of the ocean. The scatter of the parameters is shown in the figure.

sediments is the porosity κ, which is the ratio of the volume occupied by seawater to the total volume of the ground sample under consideration. Within the framework of the simplified model used in our study, the geoacoustic parameters of the bottom sediments are expressed through the values of porosity. Namely, the propagation velocity of longitudinal waves and the density in the sea floor, c_1 and ρ_1, can be adequately described by the formulas [8]

$$\begin{aligned} c_1 &= c_H(1.631 - 1.78\kappa + 1.2\kappa^2), \\ \rho_1 &= \rho_H(2.604 - 1.606\kappa), \end{aligned} \tag{3}$$

where c_H and ρ_H are the sound velocity in water and the water density near the sea floor, respectively. Now, let us consider the propagation loss in sediments that are described by either the dimensionless coefficient α or the coefficient β, which has the dimension of the reciprocal length. The main idea of this paper is the separation of the two basic mechanisms that in our opinion are responsible for the sound attenuation in the sea floor. The first mechanism is the sound absorption (the transformation of the sound energy to heat). We will denote the contribution of this mechanism by the coefficient α_a (or β_a, respectively). The second mechanism is the sound scattering by volume inhomogeneities. In this case, the sound energy dissipates from the beam in various directions. The contribution of this mechanism is characterized by the loss coefficient α_v (or β_v, respectively).

As experiments show, the coefficient β_a measured for the ground in shallow-water regions is proportional to the sound frequency f in a wide frequency range from 10 Hz to 1 MHz, $\beta_a = \beta_{af} f$, which corresponds to a constant value of the parameter α_a connected with the absorption coefficient β_{af} by the relationship $\alpha_a = \frac{c_1[\text{km/s}]}{27.3}\beta_{af}$ [dB/km Hz]. According to the literature data [8, 9], the quantity β_{af} is determined by the semi-empirical expressions

$$\beta_{af}\left[\frac{\text{dB}}{\text{km Hz}}\right] = \begin{cases} 0.2747 + 0.527\kappa, & 0 < \kappa < 0.472 \\ 4.903 - 1.7688\kappa, & 0.472 < \kappa < 0.52 \\ 3.3232 - 4.89\kappa, & 0.52 < \kappa < 0.65 \\ 0.7602 - 1.487\kappa + 0.78\kappa^2, & 0.65 < \kappa < 0.9. \end{cases} \tag{4}$$

This mechanism can be represented mainly as the result of friction between particles. An increase in the sound frequency means that each particle performs more vibrations per unit time, which makes the loss proportional to frequency. Figure 2 demonstrates the dependence of the absorption coefficient β_{af} on porosity according to empirical Eq. (4). The scatter of the experimental data obtained for β_{af} in different regions of the ocean is also shown in this figure.

We note that, in the theory of water-saturated porous media [9, 10], the absorption mechanism due to the motion of the pore liquid relative to the ground skeleton is considered in addition to the losses caused by friction between particles. In this case, the viscous friction force arises, which opposes the relative motion of the liquid and solid phases. This also leads to a dissipation of the wave energy and its transformation to heat. At low frequencies, this mechanism must lead to a quadratic dependence of the absorption coefficient on frequency [10]. However, the measurements performed for the sediments of the continental shelf demonstrate a relative smallness of the contribution of this mechanism to the total loss. We should indicate one more mechanism of losses in highly porous sediments (suspensions) where particles do not contact each other but are kept at a distance by the forces of an electrochemical nature. In this case, the friction between particles is absent. As a result, the frequency dependence of the absorption coefficient is not linear. However, this is true for deep-water clays [11].

Another mechanism responsible for the propagation loss is the scattering of sound by the surface and volume inhomogeneities [12, 13]. Since most of shallow-water regions of the oceanic shelf have a smooth bottom relief, in describing the sound propagation at low frequencies (<100 Hz) it is sufficient to take into account only the general change in depth along the acoustic path, and this change is usually known. The dimensions of the surface inhomogeneities relative to the general relief in this case are much smaller than the wavelength, and their scattering properties can be ignored. Thus, the second mechanism is the scattering by volume inhomogeneities that we describe by the total coefficient of volume scattering β_V. It is determined as the ratio of the sound power W scattered by a unit volume in all directions to the intensity I_0 of the incident plane wave:

$$\beta_V = \frac{W}{I_0}. \tag{5}$$

For volume inhomogeneities of various dimensions, one can obtain [14, 15] that the total coefficient of volume scattering depends on frequency according to a power law with the power index varying from four to two, depending on the characteristic size of the inhomogeneities. This means that, in the case of inhomogeneities comparable to the wavelength, an intermediate frequency dependence must be observed: $\beta_V \sim f^{2–4}$. We approximately describe the combined effect of scattering from all inhomogeneities by the power dependence $\beta_V \sim f^b$ or

$$\beta_V = \frac{2\pi\alpha_V}{c_1} f, \tag{6}$$

where α_V is the frequency-dependent specific coefficient of volume scattering, which can be represented in a form analogous to Eq. (2): $\alpha_V = \alpha_V^0 (f/f_0)^{b-1}$, $b = 2–4$. According to the closeness of the value of b to one or another value, it is possible to qualitatively evaluate the size of inhomogeneities that make the greatest contribution to the losses caused by the volume scattering of sound. The value of α_V characterizes the power of the field scattered in all directions (divided by a unit volume, a unit intensity of the incident wave, and one hertz). The specific values of α_V^0 and b are assumed to be such that Eq. (6) most closely describes the frequency dependence of the signal in the range under consideration. In this case, the parameters α_V^0 and b are, generally speaking, different for the same bottom but for different frequency bands, because the variation of the frequency band changes the relationships between the dimensions of inhomogeneities and the wavelengths, which changes the characteristics of the scattering.

Thus, assuming that the losses in the bottom are caused mainly by the two indicated mechanisms, we have a corresponding frequency dependence for the absorption coefficient:

$$\alpha = \alpha_a + \alpha_V = \alpha_a + \alpha_V^0 (f/f_0)^{b-1}. \tag{7}$$

Let us evaluate the values of the coefficients in Eq. (7) by comparing the calculated and experimental interference structure of the acoustic field in the frequency domain. The basis for our calculation is the following well-known expression for the sound field produced in a waveguide at a point with the coordinates (r, z) by a tone source located at the point $(0, z_0)$:

$$u(r, z;\ f) \approx -A\sqrt{\frac{i}{8\pi}} \sum_n \psi_n(z_0)\psi_n(z) \frac{\exp(i\xi_n r)}{\sqrt{\xi_n r}}, \tag{8}$$

where the complex coefficient A characterizes the spectral power $W(f)$ and the initial phase of the radiator, $|A| = \sqrt{8\pi\rho c(z_0) W(f)}$; $\psi_n(z)$ and ξ_n are the eigenfunctions and eigenvalues ($\mathrm{Re}\{\xi_n\} > 0$; $\mathrm{Im}\{\xi_n\} > 0$) of the Sturm–Liouville problem:

$$\begin{cases} \left[\dfrac{d^2}{dz^2} + \left(\dfrac{2\pi f}{c(z)}\right)^2 - \xi_n^2\right]\psi_n(z) = 0; \\ \psi_n(0) = 0; \quad \psi_n(H) + \dfrac{m}{\sqrt{\xi_n^2 - k_1^2}} \left.\dfrac{d\psi_n(z)}{dz}\right|_{z = H} = 0. \end{cases} \tag{9}$$

Here, $m = \rho_1/\rho_H$. We note that the frequency dependence of the received signal in Eq. (8) is determined by all terms on the right-hand side of the equation, because the eigenfunctions and eigenvalues depend on frequency. Using Eq. (8) at fixed positions of the source and the receiver and assuming that the eigenfunctions and eigenvalues depend on frequency as on a parameter, in the case of our model we calculate a set of dependences $|u(r, z; f)|^{(\mathrm{theor})}$ (i.e., we determine the interference structure of the sound field in the frequency domain) for different values of the coefficients in Eq. (7). The dependence $c(z)$ measured in the experiment is used in these calculations.

As in our previous paper [5] we used the interference structure of the sound field experimentally measured at a stationary path in the Barents Sea as the experimental dependence $|u(r, z; f)|^{(\exp)}$. Let us recall the major parameters of the experiment. Sounding was performed with the help of a piston-type radiator, which excited wide-band pulsed signals with a linear frequency modulation in the band 25–95 Hz. The duration of each signal was 40 s. The radiator was lowered to a depth of 70 m. The signal reception was performed by a single hydrophone at a depth of 151.5 m. The distance between the source and the receiver was 13.82 km. The sea depth was varying weakly along the path and was equal to $H \approx 170$ m. According to the data of a Parasound parametric echo-sounder, the upper layer of the bottom sediments along the stationary path was almost homogeneous down to the maximal depth of echo-sounding ≅40 m. We note that the hypothesis on a quasi-homogeneous sea bottom (a two-component medium) was put forward proceeding just from these data limited in depth. This hypothesis served as the basis for the waveguide model used in this paper. We do not have any detailed data on the geological structure of the bottom along the stationary path. On the other hand, the utilization of geological data obtained in other regions of the Barents Sea is not justified because of their strong variation. The main experimental result

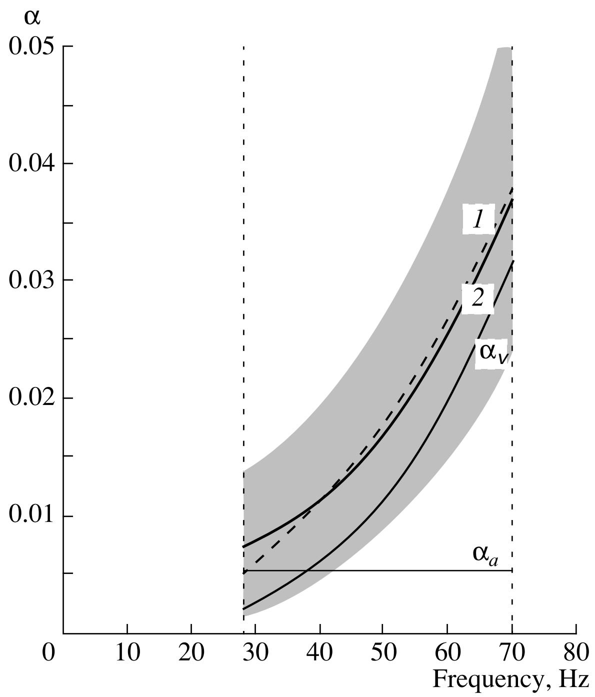

Fig. 3. Frequency dependences of the loss coefficients α. (*1*) The dashed line corresponds to the result of our previous paper [5] $\alpha = 2.8 \times 10^{-6} f^{2.24}$ without separation of the loss mechanisms. (*2*) The thick line shows the total loss according to the results of this paper, $\alpha = \alpha_a + \alpha_V$. The thin lines represent the frequency dependences of the coefficients of absorption α_a and scattering α_V. The gray area shows the scatter of data due to the fluctuations of the experimental spectra.

used in this study is the spectrum of the received signal averaged in the frequency band 5 Hz. Precisely this spectrum represented the interference structure of the sound field in the frequency domain at the observation point $|u(r, z; f)|^{(\mathrm{exp})}$. It should be noted that, after the averaging, the signal spectrum did not depend on time; i.e., it did not change from pulse to pulse during the whole time of measurement. In other words, the averaged interference structure obtained in such a way did not depend on the fluctuations of the waveguide parameters determined by the mesoscale variability of the medium (tides and internal waves) and could be used for the determination of the desired acoustic characteristics of the sea floor. Therefore, the calculated dependences $|u(r, z; f)|^{(\mathrm{theor})}$ were also averaged in the frequency band 5 Hz.

The rms deviation σ of the theoretical dependence from the experimental one was used as a comparison test. Let there be the experimental and theoretical spectra, $|u|_i^{(\mathrm{exp})}$ and $|u|_i^{(\mathrm{theor})}$, that consist of M frequency readings of the of the sound field magnitude: $|u|_i = |u(r, z; f_i)|$; $i = 1, \ldots, M$. Then, we have

$$\sigma = \sqrt{\sum_{i=1}^{M} (|u|_i^{(\mathrm{exp})} - |u|_i^{(\mathrm{theor})})^2}. \qquad (10)$$

The minimum σ (ideally, equal to zero) corresponds to the best choice of the bottom model, and the parameters of the latter can be considered close to reality.

We take the quantities κ, α_a, α_V^0, and b as the unknown characteristics of the bottom and assume that the velocity and density in the bottom are defined through the porosity by Eq. (3). As for the connection of porosity with the absorption coefficient defined by Eq. (4), the absorption calculated according to the averaged formula (4) can widely differ from the real data corresponding to a specific region because of the large scatter of the experimental data obtained in different regions of the ocean (see Fig. 2). Therefore, we assume that the absorption coefficient α_a must be determined independently, along with the porosity and the parameters of volume scattering. In this case, the complete list of values on which the theoretical spectrum depends is as follows: z_0, z, r, $c_0(z)$, c_H, H, κ, α_a, α_V^0, and b. The values of the first six parameters can be measured directly, while the last four parameters are determined from the matching conditions. An essential point for the procedure of matching used in this study is the difference in the effect of the variation of single parameters on the spectrum. For example, the variation of the porosity κ leads to a shift of the spectral pattern as a whole in frequency. The other three parameters (α_a, α_V^0, and b) mainly influence the energy characteristics of the spectrum and do not cause its shift in frequency. Thus, at the first stage, we determine the value of porosity in such way that the interference peaks of the theoretical spectra coincide in frequency with the corresponding experimental peaks. Taking into account the interval of realistic values, the desired value of the ground porosity lies within the limits 0.3–0.4. The next stage is a search for the optimal parameters of damping. According to previous calculations [5] that qualitatively testify to the domination of the volume scattering by small-scale inhomogeneities, the optimal value of the power index is sought in the region $b \sim 4$ together with the determination of the coefficients α_a and α_V^0 by an exhaustive search. The coefficient A is also selected to satisfy the condition of the minimal σ for each combination of parameters. (The exact value of the coefficient A in the process of experimenting was unknown because of the insufficient precision of the absolute calibration of the source.)

As calculations show, the best coincidence of the theory and experiment is observed in the frequency band 28–70 Hz with the effective value of porosity being equal to 0.3.[2] According to empirical formulas (1) and (2), this corresponds to the relative density of the ground $\rho_1/\rho_H = 2.1$ and to the sound velocity in the sea floor $c_1 = 1765$ m/s. The values obtained for the specific

---

[2] A good agreement of experimental and calculated data was achieved only in this frequency band.

coefficients of absorption α_a and volume scattering α_v are as follows: $\alpha_a = 0.005$ and $\alpha_v = 9.3 \times 10^{-8}f^3$, or $\alpha = 0.005 + 9.3 \times 10^{-8}f^3$, where f is the frequency in Hz. The dependences (α_a, α_v, α) are given in Fig. 3. The same figure shows the boundaries of the spread in the values of the parameter α due to the random fluctuations of the received spectra.

The curves demonstrate the similarity of the results obtained by determining the frequency dependence of the absorption coefficient on the basis of the technique used in this paper and the results presented in our previous paper [5]. Moreover, we can make some conclusions about the mechanisms of losses in the sea floor. One can see from Fig. 3 (in particular) that, at the frequencies lower than 40 Hz, the general losses in the sea floor are caused mainly by absorption, whereas, at the frequencies higher than 40 Hz, the volume scattering dominates.

The numerical value of the specific absorption coefficient expressed in more common units is $\beta_{af} \approx 0.1$ dB/km Hz. This value is much smaller than the one calculated by the empirical formula (4) (0.4 dB/km Hz), although it lies generally within the scatter of data. It should be noted that other methods used for the determination of the damping coefficient (for example, by the averaged decay curve representing the decrease in the sound field intensity with distance [16], or by a direct measurement of the ground samples in the laboratory) also lead to values much lower than those obtained from the empirical formula (4). Presumably, the explanation of this fact is connected with the specific types of ground that occur in this water area. They consist mainly of highly porous clay mixed with stones. As a result, the average porosity is low (~0.3) because of the presence of solid inclusions, and absorption is determined mainly by the clay filler; i.e., it is characterized by the values corresponding to absorption in the case of porosity equal to 0.7–0.9. Turning to Fig. 2, we can conclude that in the Barents Sea the absorption coefficients for ground with the porosity ~0.3 (thin clay with stone inclusions) and ~0.8 (homogeneous clay, silt) must approximately coincide and be equal to ~0.1 dB/km Hz. As one can see from the same figure, the scatter of experimental data at $\kappa \sim 0.3$ really has similar values near the lowest boundary, which confirms the reasoning given above. At the same time, the wide difference between the minimal values of absorption and the average coefficient of absorption in the case of porosity equal to 0.3 demonstrates in our opinion the particular features of the ground of the Barents Sea, while for other regions of the ocean, the typical ground has the form of coarse-grained sand with a porosity of 0.3. In this case, the sound absorption is 3–5 times greater than in homogeneous clay ground, or, in the case under study, in the inhomogeneous ground of the Barents Sea type.

On the whole, in our opinion the results of this study are the evidence in favor of the use of the two-component model of the sea floor for describing the sound propagation in many regions of the Barents Sea.

ACKNOWLEDGMENTS

This work was supported by the Russian Foundation for Basic Research, project nos. 97-05-64878 and 99-02-17671.

REFERENCES

1. B. G. Katsnel'son and V. G. Petnikov, *Acoustics of a Shallow Sea* (Nauka, Moscow, 1997).
2. A. I. Eller and D. A. Gershfeld, J. Acoust. Soc. Am. **78**, 622 (1985).
3. P. W. Smith, Jr., J. Acoust. Soc. Am. **79**, 71 (1986).
4. J. X. Zhou, X. Z. Zhang, P. H. Rogers, and J. Jarzynski, J. Acoust. Soc. Am. **82**, 2068 (1987).
5. V. A. Grigor'ev, B. G. Katsnel'son, and V. G. Petnikov, Akust. Zh. **42**, 712 (1996) [Acoust. Phys. **42**, 627 (1996)].
6. F. B. Jensen and W. A. Kuperman, J. Acoust. Soc. Am. **73**, 813 (1983).
7. M. V. Hall, in *ICA/ASA'98 Proceedings* (Seattle, 1998), pp. 1635–1636.
8. T. Akal, in *Physics of Sound in Marine Sediments*, Ed. by L. Hampton (Plenum, New York, 1974; Mir, Moscow, 1977).
9. E. L. Hamilton, J. Acoust. Soc. Am. **59**, 528 (1976).
10. M. A. Biot, J. Acoust. Soc. Am. **28**, 168 (1956).
11. D. T. Smith, in *Physics of Sound in Marine Sediments*, Ed. by L. Hampton (Plenum, New York, 1974; Mir, Moscow, 1977).
12. Yu. P. Lysanov, Dokl. Akad. Nauk SSSR **251** (3), 714 (1980) [Sov. Phys. Dokl. (1980)].
13. A. N. Ivakin and Yu. P. Lysanov, Akust. Zh. **31**, 807 (1985) [Sov. Phys. Acoust. **31**, 493 (1985)].
14. S. D. Chuprov and R. F. Shvachko, in *Acoustics of the Ocean*, Ed. by L. M. Brekhovskikh (Nauka, Moscow, 1974), pp. 559–614.
15. L. M. Brekhovskikh and Yu. P. Lysanov, *Fundamentals of Ocean Acoustics* (Gidrometeoizdat, Leningrad, 1982; Springer, New York, 1991).
16. F. V. Bunkin, B. G. Katsnel'son, Yu. A. Kravtsov, *et al.*, Akust. Zh. **35**, 1 (1989) [Sov. Phys. Acoust. **35**, 1 (1989)].

Translated by M. Lyamshev

Acoustical Physics, Vol. 47, No. 3, 2001, pp. 282–285. Translated from Akusticheskiĭ Zhurnal, Vol. 47, No. 3, 2001, pp. 336–340.
Original Russian Text Copyright © 2001 by Joshi, Zaĭtsev, Kuznetsova.

SH Acoustic Waves in a Lithium Niobate Plate and the Effect of Electrical Boundary Conditions on Their Properties

S. G. Joshi*, B. D. Zaĭtsev*, and I. E. Kuznetsova**
**Marquette University, Milwaukee, WI 53201, USA*
***Institute of Radio Engineering and Electronics, Russian Academy of Sciences,*
Saratov Branch, ul. Zelenaya 38, Saratov, 410019 Russia
e-mail: iren@ire.san.ru

Received June 2, 1999

Abstract—It is theoretically and experimentally confirmed that the electromechanical coupling coefficient of SH waves propagating in a *Y*-cut lithium niobate plate along the *X* direction can exceed 30% when the plate thickness satisfies the condition $h/\lambda = 0.02–0.15$. This value of the coupling coefficient is approximately six to seven times greater than the maximal value obtained for SAW in the same material. Such a high value of K^2 offers a possibility to control the wave velocity by varying the electrical boundary conditions, e.g., by moving a conducting screen toward the plate surface. The effect of such a screen on the properties of the SH waves is studied both theoretically and experimentally. On the whole, the results of the study show that the use of SH waves offers considerable improvements in the parameters of the known SAW devices and also opens up the possibilities for the development of new devices and sensors that have to operate in contact with a liquid medium. *© 2001 MAIK “Nauka/Interperiodica”.*

Shear horizontal (SH) waves propagating in thin piezoelectric plates are attracting the interest of many researchers today [1–3]. A distinctive feature of these waves is the almost total absence of the surface-normal component of particle displacement when the condition $h/\lambda \ll 1$ is satisfied (here, h is the plate thickness and λ is the wavelength). Because of this feature, the waves can propagate in a plate that is contact with a liquid without any considerable energy loss through the wave excitation of the liquid medium. Thus, on the basis of SH waves, it is possible to develop devices and sensors that can be efficiently operated in contact with a liquid. It should be noted that similar sensors based on surface acoustic waves (SAW) usually fail, because the Rayleigh SAW strongly attenuate when the surface of their propagation is in contact with a liquid medium. The other distinctive feature of SH waves in plates is the very high value of the electromechanical coupling coefficient (K), as compared to the case of SAW [2–4].

The purpose of this paper is to determine the cut and thickness of the lithium niobate plate and the direction of the SH wave propagation in it to obtain the maximal value of the electromechanical coupling coefficient. The theoretical analysis shows that, for the *Y*-cut with the *X*-propagation, the square of the electromechanical coupling coefficient for SH waves, K^2, exceeds 30% when the plate thickness is within $h/\lambda = 0.02–0.15$. This conclusion was confirmed experimentally. Such a high value of K^2 offers the possibility to control the wave velocity by varying the electrical boundary conditions. The latter can be accomplished, e.g., by moving a conducting screen toward the plate surface. Below, we describe the theoretical and experimental studies of the effect of such a screen on the properties of the waves under investigation.

We analyze the acoustic wave propagation in a plate of an arbitrary piezoelectric material. We consider a wave that propagates along the x_1 direction of a piezoelectric plate bounded by the planes $x_3 = 0$ and $x_3 = h$. The x_3 axis is directed into the plate, and the region $x_3 > h$ corresponds to the vacuum. We write the equation of motion of the medium and the Laplace equation for the plate in the form

$$\rho\frac{\partial^2 u_i}{\partial^2 t} = C_{ijkl}\frac{\partial^2 u_l}{\partial x_j \partial x_k} + e_{kij}\frac{\partial^2 \Phi}{\partial x_j \partial x_k},$$

$$\varepsilon_{jk}\frac{\partial^2 \Phi}{\partial x_j \partial x_k} - \varepsilon_{jlk}\frac{\partial^2 u_l}{\partial x_j \partial x_k} = 0,$$

where u_i is the particle displacement in the plate; x_j represents the spatial coordinates; t is time; Φ is the electric potential in the plate; ρ is the density of the medium; and C_{ijkl}, e_{kij}, and ε_{jk} are the elastic, piezoelectric, and dielectric constants.

In the vacuum region $x_3 > h$, the electric potential must obey the Laplace equation

$$\frac{\partial^2 \Phi^{II}}{\partial^2 x_i} = 0,$$

1063-7710/01/4703-0282$21.00 © 2001 MAIK “Nauka/Interperiodica”

where Φ^{II} is the electric potential in vacuum in the region $x_3 > h$.

The mechanical and electrical boundary conditions for the plane $x_3 = h$ have the form

$$T_{i3}e^{(2\pi h/\lambda)} = 0, \quad \Phi e^{(2\pi h/\lambda)} = \Phi^{II}e^{(2\pi h/\lambda)},$$

$$D_3 e^{(2\pi h/\lambda)} = D_3^{II}e^{(2\pi h/\lambda)},$$

where $T_{ij} = C_{ijkl}\partial u_k/\partial x_l + e_{kij}\partial\Phi/\partial x_k$ is the mechanical stress in the plate and D_3 and D_3^{II} denote the electric induction in the piezoelectric plate and in a vacuum (in the region $x_3 > h$), respectively. To solve the problem formulated above, we used the known method [5], which allowed us to calculate the electromechanical coupling coefficient of the SH wave for different cuts and thicknesses of the lithium niobate piezoelectric plate and for different propagation directions. The maximal electromechanical coupling coefficient was obtained for the case of the *Y*-cut plate with the wave propagation along the *X* direction: $K^2 = 36\%$. This value is several times greater than the maximal value of the corresponding coefficient for the Rayleigh SAW ($K^2 = 5\%$). Therefore, we selected the aforementioned cut for measuring the coefficient K^2. The measurements were performed by two independent methods.

Method 1. At the center of a lithium niobate plate *1* with the dimensions 20×35 mm^2, we placed an interdigital transducer *2*, which had a period of 1.26 mm, an aperture of 13 mm, and the number of finger pairs $N = 6$ (Fig. 1a). The plate was glued to a specially designed glass unit *3* whose dimensions were $50 \times 50 \times 6$ mm^3. At the center of this unit, a rectangular window with the dimensions 24×18 mm^2 was made. The plate was fixed to the unit by an epoxy adhesive in such a way that the transducer was inside the window. Such a structure allowed us to change the plate thickness from 530 to 80 μm by grinding and polishing the back side of the plate, which corresponded to the variation of the ratio h/λ from 0.42 to 0.064. At the same time, in this structure, the condition that the surfaces remained mechanically free within the wave aperture was satisfied. In addition, the effect of changes in the electrical contacts on the results of measurements was eliminated, because all electrical connections were inside the window and remained unaffected in the course of the experiment. To maintain the plane-parallel configuration of the plate, additional silicon plates were glued to the unit along its perimeter, and grinding was performed in the presence of these plates whose hardness was higher than that of $LiNbO_3$. The thickness of the plate under investigation and its plane-parallel configuration were controlled by a vertical telescope caliper with a scale division of 2.5 μm. The edges of the $LiNbO_3$ plate had a jagged form to prevent the reradiation of acoustic waves.

For each selected value of the plate thickness, we measured the frequency dependence of the real and imaginary parts of the transducer conductivity by using an HP4192A impedance meter. The dependences exhibited characteristic resonance peaks [2], which corresponded to the excitation of acoustic waves. The electromechanical coupling coefficient was determined from the well-known relation [2, 3]

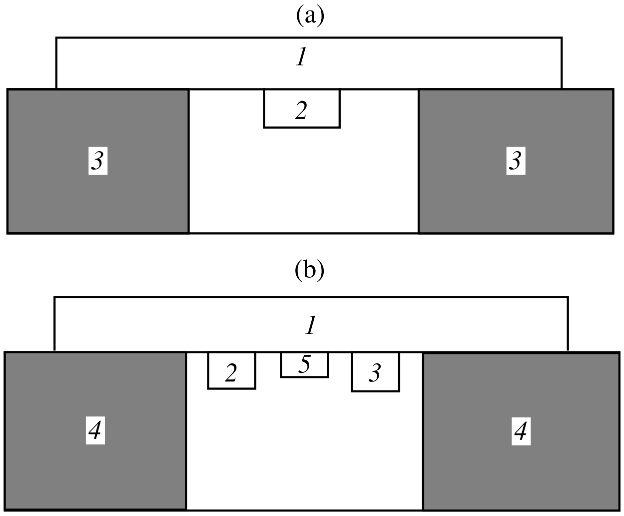

Fig. 1. Device for measuring the electromechanical coupling coefficient as a function of the plate thickness. (a) Method 1: (*1*) the $LiNbO_3$ plate, (*2*) an interdigital transducer, and (*3*) a glass unit; (b) method 2: (*1*) the $LiNbO_3$ plate, (*2*, *3*) two interdigital transducers, (*4*) a glass unit, and (*5*) a metal electrode.

$$K^2 = \Gamma_{\max}/8 f_0 C N,$$

where $\Gamma_{\max}$ is the maximal conductivity at the resonance frequency f_0, C is the capacitance of the transducer, and N is the number of finger pairs. The values of $\Gamma_{\max}$ and f_0 were determined from the measured frequency dependence of the real conductivity component. As for the capacitance C, we first tried to determine its value from the frequency dependence of the imaginary conductivity component. However, its complex shape, which was caused by the reradiation of acoustic waves inside the transducer, as well as the presence of the stray capacitances and inductances, did not allow us to obtain this value with sufficient accuracy. Therefore, to determine C as a function of h/λ, we used the known relation [6]

$$C = M\tan\left(\frac{2\pi h(\varepsilon_{11}\varepsilon_{33} - \varepsilon_{13}^2)^{1/2}}{\lambda\varepsilon_{33}}\right),$$

where M is a coefficient that depends on the ratio of the transducer strip width to its period, on the aperture, and on the dielectric constant; ε_{ij} represents the components of the dielectric constant tensor of $LiNbO_3$. The coefficient M was determined by equating the theoretical and experimental values of K^2 for the initial plate thickness. The resulting experimental values of K^2 obtained with

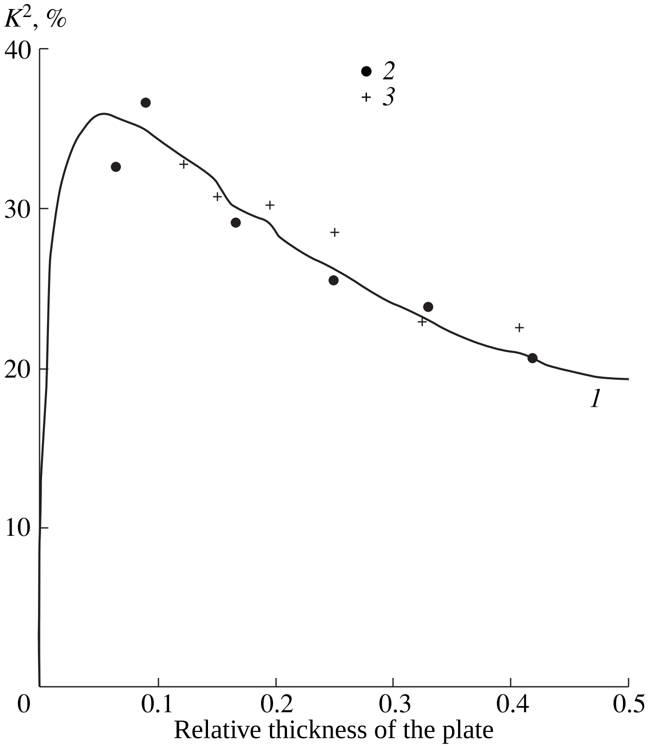

Fig. 2. Dependence of the square of the electromechanical coupling coefficient of SH waves on the normalized thickness of the $LiNbO_3$ plate (the *Y*-cut plate with the *X*-propagation): (*1*) theoretical curve, (*2*) experimental data obtained by method 1, and (*3*) experimental data obtained by method 2.

this method are presented in Fig. 2 as a function of the plate thickness.

Method 2. The other method of measuring K^2 was as follows. Two identical interdigital transducers *2* and *3* were placed on a lithium niobate plate *1*. The dimensions and the cut of the plate and the propagation direction were the same as in the first method. The interdigital transducers were characterized by a period of 1.26 mm, an aperture of 13 mm, and the number of the finger pairs $N = 2$ (Fig. 1b). The distance between the transducers was 21 mm. A rectangular metal electrode *5* 20 mm long and 6.5 mm wide was placed between the transducers. Such a delay line geometry resulted in a periodic variation of the output signal amplitude with frequency. By measuring the frequency variation Δf between two adjacent maximums, it was possible to determine the velocity difference between the nonmetallized and metallized surfaces:

$$\Delta V/V = 1/(\Delta f \tau_m),$$

where τ_m is the delay time for the signal propagating below the metal electrode. Then, we obtain

$$K^2 = 2\Delta V/V.$$

The results obtained with this method for different values of the plate thickness are also presented in Fig. 2.

On the whole, our study showed a good agreement between the theoretical and experimental data and confirmed that, for SH waves, it is possible to obtain the value of the electromechanical coupling coefficient $K^2 = 36\%$, which far exceeds the maximal value of K^2 achieved for SAW in the same material.

Now, we consider the propagation of SH waves in a plate when a perfectly conducting screen is placed near it in the plane $x_3 = -d$. In this case, the mechanical and electrical boundary conditions have the form

$$T_{i3} = 0, \quad \Phi = \Phi^I, \quad D_3 = D_3^I, \text{ at } x_3 = 0,$$

$$\Phi^{III} e^{(-2\pi hd/\lambda)} = 0, \text{ at } x_3 = -d.$$

Here, Φ^I and D_3^I are the electric potential and induction in vacuum in the region $0 > x_3 > -d$ and Φ^{III} is the electric potential at the boundary of the metal screen $x_3 = -d$.

As a result of our calculations, we obtained the dependences of the relative velocity variation on the normalized width of the vacuum gap, d/h, between the conducting screen and the piezoelectric plate for different values of the quantity h/λ (Fig. 3a). These dependences do not involve the wave frequency. One can see that, as the gap widens, the velocity of the SH waves increases. The maximal value of the wave velocity variation corresponds to the difference between velocities in the plate with a metallized surface and a plate with a nonmetallized surface, i.e., to the square of the electromechanical coupling coefficient.

The experimental study of the effect of the conducting screen on the velocity of SH waves was also performed. We used the delay line shown in Fig. 1b, but without the metal electrode. The plate thickness was 140 μm ($h/\lambda = 1.1$). To increase the output signal amplitude, we used an inductance for compensating the capacitance of the transducer and an r.f. transformer for matching the active component of the transducer impedance with the wave resistance of the cable. As a result, the level of the delayed signal exceeded the level of the undelayed electromagnetic interference by 15 dB, which allowed us to perform reliable measurements in a continuous mode.

We used a specially developed precision mechanical system, which provided the possibility to vary the width of the gap between the electrode and the piezoelectric plate. The gap width was controlled by a clock indicator of microdisplacements with an accuracy of 2.5 μm. The master r.f. oscillator was an HP3335 frequency synthesizer. The phase of the delayed signal relative to the reference one was measured by an HP8405A phase difference meter. It was found that the variation of the gap width did not cause any changes in the amplitude of the output signal, but only shifted its phase. The experimental dependence of the phase shift on the gap width is shown in Fig. 3b. This figure also presents the phase values predicted theoretically. One can see that the theory and the experiment agree well

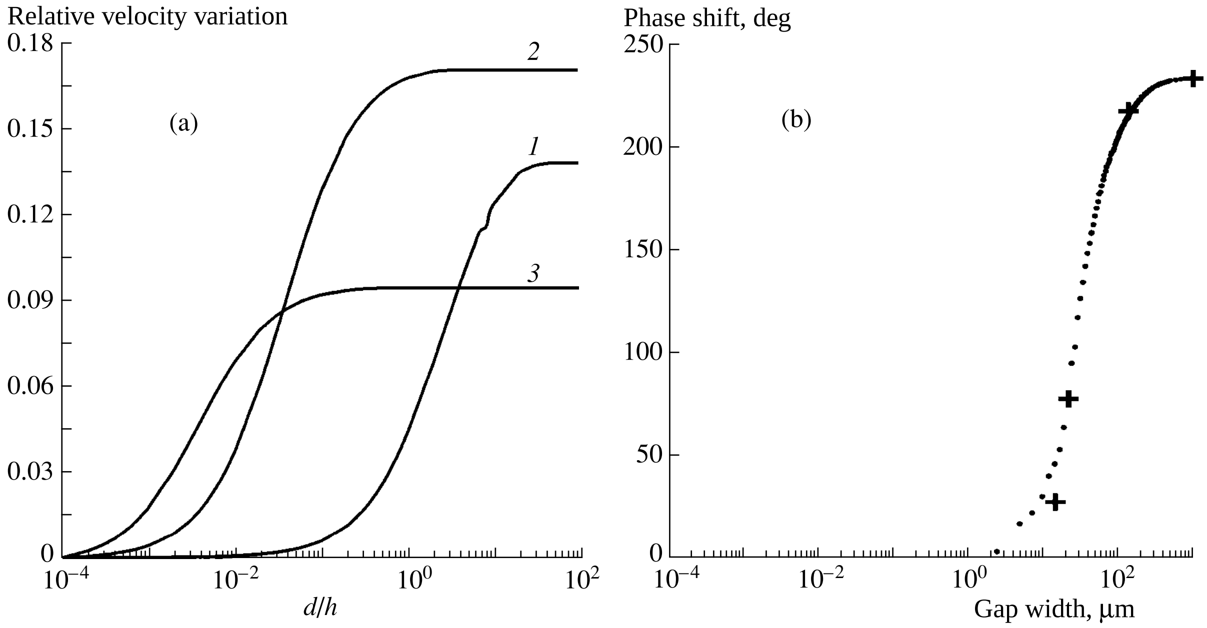

Fig. 3. (a) Dependence of the relative variation of the SH wave velocity on the normalized width d/h of the gap between the lithium niobate plate (*Y*-cut, *X*-propagation) and a perfectly conducting screen for h/λ = (*1*) 0.01, (*2*) 0.1, and (*3*) 0.5. (b) Dependence of the phase of an SH wave on the width d of the gap between the lithium niobate plate (*Y*-cut, *X*-propagation) and a metal screen for h/λ = 1.1: (●) theoretical and (+) experimental data.

when the gap width exceeds 20 μm. The discrepancy between theory and experiment for smaller values of the gap width can be explained by the imperfect parallelism and flatness of the two surfaces. The total phase variation was 234° when the gap width varied within 0–200 μm, the corresponding velocity variation being about 6%.

Thus, we confirmed both theoretically and experimentally that the coefficient of electromechanical coupling of SH waves propagating in lithium niobate plates can exceed 30%. This value is approximately six to seven times greater than the maximal value obtained for SAW in the same material. We theoretically and experimentally demonstrated the possibility of controlling the wave velocity by moving a conducting screen toward the plate. On the whole, the results of our study show that the use of SH waves offers considerable improvements in the parameters of the known SAW devices and opens up the possibilities for the development of new devices and sensors intended for operation in contact with a liquid medium.

ACKNOWLEDGMENTS

This work was supported in part by the US National Science Foundation and the program “Federal Support of Integration of Higher Education and Basic Research for 1997–2000”(project no. 696.3).

REFERENCES

1. S. J. Martin, A. J. Ricco, T. M. Niemczyk, and G. C. Frye, Sens. Actuators **20**, 253 (1989).
2. Y. Jin and S. G. Joshi, IEEE Trans. Ultrason. Ferroelectr. Freq. Control **43**, 491 (1996).
3. B. D. Zaitsev, S. G. Joshi, and I. E. Kuznetsova, Smart Mater. Struct. **6**, 739 (1997).
4. S. G. Joshi and Y. Jin, Ultrasonics **34**, 507 (1996).
5. M. K. Balakirev and I. A. Gilinskiĭ, *Waves in Piezoelectric Crystals* (Nauka, Novosibirsk, 1982).
6. Y. Jin, PhD Dissertation (Marquette University, USA), p. 128.
7. A. V. Chaplik, Pis’ma Zh. Tekh. Fiz. **10**, 1385 (1984) [Sov. Tech. Phys. Lett. **10**, 584 (1984)].

Translated by E. Golyamina

Acoustical Physics, Vol. 47, No. 3, 2001, pp. 286–290. Translated from Akusticheskiĭ Zhurnal, Vol. 47, No. 3, 2001, pp. 341–345.
Original Russian Text Copyright © 2001 by Eliseevnin.

Determination of the Source Bearing in a Waveguide by Using the Sound Field Interference Pattern

V. A. Eliseevnin
Andreev Acoustics Institute, Russian Academy of Sciences, ul. Shvernika 4, Moscow, 117036 Russia
e-mail: bvp@akin.ru

Received May 16, 2000

Abstract—The feasibility of determining the source bearing in a waveguide by an extended horizontal line array with the use of the sound field interference pattern is studied. The sound field is generated by an omnidirectional monochromatic point source and is represented as a sum of modes. The case of a small number of low-frequency modes is considered. © *2001 MAIK "Nauka/Interperiodica".*

The directional properties of an extended horizontal line array in an underwater acoustic waveguide have been studied in a series of papers [1–5]. The sound field was represented as a sum of a small number of modes, which allowed the physical interpretation of the results. The effect of ambiguity in the determination of the exact source bearing because of the sound dispersion in the waveguide was investigated in detail. A method for determining the exact source bearing by multichannel processing of the signal received by the array was described in [6].

In the cited papers, the array response is determined as the Fourier transform of the pressure field U at the array aperture with respect to spatial frequencies [7]. Below, we investigate the directional properties of the same array when the Fourier transformation is performed for the pressure field intensity UU^* at the array aperture. We consider a method for determining the source bearing that is similar to the method presented in [6].

In the sea and ocean waveguides, due to the interference between modes in the case of low frequencies and between rays in the case of high frequencies, the spatial oscillations of the total sound field intensity take place [8, 9]. In this case, the interference between a pair of modes (rays) forms the simplest interference pattern. Below, we consider the operation of a horizontal receiving array simultaneously crossing several such interference patterns.

An extended horizontal line array of aperture L is located in an underwater acoustic waveguide where a sound field is generated by an omnidirectional monochromatic point source. The latter is located in the far zone of the array (the Fraunhofer zone). The angle of the array rotation in the horizontal plane with respect to the direction to the source is denoted by α, and the horizontal distance between the source and the center of the array is denoted by R. The array is equipped with a compensator, which provides the compensation for a given angle β in the horizontal plane by introducing a linear phase distribution over the aperture [10].

The sound field in a waveguide is represented as a sum of the modes propagating along the waveguide, each with its own phase velocity C_1 [11]. We eliminate from our consideration the attenuating modes and the lateral waves, since their intensity rapidly decays with distance. The array output signal compensated by the angle β is proportional to the quantity (for the considered way of processing)

$$U_A = \int_{-\frac{L}{2}}^{\frac{L}{2}} U_X(x) U_X^*(x) \exp(-jK_K x \sin(\beta)) dx.$$

Here, $U_X(x)$ is the sound pressure at the array segment located at the distance X from its center, $U_X(x) U_X^*(x)$ is the sound field intensity at this segment, and K_K is the wave number which the compensator is tuned to. Tuning the compensator to a given phase velocity implies the realization of a signal delay in every channel of the receiving array according to the phase velocity $C_K = \omega/K_K$, where ω is the emission frequency.

The propagation of m unattenuating modes in a waveguide is described by the expression

$$U_X(x) = \frac{1}{\sqrt{R}} \sum_{l=1}^{m} A_l(b_l, \xi_l, Z_0, Z, R) \times \exp[j\xi_l(R + x\sin(\alpha)) - j\omega t], \tag{1}$$

where A_l characterizes the degree of excitation of the lth mode and is defined by the eigenfunctions and eigenvalues of the respective Sturm–Liouville problem with given boundary conditions [11], ξ_l and b_l are the horizontal and vertical components of the wave vector of the lth mode, Z_0 and Z are the depths of the emission and reception, and t is the current time.

With allowance for Eq. (1), the signal at the array output can be presented as

$$U_A = \frac{1}{R}\sum_{l=1}^{m}\sum_{q=1}^{m} A_l A_q \exp[j(\xi_l - \xi_q)R]$$

$$\times \int_{-\frac{L}{2}}^{\frac{L}{2}} \exp\{j[(\xi_l - \xi_q)\sin(\alpha) - K_K \sin(\beta)]x\}dx$$

$$= \frac{1}{R}\sum_{l=1}^{m}\sum_{q=1}^{m} D_{lq} \exp[j(\xi_l - \xi_q)R],$$

where

$$D_{lq} = A_l A_q \frac{\sin\left\{\frac{L}{2}[\xi_l - \xi_q \sin(\alpha) - K_K \sin(\beta)]\right\}}{\frac{L}{2}[(\xi_l - \xi_q)\sin(\alpha) - K_K \sin(\beta)]}. \quad (2)$$

Here, D_{lq} is the array response to the interference pattern of the lth and qth modes under the processing of the signal intensity over the array aperture and the role of the wave number is played by the quantity equal to the difference in the horizontal components of the wave numbers of these modes $\xi_l - \xi_q$. As is seen from Eq. (2), the response D_{lq} contains the information about the source bearing characterized by the angle α. This fact is due to the dispersion of sound in the waveguide when the modes arrive at the array with different phase velocities. It is evident that a similar processing of the sound intensity over the array aperture in free space provides no information on the source bearing. In this case, only one mode arrives at the array with the phase velocity C in free space.

As in the previous papers [1–3], we determine the array response as the signal intensity (normalized to its maximum) at the array output, this intensity depending on the angles α and β (hereafter the normalizing factor is omitted):

$$D(\alpha, \beta) = \left\{\sum_{l=1}^{m}\sum_{q=1}^{m} D_{lq}\cos[(\xi_l - \xi_q)R]\right\}^2$$
$$+ \left\{\sum_{l=1}^{m}\sum_{q=1}^{m} D_{lq}\sin[(\xi_l - \xi_q)R]\right\}^2. \quad (3)$$

It is evident that the array response $D(\alpha, \beta)$ is a superposition of responses D_{lq} to individual pairs of modes forming respective interference patterns in the waveguide.

According to Eq. (2), the direction of the main lobe of the response $D_{lq}(\beta)$ on the axis of compensation angles β, i.e., the quantity β_{lq}^M, can be determined from the condition

$$(\xi_l - \xi_q)\sin(\alpha) - K_K \sin(\beta_{lq}^M) = 0$$

or

$$\beta_{lq}^M = \arcsin\left(\frac{\xi_l - \xi_q}{K_K}\sin(\alpha)\right). \quad (4)$$

It is evident that the position of β_{lq}^M is determined by the value of the wave number of the compensator K_K. If $K_K = \xi - \xi_q$, we have $\beta_{lq}^M = \alpha$ and the maximum of the response D_{lq} is directed toward the source. When $K_K < \xi_l - \xi_q$, the angle is $\beta_{lq}^M > \alpha$, and when $K_K > \xi_l - \xi_q$, the angle is $\beta_{lq}^M < \alpha$. Correspondingly, the response D_{lq} is shifted to the right or to the left of the value $\beta = \alpha$ on the axis of the angles β.

Now, we proceed to the numerical results. As a waveguide, we chose an isovelocity water layer with a pressure-release surface and a rigid bottom. In this case [11], we have

$$A_l = \frac{1}{\sqrt{\xi_l}}\cos(b_l Z_0)\cos(b_l Z)$$

(the origin of coordinates is at the bottom, and the Z axis is directed upward).

Figure 1 shows the scanogram $D(\beta)$ of an array of aperture $L = 20\lambda$ placed in a waveguide of thickness $H = 1.5\lambda$, where λ is the sound wavelength. The source and the receiving array are placed at the bottom, $Z_0 = Z = 0$, at the distance $R = 100\lambda$ apart. The direction to the source is $\alpha = 60°$. In such a waveguide, three modes can propagate without attenuation and three interference patterns of respective pairs of modes are formed. The curve $D(\beta)$ exhibits three maxima, namely, max-

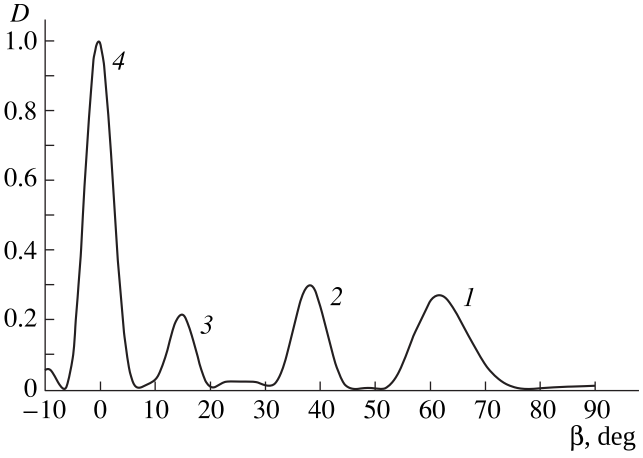

Fig. 1. Scanogram of an array in a waveguide: the responses to the interference patterns formed by the (*1*) first and second, (*2*) first and third, and (*3*) second and third modes and (*4*) the response D_K.

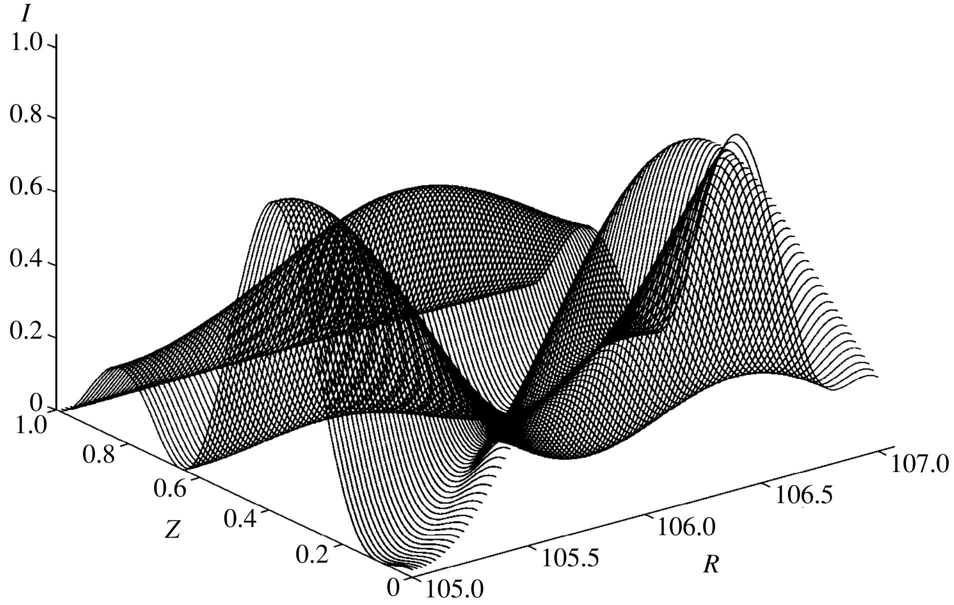

Fig. 2. Sound field intensity in the case of the propagation of the first and third modes in a waveguide.

ima *1–3*, that correspond to these patterns. The wave number of the compensator $K_K = \xi_1 - \xi_3$ and, according to Eq. (4), the angular position of the maximum of the response D_{13}, i.e., maximum *1*, corresponds to the direction to the source $\beta_{13}^M = \alpha$. Two other maxima, *2* and *3*, are shifted along the axis of angles β to the left.

As an illustrative example, Fig. 2 shows the interference pattern of the wave field formed by the first and third modes at some segment of the waveguide (maximum *1* in Fig. 1 corresponds to the response to this pattern). The coordinates (R, Z) lie in the horizontal plane, and the sound intensity normalized to its maximal value is represented by the vertical axis:

$$I(R, Z) = U(R, Z)U^*(R, Z)$$
$$= \frac{1}{R}\{A_l^2 + A_q^2 + 2A_lA_q\cos[(\xi_l - \xi_q)R]\}.$$

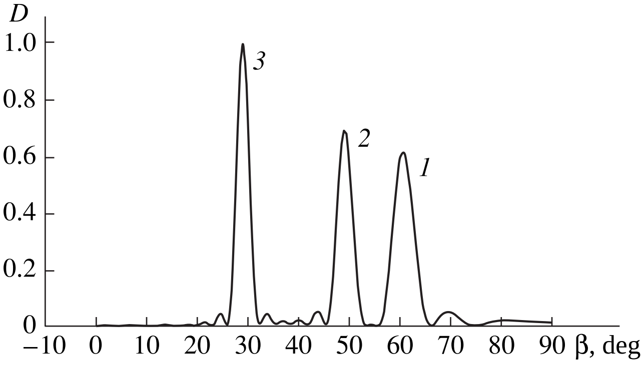

Fig. 3. Scanogram of an array in a waveguide: the responses to the (*1*) first, (*2*) second, and (*3*) third modes.

For comparison, Fig. 3 shows the usual scanogram obtained with the same array when the sound field over its aperture is processed rather than its intensity. Here, maxima *1–3* correspond to the responses to three modes propagating in the waveguide. In this case, the wave number of the compensator is equal to the horizontal wave number of the first mode $K_K = \xi_1$ and, as a consequence, $\beta_1^M = \alpha$ [1–3].

Let us return to Eq. (3) for the array response. It can be written as follows

$$D(\alpha, \beta)$$
$$= \left\{D_K\sum_{l=1}^{m}A_l^2 + 2\sum_{l=1}^{m-1}\sum_{q=l+1}^{m}D_{lq}\cos[(\xi_l - \xi_q)R]\right\}^2 \quad (5)$$
$$+ \left\{D_K\sum_{l=1}^{m}A_l^2 + 2\sum_{l=1}^{m-1}\sum_{q=l+1}^{m}D_{lq}\sin[(\xi_l - \xi_q)R]\right\}^2,$$

where

$$D_K = \frac{\sin\left(\frac{L}{2}K_K\sin(\beta)\right)}{\frac{L}{2}K_K\sin(\beta)}$$

is the scanogram of the array at the angle $\alpha = 0$, and it is determined by the array aperture L and the wave number of the compensator K_K. The quantity $\sum_{l=1}^{m}A_l^2$ is a constant, and the first terms in the braces on the right-hand side of Eq. (5) correspond to maximum *4* in Fig. 1. In what follows, we will consider the angles α

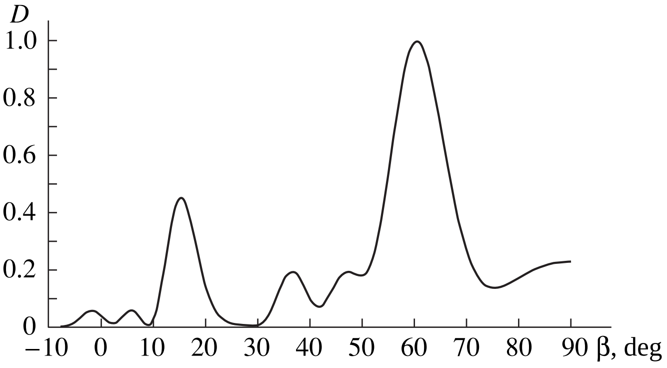

Fig. 4. Total response of an array tuned to three interference patterns.

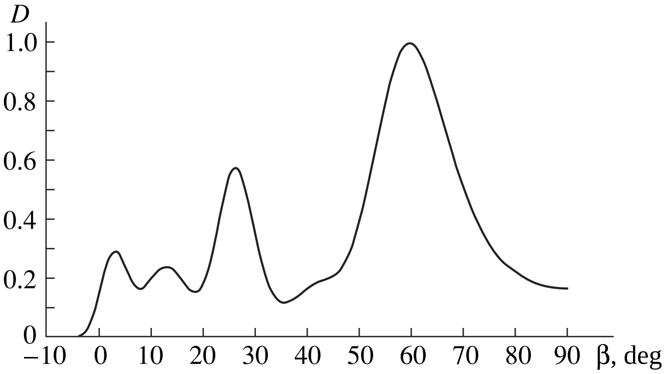

Fig. 5. Total response of an array tuned to ten interference patterns.

that widely differ from zero. Maximum *4* in the scanogram of Fig. 1 in the region of the zero values of the angle β can easily be eliminated by an adaptive processing of the signal received by the array [12]. Therefore, we can eliminate this maximum from our consideration, and we will ignore it in our calculations.

A continuous line array can be replaced by a discrete equidistant array of the same aperture, which consists of N omnidirectional receivers of identical sensitivity (taken as unity in our calculations). In this case, the response D_{lq} is determined as

$$D_{lq} = A_l A_q \frac{\sin\left\{N\frac{d}{2}[(\xi_l - \xi_q)\sin(\alpha) - K_K\sin(\beta)]\right\}}{N\sin\left\{\frac{d}{2}[(\xi_l - \xi_q)\sin(\alpha) - K_K\sin(\beta)]\right\}}.$$

Here, d is the separation between adjacent receivers of the array, which acoustically are not coupled to one another. For a discrete array in free space, the absence of secondary diffraction maxima equal to the main one in its response is determined by the condition $d \le \lambda/2$ [10]. In the case under consideration, a similar condition also takes place: $d \le \Lambda_{lq}/2$, where $\Lambda_{lq} = 2\pi/(\xi_l - \xi_q)$ is the wavelength of the interference pattern of the lth and qth modes [8, 9]. It is evident that $\Lambda_{lq} > \lambda$ and, for example, for the case under study, $\Lambda_{12} = 8.4\lambda$, $\Lambda_{13} = 2.3\lambda$, and $\Lambda_{23} = 3.3\lambda$. Therefore, the condition that the array response has only one, main, maximum is written as

$$d \le \frac{1}{2}\min\{\Lambda_{lq}\}.$$

Thus, in the case under consideration, if the previous array size L is retained, the number of array elements can be reduced by half with the corresponding twofold increase in the interelement distance d.

Let us consider the determination of the source bearing by processing the intensity field at the array aperture. This problem is solved by a method that is similar to that described previously [6], but with a simultaneous use of several compensators. Their number should not exceed that of the interference patterns in the waveguide. Each compensator is tuned to its own interference pattern. In this case, the tuning of the compensator means that a signal delay is introduced according to the phase velocity $C_K = \omega/(\xi_l - \xi_q)$ in the channel of each array receiver. Having tuned the compensators to various interference patterns and combining the signals from their outputs incoherently (without considering their phases), we obtain a total response. The latter exhibits one large maximum directed toward the source, $\beta_{\max} = \alpha$, and many small maxima forming the background on the axis of the compensation angles β. The appearance of the large maximum is caused by the fact that, in the curve of the response of each compensator, there is only one maximum directed exactly to the source and corresponding to the interference pattern to which it is tuned. Being added together, all these maxima give one large maximum in the curve of the total response, and this maximum is directed toward the source. A random summation of the peaks corresponding to other responses to various interference patterns forms the background at the angles $\beta \ne \alpha$.

Figure 4 presents the result of combining the responses from three compensators, each being tuned to its own interference pattern in the waveguide. The angular position of the main maximum corresponds to the direction to the source $\beta_{\max} = \alpha = 60°$. Figure 5 presents the result of the summation of the signals from the outputs of ten compensators of the same array in a waveguide of thickness $H = 2.5\lambda$. In such a waveguide, five unattenuating modes can form ten interference patterns. Other parameters of the problem are the same as before. Here, we also have $\beta_{\max} = \alpha = 60°$.

In order to determine the exact source bearing in the waveguide, it is necessary to know the sound propagation conditions, namely, the phase velocities and the eigenfunctions of modes, at the array site [6]. It is assumed that they are determined just before the determination of the source bearing.

At large angles α and with the use of extended arrays, all or most of the interference patterns appear as separate peaks in the response curve. However, depending on the technical conditions, only part of the interference patterns may be separated. In this case, the number of the processing channels is limited by the number of the separated interference patterns, and the compensators are tuned to their reception. Then, the source bearing is determined by only a part but not all of the interference patterns existing in the waveguide.

For arbitrary angles α, the solution can be obtained with the use of two horizontal arrays placed at right angles to one another. Each of the arrays will operate at large angles α, for example, from 45° to 90°. In this case, small angles for one array will be large for the other array and vice versa. This means that, for any direction to the source, one of the arrays can separate several interference patterns and, according to the results presented above, the exact source bearing can be determined.

REFERENCES

1. V. A. Eliseevnin, Akust. Zh. **25**, 227 (1979) [Sov. Phys. Acoust. **25**, 123 (1979)].
2. V. A. Eliseevnin, Akust. Zh. **29**, 44 (1983) [Sov. Phys. Acoust. **29**, 25 (1983)].
3. V. A. Eliseevnin, Akust. Zh. **35**, 468 (1989) [Sov. Phys. Acoust. **35**, 274 (1989)].
4. W. Carey, J. Reese, and H. Bucker, J. Acoust. Soc. Am. **104**, 133 (1998).
5. T. C. Yang and T. Yates, J. Acoust. Soc. Am. **104**, 1316 (1998).
6. V. A. Eliseevnin, Akust. Zh. **42**, 208 (1996) [Acoust. Phys. **42**, 182 (1996)].
7. V. A. Zverev, *Radiooptics* (Sov. Radio, Moscow, 1975).
8. *Interference of Broadband Sound in the Ocean*, Ed. by V. A. Zverev and E. F. Orlov (Inst. Prikl. Fiz., Akad. Nauk SSSR, Gorkiĭ, 1984).
9. E. F. Orlov and G. A. Sharonov, *Interference of Sound Waves in the Ocean* (Dal'nauka, Vladivostok, 1998).
10. M. D. Smaryshev, *Directivity of Hydroacoustic Arrays* (Sudostroenie, Leningrad, 1973).
11. L. M. Brekhovskikh, *Waves in Layered Media* (2nd ed., Nauka, Moscow, 1973; Academic, New York, 1980).
12. R. A. Monzingo and T. W. Miller, *Introduction to Adaptive Arrays* (Wiley, New York, 1980; Radio i Svyaz', Moscow, 1986).

Translated by Yu. Lysanov

Acoustical Physics, Vol. 47, No. 3, 2001, pp. 291–296. Translated from Akusticheskiĭ Zhurnal, Vol. 47, No. 3, 2001, pp. 346–351.
Original Russian Text Copyright © 2001 by Efimtsov, Lazarev.

Sound Transmission Loss of Panels with Resonant Elements

B. M. Efimtsov and L. A. Lazarev
State Research Center Zhukovskiĭ Central Aerohydrodynamics Institute,
ul. Radio 17, Moscow, 107005 Russia
e-mail: ayzverev@hotmail.com

Received June 30, 2000

Abstract—Various types of resonant elements that can be used for increasing the transmission loss of panels in narrow frequency bands are analyzed. The main physical phenomena determining the transmission loss of sound waves in panels with resonant elements are studied. Three main principles of increasing the transmission loss realized in panels with resonant elements are described: the principle of soft reflection, the principle of hard reflection, and the principle of compensation. The relations for estimating the transmission loss of panels with resonant elements, which model the main physical phenomena governing the propagation of sound waves, are presented. *© 2001 MAIK “Nauka/Interperiodica”.*

In solving practical problems of noise control in industry and transportation, it is often necessary to considerably increase the transmission loss of panels in a narrow frequency band. This problem becomes particularly important when discrete low-frequency components dominate in the spectrum of noise to be suppressed. The transmission loss of panels in a low-frequency band, as a rule, is restricted from above by the “mass law.” The required increase in the transmission loss of a panel in this frequency band (compared to the loss expected according to the mass law) with strict limitations on the mass and size can be achieved by mounting resonant elements on the panel.

There are a great number of publications devoted to the study of various types of mechanical and acoustic resonant elements mounted on panels that are used for reducing the vibration and increasing the sound absorption. But the number of similar publications dedicated to the increase in the transmission loss of panels is quite limited. Here, we can mention the papers [1–4] where design and experimental data are presented that demonstrate the possibility of using resonant elements for a narrow-band increase in the transmission loss of panels.

However, as far as we can judge from the publications, a clear description of the physical phenomena that determine the effects of the increase in the transmission loss of panels with resonant elements is currently lacking. Our paper fills in this gap. It is devoted to the study of the nature of these physical phenomena and their generalized description.

To establish the main physical processes that determine the increase in the transmission loss of a panel with resonant elements, we restrict our consideration to the simplest model—an unbounded, purely inertial plane panel with a system of resonators, which is excited by a normally incident plane sound wave. The action of the resonant elements on the panel is considered to be uniformly distributed over the panel surface. With these simplifications, the process can be described by a system of one-dimensional linear equations in which all the quantities characterizing the system are averaged over the surface.

For the analysis, we use a known method according to which the relationship between the pressures P_j and the velocities V_j on either side of the panel is described by the transfer matrix A:

$$\begin{pmatrix} P_2 \\ V_2 \end{pmatrix} = A\begin{pmatrix} P_1 \\ V_1 \end{pmatrix}, \tag{1}$$

where P_1, P_2, V_1, and V_2 are the complex amplitudes of the corresponding quantities. The subscript 1 corresponds to the physical quantities on the side of the incident waves and the subscript 2 corresponds to the quantities on the side of the transmitted waves. The positive direction of the particle velocity is opposite to the direction of propagation of the incident sound wave.

The transmission loss is described by the following relation in terms of the transfer matrix elements and the impedances of the media:

$$\begin{gathered} R = 10\log\left(\left|\frac{P_i}{P_t}\right|^2\frac{\rho_2c_2}{\rho_1c_1}\right), \\ \frac{P_i}{P_t} = \frac{1}{2}\left(a_{22} + \rho_1c_1a_{21} + \frac{1}{\rho_2c_2}(a_{12} + a_{11}\rho_1c_1)\right). \end{gathered} \tag{2}$$

Here, ρ_1 and ρ_2 are the media densities, c_1 and c_2 are the sound speeds in the media, and P_i and P_t are the complex pressure amplitudes in the incident and transmitted waves, respectively. Below, the parameters of the media are assumed to be equal.

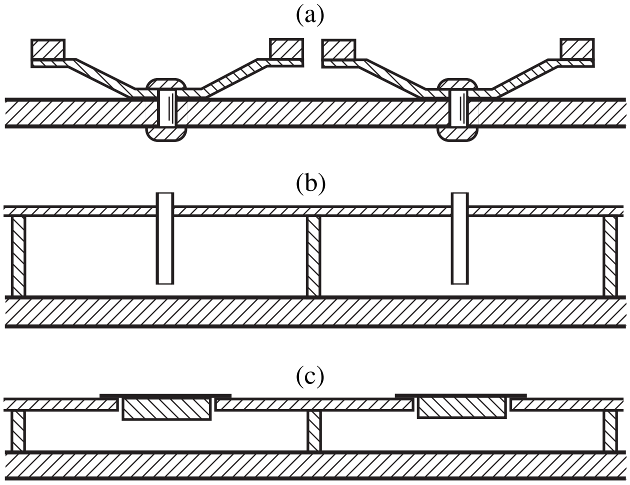

Fig. 1. Panels with resonant elements realizing the principles of (a) hard reflection, (b) soft reflection, and (c) compensation.

We consider the simplest cases when identical resonant elements are located on one side of the panel. Each element consists of one inertial body and an elastic bond. The resonant elements can be excited in three ways: by vibration of the panel on which they are mounted, by the sound pressure directly applied to the inertial body, and by a combined effect of the panel vibration and the sound pressure.

The first case, when the resonant element is excited by panel vibration, corresponds, in particular, to dynamic vibration dampers, which consist of inertial bodies elastically connected with the panel and practically not interacting directly with the medium (Fig. 1a). At the resonance frequency, due to the effect of antiresonance, the input impedance of the panel sharply increases and a hard reflection of sound waves takes place. Consequently, for the principle of increasing the transmission loss on the basis of the effect of antiresonance, we will use the term "the principle of hard reflection." Panels with resonant elements realizing the principle of hard reflection will for brevity be called hard reflectors.

The main parameters characterizing a resonant element of a hard reflector are the resonance frequency ω_r, the Q-factor, and the mass per unit area of inertial bodies m. The transfer matrix A_{HR} of a hard reflector can be written as a product of the matrix of the inertial partition and the matrix of the layer of resonators

$$A_{\mathrm{HR}} = \begin{pmatrix} 1 & i\omega M \\ 0 & 1 \end{pmatrix}\begin{pmatrix} 1 & i\omega m(1+\alpha^2/\Omega) \\ 0 & 1 \end{pmatrix}, \quad (3)$$

$$\Omega = 1-\alpha^2 + i\alpha/Q, \quad \alpha = \omega/\omega_r,$$

where M is the mass per unit area of the panel. At the resonance frequency, the increase in the transmission loss compared to the transmission loss in a panel without resonators is determined by the following approximate relation

$$\Delta R_{\mathrm{HR}}(\omega_r) \approx 10\log(1+\beta_{\mathrm{HR}}^2), \quad \beta_{\mathrm{HR}} = mQ/M, \quad M\omega_r \gg \rho c. \quad (4)$$

The second case, when a resonant element is excited by the sound pressure acting directly on the inertial body, corresponds, in particular, to Helmholtz resonators (Fig. 1b), as well as to resonant elements that vibrate only in the plane of the panel and, consequently, are not excited by its transverse vibrations. At the resonance frequency, the input impedance of such a structure can be much less in absolute value than the wave impedance of the medium. In this case, the incident sound waves are reflected from it as from a layer of a material with a considerably lower impedance. Hence, for the principle of increasing the transmission loss on the basis of a high resonant compressibility, we will use the term "the principle of soft reflection," and the systems working on this principle will be called soft reflectors.

The main parameters of the resonant elements of soft reflectors include the resonance frequency, the Q-factor, and the average thickness of the air cavity h, which is equal to the ratio of the total volume of cavities to the panel area. For a Helmholtz resonator, the direct influence of the size of its neck on the transmission loss is practically not observed. This is explained by a negligibly small effect of the interaction between the resonators and the panel. The transfer matrix A_{SR} of soft reflectors with resonant elements located on the side of incident sound can be written as a product of the matrix of the inertial partition and the matrix of the layer of resonators:

$$A_{\mathrm{SR}} = \begin{pmatrix} 1 & i\omega M \\ 0 & 1 \end{pmatrix}\begin{pmatrix} 1 & 0 \\ i\omega/k\Omega & 1 \end{pmatrix}, \quad k = \rho c^2/h. \quad (5)$$

The increase in the transmission loss of the panel that realizes the principle of soft reflection can be estimated at the resonance frequency by using the relation

$$\Delta R_{\mathrm{SR}}(\omega_r) \approx 10\log(1+\beta_{\mathrm{SR}})^2, \quad \beta_{\mathrm{SR}} = h\omega Q/c = Q2\pi h/\lambda, \quad M\omega_r \gg \rho c, \quad (6)$$

where λ is the sound wavelength.

We consider the third case (Fig. 1c) when a resonant element is excited simultaneously by the panel vibrations (as in hard reflectors) and by the sound pressure (as in soft reflectors). In this case, a sharp increase in the transmission loss can be achieved on the basis of the "compensation principle." When the resonant elements are located on the side of incident waves, at frequencies higher than the resonance frequency, their inertial bodies vibrate out of phase with the sound pressure. At a certain frequency, which can be called the frequency of compensation, the forces of pressure acting directly on the panel are compensated by the forces of pressure arising in cavities due to the vibrations of the inertial bodies of resonators. The resonant systems realizing this principle can be called compensators.

When the resonant elements are located on the side of the transmitted waves, the increase in the transmission loss at the frequency of compensation is explained by the fact that the volume velocity of the panel is compensated by the volume velocity of the inertial bodies of resonators vibrating out of phase with the panel.

The main parameters characterizing the resonant elements of compensators are the Q-factor, the frequency of compensation ω_c, the average thickness of the air cavity h, and the relative area of openings σ in which inertial bodies of mass m are located. These parameters are related by the equation

$$\omega_c^2 = \frac{k\sigma^2}{m(1-\sigma)}, \quad k = \rho c^2/h. \tag{7}$$

The transfer matrix of a compensator can be written as

$$A_{\mathrm{CR}} = \begin{pmatrix} 1 & i\omega M \\ 0 & 1 \end{pmatrix} \begin{pmatrix} 1 & i\omega m(1+\alpha^2/\Omega) \\ 0 & 1 \end{pmatrix}$$

$$\times \begin{pmatrix} \Omega_c/\Omega & 0 \\ 0 & \Omega/\Omega_c \end{pmatrix} \begin{pmatrix} 1 & 0 \\ i\omega/k\Omega & 1 \end{pmatrix}, \tag{8}$$

$$\Omega_c = 1-\alpha_c^2 + i\alpha/Q, \quad \alpha_c = \omega/\omega_c,$$

$$\alpha = \omega/\omega_r, \quad \omega_r^2 = k\sigma^2/m.$$

Comparing this expression with Eqs. (3) and (5), one can see that the transfer matrix of the layer of resonators, Eq. (8), can be represented as a product of the matrix of the layer of resonators of a hard reflector; the diagonal matrix; and the matrix of the layer of resonators of a soft reflector with the same thickness, Q-factor, and resonance frequency. Consequently, depending on the parameters, the resonant system described by Eq. (8) can realize one of the three principles of increasing the transmission loss. Expression (8) is common for all three types of resonators possessing one degree of freedom and located on the side of the incident waves. Expressions (3) and (5) are the limiting cases, when one of the two ways of the resonator excitation is neglected. Depending on which of the three principles determines the increase in the transmission loss to a greater extent, the panel with resonators should be assigned to one of the three types of resonant systems.

When the mass of the panel is sufficient and the influence of a close resonance frequency is not strong, the increase in the transmission loss at the frequency of compensation can be obtained from the approximate relation

$$\Delta R_{\mathrm{CR}}(\omega_c) \approx 10\log(1+\beta_{\mathrm{CR}}^2) + 10\log\left(1-\frac{m}{M}\frac{(1-\sigma)}{\sigma}\right)^2$$

$$+ 10\log\left(1+\frac{h\rho}{m}(1-\sigma)\right), \tag{9}$$

$$M\omega_c \gg \rho c, \quad \beta_{\mathrm{CR}} = Q\sigma/\sqrt{1-\sigma}$$

$$= Q\omega\sqrt{mh\rho}/\rho c \approx \sigma Q.$$

The first term on the right-hand side of Eq. (9) describes the increase in the transmission loss due to the compensation of pressure. The second term describes the influence of the inertial properties of resonators. The third term describes the influence of the compressibility on the increase in the transmission loss at the frequency of compensation.

We assume that limitations are imposed on the mass of the vibrating body of a resonator and on its thickness. Let the Q-factors of various types of resonators be known beforehand. Then, by comparing the dimensionless parameters β_{HR}, β_{SR}, and β_{CR}, it is possible to determine which of the three types of resonators can provide the greatest increase in the transmission loss when mounted on a single inertial partition.

In the case of equal Q-factors of the resonators, compensators are more efficient than soft reflectors when the condition $m/h\rho > 1$ is satisfied, i.e., when the mass of the vibrating body of the resonator is greater than the mass of air in the resonator cavity. Hard reflectors are more efficient than the soft ones when $m/h\rho > M\omega_r/\rho c$ or $m/M > 2\pi h/\lambda$, i.e., when the ratio of the mass of vibrating bodies to the mass of the panel is greater than the ratio of the resonator thickness to the sound wavelength divided by 2π. Hard reflectors become preferable to compensators when $m/h\rho > (M\omega/\rho c)^2$. These conclusions are valid when the Q-factors are sufficiently large and the condition $M\omega \gg \rho c$ is satisfied.

Figure 2 shows the transmission loss calculated for panels with various types of resonators that have equal Q-factors ($Q = 25$) and provide the same effect (9.5 dB) at a resonance frequency of 100 Hz. Hard reflectors have a dip in the transmission loss curve at the frequency of the mass–elasticity–mass resonance ($\omega_{mM} = \omega_r\sqrt{(m+M)/M}$). Compensators have a dip at the resonance frequency ($\omega_r = \omega_c\sqrt{1-\sigma}$), because at this frequency the effect of the resonators on the panel is enhanced. Soft reflectors, unlike the resonators of other types, increase the transmission loss of panels at all frequencies.

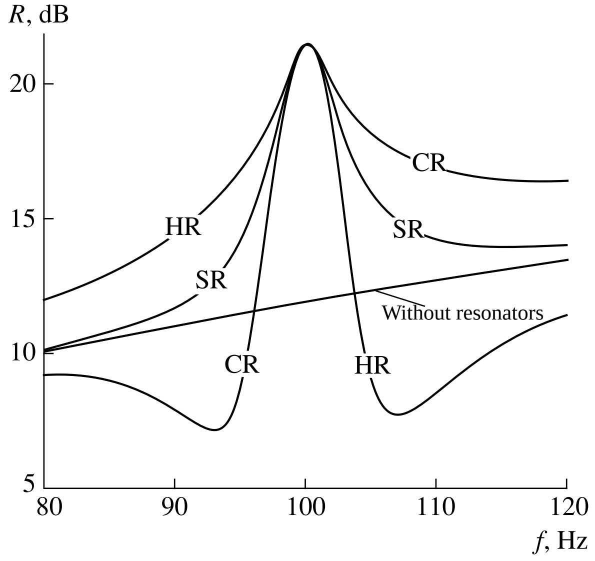

Fig. 2. Transmission loss for three types of resonators with an equal effect of increasing the transmission loss and equal Q-factors: HR corresponds to a hard reflector, SR to a soft reflector, and CR to a compensator; Q = 25, M = 5 kg/m^2, h_{SR} = 0.05 m, h_{CR} = 0.025 m, m_{CR} = 0.4 kg/m^2, m_{HR} = 0.5 kg/m^2, and $f_r = f_c$ = 100 Hz.

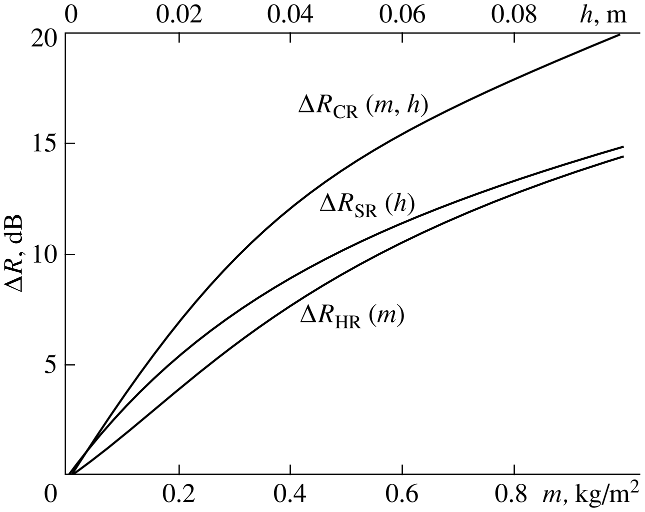

Fig. 3. Increase in the transmission loss at the resonance frequency for three types of resonators at a constant ratio of the mass of inertial bodies to the mass of air in the resonators ($m/h\rho$ = 8.3); Q = 25, M = 5 kg/m^2, and $f_r = f_c$ = 100 Hz.

For the case of the resonators with the parameters used in Fig. 2 and with equal efficiency, the mass of the inertial body of compensators is less than the mass of the inertial body of hard reflectors. The thickness of the air cavity of compensators is half as great as the thickness of the air cavity of soft reflectors. Thus, when limitations are simultaneously imposed on the mass and the thickness of a panel with resonators, compensators can be much more efficient, as compared to soft and hard reflectors.

Figure 3 illustrates the increase in the transmission loss at the resonance frequency after three types of resonators with equal Q-factors are mounted on the panel. For hard reflectors, the abscissa axis represents the mass of vibrating elements, and, for soft reflectors, the abscissa is the average thickness of the air cavity. Compensators are determined by these two parameters. The ratio of the mass of vibrating elements to the mass of air confined in the resonators is constant in this figure ($m/h\rho$ = 8.3). Since this ratio is close to the dimensionless mass of the panel ($M\omega_c/\rho c$ = 7.6), compensators are more efficient than the two other types of resonators for this ratio of masses, which is clearly seen in Fig. 3.

Figure 4 illustrates the efficiency of compensators as a function of the ratio of the mass of the vibrating body to the mass of air in the resonators for a constant product of these masses and, hence, for a constant β_{CR} = 5. The abscissa axis represents the logarithm of the mass ratio. The zero abscissa value corresponds to the mass ratio for which the dimensionless parameters of compensators and soft reflectors are equal; the unit value corresponds to the equality of the dimensionless parameters of hard and soft reflectors; and the value 2 corresponds to the equality of the dimensionless parameters of compensators and hard reflectors. For comparison, the figure shows the increase in the transmission loss that does not depend on the ratio of the mass of the vibrating body to the mass of air in resonators and is obtained without regard for the compressibility and the inertial properties of resonators (the second and fourth matrices in Eq. (8) are omitted).

From Eq. (9) and Fig. 4, it is seen that the compressibility contributes to the transmission loss of compensators. As the mass ratio decreases, the effect of compressibility increases and, when $m < h\rho$, the resonant system can be attributed to soft reflectors. The inertial properties of the resonant elements of a compensator adversely affect the transmission loss. With an increase in the mass ratio (their product remaining constant), the efficiency of compensators drops.

When the equality $m/M = \sigma/(1 - \sigma)$ is fulfilled, a minimum is observed in the efficiency of compensators (a dip in Fig. 4 for $m/h\rho \approx (M\omega/\rho c)^2$). In this case, the frequency of compensation coincides with the frequency of mass–elasticity–mass resonance of the panel with resonators. The panel and the inertial body of a resonator gain the same acceleration due to the action of pressure before the compensators.

For masses of vibrating elements commensurable with the panel mass, the influence of the inertial properties of resonators at the frequency of compensation is significant, which can considerably decrease the efficiency of compensators. To reduce this undesirable effect and to shift the frequency of the mass–elasticity–mass resonance, it is necessary to decrease the mass of the inertial body, which will reduce the effect of compensation. More complicated resonant systems based on the compensation principle make it possible to solve this problem without reducing the efficiency.

The transfer matrices of panels with a system of uniform resonant elements with one degree of freedom are represented in Eqs. (3), (5), and (8) as the products of more simple matrices. Every matrix used in the expansions is determined by one function expressing the inertial, elastic, or compensating properties of the panel with resonators. Since each of these elementary matrices satisfies the reciprocity principle, i.e., its determinant equals unity, we can represent a panel with a system of resonators as a sequence of layers in which inertial, compensatory, and elastic properties are concentrated. They can be interpreted as inertial, compensating, and elastic elementary layers, respectively.

In general, an arbitrary sound insulating system described by a transfer matrix can be represented as a sequence of three elementary layers

$$\begin{pmatrix} a_{11} & a_{12} \\ a_{21} & a_{22} \end{pmatrix} = \begin{pmatrix} 1 & i\omega M(\omega) \\ 0 & 1 \end{pmatrix}$$

$$\times \begin{pmatrix} C^{-1}(\omega) & 0 \\ 0 & C(\omega) \end{pmatrix} \begin{pmatrix} 1 & 0 \\ i\omega/K(\omega) & 1 \end{pmatrix},$$

$$i\omega M(\omega) = a_{12}/a_{22} = P_2/V_2|_{P_1 = 0},$$

$$K(\omega)/i\omega = a_{22}/a_{21} = -P_1/V_1|_{V_2 = 0},$$

$$C(\omega) = a_{22} = V_2/V_1|_{P_1 = 0} = P_1/P_2|_{V_2} = 0.$$

The expression $i\omega M(\omega)$ has the meaning of the input impedance from the side of the transmitted waves in the absence of pressure on the opposite side. The expression $K(\omega)/i\omega$ has the meaning of the input impedance from the side of the incident waves with an immovable opposite surface of the system. The function $C(\omega)$ represents a coefficient connecting the pressures on both sides of the system for an immovable surface on the side of transmitted waves, as well as the coefficient connecting the velocities on both sides of the system in the absence of pressure on the side of incident waves.

Drawing a mechanical analogy, we consider an elementary inertial layer as the mass $M(\omega)$ and an elementary elastic layer as the stiffness $K(\omega)$. Then an elementary compensating layer can be considered as a lever with the ratio of the lever arms $C(\omega)$ (Fig. 5).

Thus, by using resonant elements mounted on a panel, it is possible to achieve a considerable increase in its transmission loss in a narrow band of low frequencies. The increase in the transmission loss can be based on one of three principles. The principle of hard reflection is realized by using resonant elements excited by vibrations of the panel and operating on the basis of the antiresonance effect. The principle of soft reflection is realized by using resonant elements excited directly by the sound pressure and operating due to the large resonant compressibility. The principle of compensation is realized by using resonant elements excited by both panel vibrations and sound pressure.

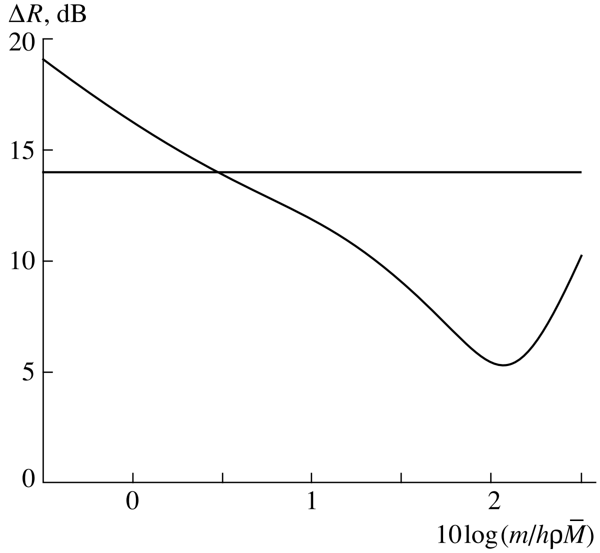

Fig. 4. Increase in the transmission loss at the resonance frequency for a compensator at a constant dimensionless parameter β_{CR} as a function of the ratio $m/(h\rho\bar{M})$, where $\bar{M} = M\omega_c/\rho c$.

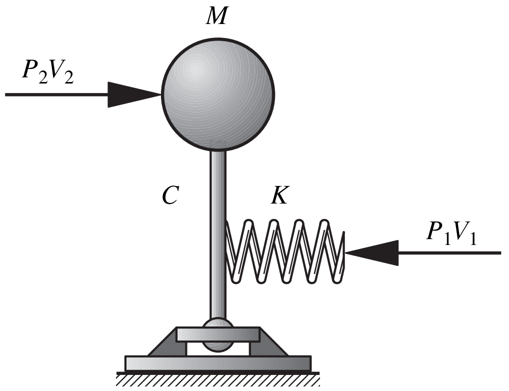

Fig. 5. Schematic representation of the sequence of three elementary layers.

From the point of view of the sound transmission, an arbitrary sound insulating system described by a transfer matrix can be represented as a sequence of three elementary layers: a layer with inertial properties, a layer with compensating properties, and a layer with elastic properties. In each of these layers, the corresponding principle of increasing the transmission loss can be realized. Each elementary layer is determined by one complex function of frequency, so that an arbitrary sound insulating system can be characterized by three frequency functions, which determine its inertial, compensating, and elastic properties.

ACKNOWLEDGMENTS

This work was supported by the Russian Foundation for Basic Research (project no. 98-02-16239) and by the INTAS (project no. 99-0088).

REFERENCES

1. L. D. Pope, R. A. Prydz, L. S. Wirt, and H. L. Kuntz, J. Acoust. Soc. Am. **87**, 1597 (1990).
2. J. M. Mason and F. J. Fahy, J. Sound Vibr. **124**, 367 (1988).
3. Zhaohui Sun, Jincai Sun, Chong Wang, and Yang Dai, Appl. Acoust. **48**, 311 (1996).
4. Z. N. Kitts and R. A. Burdisso, in *Internoise 98 Conference Proceedings* (Christchurch, New Zealand, 1998), No. 125.

Translated by A. Svechnikov

Acoustical Physics, Vol. 47, No. 3, 2001, pp. 297–302. Translated from Akusticheskiĭ Zhurnal, Vol. 47, No. 3, 2001, pp. 352–358.
Original Russian Text Copyright © 2001 by Zverev, Pavlenko.

Beamforming for a Flexible Acoustic Array

V. A. Zverev and A. A. Pavlenko
Institute of Applied Physics, Russian Academy of Sciences,
ul. Ul'yanova 46, Nizhni Novgorod, 603600 Russia
e-mail: zverev@hydro.appl.sci-nnov.ru

Received December 15, 1999

Abstract—A method is considered for processing the signal received by a flexible acoustic array bent in such a way that random phase shifts exceeding 2π occur between the receiving elements. It is shown that these phase shifts can be filtered out if the random bends of the array are characterized by a low-frequency spatial spectrum. The efficiency of the method is tested by numerical modeling. *© 2001 MAIK "Nauka/Interperiodica".*

An advantageous and sometimes the only possible way for the acoustical monitoring of media is forward-scattering location (FSL). The advantages of FSL consist in using a signal that is scattered by the located object in the direction corresponding to the maximal level of scattering. In this direction, which coincides with that of the propagation for the insonifying sound field, the signal scattered by the object exists even when the object completely absorbs the incident field. The ordinary reflection location is useless in this case. However, the aforesaid advantage of the FSL is accompanied by a number of difficulties in its implementation. Two such difficulties are most significant. The first one is the need in a nearly full suppression of the insonifying field for the scattered signal to be detected in the same direction. The second difficulty consists in the presence of a high-level background (the forward reverberation) that is caused by the sound scattering by multiple small-scale inhomogeneities of the water bulk, bottom, and surface of the basin.

Recently, a number of works have appeared that seek for ways to overcome the aforementioned difficulties. The direct signal of the projector can be attenuated by the special-purpose dark field methods [1–3]. This signal can also be eliminated by improving the spatial resolution of the locator. The forward reverberation can be effectively suppressed by using a focused extended array [4]. The properties of the near-field reverberation in a shallow sea (where it is most important) have been studied in a number of papers [5–8]. From these studies, the conclusion can be drawn that the near-field reverberation has statistical properties which are close to those of the additive noise familiar to acousticians. The only difference is that the effect of additive noise can be reduced by increasing the signal intensity, whereas the near-field reverberation cannot be eliminated in such a way. The only way to suppress the near-field reverberation relative to the transmitted signal is to increase the aperture of the receiving array.

Fixed acoustic arrays that have the required net apertures are complex and expensive systems which, in addition, are not transportable. The problem of constructing mobile large arrays can be successfully solved by switching to arrays in the form of long cables of neutral buoyancy with built-in acoustically active elements. The neutral buoyancy of such devices implies the possibility for a nearly unlimited elongation of the array to produce very large apertures. For a cable array, the spatial separations of adjacent elements are fixed and, therefore, they must be stiff for the array to operate properly. The requirements for the stiffness of a long array become more strict as the array length increases. These requirements are just what impedes the manufacturing of flexible arrays with large apertures.

Let us assume that we can produce a flexible array that is sufficiently stiff up to the aperture A. Consider how an array of much greater aperture, say $10A$, will work. It will be randomly bent, but the spatial spectrum of the bends will be limited by some spatial frequency band lying below $2\pi/A$. Because of bending, the phases of the signals received by different array elements will considerably (by more than π) differ from those received by a linear array. Because of the random and variable nature of such phase shifts, they can hardly be compensated for by processing the received signal. As a result, the array operation will be ineffective.

The objective of this paper is to study the applicability of cepstral analysis for improving the efficiency of an FSL system with a long flexible focused array. As far as we are aware, the problem of applying cepstral analysis to signal processing in arrays has never been investigated. The results of this study lead to some conclusions that can be applied not only to FSL but also to some other problems.

Let a long flexible array operate in the FSL mode. This means that the sound field received by the array is mainly produced by a single high-power monochromatic source, which is of primary importance for us. An additive noise and a forward reverberation are added to this field. The reverberation can also be included into the additive noise, apart from the effects that accompany an increase in the intensity of the direct signal. We assume that the power of the source is sufficient for the interference to be entirely determined by the level of the near-field reverberation. We use the term "array shape" for the phase shifts at the array elements, which are caused by both offsets of the elements from their undisturbed positions and the effects of the medium inhomogeneities. We also assume that the spatial spectrum of the array shape is much narrower than the entire frequency band of the array. The spatial frequency band of the array is determined by the modulus of the wave vector, $\pm\frac{2\pi}{\lambda}$, where λ is the wavelength. We normalize this quantity to the array resolution, which is equal to the separation of the array side lobes, $\frac{2\pi}{L}$, where L is the array aperture. The normalized bandwidth of the spatial spectrum of the received signals is the ratio of the array aperture to the half-wavelength. We assume that the spatial spectrum of the array bends has a much smaller bandwidth and begins from zero frequency. The spatial spectrum of the signal is also narrow: its bandwidth is much smaller than the array resolution, and this spectrum lies within the domain determined by the angle at which the direct signal arrives at the array. By positioning the sound source far enough from the normal to the array aperture, one can prevent the spectra of the signal and the array bending from overlapping. Let us try to make use of this fact to filter out the array bending from the signal.

The array is supposed to work in a monochromatic wave field. Then, the signals received by its elements can be represented as complex numbers whose modulus characterizes the amplitude of the received oscillation and the argument indicates its phase [9]. The received signal characterized by random phase shifts between the array elements can be written as

$$P(x) = M(x)\exp[i\Phi(x)], \tag{1}$$

where $M(x)$ is the complex signal (complex amplitude [9]) received by the array that has no phase distortions and $\Phi(x)$ represents random phase changes at the receiving elements. The values of the phase shifts are not limited, and it is possible that $|\Phi(x)| \geqslant 2\pi$ for nearly all values of x.

Only the quantity $P(x)$ is to be subjected to filtering or to other manipulations, because individual factors in Eq. (1) are not observable. Figure 1 shows the spectrum of $P(x)$ for a situation when $M(x)$ is a sum of three plane waves of different directions. The curves are plotted for different array bends. Figure 1a corresponds to the absence of bends. In the subsequent figures, the bends increase, the array shape being the same. For a small bend (Fig. 1b), the discrete spectral line that corresponds to the plane wave is still well pronounced. For stronger bending, the pattern features merge to yield a continuous spectrum. The plane-wave discrete line is also present in Fig. 1d, but its level is too low to be distinguished. The level of the discrete line becomes higher as the array length increases. However, it is not the proper way to reach the required selectivity: Fig. 1d is more realistic than Fig. 1b, and the array length (524 wavelengths) is large enough in the sense that it is close to the value required for the array to be robust with respect to the forward reverberation.

Thus, in spite of the differences in the spectra, the ordinary method does not allow one to filter out random phase shifts at the array elements from the received wave field, because these processes are coupled in a multiplicative manner. Nevertheless, there exists a way to spectrally separate the wave field and the array bending. This way is the well-known method of cepstral analysis [10]. The technique of cepstral analysis had been specially developed for separating multiplied signals. However, as far as we know, this technique had only been for a spectral separation of the signal spectra. With this method, an outstanding problem was solved by Oppenheim *et al.* [10]: with the use of nothing but the result of filtering (a speech signal), the signal generated by vocal cords and fed to the filter input was reconstructed, and the frequency response of the filter (larynx) was measured. Such an operation has never been applied to arrays and to multiplied signals.

The spectral selection of multiplied signals is based on taking the logarithm of them. Let us take the logarithm of Eq. (1) in view of the fact that the logarithm of a complex quantity is defined as

$$\log(z) = \log(|z|) + i\arg(z).$$

Then, we obtain

$$\log(P(x)) = \log(|M(x)|) + i[\arg(M(x) + \Phi(x))]. \tag{2}$$

Transformation (2) is realized in the following way. The logarithm of the function modulus is calculated. The function argument is determined from the arctangent of the ratio of the imaginary and real parts of the function. This procedure yields the argument of the complex function to an accuracy of 2π, because the exponential of the imaginary argument is multivalued. Thus, after each $\pm\pi$, the argument found in this way will exhibit a jump of 2π. As a result, the spectrum of the argument will broaden, and no subsequent filtering will be possible. The jumps should be eliminated. To this end, the value 2π should be added or subtracted at the instants of the argument jumps. Upon this eliminating procedure, we will obtain the value of the function argument. In [11], a condition is obtained for this procedure to yield the true phase value in digitizing the points of the space. The condition requires the function spectrum to considerably decrease toward high frequencies and to be limited. The discrete samples of the function must be separated in accordance with the Kotel'nikov theorem; i.e., the separation should be smaller than the inverse width of the function spectrum.

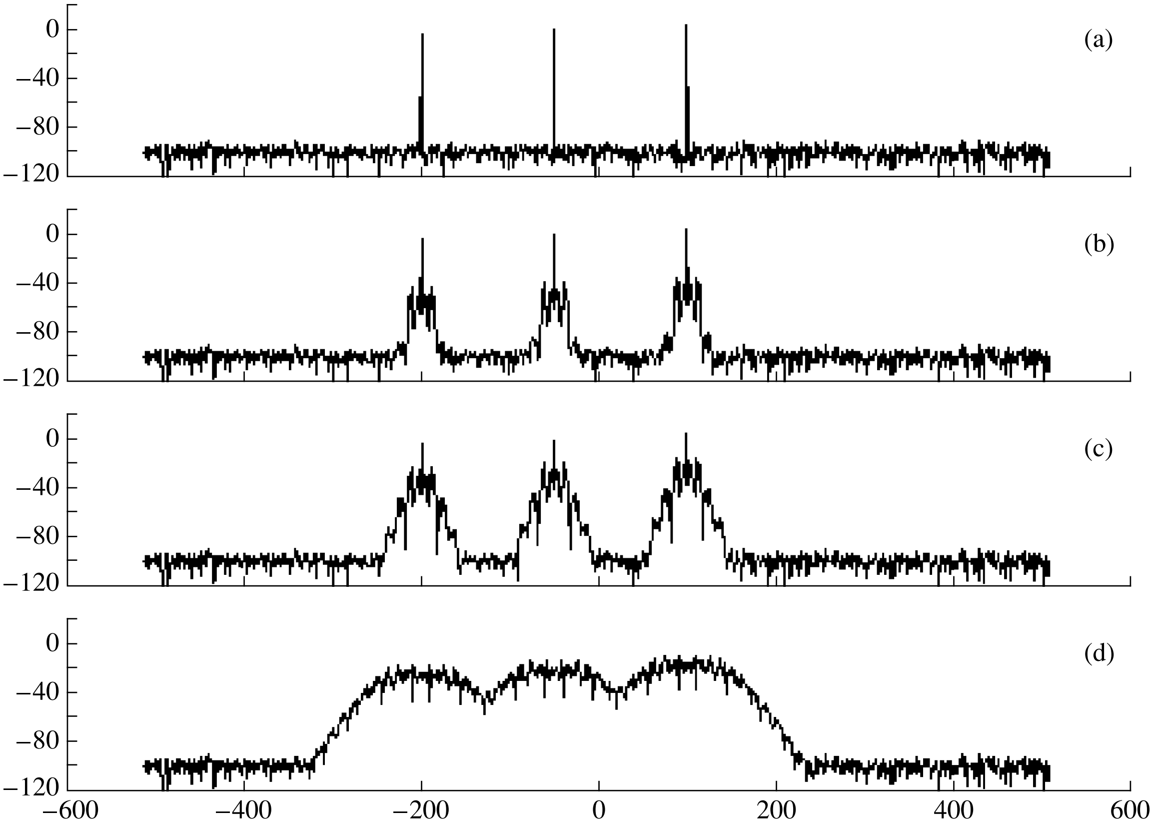

Fig. 1. Spectrum of the spatial frequencies (angular spectrum) for a bent array receiving three plane waves: (a) no bending; (b) small bends (the phase changes by less than π); (c) ten times greater bends; (d) ten times greater bends, as compared to the previous plot. The horizontal axis represents the spatial frequencies normalized to the inverse aperture of the array; the vertical axes represent the spectral level (in dB).

According to Fig. 1, these conditions are met in our case.

As a result of taking the logarithm of the complex signal received by the array, the following quantities are obtained: the real component in the form of the logarithm of the amplitude distribution for the received signals undisturbed by the phase shifts at the array elements and the imaginary part that is represented by the *sum* of phases of the signal and noise. Thus, the problem of signal and noise selection is reduced to an additive one. Note that taking a logarithm is the only mathematical transformation that meets this condition. No other “ordinary” procedures will yield the same result in separating multiplied signals. If logarithms of the signal and noise (or their arguments, as in our case) have nonoverlapping spectra, they can be separated. Thereby, in principle, the signal can be extracted from noise. If this is done, one can use the array as if there were no random phase shifts at its elements.

The problem is whether it is possible that the signal and noise spectra do not overlap, and, if such a possibility exists, does it exist in all cases or only in certain special cases. The spectrum of the second summand in Eq. (2) is a low-frequency one by definition. This summand can be filtered out. The situation is more complicated for the first summand of the real part in Eq. (2), i.e., for the wave field.

Let us write down this term as a sum of plane waves. To be specific, let us take four waves of different propagation directions:

$$\begin{aligned} M(x) &= 1 + a_1\exp(i\alpha_1 x) \\ &\quad + a_2\exp(i\alpha_2 x) + a_3\exp(i\alpha_3 x). \end{aligned} \tag{3}$$

Here, α_k represents not only the spatial frequency of the signal received by the array but also the angle of incidence of the plane wave [3]. Unity stands for the zero spatial frequency (the wave that is incident on the array at the zero angle). The argument of sum (3) is the angle at which the sum of vector summands is observed, these summands representing individual terms of the sum (3). In this case, the mathematical model (1) is not valid if the phase shifts are caused by the array bending. Actually, in such a situation, the phase shift of each wave is determined not only by the array shape, which is common for all waves, but also by the propagation direction of each wave. Let us assume for a while that the phase shifts are not governed by the array bending but caused by mechanisms independent of the propagation direction of the wave. At first, we consider the signal separation in this simplified situation and determine the conditions for selecting the spectra. After that, we can return to the case of a bent array.

The spectrum of the argument of the wave field at the array is governed by the velocity of rotation of the resulting vector about the origin of coordinates, this velocity depending on x. Note that, if the resulting vector rotates in a full circle and produces one or several rotations about the origin of coordinates, the argument spectrum (3) will be rather high-valued in the low-frequency band. In this case, the argument spectra of the signal and noise cannot be separated. However, if the resulting vector only oscillates about some position, the spectrum of its oscillations will be fully determined by the rotational velocities of individual summands around the end of the resulting vector. In this case, the argument spectrum (3) will occupy the same region as the signal spectrum. Thus, the argument spectrum of the sum of waves that arrive at the array at sufficiently high angles and the argument spectrum of the random phase changes at the array elements can be separated.

For this opportunity to come true, it is necessary and sufficient that sum (3) involve unity and the modulus of the sum of the remaining terms in Eq. (3) be no greater than unity. One of these conditions can be replaced by a weaker requirement. Sum (3) may not include unity, but it must contain the plane wave whose amplitude exceeds the sum of all remaining terms for an arbitrary x. In this case, prior to the signal processing, the spectrum should be shifted by multiplying it by the exponential of the imaginary argument of the quantity at which the highest summand becomes equal to unity.

After that, the selected phase should be filtered:

$$\Theta(x_m) = \sum_n G(x_m - x_n)\Psi(x_n),$$

where $G(x)$ is the impulse response function of the filter [9]. Upon filtering, the signal should be transformed to the initial form by the following procedure:

$$S(x) = B(x)\exp[i\Theta(x)],$$

where $B(x)$ is the modulus of the received signal that was not distorted by phase shifting at the array elements.

An additive noise cannot crucially change the situation. Actually, let us add the additive noise to Eq. (1):

$$P(x) = M(x)\exp[i\Phi(x)] + N(x). \tag{4}$$

One would infer from Eq. (4) that adding the noise can fully destroy the algorithm, because now the output signal is a product of the two functions that are to be separated by using the phase of this product; i.e., we have a more complicated mathematical dependence. However, this dependence is simplified if the added noise level is much lower than at least one of the signals. Let us reduce Eq. (4) to the logarithmic form:

$$P(x) = M(x)\exp[i\Phi(x)]\left\{1 + \frac{N(x)}{M(x)\exp[i\Phi(x)]}\right\}. \tag{5}$$

It follows from Eq. (4) that the added noise does not change the situation if its level is lower than that of the signal. Again, we have two cofactors. The first one is given by Eq. (1). As earlier, its phase is additive with respect to the signal and its distortions. The phase of the second cofactor (which is braced in Eq. (4)) is simply added in the form of additive noise to the sum of the phases of the signal and its distortions, because the noise level is low relative to the signal. Hence, the described nonlinear transformation results in that the additive noise remains. All illustrations are shown with the additive noise.

The proposed algorithm was numerically modeled. The initial signal is shown in Fig. 1d. Figure 1a presents the result of signal processing with the separation of the spectra of the wave field and phase changes at the array elements. This result confirms the statement that, if the filtering is successful, the array can work either with random low-frequency phase shifts or without them.

Let us now consider what can be done to solve the FSL problem. In this case, the array “sees” a single signal (all other signals are treated as an additive noise). For the single direction, random phase shifts can be caused by the array bending.

Let the array receive two spherical waves: one from the source and the other, with another curvature of the wave front but with the same arrival direction, from the scatterer. We assume that the scatterer is located just opposite the sound projector:

$$\begin{aligned} M(x) &= \exp(i\alpha x + Q(R_1, x)) \\ &\quad + r\exp(i\alpha x + Q(R_2, x)), \end{aligned} \tag{6}$$

where

$$Q = \beta(x - 0.5L)^2, \quad \beta = \frac{2\pi}{L}\sqrt{\left(\frac{2R}{L}\right)^2 + 1} - \frac{2R}{L}.$$

Here R_1 is the distance to the source, R_2 is the distance to the scatterer, and α is a factor that depends on the propagation direction of the wave. This factor is common for both the source and the scatterer: they differ in nothing but distances and signal levels.

Let us introduce the following additional procedure. Multiply Eq. (1), with Eq. (5) substituted into it, by the factor

$$E(x) = \exp(-i\alpha x).$$

To do so, one must know the angle α. Its value can be roughly estimated from the position of the maximum in the response of the bent array, and, then, it can be refined by fitting. Fitting proceeds until the minimal spectral width of the array response is achieved in the

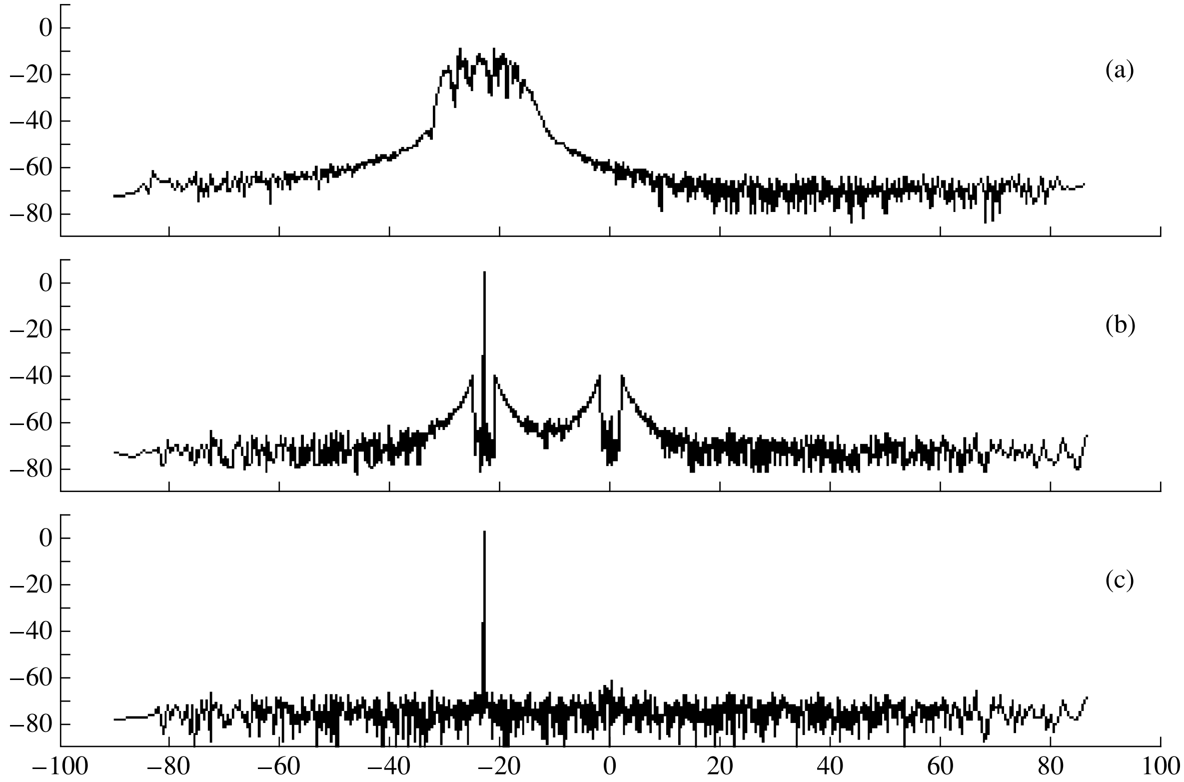

Fig. 2. Angular signal spectrum for the bent array receiving a spherical wave: (a) without filtering out the bend-caused distortions; (b) and (c) with filtering. The compensation for the sphericity of the wave front is performed (a) partially and (c) completely. The axes are the same as in Fig. 1.

signal processing. This processing procedure uses the cepstrum in the same way as above, with the exception that the sphericity of the wave front is compensated for. The compensation is required to obtain the dark field (to eliminate the direct signal of the source). To this end, it is sufficient to subtract the value of $Q(x)$, which is calculated by Eq. (6) for the actual distance to the source, from the phase obtained by taking the logarithm. If the distance is unknown, it can also be determined by fitting. Figure 2 is an example. According to Fig. 2, a partial compensation for the spherical spread of the wave broadens the spectrum of the received signal beyond the filter band. So, an indication is obtained that can be used to fully compensate for the sphericity of the wave and to estimate the distance to the source [4].

As a result of such a processing in the FSL procedure, we obtain the necessary and sufficient conditions for separating the spectra of logarithms of the cofactors in Eq. (1). Actually, multiplying the complex-conjugated exponentials yields the required unity, and the added signal of the scatterer is much smaller than unity.

Figure 3 illustrates the numerical modeling of the proposed FSL signal processing. This figure is analogous to that presented in [4] for a purely linear array, but it shows a fragment of the pattern received by a bent focused array. In modeling, the level of the scattered signal received by the array was specified to be –60 dB relative to the source signal level at the same array. The level of the additive noise (the forward reverberation) was also –60 dB.

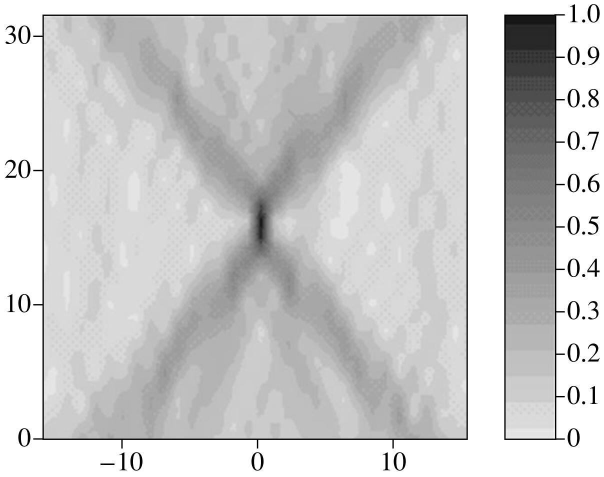

Fig. 3. Fragment of the pattern received by a bent array (as in Fig. 1c) that operates in the FSL mode [4]. The scattered signal is 60 dB lower than the signal from the source, but arrives from the same direction. The noise level is also –60 dB. The horizontal axis represents the azimuth angle (in the same units as in Fig. 1); the vertical axis represents the distance (in units of the array resolution [4]).

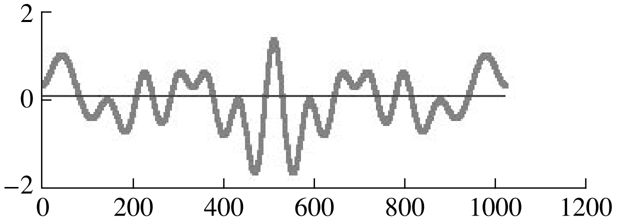

Fig. 4. Reconstruction of the array shape. The horizontal axis shows the coordinates of the array; the vertical axis shows the phase shifts (in radians). The thick line indicates the phase shifts determined by processing the signal received by the array from one of the sources; the thin line shows the difference between the reconstructed array shape and the shape preset in modeling.

In principle, cepstral signal processing can be successfully applied not only to FSL. When there is more than one signal, the waves should be preliminarily selected in their directions by using the response of the bent array, if it is possible. To this end, the array bends must be closer to the case shown in Fig. 1c. Among these responses, at least one should be found for which the processing yields the response shown in Fig. 1a. With this signal as a basis, one can determine the array shape for the proper phasing of all array elements as applied to all possible directions of signal arrivals.

To determine the array shape, one should separate low frequencies from high ones in the course of filtering and, then, reconstruct only the low frequencies. If this procedure is performed for a single source, it results in the true shape of the array. Figure 4 illustrates the modeling of this procedure.

By using the proposed signal processing, we can create arrays whose sizes are sufficient for implementing the FSL scheme.

The numerical experiments were performed for the following values of the parameters: the array was assumed to contain $L = 1024$ receiving elements spaced at 0.5λ. A possible realization of the array shape is shown in Fig. 4. This shape is obtained by using the method whose detailed description can be found in [8]. It is a realization of a normally distributed random function with a given spectrum. The spectrum was specified by its samples spaced at intervals of $\frac{2\pi}{L}$. The array shape was determined by 15 frequency values (with two spectrum samples for each frequency). These frequencies began from zero, and, in total, there were 512 possible frequency values.

ACKNOWLEDGMENTS

We are grateful to B.M. Salin, V.I. Turchin, and A.L. Matveev for useful discussions. We also thank the reviewer of this paper for the comments that allowed us to make the objectives and results of the work clearer.

This work was supported by the Russian Foundation for Basic Research (project nos. 99-02-16401 and 00-15-9674).

REFERENCES

1. V. A. Zverev, Akust. Zh. **40**, 401 (1994) [Acoust. Phys. **40**, 360 (1994)].
2. V. A. Zverev, Akust. Zh. **46**, 75 (2000) [Acoust. Phys. **46**, 62 (2000)].
3. V. A. Zverev, P. I. Korotin, A. L. Matveev, *et al.*, Akust. Zh. **46**, 650 (2000) [Acoust. Phys. **46**, 569 (2000)].
4. V. A. Zverev, A. L. Matveev, M. M. Slavinskiĭ, and A. A. Stromkov, Akust. Zh. **43**, 501 (1997) [Acoust. Phys. **43**, 429 (1997)].
5. A. B. Gershman, V. I. Turchin, and V. A. Zverev, IEEE Trans. Signal Process. **43**, 2249 (1995).
6. V. A. Zverev, Akust. Zh. **42**, 220 (1996) [Acoust. Phys. **42**, 192 (1996)].
7. V. A. Zverev, Akust. Zh. **44**, 456 (1998) [Acoust. Phys. **44**, 389 (1998)].
8. V. A. Zverev and N. V. Litvak, Akust. Zh. **45**, 807 (1999) [Acoust. Phys. **45**, 727 (1999)].
9. V. A. Zverev, *Physical Foundations of Image Formation by Wave Fields* (Inst. Prikl. Fiz., Akad. Nauk SSSR, Nizhni Novgorod, 1998).
10. A. V. Oppenheim, R. W. Schafer, and T. G. Stockham, IEEE Trans. Audio Electroacoust. **AU-16**, 437 (1968).
11. V. A. Zverev and A. A. Pavlenko, Izv. Vyssh. Uchebn. Zaved. Radiofiz. **43**, 652 (2000).

Translated by E. Kopyl

Acoustical Physics, Vol. 47, No. 3, 2001, pp. 303–307. Translated from Akusticheskiĭ Zhurnal, Vol. 47, No. 3, 2001, pp. 359–363.
Original Russian Text Copyright © 2001 by Zemlyanukhin, Mogilevich.

Nonlinear Waves in Inhomogeneous Cylindrical Shells: A New Evolution Equation

A. I. Zemlyanukhin and L. I. Mogilevich
Saratov State University, Astrakhanskaya ul. 83, Saratov, 410026 Russia

Received June 30, 1999

Abstract—A fifth-order evolution equation with cubic nonlinearity is derived for describing the wave processes in nonlinearly elastic, inhomogeneous deformed structures. The Backlund transform and an exact soliton-like solution are obtained for this equation. A relation between this equation and the nonlinear Schrödinger equation is pointed out. © *2001 MAIK “Nauka/Interperiodica”.*

The main condition for deriving soliton evolution equations is the mutual compensation of effects associated with nonlinearity, dispersion, and the property that the structure is thin-walled. Dispersion of strain waves propagating in thin-walled structures is connected with inertia characterizing the normal motion. Mathematically, this means that all soliton solutions rely on the momentless component of the mode of deformation, because the contribution of the couple stress to the wave process is provided by quantities of a higher order of smallness. At the same time, for some materials, the couple stress cannot be ignored. Among these are media with a microstructure, media with inclusions whose rigidity is much higher than the rigidity of the shell, some composites, etc. In these problems, the question arises as to how adequately the nonlinear wave process can be described by the Korteweg–de Vries-type equations. To answer this question, one should qualitatively study the nonintegrable evolution equations that appear when the couple stress is taken into account.

One of the methods for simulating the behavior of shells and plates whose inhomogeneity is caused by the distribution of their material rather than by its quality is the constructive anisotropy method (CAM) [1]. The essence of this method is that, instead of the inhomogeneous shell, it considers a homogeneous shell with the equivalence being provided by additional terms in the expressions for stresses and moments, which allow for the inhomogeneity.

Consider a cylindrical Kirchhoff–Love shell reinforced in two directions with mutually orthogonal ribs placed symmetrically on both sides of the median surface. Assume that the shell is made of a nonlinearly elastic material with a cubic stress–strain dependence:

$$\sigma_i = Ee_i - me_i^3,$$

where σ_i is the stress, e_i is the strain, E is the Young modulus, and m is the constant characterizing the shell material. We assume that the ribs exhibit rigidity only under flexure in their planes and ignore their rigidity under flexure in the orthogonal directions and under torsion [1]. Note that the rib’s flexural rigidity per unit length of the space between the ribs is usually much higher than the flexural rigidity of the shell, while the rib’s cross-sectional area referred to the unit length of the space between the ribs usually is several times smaller than the shell thickness.

The equations of motion for an element of a nonlinearly elastic cylindrical shell, when written in terms of stress and moments, coincide with the corresponding equations for an elastic shell and have the form [2]

$$\frac{\partial N_x^n}{\partial X} + \frac{\partial T^n}{\partial Y} = \frac{\gamma}{g}h\frac{\partial^2 U}{\partial t^2},$$

$$\frac{\partial T^n}{\partial X} + \frac{\partial N_y^n}{\partial Y} = \frac{\gamma}{g}h\frac{\partial^2 V}{\partial t^2},$$

$$\frac{\partial^2 M_x^n}{\partial X^2} + \frac{\partial^2 M_y^n}{\partial Y^2} + k_y N_y^n + \frac{\partial}{\partial X}\left(N_x^n\frac{\partial W}{\partial X} + T^n\frac{\partial W}{\partial Y}\right) \tag{1}$$

$$+ 2\frac{\partial^2 H^n}{\partial X \partial Y} + \frac{\partial}{\partial Y}\left(T^n\frac{\partial W}{\partial X} + N_y^n\frac{\partial W}{\partial Y}\right) = \frac{\gamma}{g}h\frac{\partial^2 W}{\partial t^2},$$

where U, V, and W are the displacements of the median surface of the shell in the x, y, and z directions, respectively; γ is the specific weight of the shell material; g is the free fall acceleration; t is time; h is the shell thickness; and the superscript n indicates the stresses and moments in the region of nonlinear elasticity.

1063-7710/01/4703-0303$21.00 © 2001 MAIK “Nauka/Interperiodica”

In compliance with the CAM and according to [2], the stresses and moments of an inhomogeneous nonlinearly elastic shell can be written as

$$N_x^n = \frac{1}{1-\mu^2}[I_1(\varepsilon_x + \mu\varepsilon_y)],$$

$$N_y^n = \frac{1}{1-\mu^2}[I_1(\varepsilon_y + \mu\varepsilon_x)],$$

$$M_x^n = \frac{1}{1-\mu^2}[I_3(\kappa_x + \mu\kappa_y)] - \frac{E_1 J_1}{d_1}\kappa_x, \tag{2}$$

$$M_y^n = \frac{1}{1-\mu^2}[I_3(\kappa_y + \mu\kappa_x)] - \frac{E_2 J_2}{d_2}\kappa_y,$$

$$H^n = \frac{1}{2(1+\mu)}[I_3\gamma_{xy}], \quad T^n = \frac{1}{2(1+\mu)}[I_1\gamma_{xy}],$$

where $I_k = \int_{-h/2}^{h/2}\frac{\sigma_i}{e_i}z^{k-1}dz$, $(k = 1, 3)$; μ is the Poisson ratio; $\varepsilon_x = U_x$; $\varepsilon_y = V_y - k_y W$; $\gamma_{xy} = U_y + V_x$; κ_x and κ_y are the parameters of the curvature variation; E_1 and E_2 are the Young moduli of the ribs parallel to the x and y axes, respectively; J_1 and J_2 are the moments of inertia of the cross-sections of these ribs with respect to the lines that pass through their centers of gravity; and d_1 and d_2 are the distances between the ribs in the y and x directions.

Relationships (1) and (2) can be used to derive the equations of motion of a shell element in terms of displacements. Assuming that the wave process is axially symmetric, we write the equations for the longitudinal and normal displacements:

$$\begin{aligned} &U_{xx} - \mu k_y W_x - \frac{4m}{3E}(3U_x^2 U_{xx} - 2(\mu+1)k_y U_x U_{xx} W \\ &- (\mu+1)k_y U_x^2 W_x + (\mu+1)k_y^2 U_{xx} W^2 + 2(\mu+1) \\ &\times k_y^2 U_x W W_x - 3\mu k_y^3 W^2 W_x + \ldots) = \frac{\gamma}{g}\frac{1-\mu^2}{E}U_{tt}, \end{aligned} \tag{3}$$

$$\begin{aligned} &\mu k_y U_x - k_y^2 W - \frac{4m}{3E} \\ &\times (k_y \mu U_x^3 - (1+\mu)[k_y^2 U_x^2 W - k_y^3 U_x W^2] - k_y^4 W^3) \\ &- \frac{E_1 J_1(1-\mu^2)}{E d_1}W_{xxxx} + \ldots = -\frac{\gamma(1-\mu^2)}{gE}W_{tt}. \end{aligned} \tag{4}$$

To study equations of motion (3) and (4), we introduce independent and dependent dimensionless variables

$$\begin{aligned} &U^* = \frac{U}{A}, \quad V^* = \frac{V}{A}, \quad W^* = \frac{W}{h}, \quad X^* = \frac{x}{l}, \\ &Y^* = \frac{y}{R}, \quad t^* = \sqrt{\frac{Eg}{\gamma(1-\mu^2)}}\frac{t}{l}, \end{aligned} \tag{5}$$

where A is the amplitude disturbance parameter, l is the characteristic wavelength, and R is the radius of curvature of the median surface. Below, we omit the asterisks marking the dimensionless variables.

The substitution of variables (5) into Eqs. (3) and (4) reveals three small parameters

$$\varepsilon = \frac{A}{l}, \quad \delta_1 = \frac{(hR)^{1/2}}{l}, \quad \delta_2 = \frac{h}{R},$$

which characterize the nonlinearity of the wave process, its dispersion, and the shell's property of being thin-walled.

We consider the case when these three parameters are of the same order of smallness ($\varepsilon \sim \delta_1 \sim \delta_2$).

Assume that the disturbance propagates along the generatrix of the shell at a constant velocity and slowly changes its parameters in time. According to the multiple scale method [3], we consider new independent variables and the expansions of the dependent variables into series in powers of the small parameter ε, which correspond to the assumption concerning the character of the disturbance:

$$\begin{aligned} &\xi = x - Ct, \quad \tau = \varepsilon t, \\ &U = U_0 + \varepsilon U_1 + \ldots, \quad W = W_0 + \varepsilon W_1 + \ldots. \end{aligned} \tag{6}$$

Substituting Eqs. (6) into the equations of motion, we obtain a system of equations in the lowest order in ε:

$$(1 - C^2)U_{0\xi\xi} - \mu W_{0\xi} = 0, \tag{7}$$

$$W_0 - \mu U_{0\xi} = 0. \tag{8}$$

From Eq. (8), we derive the relationship between the normal and longitudinal displacements:

$$W_0 = \mu U_{0\xi}. \tag{9}$$

By substituting Eq. (9) into Eq. (7), we obtain the expression for the dimensionless velocity of the longitudinal wave in the shell: $C^2 = 1 - \mu^2$.

When the conditions $\frac{E_1J_1R}{Ed_1l^4} = 0(\varepsilon^2)$ and $\frac{m}{E} = 0(\varepsilon^{-1})$ are satisfied, we obtain the following system of equations in the first order nonlinear in ε:

$$\begin{gathered}\mu^2U_{1\xi\xi} - \mu W_{1\xi}\\ -\frac{4m}{E}(1-\mu-\mu^2)U_{0\xi}^2U_{0\xi\xi} + 2CU_{0\xi\tau} = 0,\\ \mu U_{1\xi} - W_1 + \frac{4m}{3E}\mu^2U_{0\xi}^3\\ + C^2W_{0\xi\xi} - (1-\mu^2)W_{0\xi\xi\xi\xi} = 0.\end{gathered} \tag{10}$$

The only variation of these equations from the corresponding equations for a homogeneous shell [4] is that Eq. (10) contains a term with the fourth derivative, which describes the effect of the couple stress on the wave process. By virtue of Eq. (9), this system yields the following equation for the longitudinal strain component $\Psi = U_{0\xi}$:

$$\Psi_\tau - \alpha\Psi^2\Psi_\xi - \beta\Psi_{\xi\xi\xi} + \omega\Psi_{\xi\xi\xi\xi\xi} = 0, \tag{11}$$

where $\alpha = \frac{2m}{3}(1-\mu-\mu^2-\mu^3)(1-\mu^2)^{-1/2}$, $\beta = \frac{\mu^2}{2}(1-\mu^2)^{1/2}$, and

$$\omega = 0.5(1-\mu^2)^{1/2}\mu^2.$$

Equation (11) obtained above was never mentioned earlier in the literature on the theory of solitons and its applications. Note that the scale transformations

$$\Psi^* = \alpha^{-3/2}\omega^{1/2}\Psi, \quad x^* = \alpha^{1/2}\xi, \quad t^* = \alpha^{5/2}\omega^{-1}\tau$$

reduce this equation to the form (asterisks are omitted)

$$\Psi_t - \Psi^2\Psi_x - \sigma\Psi_{xxx} + \Psi_{xxxxx} = 0, \tag{12}$$

where $\sigma = \frac{\alpha\beta}{\gamma}$. Equation (12) is also invariant under the transformations $\Psi \mapsto -\Psi$, $x \mapsto -x$, and $t \mapsto -t$.

RELATION BETWEEN EQUATION (12) AND THE NONLINEAR SCHRÖDINGER EQUATION (NSE)

The relation between Eq. (12) and the NSE manifests itself when the solution to Eq. (12) is sought in the form of a slowly modulated wave train [5].

Let the solution to Eq. (12) have the form

$$\Psi(x,t) = \sum_{n=1}^{\infty}\varepsilon^n\Phi_n(x,t). \tag{13}$$

We assume that the expansion parameter is small, $\varepsilon \ll 1$, and the functions Φ_n slowly vary within the wavelength and within one cycle. We consider a disturbance that is much longer than the wavelength and moves at some velocity C. The profile of the disturbance slowly varies in time. This can be taken into account by introducing the variables $\xi = \varepsilon(x - Ct)$ and $\tau = \varepsilon^2 t$. Thus, Φ_n can be represented as

$$\Phi_n(x,t) = \sum_{l=-\infty}^{\infty}\zeta^{(n,l)}(\xi,\tau)e^{il(kx-\omega t)}. \tag{14}$$

For Φ_n to be real, the condition $\zeta^{(n,-l)} = \zeta^{(n,l)*}$ must be satisfied (here, the asterisk means complex conjugation). Then, the time and space derivatives in Eq. (12) are replaced as follows:

$$\begin{gathered}\frac{\partial}{\partial t} \longrightarrow \frac{\partial}{\partial t} - \varepsilon C\frac{\partial}{\partial\xi} + \varepsilon^2\frac{\partial}{\partial\tau},\\ \frac{\partial}{\partial x} \longrightarrow \frac{\partial}{\partial x} + \varepsilon\frac{\partial}{\partial\xi},\\ \frac{\partial}{\partial x^m} \longrightarrow \frac{\partial}{\partial x^m} + \varepsilon C_m^1\frac{\partial^m}{\partial x^{m-1}\partial\xi} + \ldots + \varepsilon^m C_m^m\frac{\partial^m}{\partial\xi^m}.\end{gathered} \tag{15}$$

In expressions (15), the derivatives with respect to x and t refer to the phase and the derivatives with respect to ξ and τ refer to the amplitude.

By substituting expansion (13) into Eq. (12) and equating the terms with the first three powers of ε, we obtain

$$\Phi_{1t} - \sigma\Phi_{1xxx} + \Phi_{1xxxxx} = 0, \tag{16}$$

$$\begin{gathered}\Phi_{2t} - \sigma\Phi_{2xxx} + \Phi_{2xxxxx}\\ = C\Phi_{1\xi} - \sigma C_3^1\Phi_{1xx\xi} + C_5^1\Phi_{1xxxx\xi},\end{gathered} \tag{17}$$

$$\begin{gathered}\Phi_{3t} - \sigma\Phi_{3xxx} + \Phi_{3xxxxx} = C\Phi_{2\xi} + \sigma C_3^1\Phi_{2xx\xi}\\ - C_5^1\Phi_{2xxxx\xi} + \sigma C_3^2\Phi_{3x\xi\xi} - C_5^2\Phi_{3xxx\xi\xi} - \Phi_{1\tau} + \Phi_1^2\Phi_{1x}.\end{gathered} \tag{18}$$

Substituting Eq. (14) into Eq. (16) and combining the terms with equal values of l, we obtain

$$il(\omega - \sigma k^3 - k^5)\zeta^{(1,l)} = 0.$$

The case $l = 0$ is not informative. At $l = \pm 1$, we obtain the dispersion relation for the linearized problem:

$$\omega = \sigma k^3 + k^5.$$

Equation (17) yields $\zeta_\xi^{(1,0)} \equiv 0$ and $\zeta^{(1,0)} = f(\tau) = 0$. For $|l| \geq 2$, it is necessary that $\zeta^{(2,l)} = 0$. Then, the propagation velocity C of the disturbance can be calculated as

$$C = 3\sigma k^2 + 5k^4 = \frac{d\omega}{dk}.$$

At $l = \pm 3$, Eq. (18) gives

$$\zeta^{(3,\pm 3)} = -\frac{k}{-3\omega + 27\sigma k^3 + 243k^5}(\zeta^{(1,\pm 1)})^3.$$

For $|l| > 3$, we have $\zeta^{(3,l)} \equiv 0$.

As a result, Eq. (18) yields the NSE for $\zeta^{(1,1)}$:

$$i\zeta_{\tau}^{(1,1)} - (3\sigma k + 10k^3)\zeta_{\xi\xi}^{(1,1)} - k\left|\zeta^{(1,1)}\right|^2\zeta^{(1,1)} = 0. \quad (19)$$

Since $3\sigma k + 10k^3 = \frac{1}{2}\frac{dC}{dk} = \frac{1}{2}\frac{d^2\omega}{dk^2}$, we can recast Eq. (19) in the form

$$i\zeta_{\tau}^{(1,1)} - \frac{1}{2}\frac{d^2\omega}{dk^2}\zeta_{\xi\xi}^{(1,1)} - k\left|\zeta^{(1,1)}\right|^2\zeta^{(1,1)} = 0. \quad (20)$$

In fact, the above procedure relates the NSE to the evolution equation of the form

$$\Psi_t - \Psi^2\Psi_x - \sigma\Psi_{xxx} + \sum_{k=2}^{N+1}\frac{\partial^{2k+1}\Psi}{\partial x^{2k+1}} = 0,$$

where N is the number of terms with odd derivatives with respect to x beginning with the fifth one (the case $N = 1$ is considered above). The dispersion relation and the disturbance propagation velocity take the form

$$\omega = \sigma k^3 + \sum_{n=2}^{N+1} k^{2n+1},$$

$$C = \frac{d\omega}{dk} = 3\sigma k^2 + \sum_{n=2}^{N+1}(2n+1)k^{2n},$$

and the coefficient of $\zeta_{\xi\xi}^{(1,1)}$ in Eq. (20) is calculated by the formula

$$\frac{1}{2}\frac{d^2\omega}{dk^2} = 3\sigma k + \sum_{n=2}^{N+1} n(2n+1)k^{2n-1}.$$

THE BACKLUND TRANSFORM AND THE EXACT SOLUTION TO EQUATION (12)

According to the singular manifold technique [6, 7], we seek a solution to Eq. (12) in the form of the series

$$\Psi = \sum_{0}^{\infty}\Psi_j F^{j-2}, \quad (21)$$

where Ψ_j and F are the new unknown functions of independent variables. By substituting Eq. (21) into Eq. (12), we obtain the equalities

$$\Psi_0 = \pm 6\sqrt{10}F_x^2,$$

$$\Psi_1 = \mp 6\sqrt{10}F_{xx},$$

$$\Psi_2 = \pm 2\sqrt{10}\frac{F_{xxx}}{F_x} \mp \frac{3}{2}\sqrt{10}\frac{F_{xx}^2}{F_x^2} \mp \frac{\sigma}{(10)^{1/2}}.$$

From Eq. (21), it follows that the function Ψ_2 must satisfy the original equation

$$\Psi_{2t} - \Psi_2^2\Psi_{2x} - \sigma\Psi_{2xxx} + \Psi_{2xxxxx} = 0.$$

By setting $\Psi_j = 0$ for $j \geq 3$, we obtain the following transformation for the solutions to Eq. (12):

$$\Psi = \mp 6\sqrt{10}\frac{\partial^2}{\partial x^2}(\ln F) + \Psi_2. \quad (22)$$

This relationship is the Backlund transform. It allows one to find the exact solutions to Eq. (12) if the function F satisfies the overdetermined system of nonlinear equations the first two of which have the form (we omit the remaining equations, because they are lengthy):

$$\frac{F_{xxxx}}{F_x} - 4\frac{F_{xxx}F_{xx}}{F_x^2} + 3\frac{F_{xx}^3}{F_x^3} = 0. \quad (23)$$

$$\begin{gathered}\frac{F_t}{F_x} + \frac{135}{2}\frac{F_{xx}^4}{F_x^4} + 15\frac{F_{xxx}F_{xx}^2}{F_x^3} - 15\frac{F_{xxxx}F_{xx}}{F_x^2} \\ - 90\frac{F_{xxx}^2}{F_x^2} + 21\frac{F_{xxxxx}}{F_x} - \frac{\sigma^2}{10} = 0.\end{gathered} \quad (24)$$

Assuming that $F = 1 + \exp(k_0x - \omega_0t)$, we obtain that all equations of system (23), (24) are satisfied identically if ω_0 depends on k_0 as

$$\omega_0 = -\frac{\sigma^2}{10}k_0 - \frac{3}{2}k_0^5.$$

A soliton solution to Eq. (12) can be obtained by substituting expression $F = 1 + \exp(k_0x - \omega_0t)$ into transformation (22) at $\Psi_2 = 0$. In this case, we have

$$k_0^2 = \frac{\sigma}{5}, \quad \omega_0 = -\frac{4}{25}\sigma^2 k_0$$

and the desired exact solution has the form

$$\Psi = \frac{3}{\sqrt{10}}\sigma\,\mathrm{sech}^2\xi, \quad \xi = \left(\frac{k_0x - \omega_0t}{2}\right). \quad (25)$$

Note that solution (25) is a subsonic ($\omega_0 < 0$) soliton-like disturbance.

The singular manifold technique used in this paper allows us to extend the results to the spatially two-dimensional analog of Eq. (12):

$$\frac{\partial}{\partial x}(U_t - U^2U_x - \sigma U_{xxx} + U_{xxxx}) = \delta U_{yy}. \quad (26)$$

Equation (26) has the Backlund transform in the form of Eq. (22) and the exact soliton-like solution

$$U = \frac{3}{\sqrt{10}}\sigma\,\mathrm{sech}^2\eta, \quad \eta = \left(\frac{k_0x + k_1y - \omega_0t}{2}\right).$$

In this case, ω_0 depends on k_0 and k_1 as

$$\omega_0 = -\frac{\sigma^2}{10}k_0 - \frac{3}{2}k_0^5 - \delta\frac{k_1^2}{k_0}.$$

The results of the above analysis show that the inclusion of the couple stress in the simulation of the strain wave propagation in nonlinearly elastic, inhomogeneous thin-walled structures leads to a new fifth-order evolution equation. Although this equation is nonintegrable, it has a Backlund transform and an exact soliton solution and it is closely related to the nonlinear Schrödinger equation.

REFERENCES

1. V. V. Novozhilov, *The Theory of Thin Shells* (Sudpromgiz, Leningrad, 1962).
2. A. S. Vol'mir, *Nonlinear Dynamics of Plates and Shells* (Nauka, Moscow, 1972).
3. J. Colle, *Perturbation Methods in Applied Mathematics* (Blaisdell, Waltham, 1968; Mir, Moscow, 1972).
4. A. I. Zemlyanukhin and L. I. Mogilevich, Izv. Vyssh. Uchebn. Zaved., Prikl. Nelin. Din. **3** (1), 52 (1995).
5. G. Lamb, *Elements of Soliton Theory* (Wiley, New York, 1980; Mir, Moscow, 1983).
6. N. Kudryashov and A. Pickering, J. Phys. A **31**, 9505 (1998).
7. A. N. W. Hone, Physica D **118**, 1 (1998).

Translated by A. Khzmalyan

Acoustical Physics, Vol. 47, No. 3, 2001, pp. 308–312. Translated from Akusticheskiĭ Zhurnal, Vol. 47, No. 3, 2001, pp. 364–369.
Original Russian Text Copyright © 2001 by Kazakov, Sutin.

Pulsed Sounding of Cracks with the Use of the Modulation of Ultrasound by Vibrations

V. V. Kazakov and A. M. Sutin

Institute of Applied Physics, Russian Academy of Sciences,
ul. Ul'yanova 46, Nizhni Novgorod, 603600 Russia
e-mail: kazak@appl.sci-nnov.ru

Received November 15, 1999

Abstract—The possibility of using the effect of the modulation of ultrasound by vibrations due to the presence of cracks for the nonlinear acoustic detection of cracks is demonstrated. The method is based on a pulsed ultrasonic sounding with gating the received signal and simultaneously exciting low-frequency vibrations in the sample. The presence of a crack is characterized by the modulation of the ultrasonic wave reflected from the crack. The visualization of the crack position in a model object (a metal rod) is performed. The possibility of selecting a crack on the background of an intense signal reflected from a cavity is experimentally demonstrated. The manifestation of the nonlinear properties of a crack is studied as a function of the polarization of the flexural vibrations of the rod. *© 2001 MAIK "Nauka/Interperiodica".*

The appearance of cracks results in a change in the physicomechanical properties of samples and structures and makes the possibility of their further use problematic. If a crack has appeared, it usually grows with time. That is why the development of the methods of early diagnostics of cracks and their continuous monitoring is necessary.

The classical methods of ultrasonic flaw detection [1–3] are ineffective in the case of closed cracks of a small size. At the same time, such cracks cause a sharp increase in the nonlinear acoustic effects, which opens up possibilities for using the methods of nonlinear acoustic diagnostics in this case.

Historically, the effect of acoustic harmonic generation [4–6] was the first to be used for nonlinear acoustic diagnostics. This effect has been studied intensively up to now [7–12]. Later, other nonlinear effects were used for the diagnostics of materials: the shift of the resonant frequencies and the increase in the loss with a growing amplitude of the acoustic wave [13–15].

In our opinion, the method most sensitive to the presence of cracks is the one based on the modulation of ultrasound by vibrations [16–24]. The principle of this method is that vibrations are excited in the object under study at the low-frequency natural modes and, simultaneously, an ultrasonic wave is generated in the object. The level of the low-frequency excitation should be sufficient to cause changes in the acoustic properties of a crack under vibration. These changes result in the modulation of the ultrasonic wave. The ultrasonic wave transmitted through the object or reflected from the defects is received and processed. The result of processing is represented as a spectrum comprising both the ultrasonic carrier frequency and the products of the nonlinear interaction in the form of the side frequencies corresponding to low-frequency vibrations. The presence of cracks is determined by the presence of side frequencies in the spectrum. The methods of synchronous detection and spectral analysis make it possible to detect the side frequencies with the amplitudes 50–70 dB lower than the fundamental frequency level. Having a set of statistical data for "good" and "bad" samples obtained by the method of nonlinear acoustic diagnostics and verified by other independent methods, it is possible to evaluate reliably the degree of imperfection of such objects by using thereafter only the method of nonlinear diagnostics.

However, for solving a number of practical problems, it is of interest not only to reveal the presence of defects in an object but also to determine their positions. Therefore, we propose to develop the method of nonlinear acoustic diagnostics by using the method of pulsed ultrasonic sounding with gating the received signal.

The first observation of the modulation of a pulsed signal reflected from a crack was reported in [25]. Later, the technique based on recording the modulation of a pulse sequence was realized in our experiments [26].

This paper presents a closer investigation of this technique, its preliminary version being published in our preprint [27]. One of the purposes of this paper is to show the possibility of determining the type of defects that cause a strong linear reflection but differ in the nonlinear response, namely, cracks and cavities in a solid. Another aspect is connected with the investigation of the possibilities of this method in relation to the polarization of the excited vibrations.

The measuring technique is as follows. The sample under study is excited at a low-frequency flexural mode of frequency *F*. Simultaneously, by using a piezoelectric transducer, a sequence of ultrasonic pulses with the repetition frequency f_0 and the carrier frequency f is radiated into the sample. Ultrasonic pulses reflected from various defects of the sample are received and range-gated. For a fixed position of the gate pulse, the spectral analysis of the gated signal is carried out during the time corresponding to several periods of the frequency F.

Obviously, in the general case, the spectrum of the analyzed signal consists of a set of harmonics corresponding to the following frequencies: $kf \pm (nf_0 \pm mF)$, where k, n, $m = 0, 1, 2, 3, \ldots$. When a defect does not exhibit nonlinear properties (for instance, a cavity), the received signal has no side components determined by the modulation of ultrasound by vibrations; i.e., $k \neq 0$ and $m = 0$. If the defect exhibits nonlinear properties (a crack), the received signal is modulated by vibrations and the spectrum of the signal contains the whole set of the aforementioned frequencies ($k = 0, 1, 2, \ldots$ and $m \neq 0$). The spatial position of the gated signal is determined according to the known method by its time delay relative to the beginning of the radiation of the ultrasonic wave. Thus, the problem of the crack visualization is reduced to determining the presence and the level of the modulation with the frequency F in the gated signals and to plotting the dependence that represents the distance versus the level of the modulation with the frequency F.

When the defect is a crack, various combinations of internal structures having linear or nonlinear properties may occur along the direction of sounding. Therefore, in our model experiment, we investigated two main cases: with a cavity lying before a crack along the direction of radiation and with a crack before a cavity. The results obtained by using the nonlinear technique were compared with the dependence representing the amplitude of the reflected signal versus the depth of sounding and measured by the conventional linear technique using the amplitude detection of the signal of the received ultrasonic wave.

As an object of investigation, we used a duralumin rod with a length of 770 mm and a diameter of 10 mm. The rod had a crack and a cavity, each of them being at a distance of 310 mm from one of the rod ends. To make a crack, a saw cut 0.5 mm wide and 4 mm deep was made in the rod. A mica plate was inserted in the cut, and then it was sealed with epoxy resin. After the resin hardened, the rod was loaded until the appearance of a crack at the plate site. As a cavity, we used a hole of diameter 1.6 mm. The axis of the hole was perpendicular to the bottom of the crack.

The experimental setup is schematically represented in Fig. 1.

The rod rests on two V-shaped supports at a distance of 100 mm from its ends. A load with the mass 560 g, which consists of a metal disc, an electrodynamic vibrator, and an accelerometer rigidly connected to each other, is suspended from the center of the rod. The vibrator excites the rod at the first mode of flexural vibrations ($F = 12$ Hz). The amplitude of vibrations at the center of the rod equals 1 mm. Ultrasonic transducers of a combined type are glued to the ends of the rod. Ranging and reflection are used. Connecting the first or second transducer to the ultrasonic sounder, the sounding can be carried out from the side of the crack or from the side of the cavity. The frequency of the radiated wave is 1.2 MHz, the width of the ultrasonic pulse is 20 μs, and the sounding frequency is 293 Hz. The presence of the modulation of frequency F in the received signal was determined as follows. The received signal of the ultrasonic wave was successively subjected to synchronous phase detection, gating, averaging over the gate pulse duration, and storage by a sample-and-hold circuit until the next gated signal was received. The gate pulse of width 0.5 μs and period 3.73 s was automatically retuned with a step of 1 μs (the range resolution was 2.6 mm).

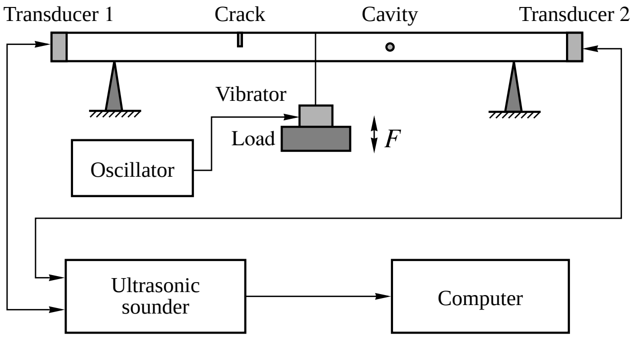

Fig. 1. Schematic view of the measuring setup.

For a fixed position of the gate pulse, the rod made about 44 vibrations. During this time, the transient connected with the retuning of the gate pulse died out and the analysis of the signal was performed. For the analysis, the gated signal was fed to a narrow-band filter with a resonance frequency of 12 Hz and subjected to the amplitude detection. The peak value of the detected signal was stored by a sample-and-hold circuit, and, via an A/D-converter, it was fed to a computer where it was recorded for the whole cycle of the gate pulse retuning, from the beginning of the radiation of the ultrasonic pulse to its reflection from the opposite end of the rod. In total, 149 steps of gate pulse retuning were used. The total time of the analysis was 556 s.

The specially designed gating device made it possible to perform the measurements in two regimes. In the first regime, the position of the gate pulse was set manually. In this case, the signal was analyzed at a fixed range, which made it possible to investigate its spectral characteristics for various levels of excitation of the rod vibrations. In the second regime, the gate pulse position was tuned automatically. This regime allowed us to determine the change in the signal characteristics along the whole length of the rod, but only for a fixed level of excitation.

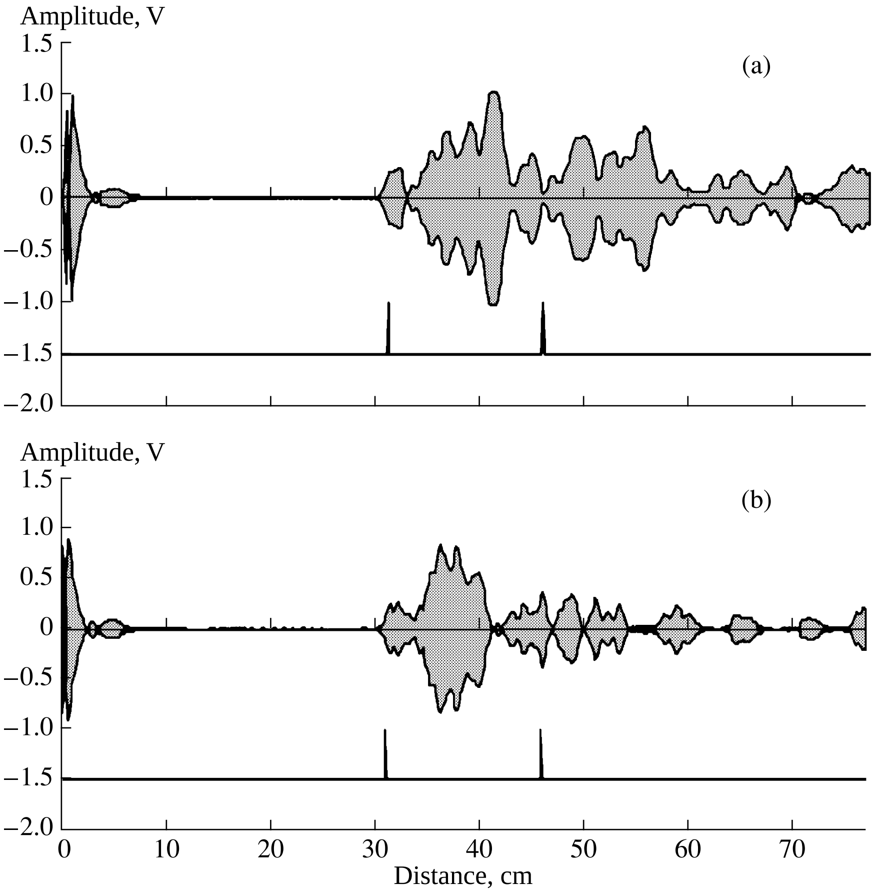

Fig. 2. Oscillograms of the received signal for sounding from the side of (a) the cavity and (b) the crack (the abscissa axis represents the distance).

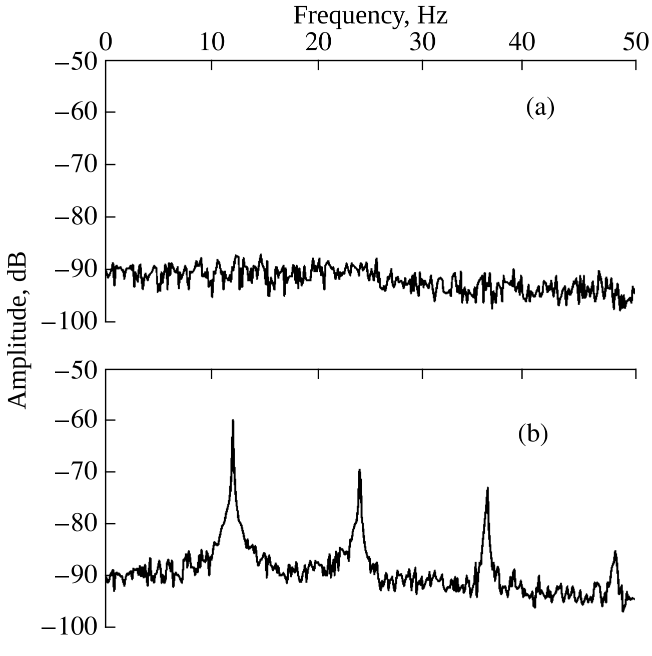

Fig. 3. Spectra of the gated signal reflected from (a) the cavity and (b) the crack.

Figure 2 shows the variations of the signal amplitude at the ultrasonic transducer, which were obtained for the sounding from the side of the cavity and from the side of the crack, and the marks indicating the positions of the cavity and the crack. The abscissa axis represents the distance determined from the delay time of the received signal t by the formula $r = 2ct$, where $c = 5167$ m/s is the measured velocity of the longitudinal ultrasonic wave in the rod.

From these figures, it is seen that, after the reflection from the first defect, the signal envelope strongly changes. The reflected signal is tailed due to the dispersion and interference of waves in the rod. One can see that the pulsed sounding with the use of amplitude detection of the signal of the reflected ultrasonic wave makes it possible to determine the presence of a defect but does not allow one to determine its type.

For illustrating the use of the nonlinear method, we make the gate pulse coincident with the first maximum of the signal reflected from a defect and perform a spectral analysis of the gated signal. The resulting spectrograms are given in Fig. 3.

The spectrograms show that, by the presence of harmonic components, it is possible to reliably identify the

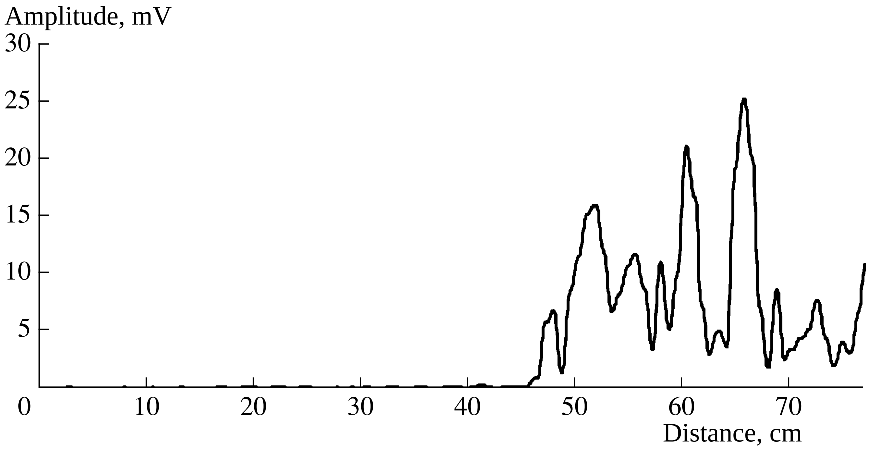

Fig. 4. Variation of the modulation depth for sounding from the side of the cavity.

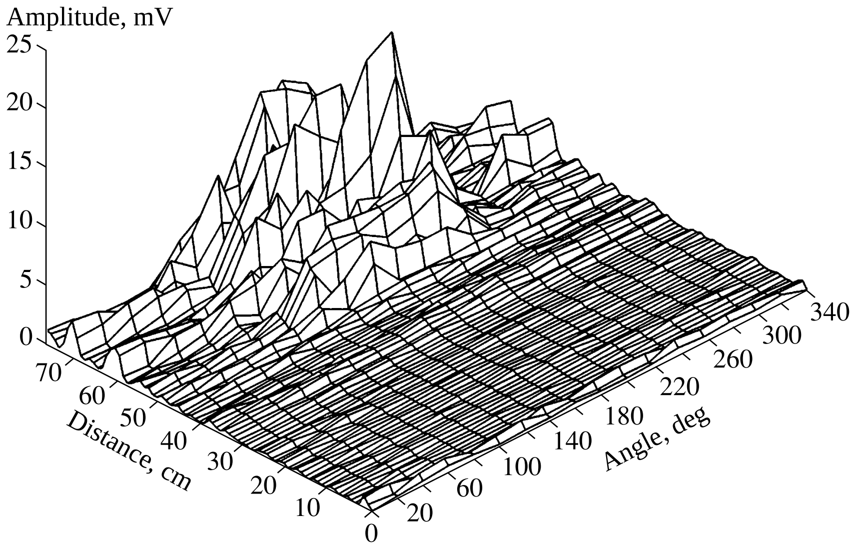

Fig. 5. The modulation depth as a function of the crack orientation and the gate pulse position. The crack is at a distance of 46 cm, and the cavity is at a distance of 31 cm from the radiator.

type of the revealed defect—a cavity or a crack. By using additional rods with various models of the crack and the cavity, it was shown that a crack caused the appearance of harmonics with the levels within –20 to –60 dB relative to the amplitude of the reflected signal, depending on the type and amplitude of the excitation of flexural vibrations. The presence of modulation can be determined even at the stage of gating the front of the received signal.

Figure 4 illustrates the change in the amplitude of the harmonic of frequency *F* in the case of the automatic tuning of the gate pulse. It is seen from the figure that the distance at which the spectral components with the frequency of flexural vibrations appear in the reflected signal corresponds to the distance to the crack. The detection of the crack by the nonlinear method is possible on the background of the ultrasonic wave scattering by the cavity, whereas the conventional amplitude detection of the received signal is unable to solve this problem (see Fig. 2).

The nonlinear characteristics of a crack manifest themselves in a different way, depending on the polarization of vibrations relative to the crack. To investigate this effect, the rod was rotated about its axis and the dependence of the modulation depth on the rotation angle was measured. The angle 180° corresponds to the case when the opening of the crack faces upward, and the angle 0° corresponds to the downward position of the opening. The measurements were made at 20° intervals. The results of measuring the level of modulation as a function of the angle of the crack orientation and the gate pulse distance are given in Fig. 5. As can be seen from the figure, when the crack is compressed by a static flexure under the action of load (the angle

180°), the modulation depth is maximal. When the crack faces downward, it becomes open and the low-frequency flexural vibrations of the same amplitude lead to much smaller changes in the parameters of the ultrasonic wave.

CONCLUSIONS

By the example of finding the positions of a crack and a cavity in a model object (a rod), the efficiency of using the pulsed ultrasonic sounding with gating the received signal in the method of nonlinear acoustical diagnostics is demonstrated. It is shown that the nonlinear method makes it possible to determine the position of a crack by its nonlinear properties, independently of the presence of a cavity before the crack.

It is shown that the nonlinear properties of a crack manifest themselves in different ways, depending on the polarization of the low-frequency vibrations of the object and on the static stress at the crack. This means that, in the nonlinear acoustical diagnostics of objects and structures, it is desirable to perform the measurements with the excitation of vibrations of different polarizations. One more interesting possibility of the development of the method of nonlinear acoustical diagnostics is related to nonlinear flaw detection with simultaneously applied static loads. These loads can open or close the existing cracks and change their nonlinear properties. This kind of measurements can be used for determining the internal stresses applied to a crack, as well as the opening stress of a crack.

ACKNOWLEDGMENTS

This work was supported by the International Scientific-Engineering Center, project no. 1369.

REFERENCES

1. I. N. Ermolov, N. P. Aleshin, and A. I. Potapov, *Nondestructive Testing*, Book 2: *Acoustic Methods of Testing* (Vysshaya Shkola, Moscow, 1991).
2. J. Krautkramer and H. Krautkramer, *Ultrasonic Testing of Materials* (Springer, Berlin, 1977).
3. R. E. Green, *Ultrasonic Investigation of Mechanical Properties* (Academic, New York, 1973).
4. O. Buck, W. L. Morris, and J. N. Richardson, Appl. Phys. Lett. **33**, 371 (1978).
5. W. L. Morris, O. Buck, and R. V. Inman, J. Appl. Phys. **50**, 6737 (1979).
6. V. A. Antonets, D. M. Donskoĭ, and A. M. Sutin, Mekh. Kompoz. Mater., No. 5, 934 (1986).
7. A. M. Sutin, C. Delclos, and M. Lenclud, in *Proceedings of the 2nd Symposium on Acoustical and Vibratory Surveillance Methods and Diagnostic Techniques* (Senlis, France, 1995), pp. 725–735.
8. O. V. Rudenko and Chin An Vu, Akust. Zh. **40**, 668 (1994) [Acoust. Phys. **40**, 593 (1994)].
9. O. V. Rudenko, Defektoskopiya, No. 8, 24 (1993).
10. P. B. Nagy, Ultrasonics **36**, 375 (1998).
11. D. C. Hurley, P. T. Purtscher, K. W. Hollman, and C. M. Fortunko, in *Nondestructive Characterization of Material VIII*, Ed. by R. E. Green (Plenum, New York, 1998), pp. 825–829.
12. D. V. Armyakov, A. F. Asainov, B. A. Korshak, and I. Yu. Solodov, Defektoskopiya, No. 1, 34 (1998).
13. R. A. Guyer and P. Johnson, Phys. Today **52** (4), 30 (1999).
14. P. Johnson, Mater. World **7** (9), 544 (1999).
15. V. E. Nazarov, Fiz. Met. Metalloved., No. 3, 172 (1991).
16. A. S. Korotkov, A. M. Slavinskiĭ, and A. M. Sutin, Akust. Zh. **40**, 84 (1994) [Acoust. Phys. **40**, 71 (1994)].
17. A. M. Sutin and V. E. Nazarov, Izv. Vyssh. Uchebn. Zaved., Radiofiz. **38** (3–4), 109 (1995).
18. V. Yu. Zaitsev, A. M. Sutin, I. Yu. Belyaeva, and V. E. Nazarov, J. Vibr. Control **1** (3), 335 (1995).
19. V. E. Nazarov and A. M. Sutin, J. Acoust. Soc. Am. **102**, 3349 (1997).
20. A. M. Sutin and D. M. Donskoy, in *Nondestructive Characterization of Material VIII*, Ed. by R. E. Green (Plenum, New York, 1998), pp. 133–138.
21. A. M. Sutin and D. M. Donskoy, in *Airports and Aerospace Hardware II: Proceedings of International Society for Optical Engineering* (1998), Vol. 3397, pp. 226–237.
22. K. van den Abeele, P. A. Johnson, and A. M. Sutin, Res. Nondestruct. Eval. **12** (1), 17 (2000).
23. I. N. Didenkulov, A. É. Ekimov, and V. V. Kazakov, Akust. Zh. **44**, 621 (1998) [Acoust. Phys. **44**, 535 (1998)].
24. A. E. Ekimov, I. N. Didenkulov, and V. V. Kazakov, J. Acoust. Soc. Am. **106**, 1289 (1999).
25. J. P. Kim, E. J. Kim, S. W. Yoon, and A. Sutin, J. Acoust. Soc. Am. **101**, 3029 (1997).
26. V. V. Kazakov, A. É. Ekimov, A. M. Sutin, and I. N. Didenkulov, in *Nonlinear Acoustics of Solid State: Proceedings of 8th Session of the Russian Acoustical Society*, Ed. by V. I. Erofeev (Intelservis, Nizhni Novgorod, 1998), pp. 247–250.
27. V. V. Kazakov, A. M. Sutin, and A. É. Ekimov, Preprint No. 498, IPF RAN (Inst. of Applied Physics, Russian Academy of Sciences, Nizhni Novgorod, 1999).

Translated by A. Svechnikov

Acoustical Physics, Vol. 47, No. 3, 2001, pp. 313–322. Translated from Akusticheskiĭ Zhurnal, Vol. 47, No. 3, 2001, pp. 370–381.
Original Russian Text Copyright © 2001 by Komissarova.

Sound Field Features in the Coastal Zone of a Shallow Sea with an Airborne Source of Excitation

N. N. Komissarova
Andreev Acoustics Institute, Russian Academy of Sciences, ul. Shvernika 4, Moscow, 117036 Russia
e-mail: bvp@akin.ru

Received June 13, 2000

Abstract—Features of the sound field in the coastal zone are theoretically investigated in the case of a moving airborne sound source. It is shown that two factors govern the drastic increase in the signal level measured at the observation point when the source moves near the shoreline: the directional property of the field transmitted from the air into the water and the structure of the normal wave in the wedge near the caustic. The magnitude of the increase in the sound field level depends on the depth of the reception point and, what is more essential, on the structure of the bottom. *© 2001 MAIK “Nauka/Interperiodica”.*

In an experiment carried out in the coastal zone, Gordienko *et al.* [1] revealed an interesting feature of the sound field excited by a source moving in air. The experiment was as follows. Sound pressure receivers were mounted at the bottom of the coastal shelf, at a distance of 1 km from the shoreline. The sound source was a helicopter flying at a height of 50 m along various paths differently oriented relative to the shoreline. When the source moved from the receiver toward the coast, the level of the receiving signal drastically increased at some points of the path and near the shore line, the positions of these points depending on frequency. In this paper, we try to explain this interesting phenomenon.

Features of the sound transmission from air into water are reasonably well understood. In the framework of the ray theory, the problem on the sound field excited in a liquid halfspace by a harmonic point source located in air was solved in [2, 3]. The exact solution to this problem, the errors of the ray approximation, and the field of the lateral wave were studied in [3–7]. Urick [8] reported the results of one of a few experiments with an airplane flying over the shallow sea and noted a fairly good agreement between the experiment and the theoretic calculation. The effect of the sea roughness on the sound transmission from air into water was studied in [8–10]. The mode theory of sound propagation in the waveguide with depth-dependent sound velocity was described in [11], and in [12], a comparison of the results of calculations by mathematical models based on the ray theory, the normal wave theory, and the method of the parabolic equation was carried out.

The inclusion of the features of sound propagation in the coastal zone is the most difficult part of the problem under consideration. A number of approximate mathematical methods are presently known for calculating the sound field in irregular waveguides, including the coastal zone. The method of cross sections, the ray theory, and the method of the parabolic equation are among them. The peculiarity of the sound propagation problem under consideration is that the effect experimentally observed by Gordienko *et al.* [1] falls in the region for which the validity of the known approximations either fails or, at least, appears problematic. As will be shown, an airborne source excites the most prominent normal wave at the moment when it moves over the wave caustic. The caustic is one of the most characteristic features of the sound field in wedge-shaped regions. It is the source passage over the normal wave caustics that causes the drastic increase in the field level at the reception point. For this reason, the mode approach appears natural for the problem under consideration. However, the adiabatic approximation of the method of plane cross sections, which is widely used for calculating the sound fields in irregular waveguides, is appropriate for accurate calculation of the normal wave field only for depths exceeding the critical depth of this mode [13]. The following pattern is currently adopted for the sound propagation upward over the slope. Normal waves almost do not interact in the course of the propagation up to their critical sections where an essential portion of the mode energy is transferred to the bottom in the form of a directed beam. In the critical section region, discrete modes strongly interact with the modes of the continuous spectrum and the propagating mode is transformed into an exponentially decaying nonpropagating mode. Mathematically, the field of the nonpropagating mode is the analytical continuation of the field of the propagating wave through the critical section [14]. For depths close to the critical depth, an additional term comes into play; this term was called the lateral wave and decays with distance from this section according to the power-law dependence [13, 14]. From the standpoint of the Brillouin rays corresponding to normal waves of a definite number, the passage through the critical section is known to correspond to a change in the grazing angles of the Brillouin rays from subcritical values to supercritical ones. With further propagation upward along the slope, the grazing angles of the Brillouin rays are increased and are maximal at the caustic, which separates the shadowzone from the illuminated zone of the normal wave field. This caustic is the envelope of the set of the horizontal rays which are the projections of the Brillouin rays onto the horizontal plane [15–18]. The caustic region of the normal wave is usually excluded from consideration, because it is commonly believed that the field of the normal wave is weak for depths smaller than the critical depth.

Nevertheless, it should be noted that the field near the caustic of the normal wave depends on the boundary conditions at the lower boundary of the waveguide. If the waveguide overlies a fluid halfspace that models the sand or silt bottom, the field at the caustic is actually small. However, if the bottom reflects the sound well, a significant level of the field of the normal wave can be expected at the caustic. For subcritical depths, the features of the field of normal waves are most exhaustively investigated in [19] for a homogeneous wedge overlying a liquid halfspace. The solution in this case was expanded in cylindrical sections rather than in plane cross-sections, which considerably reduces the mode interaction (see [20, 21]). However, the behavior of the field near caustics was not investigated, because the caustic field is small for the model used in these works, i.e., a wedge overlying a liquid halfspace. The use of a little-known approximate approach (the method of approximate variable separation [22]) made it possible to obtain analytical expressions for the normal wave field, including the caustic region [23]. However, this approach is of limited utility, because it essentially restricts the choice of the model of the bottom. Actually, the field of the normal wave in the caustic region is adequately investigated only for the simplest models of the coastal zone, such as a homogeneous wedge with perfectly reflecting sides, which allow an exact calculation of the caustic field.

The ray method [24] could be considered as an alternative approach to the problem on the field exited in the coastal zone by a moving airborne source. However, the increase in the field occurs in the experiment just within the time intervals when the source moves near the shoreline where the depth of the sea is small and the applicability of ray methods becomes problematic.

Because the construction of a mathematical model corresponding to the effect observed in [1] is a difficult problem, we start with the simplest problem. Consider the field exited by an airborne source in the wedge-shaped region filled with a homogeneous liquid medium with the density $\rho = 1$ g/cm^3 and the sound velocity $c = 1.5$ km/s. The lower side of the wedge is assumed to be perfectly hard. From above, the wedge adjoins the air with the density $\rho_A = \rho/m_A$ ($m_A = 800$) and the sound velocity $c_A = cn_A$ ($n_A = 2/9$). In the cylindrical coordinate system (r, y, φ), the wedge-shaped region is specified by the inequalities $0 < r < \infty$, $|y| < \infty$, and $0 < \varphi < \Phi$, the y axis coincides with the wedge edge, the half-plane $\varphi = 0$ corresponds to the water–air interface, and the wedge side $\varphi = \Phi$ is assumed to be perfectly hard. Below, we will add complexity to the model.

Consider two cases: (1) the harmonic point source of frequency $\omega = 2\pi f$ is located in the water wedge at the point $P(r_p, 0, \varphi_p)$; (2) the point source is located in air at the height h_p. In the first case, the half-plane $\varphi = 0$ can be considered as a perfectly soft boundary [11], and the sound potential $\Psi(r, y, \varphi)$ ($\Psi \sim e^{-i\omega t}$) is representable in the form of the Sommerfeld–Malyuzhinets integral [25, 26]

$$\Psi(r, y, \varphi) = \frac{1}{2\pi i}\int_{\Gamma} \frac{\exp[ikR(\alpha)]}{R(\alpha)} S(\alpha + \varphi)\,d\alpha, \quad (1)$$

where $k = \omega/c$, $S(\alpha) = \frac{\pi}{4\Phi}\left[\operatorname{cosec}\frac{\pi}{2\Phi}(\alpha - \varphi_p) - \operatorname{cosec}\frac{\pi}{2\Phi}(\alpha + \varphi_p)\right]$, and

$$R(\alpha) = \sqrt{r^2 + r_p^2 + y^2 - 2rr_p\cos\alpha}, \quad \operatorname{Re}R(\alpha) > 0. \quad (2)$$

The integration is carried out along a certain contour Γ in the plane of the complex variable α. Two representations—the mode representation and the ray representation—can be obtained from integral (1).

The exact solution in the form of the sum of normal waves is as follows:

$$\Psi = \sum_{n=1}^{\infty} \tilde{\Psi}_n(r, y, \varphi),$$

where

$$\tilde{\Psi}_n(r, y, \varphi) = -\frac{2}{\Phi} W_n(\varphi) W_n(\varphi_p) \times \int_{\Gamma_1} \frac{\exp[ikR(\alpha) + i\mu_n\alpha]}{R(\alpha)}\,d\alpha, \quad (3)$$

$$\mu_n = \left(n - \frac{1}{2}\right)\pi/\Phi, \quad W_n(\varphi) = \sin\mu_n\varphi. \quad (4)$$

A useful asymptotic representation of the integral appearing in Eq. (3) for the normal wave field $\tilde{\Psi}_n$ ($\Phi \ll \pi$) was obtained using the saddle-point method [26]. The form of this representation depends on the position of the observation point relative to the normal wave caustic separating the shadow zone from the illuminated zone. For the wedge with perfectly reflecting

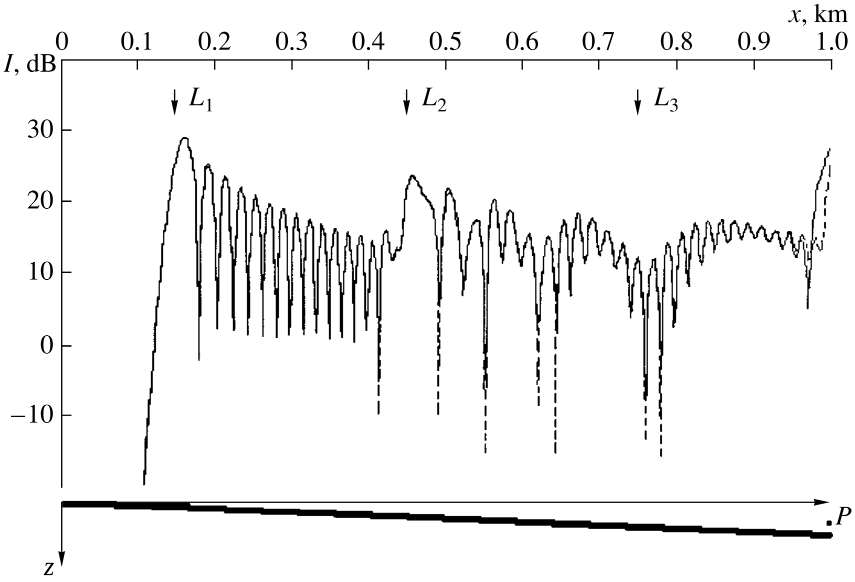

Fig. 1. Comparison of the calculations according to the mode (the dashed line) and the ray (the solid line) theories for a wedge with a perfectly hard lower side. The angle of the wedge is $\Phi = 0.05$, and the sound frequency is 50 Hz. The waterborne source is located at a depth of 40 m at a distance of 1 km from the wedge edge; x is the horizontal distance from the reception point to the wedge edge, and the reception depth is 3 m. The lower part of the figure shows the wedge section by the vertical plane $y = y_p = 0$.

sides, the caustic of the nth normal wave is described by the hyperbola

$$\sqrt{(r+r_p)^2+y^2}-\sqrt{(r-r_p)^2+y^2} = 2L_n,$$

where $L_n = \mu_n/k$ is the distance from the wedge edge to the caustic of the nth mode in the vertical plane $y = 0$. Normal waves with $r_p < L_n$ are only slightly excited by the source.

In terms of the geometric optics, the field excited by the point source in the wedge with perfectly reflecting sides can be represented, correct to a small term corresponding to the diffraction correction, as the sum of the fields of the real source and the imaginary sources located at an arc of the circle $r = r_p$, $y = 0$ [27]. In this representation, the angular coordinates of the imaginary sources $\varphi_m^{\pm}$ are determined by the angular coordinate of the real source φ_p:

$$\varphi_m^{\pm} = 2m\Phi \pm \varphi_p, \quad m = 0, \pm 1, \pm 2, \ldots.$$

Thus,

$$\Psi(r, y, \varphi) = \sum_m \left[\frac{\exp(i\chi_m^{+})}{R_m^{+}} + \frac{\exp(i\chi_m^{-})}{R_m^{-}}\right], \tag{5}$$

where

$$\chi_m^{\pm} = kR_m^{\pm} + \Delta_m^{\pm}, \tag{6}$$

$R_m^{\pm} = \sqrt{r_p^2 + r^2 - 2r_p r\cos(\varphi - \varphi_m^{\pm}) + y^2}$ is the distance from the imaginary source to the point P, and $\Delta_m^{\pm}$ is the phase step divisible by π and caused by the reflection from the perfectly soft upper side: $\Delta_m^{\pm} = m\pi$ and $\Delta_m^{-} = (m-1)\pi$. The summation in Eq. (5) is carried out over all $m = 0, \pm 1, \pm 2, \ldots$ that satisfy the condition $|\Phi_m^{\pm}| < \pi$.

The calculations carried out by Eqs. (5) (the ray representation) and (3) (the mode representation) demonstrated a fairly good agreement between their results even in the shadow zone of all normal waves. Figure 1 compares the field intensities calculated using the ray and mode representations for the depth $z = 3$ m (x, y, z are the Cartesian coordinates) and for $y = 0$. The lower part of the figure shows the section of the wedge-shaped region by the vertical plane perpendicular to the wedge edge. The number of rays arriving at every observation point is 126. The dependence of the intensity on the x coordinate of the observation point clearly shows the mode structure of the field (Fig. 1). The arrows in Fig. 1 show the positions of the caustics of the first, second, and third normal waves. These positions are determined by the expression $x \cong L_n = \mu_n/k$. For $x < L_2$, the field is determined by the first mode only. Then, the second mode comes into play, it interferes with the first mode, and so on. The difference between the ray and mode calculations occurs only near the source, which is caused by the fact that we used the asymptotic representation for the integral appearing in Eq. (3) for the fields of the normal waves. This representation is applicable when $\Phi \ll \pi$ and is appropriate for calculating the field in the caustic region and at a distance from the caustic [26], but it is inappropriate for calculating the fields near the source. It should be noted that the ray calculation gives a fairly good result even in the shadow zones of all normal waves where the waveguide depth is less than the wavelength. This fact gives grounds to expect that ray calculations will be useful for considering more complicated models of the coastal region.

It is interesting to find out how the ray calculation according to Eq. (5) yields a shadow zone near the wedge edge and a sharp increase in intensity at the caustic of the first normal wave. Let $y = 0$ for simplicity. The phase of the sound potential of an imaginary source P_m^+ at the reception point $S(r, 0, \varphi)$ is given by Eq. (6). We calculate the phase difference between the fields produced by the imaginary sources P_{m+1}^+ and P_m^+:

$$\delta\chi_m^+ = \chi_{m+1}^+ - \chi_m^+ = k(R_{m+1}^+ - R_m^+) + \pi.$$

We have, approximately,

$$R_{m+1}^+ - R_m^+ = \frac{\partial R_m^+}{\partial m}\delta m = \frac{\partial R_m^+}{\partial \varphi_m^+}\frac{\partial \varphi_m^+}{\partial m}\delta m$$
$$= \frac{2\Phi r_p r}{R_m^+}\sin(\varphi_m^+ - \varphi).$$

Assuming that $r_p \gg r$ for simplicity, we obtain

$$\begin{aligned}\delta\chi_m^+ &= \pi + 2\Phi r \sin(\varphi_m^+ - \varphi)\\ &= \pi\left[1 + \frac{r}{L_1}\sin(\varphi_m^+ - \varphi)\right].\end{aligned} \tag{7}$$

Note that Eq. (7) obtained in ray terms involves the parameter $L_1 = \pi/(2\Phi k)$, which is the distance from the wedge edge to the caustic of the first normal wave. This formula demonstrates that, if the reception point S approaches the wedge edge ($r \longrightarrow 0$), the phase difference is $\delta\chi_m^+ \longrightarrow \pi$; i.e., the fields of every pair of imaginary sources, P_{m+1}^+ and P_m^+, are added with opposite phases. A similar situation takes place for every pair of imaginary sources P_{m+1}^- and P_m^-. Thus, the summation yields small fields in the shadow zones of all normal waves.

Similar considerations and exact calculations show that, if the observation point S is at the caustic of the normal wave, numerous groups of imaginary sources (with angular coordinates $\varphi_m^\pm \sim \pm\pi/2$) produce fields with relative phase shifts divisible by 2π, which causes an increase in the intensity at the caustics. For the observation points S located near the midpoint between the caustics, the phase shifts between the fields of adjacent imaginary sources are equal to π multiplied by an odd number. Thus, the features of the field in a wedge that can be easily interpreted in terms of normal waves (like shadow and caustic zones) are explained by the phase relations between the rays in terms of the geometric optics approach.

Consider now the second case: a harmonic point source is located in air at the height h_p above the water wedge with a perfectly hard lower side. Solving this problem, we again will use both the ray and the mode approaches.

According to [11], in a plane waveguide contacting with air from above, the field of the normal wave excited by an airborne source differs from the field of the normal wave excited by a source in water by a factor describing the excitation coefficient of this normal wave as a function of the vertical coordinate of the source. For example, for the waveguide of depth H whose lower boundary is perfectly hard and the upper boundary is with air, we have the following expressions for the sound potential of the normal wave at the reception point $S(\rho, z)$ (ρ and z are the coordinates in the cylindrical coordinate system of the plane waveguide):

$$\bar{\Psi}_n^W = \frac{2\pi i}{H}\bar{W}_n(z)\bar{W}_n(z_p)H_0^{(1)}\left(\sqrt{k^2 - \varsigma_n^2}\rho\right), \tag{8}$$

where

$$\bar{W}_n(z) = \sin\varsigma_n z, \quad \varsigma_n = (n - 1/2)\pi/H$$

for the waterborne source located at the point $P(0, z_p)$ and

$$\bar{\Psi}_n^{\mathrm{A}} = \frac{2\pi i}{H}\bar{W}_n(z)\bar{A}_n(h_p)H_0^{(1)}\left(\sqrt{k^2 - \varsigma_n^2}\rho\right),$$

where

$$\begin{aligned}\bar{A}_n(h_p) &= \frac{i\varsigma_n}{m_{\mathrm{A}} q_n}\exp\left(iq_n h_p + \frac{\varsigma_n^2}{m_{\mathrm{A}} H q_n^2}h_p\right),\\ q_n &= \sqrt{\varsigma_n^2 + k^2\frac{1 - n_{\mathrm{A}}^2}{n_{\mathrm{A}}^2}}\end{aligned} \tag{9}$$

for the airborne source located at the point $P(0, -h_p)$. The small term $\varsigma_n^2 h_p/(m_{\mathrm{A}} H q_n^2)$ appearing in the exponent in Eq. (9) describes an exponential increase of the field with increasing height of the source. This increase is caused by the features characteristic of the fields of leaky-wave modes. We will not consider these modes because, in the conditions of our calculations, the small term is below 0.0005. Additionally, we note that the absolute value of the excitation coefficient of the nth mode, $|\bar{A}_n|$, is independent of the horizontal coordinates of the source P.

For the wedge-shaped region whose one side is perfectly soft and the other side is perfectly hard, the field of the normal wave excited by a waterborne harmonic point source located at the point $P(r_p, y_p, \varphi_p)$ is described by Eq. (3). One can show that, if the angle of the wedge is sufficiently small and the observation point is near the source, Eq. (3) is reduced to Eq. (8) where the depth H of the reference waveguide is the depth of the wedge at the source site H_p. Taking this fact into account, we replace the factor $W_n(\varphi_p)$ in Eq. (3)

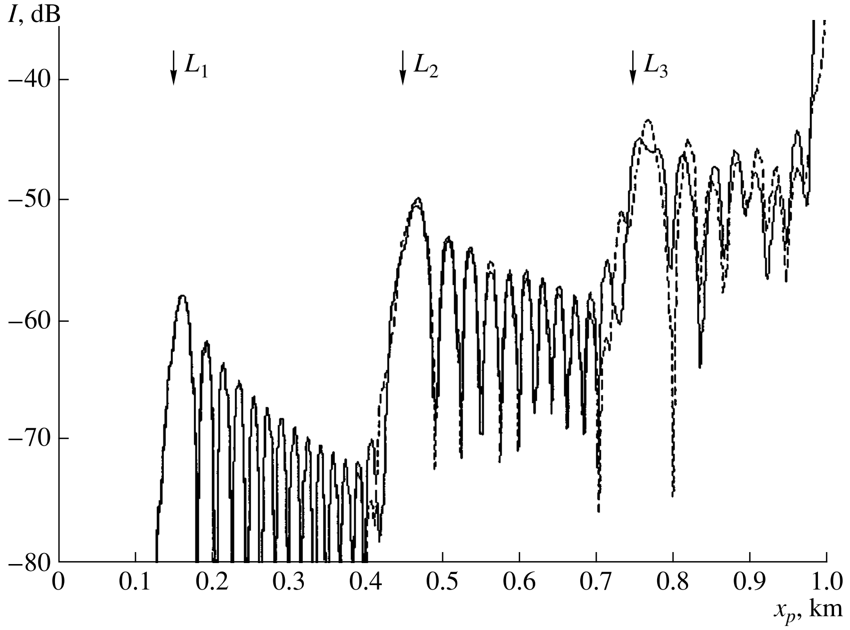

Fig. 2. Comparison of the calculations according to the mode (the dashed line) and the ray (the solid line) theories for a wedge with a perfectly hard lower side and a moving airborne source. The angle of the wedge is $\Phi = 0.05$, and the sound frequency is 50 Hz. The signal is received at the point S located at a depth of 3 m at a distance of 1 km from the wedge edge.

valid for the normal wave excited in the wedge by a waterborne source by the factor $A_n(h_p)$:

$$A_n(h_p) = \frac{i\varsigma_{np}}{m_A q_{np}} \exp(iq_{np}h_{np}), \tag{10}$$

where $\varsigma_{np} = (n - 1/2)\pi/H_p$, $q_{np} = \sqrt{\varsigma_{np}^2 + k^2(1 - n_A^2)/n_A^2}$, and will use the expression thus obtained for describing the field of the normal wave excited in the wedge by an airborne source. In so doing, we obtain that the sound potential of the nth mode excited by an airborne source is given by the following approximate expression:

$$\Psi_n(r, y, \varphi) = -\frac{2}{\Phi} W_n(\varphi) A_n(h_p) \times \int_{\Gamma_1} \frac{\exp[ikR(\alpha) + i\mu_n\alpha]}{R(\alpha)} d\alpha. \tag{11}$$

In the calculations by the ray theory, we computed the parameters of the sound field excited in water by an airborne source according to the formulas given in [2, 3] and used the method of imaginary sources [28] that considerably simplifies the calculation of the parameters of the ray propagating in the wedge. Figure 2 shows the results of the calculation for an airborne harmonic point source located at the height $h_p = 50$ m. The solid and dashed lines correspond to the results obtained according to the ray and mode approaches, respectively, and show the sound intensity as a function of the coordinate x_p of the source. As one can see, the calculated results are in good agreement and demonstrate clearly defined pattern of normal waves.

The excitation coefficient $W_n(\varphi_p)$ of the normal wave in the case of a moving waterborne source, Eq. (4), depends on the angular coordinate φ_p of the source and is independent of the coordinate r_p. For a moving airborne source, the situation is different: the excitation coefficient of the normal wave A_n given by Eq. (10) depends on the coordinate x_p, which is the horizontal distance from the source to the wedge edge. This dependence follows from the fact that the parameters q_n and ς_{np} appearing in Eq. (10) for A_n depend on the wedge depth at the source site, $H_p = x_p \tan\Phi$. Figure 3 gives an example of this dependence; it shows the absolute value of the excitation coefficient $|A_n|$ of the nth mode as a function of the coordinate x_p of the moving airborne source for different mode numbers n. The parameter $L_1 = \mu_1/k = \pi/(2\Phi k)$ is the distance from the wedge edge to the caustic of the first normal mode; the distance between the edge and the caustic of the nth mode is $L_n = (2n - 1)L_1$. One can see that the excitation coefficient of the nth mode is maximal at $x_p = L_n$, i.e., at the moment the moving airborne source appears over the caustic of this normal wave. With a further increase in x_p (i.e., as the source moves from the caustic toward greater depths), the excitation coefficient of this mode decreases. At $x_p = L_n$ (i.e., at the moment the source appears over the caustic of the nth normal mode), all excitation coefficients A_n coincide: $A_n = n_A/m_A$.

Compare now the sound fields excited in the water wedge by airborne and waterborne moving sources. Figure 4 shows the sound field intensity (in dB) as a function of the coordinate x_p of the source P measured

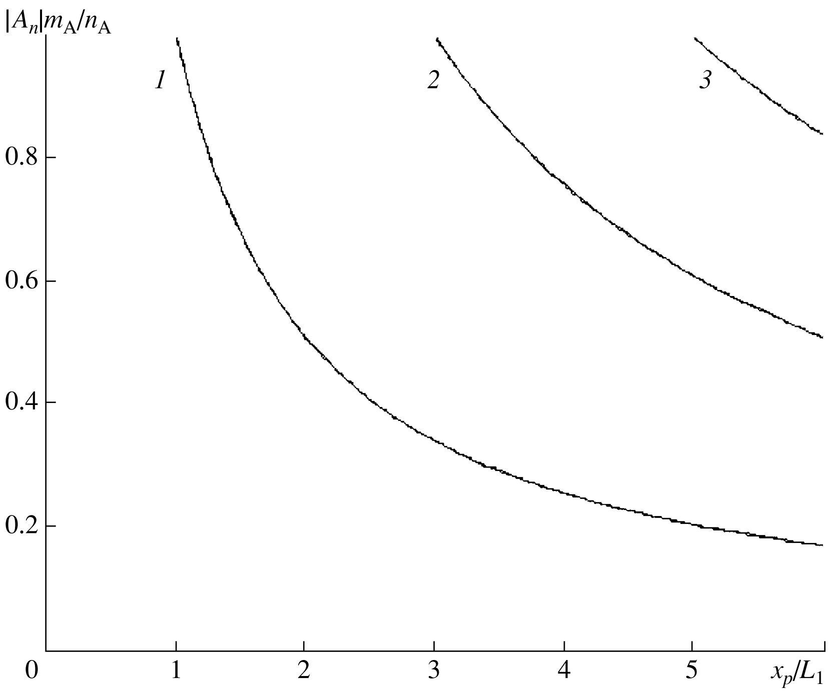

Fig. 3. Absolute value of the excitation coefficient for the (*1*) first, (*2*) second, and (*3*) third normal waves in the case of a moving airborne source.

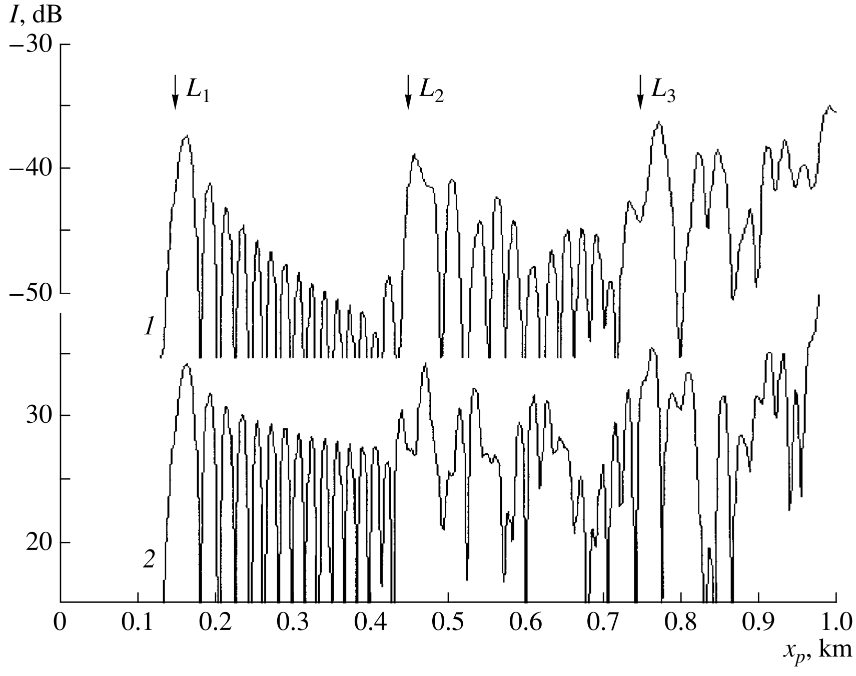

Fig. 4. Intensity of the sound field received at the point S (x = 1 km, z = 49 m) in the water wedge as a function of the horizontal distance x_p between the wedge edge and the source moving (*1*) in air at the height h_p = 50 m and (*2*) in water along the straight line φ_p = 0.045 rad. The wedge angle is Φ = 0.05 rad, and the sound frequency is 50 Hz.

from the wedge edge in the horizontal plane. The calculation was carried out for the reception point S located in the water wedge near its lower boundary, at a depth of 49 m and at a distance of 1 km from the wedge edge. An increase in the coordinate x_p corresponds to the motion of the source P away from the wedge edge; in this case, the horizontal distance between the points P and S decreases. In Fig. 4, curve *1* corresponds to the airborne source located at the height h_p = 50 m over the wedge surface and curve *2* corresponds to the waterborne source moving along the straight line $\varphi_p = 0.045$ (i.e., near the lower boundary; in this case, all normal waves are effectively excited and received). The arrows in Fig. 4 mark the positions of the caustics of normal waves. For the source coordinate x_p varying from L_1 = 0.15 km to L_2 = 0.45 km, only the first normal wave is excited. For the waterborne source, its excitation coefficient remains constant in our case (and equal to $\sin\mu_n\varphi_p$). From the comparison of curves *1* and *2* for x_p varying from L_1 to L_2, one can see that, for the airborne moving source, the field increase observed at the reception point *S* during the source motion toward the wedge edge appears to be greater than for the waterborne moving source. For the airborne moving source, this increase measures 15 dB and only 7 dB for the waterborne moving source (during the source motion, the distance from the source *P* to the reception point increases from 0.6 to 0.85 km). Thus, the closer the airborne moving source is to the caustic, the stronger it excites the normal wave.

To better understand the features of the sound field excited in the wedge by an airborne harmonic point source, we consider the pattern of the Brillouin rays corresponding to the normal wave of some definite number [15]. At the observation point *S* in the vertical plane passing through the source and perpendicular to the wedge edge, the field of the normal wave can be represented as the superposition of two plane waves; in this pattern, the Brillouin rays corresponding to the normal wave with the number *n* form a set of straight lines tangential to the circle $r = L_n$. Near the caustic, the grazing angle of the Brillouin rays approaches $\pi/2$. The farther the point from the caustic, the smaller the value of this angle. The fact that the airborne source most strongly excites the mode with number *n* at the moment it is over the corresponding caustic can be explained if we take into account the directional property of the field transmitted into the water halfspace by the airborne source: energy is predominantly transmitted in the vertical direction, and only a small portion of it is transmitted in a nearly horizontal direction [8, 11]. Such a source will excite the normal wave the stronger, the closer to vertical the Brillouin rays corresponding to this wave, which is realized at the caustic. For other models of the coastal zone, this effect must also occur, because the grazing angles of the Brillouin rays are maximal near the caustic, and this is the situation in which the major part of the energy of the airborne source is transferred to the corresponding mode. For the source located in the water wedge, the excitation coefficient is independent of the horizontal coordinate of the source.

Thus, the first feature of the sound field excited in the wedge by a moving airborne source is that the excitation coefficient of the normal wave depends on the horizontal coordinate and the normal wave is best excited when the source is located over the caustic of this wave.

It is the caustics of the normal waves that determine the sharp increases in the field intensity. It appears that, at the instant the source passes over the caustic of the normal wave with the number *n*, the absolute value of the excitation coefficient, $|A_n| = n_A/m_A$, is independent of the mode number *n*, and the field intensity in the caustic region is determined by the depth of the observation point *S*. The results of calculations shown in Figs. 2 and 4 (curve *1*) correspond to the case of an airborne source moving at a height of 50 m and differ in the depth *z* of the reception point *S*: z = 3 m (the point *S* is close to the surface) for Fig. 2 and z = 49 m (the point *S* is close to the bottom) for Fig. 4. In the first case, the field intensity at $x_p = L_n$ increases with the mode number *n* according to the linear dependence of the factor $W_n(\varphi) = \sin\mu_n\varphi \approx (n - 1/2)\pi z/H_s$ as a function of *n* for $z \ll H_s$, where H_s is the sea depth at the source site *S*. In the second case, no prominent dependence of the field on the number *n* occurs at the caustics $x_p \approx L_n$, because $z \approx H_s$ and $|W_n| \approx 1$ in this case.

Now, we will add complexity to the model of the coastal zone by introducing different models of the bottom. We will describe them by the reflection coefficient as a function of the grazing angle. Consider first the model of the coastal zone in the form of a homogeneous water wedge overlying a liquid halfspace. In the calculations, we will use the ray approach, because no accurate calculation procedure is known for the field near the normal wave caustics when the lower side of the wedge is not perfectly reflecting. The method of imaginary sources offers a possibility for a simple calculation of all parameters of rays connecting the airborne source with the observation point in the water wedge (the ray displacement accompanying the reflection from the bottom is not taken into account).

Figure 5 shows the sound intensity of the field excited by the source moving at a height of 50 m. The results were calculated for a frequency of 50 Hz and for two models of the medium: curve *1* corresponds to a wedge whose lower side is perfectly hard, and curve *2* corresponds to a wedge overlying the halfspace of sand with the density ρ_b = 1.7 g/cm^3 and the sound velocity $c_b = 1.7(1 - 0.018i)$ km/s. The angle of the wedge was set equal to $\Phi = 0.04$. The reception point was located at a depth of 39 m at a distance of 1 km from the wedge edge. In the first case (a perfectly hard bottom), a prominent increase in the field level occurs at the reception point *S* at the instant the source passes over the caustic of the first normal wave. In the second case (the bottom is the sand halfspace), the field level decreases as the source approaches the wedge edge and no increase in the field level is observed.

These calculations show that the effect observed in the experiment depends on the parameters of the bottom. Figure 6 presents the results calculated for other bottom models with intermediate reflecting properties

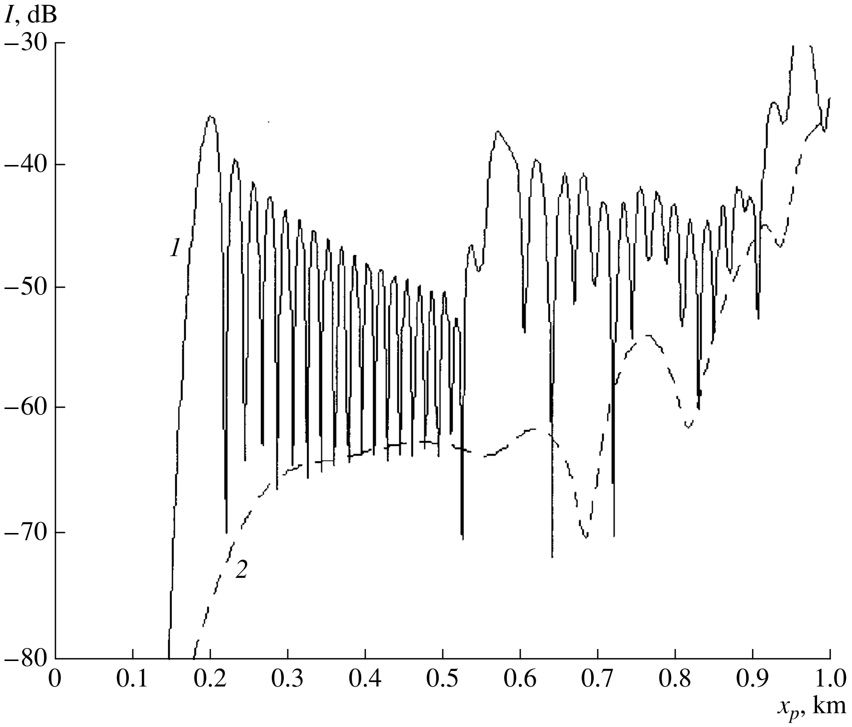

Fig. 5. Intensity of the field versus the horizontal coordinate x_p of the airborne source moving at a height of 50 m for two bottom models: (*1*) a perfectly hard bottom and (*2*) a sand halfspace. The wedge angle is $\Phi = 0.04$ rad, the sound frequency is 50 Hz, and the receiver is located at a depth of 39 m at a distance of 1 km from the wedge edge.

between the two above models. All curves are cut at a level of –65 dB. The curves are given in the order of decreasing fields in the caustic region of the first mode. The lower part of Fig. 6 schematically represents the corresponding models of the sea bottom. Below, we describe these models in the order of increasing complexity (rather than in the order given in Fig. 6).

Model (a): A wedge with a perfectly hard lower side.

Model (b): Outcrops of hard basalt rock are often characteristic of the coastal zone near the shoreline; for this reason, we consider the model composed of two wedges whose angles are $\Phi = 0.04$ and $\Phi_b = 0.02$ for the water and bottom wedges, respectively; it is assumed that the sides of the water and bottom wedges are adjacent, but the edge of the bottom wedge is shifted by a distance of $r_v = 0.3$ km relative to the edge of the water wedge. A perfectly hard boundary is assumed to underlie the wedge system. In this model, the reflection coefficient is $V = 1$ if the reflection occurs for $r < r_v$, otherwise it depends on the thickness of the sediment layer d at the point where the ray is reflected.

Model (c): A water wedge overlies an elastic halfspace (basalt) with the density $\rho_b = 3$ g/cm^3, the velocity of longitudinal waves $c_b = 6(1 - 0.002i)$ km/s, and the velocity of transverse waves $c_t = 3(1 - 0.01i)$ km/s.

Model (d): A water wedge overlies a liquid bottom wedge with a perfectly hard lower side. The liquid wedge with the angle Φ_b is used as a model of the sediment layer, because experimental data show that the thickness of the sediment layer decreases toward the shoreline [29]. By and large, the model is composed of two adjacent wedges with a common edge; the upper water wedge is characterized by the angle $\Phi = 0.04$ and the lower edge of sand (the bottom) is characterized by the angle $\Phi_b = 0.02$ and a perfectly hard lower side. In this model, the reflection coefficient of the lower side of the water wedge is specified as coincident with the reflection coefficient of a liquid layer of thickness d depending on the coordinates of the reflection point.

Model (e): This model differs from model (b) in that it uses the boundary with an elastic halfspace (basalt) instead of the perfectly hard lower boundary.

We now direct our attention to the calculations presented in Fig. 6. For the models with a well reflecting bottom, the calculation by the ray theory shows a clearly defined pattern of normal waves. A prominent intensity increase corresponding to the caustic of the first normal wave can be seen for the moments the source moves near the wedge edge. The better the bottom reflectivity, the higher the field level at the caustic of the first mode. Other increases in the field level are also related to the caustics of normal waves. The caustics of the second and third normal waves disappear for certain models of the bottom. This fact depends on the behavior of the normal wave field as a function of depth. If the depth of the reception point nearly corresponds to the minimum of this function, the corresponding caustic disappears. Figure 7 shows the

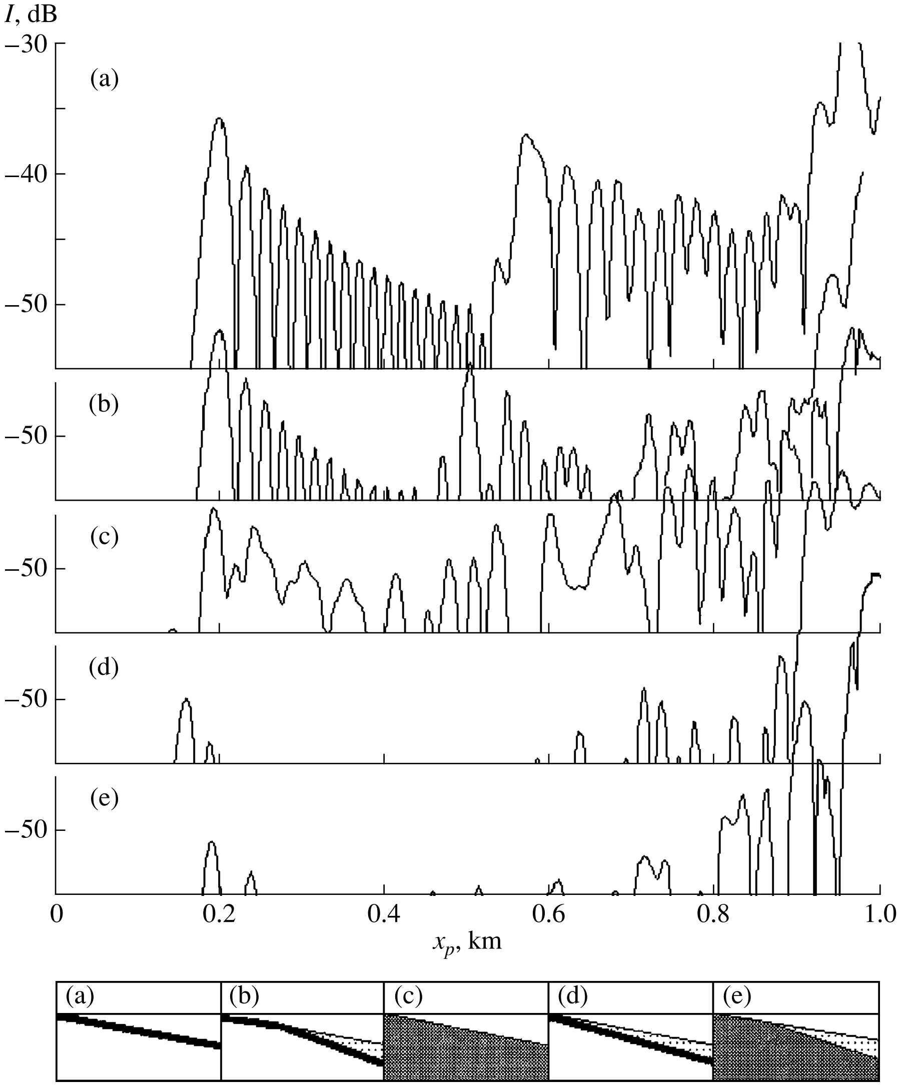

Fig. 6. Intensity of the field versus the horizontal coordinate x_p of the airborne source moving at a height of 50 m for models (a)–(e). The wedge angle is $\Phi = 0.04$ rad, and the sound frequency is 50 Hz. The receiver is located at a depth of 49 m at a distance of 1 km from the wedge edge. The lower part of the figure schematically represents the corresponding models of the sea bottom.

results of similar calculations for model (b) at a frequency of 300 Hz. The mode structure of the field is seen for small x_p.

The lack of information about the bottom structure prevents us from comparing the experimental results [1] with the calculations. Nevertheless, qualitatively, our theoretical results agree well with the experimental data. For example, Gordienko *et al.* [1] reported that, for the frequencies 60–80 Hz, the prominent increase in the signal level occurred at the moments the source moved near the shoreline over the sea with the depth $H_p = (0.2–0.3)\lambda$. This depth just corresponds to the depth $H = 0.25\lambda$ of the caustic of the first normal wave in the wedge with perfectly reflecting sides (in the vertical plane passing through the source perpendicularly to the wedge edge). The subsequent increases in the signal level occurred for the sea depths at the source site $H_p = (1.2–1.4)\lambda$ and $H_p = (1.7–2.2)\lambda$, which approximately correspond to the sea depths at the sites of caustics of the third mode $H_3 = 1.2\lambda$ and the fourth mode $H_4 = 1.75\lambda$. From the comparison of these results, one can conclude that the bottom is almost perfectly reflecting near the shoreline and may have a more complex structure in the region corresponding to the caustic of the fourth mode.

Thus, two factors govern the sharp increase in the signal measured by a waterborne receiver in the case of an airborne source moving near the shoreline. The first factor is the directional property of the field transmitted from air into water. The second point is the structure of the normal wave in the wedge. This structure is characterized by large grazing angles of the Brillouin waves at the caustic of the normal wave. As a result, the source most strongly excites the normal wave at the moments

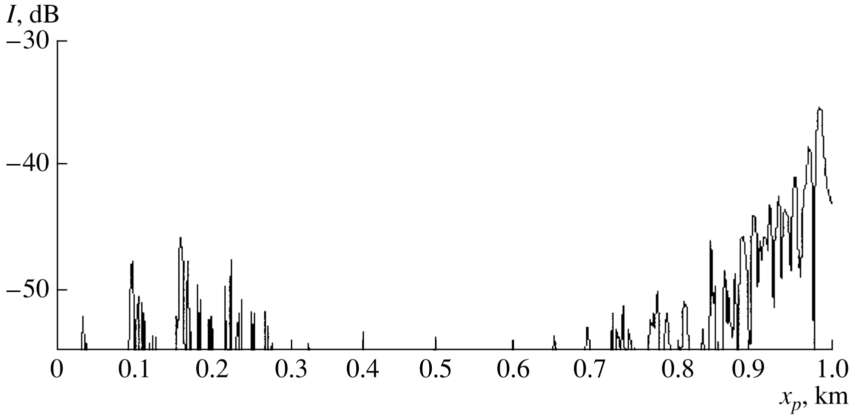

Fig. 7. Intensity of the field versus the horizontal coordinate x_p of the airborne source moving at a height of 50 m for model (b). The wedge angle is $\Phi = 0.04$ rad, the sound frequency is 300 Hz, and the receiver is located at a depth of 39 m at a distance of 1 km from the wedge edge.

it moves over the caustic. The magnitude of the sound field increase depends on the depth of the reception point and, what is more essential, on the bottom structure (the higher the bottom reflectivity, the greater the signal increase). A sediment layer with a positive gradient of sound velocity can, possibly, serve as an additional bottom model for which the effect under study can be expected. As is known [30], the pattern of the normal wave propagation over a rising bottom is drastically changed in this case: at the critical depth, the energy of the mode propagates toward the coast rather than is lost in the bottom sediments. It may appear that an increase in the signal level can occur in this case as well; however, this model was not considered above.

ACKNOWLEDGMENTS

This work was supported by the Russian Foundation for Basic Research, project no. 00-02–17694.

REFERENCES

1. V. A. Gordienko, E. L. Gordienko, L. N. Zakharov, and V. I. Il'ichev, Dokl. Acad. Nauk **333**, 503 (1993) [Phys.-Dokl. (1993)].
2. A. A. Hudimac, J. Acoust. Soc. Am. **29**, 916 (1957).
3. L. M. Brekhovskikh, *Waves in Layered Media* (2nd ed., Nauka, Moscow, 1973; Academic, New York, 1960).
4. D. I. Paul, J. Acoust. Soc. Am. **29**, 1102 (1957).
5. M. S. Weinstein and A. G. Henney, J. Acoust. Soc. Am. **37**, 899 (1965).
6. J. V. McNicholas, J. Acoust. Soc. Am. **53**, 1755 (1973).
7. A. V. Razin, Izv. Akad. Nauk SSSR, Fiz. Atmos. Okeana **20**, 208 (1984).
8. R. J. Urick, J. Acoust. Soc. Am. **52**, 993 (1972).
9. W. C. Meecham, J. Acoust. Soc. Am. **60**, 339 (1976).
10. S. C. Lubard and P. M. Hurdle, J. Acoust. Soc. Am. **60**, 1048 (1976).
11. D. M. F. Chapman and P. D. Ward, J. Acoust. Soc. Am. **87**, 601 (1990).
12. D. M. F. Chapman, D. J. Thomson, and D. D. Ellis, J. Acoust. Soc. Am. **91**, 1904 (1992).
13. A. D. Pierce, J. Acoust. Soc. Am. **72**, 523 (1982).
14. A. Kamel and L. B. Felsen, J. Acoust. Soc. Am. **73**, 1120 (1983).
15. V. K. Kuznetsov, in *Proceedings of VI All-Union Acoustical Conference* (Moscow, 1968), Vol. AIV, p. 5.
16. V. K. Kuznetsov, Akust. Zh. **5**, 170 (1959) [Sov. Phys. Acoust. **5**, 171 (1959)].
17. C. H. Harrison, J. Acoust. Soc. Am. **65**, 56 (1979).
18. C. H. Harrison, J. Acoust. Soc. Am. **62**, 1382 (1977).
19. A. D. Avdeev and Yu. K. Arkhipenko, *A Report of Institute of Physics, Leningrad State University* (NIIF LGU, Leningrad, 1987).
20. C. T. Tindle, H. Hobaek, and T. G. Muir, J. Acoust. Soc. Am. **81**, 275 (1987).
21. C. T. Tindle, H. Hobaek, and T. G. Muir, J. Acoust. Soc. Am. **81**, 287 (1987).
22. L. A. Vaĭnshteĭn, Zh. Tekh. Fiz. **27**, 2109 (1957) [Sov. Phys. Tech. Phys. **2**, 1955 (1957)].
23. N. N. Komissarova, Vopr. Sudostr., Ser. Akust., No. 9, 3 (1978).
24. C. T. Tindle and G. B. Deane, J. Acoust. Soc. Am. **78**, 1366 (1985).
25. G. D. Malyuzhinets, Doctoral Dissertation in Physics and Mathematics (Moscow, 1951).
26. N. N. Komissarova, Akust. Zh. **18**, 259 (1972) [Sov. Phys. Acoust. **18**, 214 (1972)].
27. M. P. Sakharova, Akust. Zh. **5**, 215 (1959) [Sov. Phys. Acoust. **5**, 214 (1959)].
28. N. N. Komissarova, Akust. Zh. **33**, 43 (1987) [Sov. Phys. Acoust. **33**, 25 (1987)].
29. G. J. Heard, J. Acoust. Soc. Am. **101**, 1953 (1997).
30. J. F. Miller, A. Nagl, and H. Überall, J. Acoust. Soc. Am. **79**, 562 (1986).

Translated by A. Vinogradov

Acoustical Physics, Vol. 47, No. 3, 2001, pp. 323–328. Translated from Akusticheskiĭ Zhurnal, Vol. 47, No. 3, 2001, pp. 382–388.
Original Russian Text Copyright © 2001 by Kosobrodov, Nekrasov.

Effect of the Diffraction of Sound by the Carrier of Hydroacoustic Equipment on the Results of Measurements

R. A. Kosobrodov and V. N. Nekrasov

All-Russia Research Institute of Physicotechnical and Radio Engineering Measurements,
State Metrological Center of Hydroacoustic Measurements, Mendeleevo,
Solnechnogorskiĭ raion, Moscow oblast, 141570 Russia
e-mail: gmcgi@ftri.extech.su

Received May 10, 2000

Abstract—The sound field distortions due to the diffraction by the surface of the carrier of hydroacoustic equipment are discussed. A self-contained hydroacoustic buoy in the form of a hollow spherical shell is considered as an example. The sound field formed near such a buoy is calculated with the use of approximate and exact equations of the shell motion. Results of full-scale experiments with a self-contained hydroacoustic buoy are presented. It is concluded that the effect of diffraction by the carrier of hydroacoustic equipment should be taken into account in full-scale hydroacoustic measurements. *© 2001 MAIK “Nauka/Interperiodica”.*

The changes that occur in the sound field as a result of the diffraction by different elements of the measuring equipment are discussed in the monograph by Beranek [1]. This monograph describes the perturbations of the sound field near a perfectly rigid sphere and a cylinder and presents the dependences of the perturbations on the dimensions of the bodies in terms of the wavelength, as well as on the distance and the angle of incidence. Some practical recommendations concerning the reduction of the effect of diffraction on the results of hydroacoustic measurements can be found in the book by Bobber [2].

The characteristic feature of the full-scale hydroacoustic measurements performed on the basis of stationary and self-contained hydroacoustic buoys is the presence of a large-size carrier of the measuring equipment near the hydrophone. This paper presents computational and experimental studies of the effect of the diffraction of sound waves by the surface of the equipment carrier on the measured sound pressure. As an example, we consider a self-contained hydroacouatic buoy in the form of a hollow spherical shell made of a titanium alloy and enclosing the measuring equipment. The measuring hydrophone is usually placed directly at the top of the buoy housing. Such an arrangment of the equipment is widely used in practice [3].

To calculate the sound field near the buoy, it is necessary to use the theory of scattering by an elastic spherical shell. This phenomenon has been studied in many papers. Among the earlier publications, we should note the paper by Junger [4] in which the solution was obtained for a thin spherical shell. The scattering by an elastic shell of an arbitrary thickness was considered by Goodman and Stern [5]. Most of the subsequent studies were devoted to the nature of the interaction of sound with elastic bodies [6–9]. An interesting review describing the history of research concerned with this subject was published by Lyamshev [10]. Among the recent works, we can mention papers [11–14].

Let us consider the scattering of a plain sound wave by an elastic spherical shell. We will use the results obtained in the monograph by Shenderov [15]. We introduce a spherical coordinate system with the origin O at the center of the shell. The outer and inner radii of the shell will be denoted by a_1 and a_2, respectively. Let the incident plane wave propagate in the direction opposite to the x axis. We assume that the point of observation A is determined by the coordinates r and θ. The angle θ is measured from the x axis, as shown in Fig. 1. The media inside and outside the shell are characterized by the densities ρ_1 and ρ_2 and by the sound velocities c_1 and c_2, respectively.

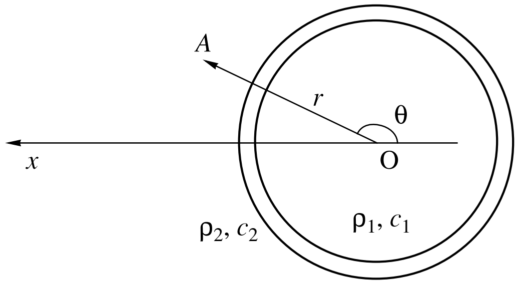

Fig. 1. Geometry of the problem.

The sound field of the incident wave can be represented in the form

$$p_0 = p\exp(ik_2 r\cos\theta), \tag{1}$$

where k_2 is the wave number in medium 2 and p is the amplitude of the sound pressure. Here and below, the factor $\exp(i\omega t)$ involved in the expressions for the sound field will be omitted for brevity.

For the incident wave p_0, for the field inside the shell p_1, and for the field of the scattered wave $p_2^{(s)}$, the following expansions are valid:

$$p_0 = p\sum_{n=0}^{\infty}(2n+1)i^n j_n(k_2 r)P_n(\cos\theta), \tag{2}$$

$$p_1 = p\sum_{n=0}^{\infty}(2n+1)i^n A_n j_n(k_1 r)P_n(\cos\theta), \tag{3}$$

$$p_2^{(s)} = p\sum_{n=0}^{\infty}(2n+1)i^n B_n h_n^{(1)}(k_2 r)P_n(\cos\theta). \tag{4}$$

Here, j_n and $h_n^{(1)}$ are the Bessel and Hankel spherical functions of order n; $P_n(x)$ is the Legendre polynomial; and A_n and B_n are the numerical coefficients determined from the conditions set at the shell boundary:

$$\begin{gathered}\frac{1}{i\omega\rho_2}\frac{\partial(p_{0n}+p_{2n}^{(s)})}{\partial r}\bigg|_{r=a1} = \frac{1}{i\omega\rho_1}\frac{\partial p_{1n}}{\partial r}\bigg|_{r=a1} = V_n,\\ [p_{1n}-(p_{0n}+p_{2n}^{(s)})]_{r=a1} = Z_n V_n,\end{gathered} \tag{5}$$

where V_n is the amplitude of the nth mode of the radial component of the particle velocity at the outer surface of the shell, Z_n is the mechanical impedance of the shell, and ω is the circular frequency.

Setting $k_2 r_1 \gg 1$, from Eqs. (5.48) and (5.49) of monograph [15], we obtain

$$A_n = \frac{w_1}{\mu_2^2 j'_n(\mu_1)h_n^{(1)'}(\mu_2)[Z_n+Z_{S1}+Z_{S2}]}, \tag{6}$$

$$\begin{gathered}B_n = -\frac{j'_n(\mu_2)}{h_n^{(1)'}(\mu_2)}\\ \times\left(1-\frac{w_2}{\mu_2^2 j'_n(\mu_2)h_n^{(1)'}(\mu_2)[Z_n+Z_{S1}+Z_{S2}]}\right),\end{gathered} \tag{7}$$

where $\mu_1 = k_1a_1$, $\mu_2 = k_2a_2$, $w_1 = \rho_1c_1$, $w_2 = \rho_2c_2$, $Z_{S1} = -iw_1 j_n(\mu_1)/j'_n(\mu_1)$, $Z_{S2} = iw_2 h_n^{(1)}(\mu_2)/h_n^{(1)'}(\mu_2)$, k_1 is the wave number in medium 1, and i is the imaginary unit.

The main difficulties encountered in calculating the diffraction of sound by elastic bodies are related to the determination of the mechanical impedances. The cited monograph [15] presents several theories of mechanical impedances of spherical shells. We selected two of them for our consideration.

According to the theory taking into account the flexural and longitudinal vibrations of the shell and ignoring the rotary and shear inertia, the mechanical impedance is equal to $Z_n = -i\omega\rho h\xi_n$, where ρ is the density of the material of the shell, h is its thickness, and ξ_n is the dimensionless quantity determined by the formula

$$\xi_n = \frac{h_{1a}}{x_{\mathrm{L}}^2}\frac{m^3+m^2g_1+mg_2+g_3}{g_4-m}. \tag{8}$$

Here, $m = n(n+1)$, $h_{1a} = h^2/(12a^2)$, $x_{\mathrm{L}}^2 = (\omega a)^2\rho(1-\sigma^2)/E$, $g_1 = -(x_{\mathrm{L}}^2+3+\sigma)$, $g_2 = (1-\sigma^2-x_{\mathrm{L}}^2)/h_{1a}$, $g_3 = (x_{\mathrm{L}}^2+1-\sigma)(x_{\mathrm{L}}^2-2-2\sigma)/h_{1a}$, $g_4 = (x_{\mathrm{L}}^2+1-\sigma)$, and E and σ are Young's modulus and Poisson's ratio of the shell material.

This theory is valid for thin shells for which the product of the wave number of flexural waves by the shell thickness is much less than unity: $k_f h \ll 1$, i.e., $[12\omega^2(1-\sigma^2)\rho h^2/E]^{1/4} \ll 1$, and for modes of vibration for which the spatial period exceeds the flexural wavelength.

To determine the mechanical impedances of a spherical shell of an arbitrary thickness, it is necessary to use an exact theory. The exact equations of the shell motion can be derived by expressing the normal and tangential stresses through the radial and tangential displacements from the Hooke law and by substituting the resulting expressions into the equilibrium equations in spherical coordinates. As a result, one obtains a system of two second-order partial differential equations. By solving this system, one can determine the mechanical impedance of the shell. According to [15], the expression for the impedance calculated in this way has the form (Eq. 5.92 from [15])

$$Z_n = \frac{-ia_1p_n/\omega}{[C_n j'_n(\mu_{\mathrm{L}1})+D_n n'_n(\mu_{\mathrm{L}1})]\mu_{\mathrm{L}1}-n(n+1)[E_n j_n(\mu_{\mathrm{t}1})+F_n n_n(\mu_{\mathrm{t}1})]}. \tag{9}$$

Here, j_n and n_n are the Bessel and Neumann spherical functions of order n;

$$\mu_{L1} = k_L a_1 = \omega a_1 / \sqrt{\frac{\lambda + 2\mu}{\rho}},$$

and

$$\mu_{t1} = k_t a_1 = \omega a_1 / \sqrt{\frac{\mu}{\rho}},$$

where k_L and k_t are the wave numbers of the longitudinal and transverse waves in the shell material and λ and μ are the Lamé constants; C_n, D_n, E_n, and F_n are the coefficients determined from the system of linear equations

$$\|a_{ij}\| \begin{bmatrix} C_n \\ D_n \\ E_n \\ F_n \end{bmatrix} = \begin{bmatrix} -p_n a_1^2/\mu \\ 0 \\ 0 \\ 0 \end{bmatrix},$$

where the elements of the matrix $\|a_{ij}\|$ are as follows:

$$a_{11} = 2\mu_{L1}^2 j_n''(\mu_{L1}) - \frac{\lambda}{\mu}\mu_{L1}^2 j_n(\mu_{L1}),$$

$$a_{12} = 2\mu_{L1}^2 n_n''(\mu_{L1}) - \frac{\lambda}{\mu}\mu_{L1}^2 n_n(\mu_{L1}),$$

$$a_{13} = 2n(n+1)[j_n(\mu_{t1}) - \mu_{t1} j_n'(\mu_{t1})],$$

$$a_{14} = 2n(n+1)[n_n(\mu_{t1}) - \mu_{t1} n_n'(\mu_{t1})],$$

$$a_{31} = 2[\mu_{L1} j_n'(\mu_{L1}) - j_n(\mu_{L1})],$$

$$a_{32} = 2[\mu_{L1} n_n'(\mu_{L1}) - n_n(\mu_{L1})],$$

$$a_{33} = -\mu_{t1}^2 j_n''(\mu_{t1}) - (n^2 + n - 2) j_n(\mu_{t1}),$$

$$a_{34} = -\mu_{t1}^2 n_n''(\mu_{t1}) - (n^2 + n - 2) n_n(\mu_{t1}).$$

The second and fourth rows of the matrix $\|a_{ij}\|$ are obtained from the first and third rows, respectively, by substituting $\mu_{L2} = k_L a_2$ for μ_{L1} and $\mu_{t2} = k_t a_2$ for μ_{t1}. The coefficient p_n is a term in the Legendre polynomial expansion of the sound pressure at the outer surface of the sphere.

After the impedances are calculated by Eq. (8) or by Eq. (9), they can be substituted into Eqs. (6) and (7). As a result, the sound field of the reflected wave and the field inside the shell will be determined.

To characterize the sound field distortions caused by the presence of the spherical shell, we will use the dimensionless complex quantity Y that is equal to the ratio of the total sound pressure in the presence of the shell to the sound pressure in its absence. For a plane wave, we obtain

$$Y = \frac{p_0 + p_2^{(s)}}{p_0} = 1 + \exp(-ik_2 r\cos\theta) \times \sum_{n=0}^{\infty} (2n+1) i^n B_n h_n^{(1)}(k_2 r) P_n(\cos\theta). \tag{10}$$

The quantity Y was calculated for a spherical shell with the outer radius $a_1 = 425$ mm and the wall thickness $h = 18$ mm; the shell material was assumed to be a titanium alloy. In our calculations, we used the following parameters: $\rho = 4550$ kg/m^3, $\sigma = 0.3$, $E = 1.1 \times 10^{11}$ Pa, $\rho_2 = 1000$ kg/m^3, $c_2 = 1500$ m/s, $\rho_1 = 1.29$ kg/m^3, and $c_2 = 346$ m/s.

The point of observation was set at the distance $r = 0.47$ m from the center of the shell in the direction opposite to the wave incidence ($\theta = \pi$), which corresponds to the hydrophone position directly on the housing of the self-contained hydroacoustic buoy. The calculations were performed for the frequency range from 100 Hz to 6 kHz ($ka \approx 0.4$–10). In Eq. (10), we retained the modes with the numbers from one to twenty inclusive.

The results of the calculations by the approximate and exact theories of mechanical impedances are presented in Fig. 2. For comparison, in the same figure, we present the frequency dependences of $|Y|$ calculated for a stiff and a compliant sphere. The complex shape of the frequency dependence of Y is determined by the elastic properties of the shell. A detailed study of the interaction of sound with an elastic body requires the separation of the scattered field into the background and the resonance components [6], after which the latter component can be analyzed by the type of waves. For this purpose, one can use, e.g., the Sommerfeld–Watson transformation [7, 8] or the resonance scattering theory [9].

The resonances caused by the natural vibrations of the shell can be determined by comparing the resonance frequencies of individual partial modes in Eq. (10) with the natural frequencies of the "dry" shell at the corresponding mode, the latter frequencies being determined from the equation $\xi_n(\omega) = 0$. The presence of the associated mass of the medium in which the shell is immersed must reduce the values of the natural frequencies. The table presents the results of calculating the first resonance frequencies for several modes of vibration with the use of the exact and approximate theories.

The frequency dependences of $|Y|$ for four partial modes are presented in Fig. 3. From the plots, one can see that the zeroth and first modes have no pronounced resonances and the resonance peak of $|Y|$ at the frequency 830 Hz ($ka = 1.5$) is caused by the mechanical resonance of the shell at the second mode.

Our calculations provide the possibility to compare the exact theory with the approximate one and to refine the limits of validity for the latter. The curves obtained

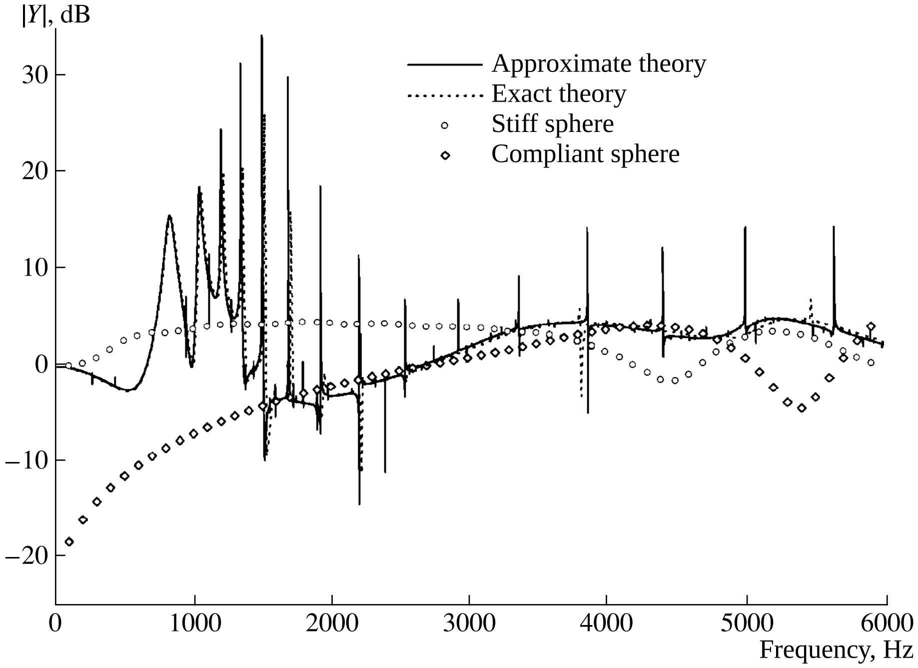

Fig. 2. Frequency dependence of $|Y|$.

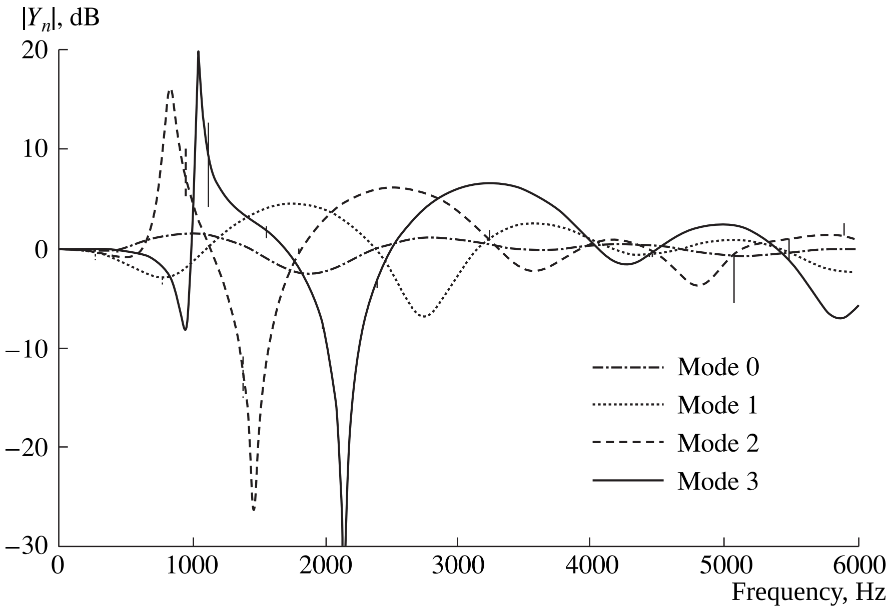

Fig. 3. Frequency dependences for four partial modes.

for the quantity $|Y|$ with the use of the two theories practically coincide, the difference being observed only for some of the resonance peaks and dips (Fig. 2). These discrepancies are explained by the deviation of the eigenfrequencies calculated for the mechanical vibrations of the shell by the two theories. From the table, one can see that the values of the resonance frequencies calculated by the approximate theory in the frequency range under study are on the average 2% less than the values provided by the exact theory. Thus, the approximate theory is applicable at least for $k_f h < 1/4$ with the amount of calculation being considerably reduced.

Now, let us consider the experimental data obtained in the full-scale conditions. The equipment carrier was a self-contained hydroacoustic buoy. Its dimensions and mechanical parameters corresponded to the values used in the calculations.

Frequencies of the natural mechanical vibrations of the spherical shell, Hz

Mode	0	1	2	3	4	5	6	7
Approximate theory	3120.02	3821.62	1358.65	1621.87	1754.48	1870.81	2012.51	2200.93
Exact theory	3188.12	3902.17	1387.99	1655.49	1789.22	1906.15	2048.45	2236.83

The source of the signal was the ambient noise of the water medium with the characteristics close to normal noise [16]. The frequency spectrum of the ambient noise in the water region under study had a smooth maximum at a frequency close to 500 Hz and gradually decreased with increasing frequency. Generally speaking, the parameters of the ambient noise vary with time, but these variations are relatively slow, and the parameters can be considered as stationary within one record. A considerable disadvantage of such a source of sound is the spatial anisotropy of the ambient noise, which can depend on the experimental site and conditions.

In the experiment, we compared the signals obtained from two hydrophones: one hydrophone was mounted directly at the top of the buoy housing, and the other was carried by a float at a distance of 7.5 m and used as reference. The buoy was placed at a depth of about 120 m, and the sea depth at the experimental site was 260 m. The digitized signals were continuously recorded for 3 min, the intervals between the records being about 16 min. The interval between the first and the last records was 11 h. The measurements were performed in the frequency range 200–2500 Hz.

The weather conditions during the experiment were characterized by a gradual decrease in the force of the wind and water waves. As a result, the ambient noise level decreased from the beginning to the end of the experiment by about 8 dB. Figure 4 shows the hydrophone signal spectra averaged over a single record. The two upper curves were obtained at the beginning of the experiment. The reference hydrophone recorded only the ambient noise of the water region under study, whereas, in the spectrum of the signal of the first hydrophone, one can see peaks and smooth maximums that are caused by the effect of the buoy housing.

The difference between the spectra of the signals obtained from the hydrophone positioned at the buoy and from the reference hydrophone provides the frequency dependence of $|Y|$. Figure 5 displays such dependences obtained at the beginning (curve *1*) and at the end (curve *2*) of the experiment. As one would expect, the value of $|Y|$ does not depend on the sound pressure level and is determined exclusively by the properties of the buoy housing: curves *1* and *2* in Fig. 5 practically coincide. The maximal sound field distortion due to the housing of the buoy reaches 10 dB.

Curve *3* in Fig. 5 corresponds to the theoretical frequency dependence of $|Y|$. Comparing the results of our calculations with the experimental data, we can see a good agreement for the resonance frequencies of modes 2–4. A small difference between the corresponding resonances frequencies for higher modes is presum-

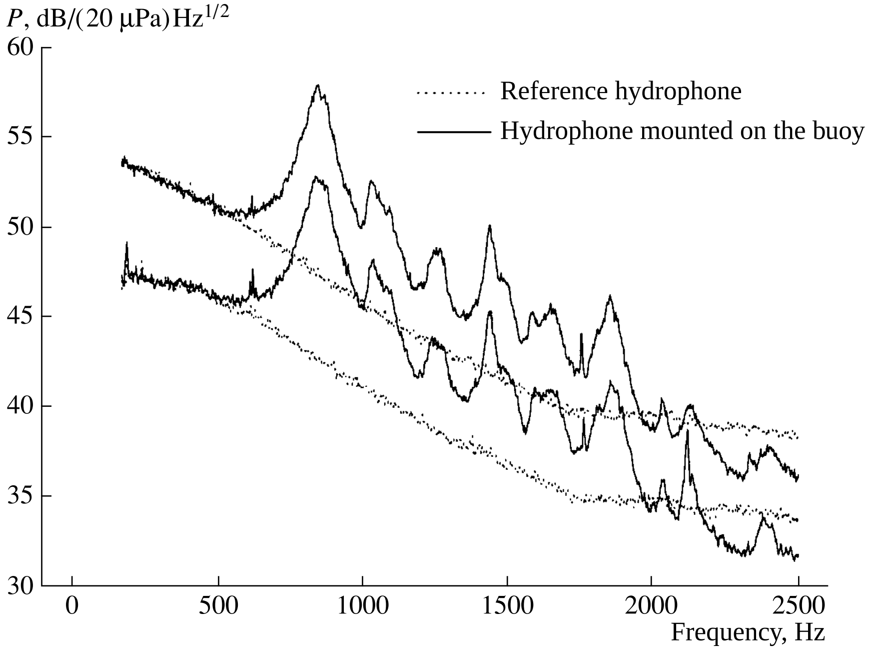

Fig. 4. Spectra of the hydrophone signals at the beginning (the two upper curves) and at the end of the experiment.

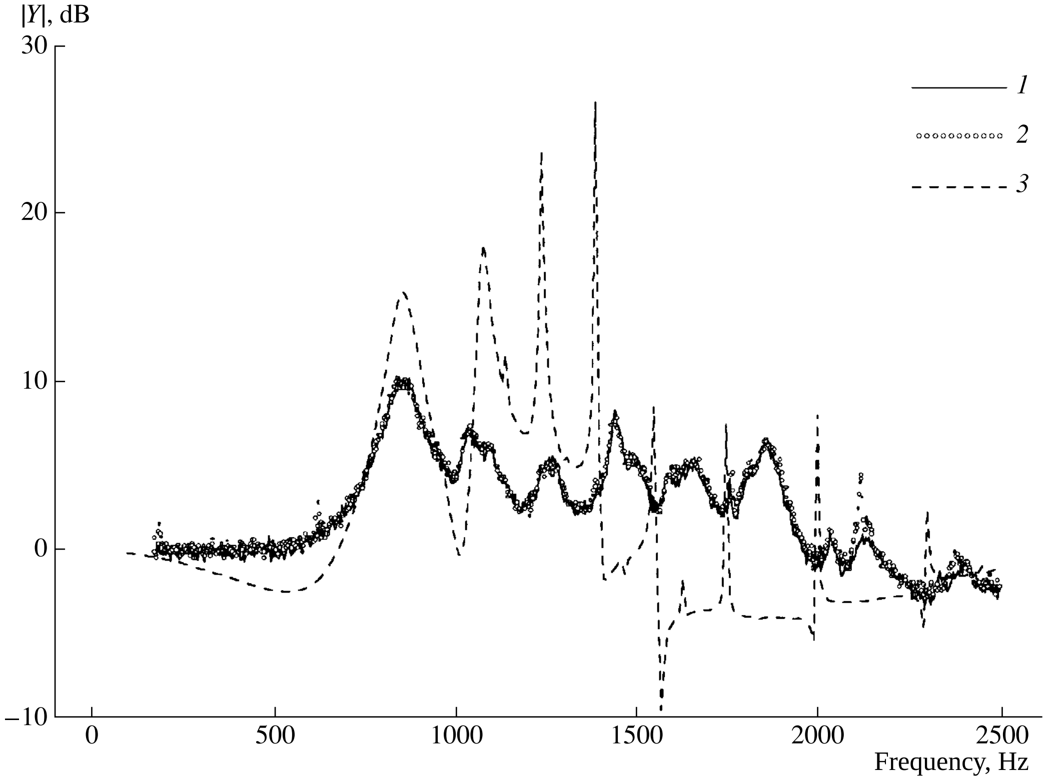

Fig. 5. Comparison of the experimental and the calculated frequency dependences of $|Y|$.

ably related to the deviations of the shell from the spherical form. The theory considerably overestimates the values in the vicinities of the resonances, because it does not take into account the losses in the shell material and the fact that the shell consists of two hemispheres.

Thus, the diffraction of a sound wave by the surface of the equipment carrier can noticeably affect the results of hydroacoustic measurements. The quantity Y characterizing the sound field distortions near the carrier has a frequency dependence of a complex shape and is determined by the mechanical parameters of the buoy housing and the position of the measuring hydrophone. The maximal distortion of the sound field is observed near the eigenfrequencies of the shell vibrations in the medium. A relatively good agreement between the theory and the experimental data makes it possible to calculate the sound field distortions at the stage of the development of hydroacoustic systems and in planning the experiments.

REFERENCES

1. L. Beranek, *Acoustic Measurements* (McGraw-Hill, New York, 1949; Inostrannaya Literatura, Moscow, 1952).
2. R. Bobber, *Underwater Electroacoustic Measurements* (Naval Res. Lab., Washington, 1970; Mir, Moscow, 1974).
3. H. O. Berteaux, *Buoy Engineering* (Wiley, New York, 1976; Sudostroenie, Leningrad, 1979).
4. M. C. Junger, J. Acoust. Soc. Am. **24**, 366 (1952).
5. R. R. Goodman and R. Stern, J. Acoust. Soc. Am. **34**, 338 (1962).
6. J. D. Murphy, J. George, A. Nagl, and H. Überall, J. Acoust. Soc. Am. **65**, 368 (1979).
7. K. L. Williams and P. L. Marston, J. Acoust. Soc. Am. **78**, 1093 (1985).
8. K. L. Williams and P. L. Marston, J. Acoust. Soc. Am. **79**, 1702 (1986).
9. L. Flax, L. R. Dragonette, and H. Überall, J. Acoust. Soc. Am. **63**, 723 (1978).
10. L. M. Lyamshev, Akust. Zh. **45**, 685 (1999) [Acoust. Phys. **45**, 619 (1999)].
11. Pei-Tai Chen, J. Acoust. Soc. Am. **105**, 106 (1999).
12. W. Q. Chen and H. J. Ding, J. Acoust. Soc. Am. **105**, 174 (1999).
13. K. A. Cunefare and S. De Rosa, J. Acoust. Soc. Am. **105**, 206 (1999).
14. H. Peine, J. Acoust. Soc. Am. **105**, 1195 (1999).
15. E. L. Shenderov, *Sound Radiation and Scattering* (Sudostroenie, Leningrad, 1989).
16. A. V. Furduev, in *Acoustics of the Ocean*, Ed. by L. M. Brekhovskikh (Nauka, Moscow, 1974), pp. 615–688.

Translated by E. Golyamina

Acoustical Physics, Vol. 47, No. 3, 2001, pp. 329–332. Translated from Akusticheskiĭ Zhurnal, Vol. 47, No. 3, 2001, pp. 389–392.
Original Russian Text Copyright © 2001 by Kravchun.

Synthesis of Linear Discrete Acoustic Arrays

P. N. Kravchun
Moscow State University, Vorob'evy gory, Moscow, 119899 Russia
e-mail: kravchun@phys.msu.su

Received June 2, 2000

Abstract—The synthesis of a linear array by a given directional pattern is considered under the only constraint that the number of array elements is specified. The formulation of the problem allows solving it with the help of the Newton method, which is the most efficient method of convex programming. It is shown that the possibility to vary the array element coordinates in the course of the array synthesis provides a much higher synthesis quality than that achieved with fixed-geometry arrays. © *2001 MAIK "Nauka/Interperiodica".*

Many different approaches to the synthesis of arrays are known at present. One of the most widespread is the synthesis by the directional pattern [1]. However, almost all known methods of synthesis by the directional pattern place significant constraints on the solution to the problem. Most frequently, they require the element coordinates to be fixed. In order to synthesize an array that provides the best fit to the given pattern with a sufficiently small number of elements, one has to use the synthesis methods based on a search through all available parameters of the array elements: their coordinates, sensitivities, and phase delays in the signal processing channels. In our opinion, in spite of its evident formulation, this problem has not received the attention it deserves in the literature on acoustic array synthesis. Works on the optimization of nonuniformly spaced arrays, which are few in number, usually study particular types of arrays (for example, wide-band arrays with interelement distances being multiples of a given minimal interval are addressed in [2], and the optimal element arrangement is discussed in [3] as applied to the problem of hydroacoustic positioning).

This paper considers the problem of the linear array synthesis by a given directional pattern under the only constraint that the number of array elements is fixed (this constraint being of no fundamental significance). We assume that the array performs the spatial processing of one frequency component of the acoustic field, consists of $2N + 1$ omnidirectional elements (transmitters or receivers), and has a phase center. In this case, its directional pattern $D_N(u, \mathbf{x})$ has the form

$$D_N(u, \mathbf{x}) = \sum_{i=1}^{N} x_{i1}\cos(x_{i2} + 2\pi u x_{i3}). \qquad (1)$$

Here, $\mathbf{x}$ is the vector with the components x_{i1}, x_{i2}, and x_{i3}, where x_{i1} is the sensitivity of the *i*th array element in the transmit or receive mode, x_{i2} is the phase shift introduced into the signal processing channel of the *i*th element, and x_{i3} is the distance from the *i*th element to the array phase center relative to the wavelength at the operating frequency, and $u = \sin\theta$, where θ is the angle with respect to the broadside direction.

Let the desired shape $D_0(u)$ of the directional pattern $D_N(u, \mathbf{x})$ of the synthesized array be given. We formulate the array synthesis problem as follows: given the desired directional pattern $D_0(u)$ and the goal function

$$C_N(\mathbf{x}) = \int_{-\infty}^{+\infty} [D_N(u, \mathbf{x}) - D_0(u)]^2 du, \qquad (2)$$

it is necessary to determine the vector $\mathbf{x}_*$ that satisfies the condition

$$C_N(\mathbf{x}_*) = \min C_N(\mathbf{x}).$$

Thus, the array synthesis problem is as usual reduced to the minimization of a multivariate goal function. It should be noted that, unlike arrays with fixed coordinates, for arrays with variable element coordinates, the solution to the problem of minimization of the above goal function can be found only numerically.

An important circumstance which determines the choice of the minimization method is the fact that the vector of the first derivatives of C_N with respect to $\mathbf{x}$ (the gradient) and the matrix of the second derivatives (the Hesse matrix or the Hessian) can be calculated analytically for the above goal function. The optimal minimization technique for the functions with such properties is the Newton method, which is characterized by a higher convergence rate and a higher stability than other known numerical minimization techniques [4]. In the problem under study, the Newton method is particularly advantageous, because the function $D_N(u, \mathbf{x})$ is a sum of terms of the same structure and, therefore, the gradient and the Hessian of the goal function have the property that the structure of their elements belonging

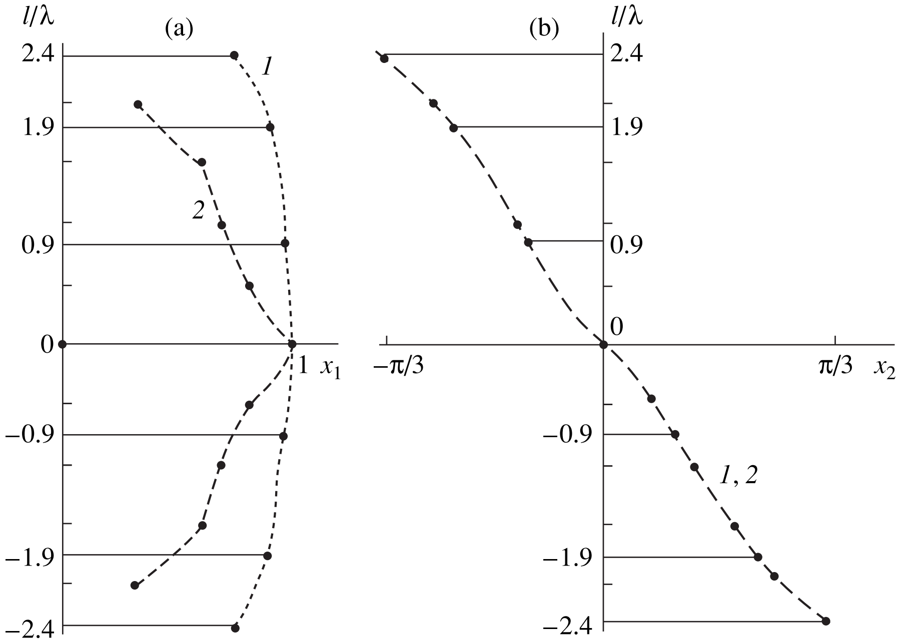

Fig. 1. (a) Amplitude and (b) phase distributions of the element sensitivity along the (*1*) nonuniformly spaced and (*2*) uniform synthesized arrays (the ordinate axis represents the normalized distance from the array phase center).

to one receiver (transmitter) of the array is the same as the structure of any other receiver (transmitter) of this array.

Let us illustrate this method of solving the problem by the example of the synthesis of a linear array whose directional pattern approximates the cosecant pattern, which is widely used in practice. Figures 1 and 2 show the results of synthesizing a seven-element, nonuniformly spaced array by a given cosecant pattern that is nonzero in the range θ = 2°–6°. For the sake of comparison, Figs. 1 and 2 also show results of the synthesis and the directional pattern of an array with a given regular arrangement of the same number of elements, which was synthesized for the same desired cosecant pattern by varying only the amplitudes and the phase delays of each element (in this case, the problem can be solved by the Fourier method [1]). These results show that the array with elements whose coordinates are varied in the course of the synthesis is much closer to the desired pattern than the regularly spaced array, the optimal positions of the array elements relative to the phase center being widely different from the regular arrangement.

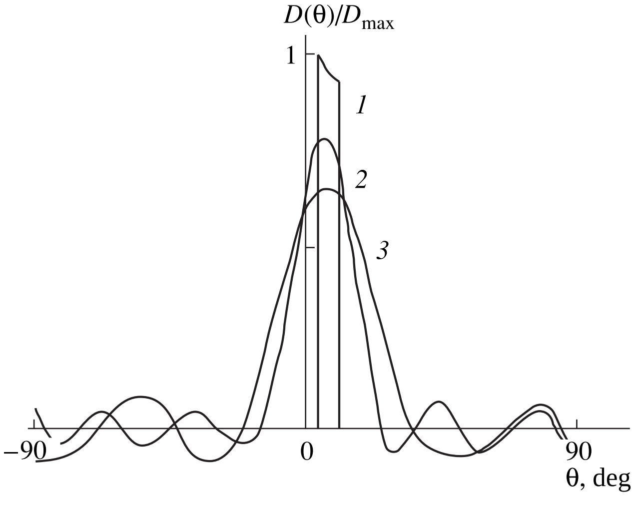

Fig. 2. (*1*) The given cosecant pattern and the directional patterns of the (*2*) nonuniformly spaced and (*3*) uniform synthesized arrays.

The quality of the nonuniformly spaced synthesized array in comparison with that of the uniformly spaced array is clearly illustrated by the standard deviation (Eq. (2)) calculated for the arrays of both types and represented as a function of the total array length and the number of the array elements. Figures 3 and 4 show these functions normalized by the maximum of the directional pattern. The comparison shows a considerable advantage of the nonuniformly spaced arrays in terms of the standard deviation at a given number of array elements. As for the dependence of the standard deviation on the array length, arrays of both types provide almost equal standard deviations irrespective of the shape of the given directional pattern when the number of the array elements is not too large.

An important characteristic of any array is its stability to deviations in the parameters of individual elements from the design values (the parametric robustness). Most frequently, these deviations are random in their nature; they are associated with a spread in the element sensitivity and in the phase delay in the processing channel, as well as with the errors in positioning the transducers in the array. We assume that these parameters are Gaussian and that their standard deviations are σ_a, σ_φ, and σ_r, respectively.

The squared directional pattern $D_{\rm er}(u, \mathbf{x})$ of the array averaged under the above assumptions was calculated in [5]:

$$M[D_{\rm er}^2(u, \mathbf{x})] = D_N^2(u, \mathbf{x}) + \Delta^2 \sum_{i=1}^{N} x_{i1}^2,$$

where M means averaging over an ensemble of patterns and Δ is the coefficient determined by variances of the array element parameters. The quantity Δ was calculated in [5] under the assumption that only the amplitude and phase errors are present. In our problem, errors in the element positions are also present. Therefore, the coefficient Δ can easily be shown to change and to become

$$\Delta = (\sigma_a^2 + \sigma_\varphi^2 + k^2 u^2 \sigma_r^2)^{1/2},$$

where k is the wave number. One can see that, in practice, the last term in this formula is far from being small relative to the first two terms.

We also estimate the average standard deviation $C_{\rm er}(\mathbf{x})$ determined by Eqs (1) and (2) with errors present in all parameters of the array elements. By removing the brackets in Eq. (2), one can easily show that

$$M[C_{\rm er}(\mathbf{x})] = C_N(\mathbf{x}) + \sum_{i=1}^{N} x_{i1}^2 \int_{-1}^{+1} \Delta^2 du. \qquad (3)$$

This expression was derived using the equality

$$M[D_{\rm er}(u, \mathbf{x})] = D_N(u, \mathbf{x}).$$

The second term on the right-hand side of Eq. (3) characterizes the effect of random errors in the parameters of the array elements on the standard deviation. The dependence of the ratio of this quantity calculated for the uniform array to that calculated for the nonuniformly spaced array on the number of array elements is plotted with a dashed line in Fig. 4. From Eq. (3), it follows that this ratio is exclusively determined by the average (theoretical) values of the array element parameters and is independent of their variances. The results presented in Fig. 4 show that, when the number of elements is small, the uniform array is more stable than the nonuniformly spaced one; however, the stability of both types of arrays becomes almost the same as the number of elements increases.

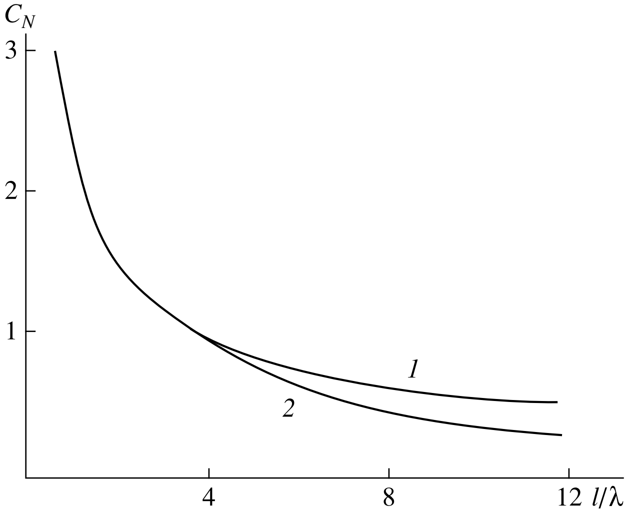

Fig. 3. Standard deviation C_N versus the array length for the (*1*) uniform and (*2*) nonuniformly spaced arrays. The horizontal axis represents the array base measured in the wavelength units.

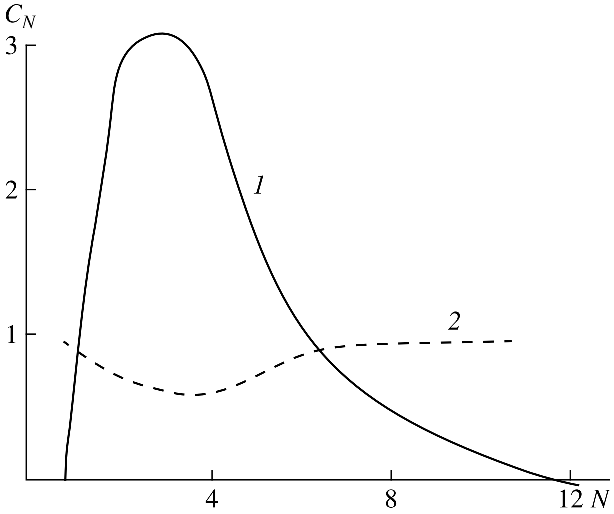

Fig. 4. (*1*) Difference $C_N^{\rm U} - C_N^{\rm NS}$ of the standard deviations for the uniform ($C_N^{\rm U}$) and nonuniformly spaced ($C_N^{\rm NS}$) arrays and (*2*) the ratio between the contribution of random errors in the array element parameters to the standard deviation for the uniform array to the corresponding quantity for the nonuniformly spaced array versus the number of array elements.

The conclusions derived above remain qualitatively valid for other types of directional patterns.

The full-scale experiments carried out in Ladoga Lake corroborate the basic results of this paper to within the experimental error.

ACKNOWLEDGMENTS

The author is grateful to K.A. Pestov for assistance in the calculations and for useful discussions; the author also acknowledges the contribution of O.S. Tonakanov (1930–1995) to the formulation of the problem and to the arrangement of the full-scale measurements.

REFERENCES

1. V. B. Zhukov, *Calculation of Hydroacoustic Arrays by the Directional Patterns* (Sudostroenie, Leningrad, 1977).
2. J. Ohga, J. Acoust. Soc. Jpn. **30**, 291 (1974).
3. S. E. Dosso and B. J. Sotirin, J. Acoust. Soc. Am. **106**, 3445 (1999).
4. P. E. Gill, W. Murray, and M. H. Wright, *Practical Optimization* (Academic, London, 1981; Mir, Moscow, 1985).
5. M. D. Smaryshev, *Directivity of Hydroacoustic Arrays* (Sudostroenie, Leningrad, 1973).

Translated by A. Khzmalyan

Acoustical Physics, Vol. 47, No. 3, 2001, pp. 333–340. Translated from Akusticheskiĭ Zhurnal, Vol. 47, No. 3, 2001, pp. 393–400.
Original Russian Text Copyright © 2001 by Makov.

Thermal Fields and Thermal Doses in Ultrasonic Surgery: A Model of a Gaussian Focused Beam

Yu. N. Makov
Moscow State University, Vorob'evy gory, Moscow, 119899 Russia
e-mail: makov@acs364.phys.msu.su

Received July 17, 2000

Abstract—The condition of equivalence of the space–time distributions of thermal sources in the focal region is introduced for the sources caused by the absorption of focused ultrasonic beams with different aperture amplitude distributions in biological tissue. The Gaussian beam model, which allows the simplest analytical solution of the biothermal equation, is used to obtain fairly accurate approximations in the form of explicit functions describing the spatial distribution and the time dynamics of thermal fields and thermal doses along the beam axis and along the radius in the focal plane. This provides an opportunity to conduct a rapid analysis (without multiple numerical integration) of the results of active surgical (thermodestructive) action of ultrasound on biological tissue and, first of all, to determine the characteristic dimensions of the zone of thermal destruction of biological tissue. The approximate analytical solutions are important for the determination of the effect of the beam parameters (the radius of the aperture and the frequency) on the characteristic dimensions of the zone of thermal destruction. *© 2001 MAIK "Nauka/Interperiodica".*

The heating (hyperthermia) of a specified region of biological tissue (in most cases, a malignant growth) due to the absorption of ultrasound transmitted through it is used as an effective therapeutic treatment or a noninvasive surgical method based on the thermal destruction of the biological tissue by a high-intensity focused ultrasonic beam [1].

In the therapeutic mode of ultrasonic hyperthermia, the temperature in a specified region of the patient's body is maintained strictly within the range 42–45°C for several dozen minutes. For this purpose, one has to use an ultrasonic intensity of the order of 10 W/cm^2 in the heated region. In the case of prolonged action, such a small overheating of the biological tissue suppresses the vital functions of cells, which leads to a so-called cytotoxicosis effect. Taking into account the maximal discrimination of the thermal action upon a malignant growth (owing to its increased thermal conductivity and a reduced blood flow in it), the therapeutic mode of hyperthermia is used to suppress the vital functions of cancer cells. Because of the long duration of the ultrasonic therapy process with the strict requirements on the admissible temperature of the heated region, it is necessary to take into account different factors affecting the heating conditions (e.g., the blood flow, the physiological reactions of the body, etc.), which is a difficult problem from both the theoretical and experimental points of view.

Another (nonthermal) approach to therapeutic ultrasonic action on the cell structures was proposed and realized by Burov [2, 3] in the middle 1950s. However, this approach was not properly developed in the following years. The distinctive feature of this approach is the exposure of the selected cells (e.g., tumor cells) to sufficiently intense ultrasound (150 W/cm^2 with a flat quartz radiator at a frequency of 1.5 MHz) at temperatures that are normal from the point of view of the vital functions of cells and do not exceed 39–40°C, which is provided by the small duration (1–3 s) of a single cycle of insonification. In this case, the ultrasonic action leads to fine cytological and functional changes causing remission of both the insonified malignant formation and the metastases produced by this formation while leaving the cells viable.

An alternative to the therapeutic modes of ultrasound utilization in medicine is the high-temperature ($T > 60$°C) action on biological tissues, which can be realized only by using focused ultrasonic beams. In this case, a high temperature (70–90°C) exceeding considerably the threshold of protein coagulation is attained in the focal region within a short time (1–10 s), which leads to a total thermal destruction (coagulation necrosis) of the selected region of the biological tissue (e.g., a malignant growth). This mode is frequently called ultrasonic surgery.[1] The focusing of an ultrasonic beam with the frequency 1–2 MHz provides an opportunity to localize the zone of thermal destruction of the biological tissue by controlling the focal region of the beam and produce the intensity 1–3 kW/cm^2 in the focal region at a realistic ultrasonic intensity (of the order of 0.5–1 W/cm^2) at the focuser. Such an intensity provides the necessary high temperature. The short duration of

---

[1] This noninvasive process is equivalent to excision of tissues in conventional surgery. Ultrasound of a much lower frequency (tens of kilohertz) is also used for dissection of tissues.

this procedure and the high temperature provide certain grounds for ignoring various factors characteristic of biological tissues (cooling by the blood circulation, physiological reactions, etc.), the characteristic manifestation times of which exceed the time of a single ultrasonic action. However, in the case of the application of ultrasonic surgery, the problem of predicting the space–time dynamics of the thermal field and, correspondingly, the zone of thermal destruction of the biological tissue with the aim for this zone to coincide with the region of the tissue to be “removed” and to cause the least possible effect on the surrounding healthy tissue is very important. Below, in order to solve this problem (for a rapid analysis of the expected results of the surgical ultrasonic action), we obtain rather simple approximate (but with a very small error) analytical expressions providing an opportunity to easily determine the characteristic dimensions of the zone of thermal destruction depending on the basic parameters, such as the duration of the ultrasonic action, the aperture radius, the operating frequency, and the basic characteristics of the biological tissue.

The resulting effects of thermal ultrasonic action on the biological tissue are determined by the space–time dynamics of the temperature field. This dynamics is described by a heat conduction equation with distributed heat sources caused by the ultrasonic absorption in the biological tissue. This equation taking into account the process of convective cooling (heat “removal”) because of the blood circulation (perfusion) is called the biothermal equation, or the Pennes equation [4]:

$$\frac{\partial(\delta T)}{\partial t} - \kappa\Delta(\delta T) + \frac{WC_b}{\rho C_t}\delta T = \frac{q}{\rho C_t}, \tag{1}$$

where $\delta T = T(x, y, z, t) - T_0$ is the excess of the current local temperature T over the normal equilibrium internal temperature of the tissue T_0 (usually, $T_0 = 37°\mathrm{C}$), Δ is the three-dimensional Laplacian, q is the volume density of thermal sources (nonstationary sources in the general case), $\rho = 1.1 \times 10^3$ kg/m^3 is the density of the biological tissue, $\kappa = 1.5 \times 10^{-7}$ m^2/s is the characteristic value of the thermal diffusivity of the biological tissue, $C_t \approx C_b \equiv C = 3.8$–$4.1$ J/kg °C are the almost equal thermal conductivities of the biological tissue and blood, $W = 0.5$–70 kg/(m^3 s) is the perfusion (the blood flow through the unit volume of the biological tissue per unit time for different types of biological tissues, from muscles to kidneys), and $\tau \equiv \left(\frac{WC_b}{\rho C_t}\right)^{-1} = 15$–$2000$ s is the perfusion time (the characteristic time scale of blood circulation).

The substitution of $\delta T = \theta e^{-t/\tau}$ eliminates the convective term from Eq. (1) and leads to the equation

$$\frac{\partial\theta}{\partial t} - \kappa\Delta\theta = \frac{q}{\rho C}e^{t/\tau}. \tag{2}$$

We can represent the density of thermal sources in the form

$$q = q(x, y, z)Q(t), \tag{3}$$

where $q(x, y, z) = -\mathrm{div}\,\mathbf{I}$ is the spatial distribution of sources due to the ultrasonic absorption in the biological tissue, $I = 0.5\mathrm{Re}(VP^*)$ is the real part of the product of the complex amplitude of the acoustic velocity V by the complex-conjugate amplitude of acoustic pressure P, and $Q(t)$ is the on–off function of the ultrasonic action.

In the simplest case, $Q(t)$ is expressed with the help of a step function (the Heaviside function) $U(t)$

$$Q(t) = U(t) - U(t - t_0), \tag{4}$$

where t_0 is the time of ultrasonic action on the tissue and $U(t)$ is equal to zero for $t < 0$ and to unity for $t \geq 0$.

The analysis of the process and result of hyperthermia is usually conducted on the basis of a time-consuming numerical solution (see, e.g., [5]) of the four-dimensional Eq. (1), which prevents a rapid determination of the necessary dependences of the resulting characteristics on the basic “input” and procedural parameters. Therefore, the most advanced (in the sense of analytical solution) models and the approximate solutions to Eq. (1), which can be determined in a finite form, are very important.

The solution of the standard inhomogeneous heat conduction equation (2) for θ with the zero initial condition can be expressed through the time and space convolution of the thermal source function with the Green function for this equation [6]. Taking into account the relation between θ and the desired function δT, as well as Eqs. (3) and (4) and the rules of integration of an expression with the step function, and simulating the region of ultrasonic propagation by the halfspace $z \geq 0$, we can represent this solution in the form

$$\delta T = \frac{1}{\rho C(2\sqrt{\pi\kappa})^3}\int_{t_1}^{t_2}\frac{e^{-t'/\tau}}{(t')^{3/2}}\left(\int_0^{\infty}\int_{-\infty}^{\infty}\int_{-\infty}^{\infty} q(x', y', z') \right. \tag{5}$$

$$\left. \times \exp\left(-\frac{(x-x')^2 + (y-y')^2 + (z-z')^2}{4\kappa t'}\right)dx'dy'dz'\right)dt',$$

where the integration limits at the stage of heating at $t \leq t_0$ are

$$t_1 = 0, \quad t_2 = t \quad (0 \leq t \leq t_0) \tag{6}$$

and, at the stage of cooling at $t > t_0$, they are

$$t_1 = t - t_0, \quad t_2 = t \quad (t > t_0). \tag{7}$$

Taking into account the temperature at the stage of cooling is important for predicting multiple ultrasonic action on the selected region (e.g., a large tumor).

In the case of the natural situation of an axially symmetric ultrasonic beam and, hence, an axially symmetric function of thermal sources q, the solution given by Eq. (5) can be simplified by integrating the Green function over the angle. The dependence on the angle manifests itself if we proceed to the cylindrical coordinates (r, φ, z) using the relation $(x - x')^2 + (y - y')^2 \equiv r^2 + r'^2 - 2rr'\cos(\varphi)$. This yields the following solution to Eq. (1) in the cylindrical coordinates for axisymmetric sources:

$$\delta T = \frac{2\pi}{\rho C(2\sqrt{\pi\kappa})^3}\int_{t_1}^{t_2}\frac{e^{-t'/\tau}}{(t')^{3/2}} \times\left(\int_0^{\infty} e^{-\frac{(z-z')^2}{4\kappa t'}}\int_0^{\infty} q(r', z')e^{-\frac{r^2+r'^2}{4\kappa t'}}I_0\left(\frac{rr'}{2\kappa t'}\right)r'dr'dz'\right)dt'. \tag{8}$$

Proceeding from sparse opportunities (see [7]) for the selection of the function $q(r, z)$ needed for taking the integrals in a finite form in Eq. (8), we can arrive at its unique form as a Gaussoid with respect to r' when the integral in Eq. (8) is taken with respect to this variable and the function corresponds to the specific model of the Gaussian focused beam in the parabolic approximation. The focusing system parameters typical of ultrasonic surgery (the radius of the focuser $a = 5$ cm, the focal distance $R = 10$ cm, the frequency $f = 1$ MHz, and the characteristic value of ultrasonic intensity at the focuser $I_0 = 1$ W/cm^2) provide an opportunity to use the parabolic approximation [8] to a high accuracy for calculating the acoustic field and the field of thermal sources in the focal region where the active ultrasonic action on the biological tissue occurs leading to its thermal destruction. In this approximation, the complex amplitude $A(r, z)$ of the pressure field $p = A(r, z)e^{ikz - i\omega t}$ of axisymmetric wave beams in a medium with the coefficient of linear absorption α is described by the equation

$$\frac{\partial A}{\partial z} + \alpha A = \frac{i}{2kr}\frac{\partial}{\partial r}\left(r\frac{\partial A}{\partial r}\right)$$

and the solution is described with the help of the boundary value of the amplitude $A(r, z = 0)$ and the Green function:

$$A(r, z) = -\frac{ik}{z}\exp\left(\frac{ik}{2z}r^2 - \alpha z\right) \times\int_0^{\infty}\exp\left(\frac{ik}{2z}r'^2\right)J_0\left(\frac{k}{z}rr'\right)A(r', 0)r'dr'.$$

It should be noted that, in the utilized frequency range, the absorption coefficient of the biological tissue depends almost linearly on frequency, and, therefore, $\alpha = \alpha_0 f$, where the value of α_0 is determined by the specific type of the biological tissue; f is the frequency in megahertz. However, we can consider $\alpha_0 \sim 5$ (1/m MHz) as the typical value.

We assume that a focused beam with the curvature radius of the wave front (the focal distance) R and with the transverse amplitude distribution described by a real function $g(r)$ normalized to the maximal value of A_0 is formed at the boundary $z = 0$. Then, we have

$$A(r, 0) = A_0 g(r)\exp\left(-\frac{ikr^2}{2R}\right).$$

Correspondingly, the function of the spatial distribution of thermal sources caused by the absorption of an axisymmetric ultrasonic beam in the biological tissue is equal to

$$q(r, z) = 2\alpha I_0 e^{-2\alpha z} \times\frac{k^2}{z^2}\left\{\left[\int_0^{\infty} g(r')\cos\left(\frac{k}{2}\left(\frac{1}{z} - \frac{1}{R}\right)r'^2\right)J_0\left(\frac{krr'}{z}\right)r'dr'\right]^2 + \left[\int_0^{\infty} g(r')\sin\left(\frac{k}{2}\left(\frac{1}{z} - \frac{1}{R}\right)r'^2\right)J_0\left(\frac{krr'}{z}\right)r'dr'\right]^2\right\}. \tag{9}$$

The model of a Gaussian focused beam

$$A(r, 0) = A_0\exp\left(-\frac{r^2}{a_g^2} - \frac{ikr^2}{2R}\right),$$

where a_g is the initial radius of the effective (with respect to the amplitude) aperture of the Gaussian beam, provides an opportunity to calculate in the final form the maximal number of integrals in the solution given by Eqs. (8) and (9) and use fairly accurate analytical approximations for all the remaining integrals that cannot be taken.

The function of the spatial distribution of thermal sources for a Gaussian focused beam being absorbed in the biological tissue is determined in the parabolic approximation by the expression

$$q_g(r, z) = 2\alpha I_0\frac{\exp\left(-\frac{2r^2}{a_g^2[(1 - z/R)^2 + (z/l_d)^2]} - 2\alpha z\right)}{(1 - z/R)^2 + (z/l_d)^2}, \tag{10}$$

where $l_d = \pi a_g^2 f/c$ is the diffraction length of the Gaussian beam and $I_0 = \frac{P_0^2}{2\rho c}$ is the maximal intensity at the transducer in the case of the Gaussian distribution of the pressure amplitude with the maximal value P_0.

In the case of the utilization of the Gaussian focused beam model in the calculation as an equivalent of a real beam, one needs to satisfy certain relations for their comparability. If a real beam is characterized by the focal length R_{ac}, the aperture radius of the radiator a_{ac}, and the initial distribution $g(r)$ normalized to the ampli-

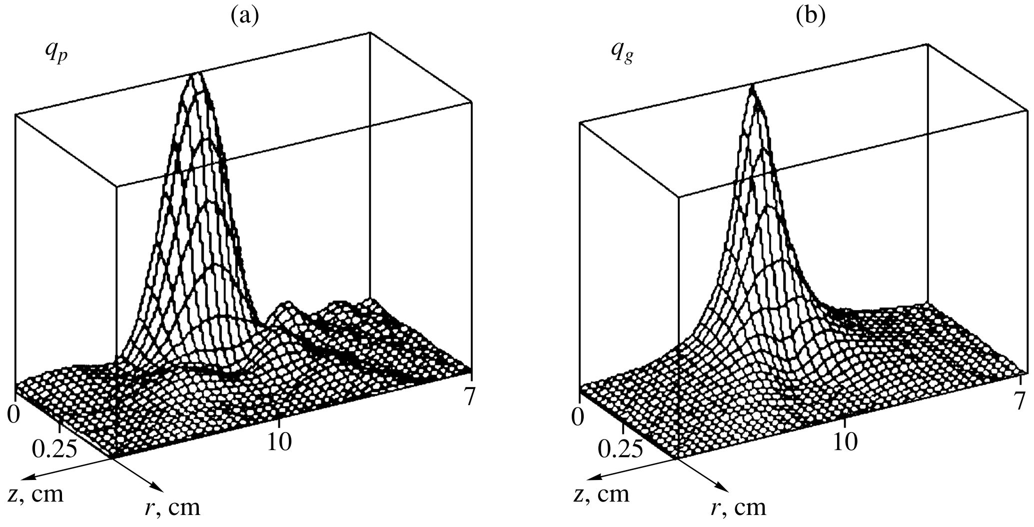

$q^{\max}_{p.,\,g.} = 88.6$ W/cm^3 $\quad I^{\max}_f = 2400$ W/cm^2

Fig. 1. Spatial distribution in the focal region of thermal sources caused by the absorption of equivalent (according to Eq. (11)) ultrasonic beams from radiators of the (a) piston and (b) Gaussian types. The beam parameters are given in the text.

tude maximum at the radiator, the equivalence relations between it and the Gaussian beam are

$$R_{ac} = R_g = R, \tag{11a}$$

$$I_0^{(ac)}\int_0^{a_{ac}} g^2(r)rdr = I_0^{(g)}\frac{a_g^2}{4}, \tag{11b}$$

$$I_0^{(ac)}\left[\int_0^{a_{ac}} g(r')r'dr'\right]^2 = I_0^{(g)}\frac{a_g^4}{4}. \tag{11c}$$

The relation given by Eq. (11b) expresses the equality of the energy "contributed" to both beams at $z = 0$, and Eq. (11c) provides the equality of the maximal values of the thermal source function at $r = 0$, $z = R$.[2] The aperture radius and the maximal "input" intensity of the model Gaussian beam are expressed unambiguously with the help of these two formulas using the analogous parameters of a real beam with which the model beam is compared. Then, we can use (to a certain approximation) the obtained "equivalent" Gaussian beam to conduct further prognostic calculations of thermal fields. For example, an ultrasonic beam radiated by a focusing transducer with a uniform aperture distribution of the pressure amplitude normalized to the maximum (a piston-type transducer), i.e.,

$$g_p(r) = \begin{cases} 1, & \text{for } r \le a_p \\ 0, & \text{for } r > a_p, \end{cases} \tag{12}$$

corresponds to an equivalent model Gaussian beam with the parameters

$$a_g = a_p/\sqrt{2}, \tag{13a}$$

$$I_0^{(g)} = 4I_0^{(p)}. \tag{13b}$$

Figure 1a shows the spatial distribution in the focal region of the function of the thermal sources caused by the absorption of a focused ultrasonic beam from a piston-type transducer; the distribution is calculated according to Eqs. (9) and (10) for $a_p = 5$ cm, $R = 10$ cm, and $I_0^{(p)} = 1$ W/cm^2. Figure 1b shows the analogous distribution for an equivalent Gaussian focused beam with the corresponding (according to Eqs. (13)) parameters $a_g = 5/\sqrt{2}$ cm, $R = 10$ cm, and $I_0^{(g)} = 4$ W/cm^2. A more obvious comparison of these two functions of thermal sources is given in Fig. 2 where the cross-sections of these functions along the z axis at $r = 0$ (Fig. 2a) and their sections by the focal pane $z = R$ (Fig. 2b) are shown. The coincidence of the focal peaks substantiates the definition of the beam equivalence (Eqs. (11)). The natural difference in the region of the base ("pedestal") of the main peak does not play any significant role in the case of short heating cycles with the duration of several seconds, when the temperatures and the thermal doses in this region do not exceed the threshold values.

Now, we use the model of the Gaussian focused beam for calculating the space–time dynamics of thermal fields. The substitution of the function of thermal sources (10) into solution (8) provides an opportunity to calculate the integral with respect to r' in it and, thus,

---

[2] The coordinate of the maximum of the thermal source function, which is determined analytically, differs to a certain extent from $z = R$. However, this difference is negligible for the considered typical parameters of the beam.

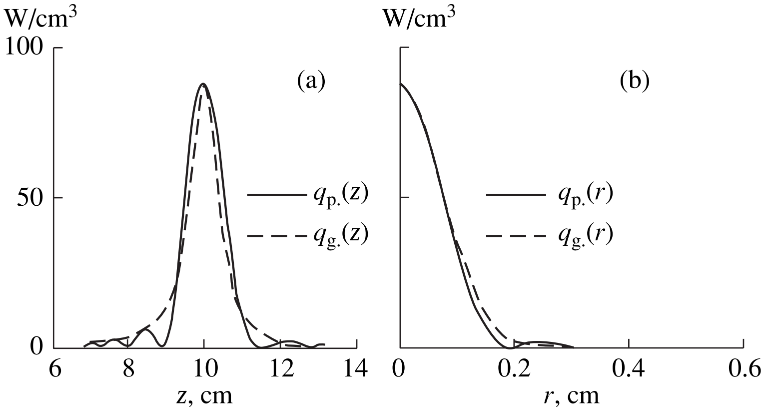

Fig. 2. Cross-sections of the spatial distributions shown in Fig. 1 by the planes (a) $r = 0$ and (b) $z = R$. The solid line corresponds to an ultrasonic beam from a piston-type radiator, and the dashed line is for the Gaussian beam.

to reduce the number of integrals that cannot be "taken" down to two. In this case, the solution takes the form

$$\delta T(r, z, t) = \frac{\alpha I_0 a_g^2}{\rho C\sqrt{\pi\kappa}}\int_{t_1}^{t_2}\frac{e^{-t'/\tau}}{\sqrt{t'}} \times\int_0^{\infty}\frac{\exp\left[-\frac{2r^2}{8\kappa t' + a_g^2F(z')} - 2\alpha z' - \frac{(z-z')^2}{4\kappa t'}\right]}{8\kappa t' + a_g^2F(z')}dz'dt', \tag{14}$$

where $F(z) = \left(1 - \frac{z}{R}\right)^2 + \left(\frac{z}{l_d}\right)^2$ and the values of t_1 and t_2 are selected according to Eqs. (6) and (7).

We stress that the model of the Gaussian beam is the only one that reduces the solution for the thermal field to two repeated integrals as against three or four such integrals for all other models. The obvious form of the solution given by Eq. (14) provides an opportunity in this case to interpret the performed integration (averaging) over r' as the reduction of the thermal problem to a problem that is one-dimensional along the z axis and has a function of thermal sources analogous in its structure to the initial one (Eq. (10)), but has the characteristic transverse scale that exhibits a time increase (diffusion) in addition to the spatial variation along the z axis.

It is possible to obtain rather accurate analytical approximations for the obtained exact but implicit solution (14) on the basis of which it is difficult to analyze the dependences of the characteristic dimensions of the thermal effect region on the fundamental parameters of the ultrasonic beam (the initial aperture radius, the initial intensity, the frequency, etc.). It is necessary to indicate first that, considering the process of ultrasonic surgery, when a high temperature in the focal region is attained after several seconds, we can assume the perfusion time in Eq. (14) to be infinite, i.e., $\tau \longrightarrow \infty$. Moreover, it is convenient to consider two selected directions: along the beam axis where $r = 0$ and along the radius in the focal plane $z = R$. The analysis of Eq. (14) shows that, in the case of integration with respect to z', the dynamics of the integrand is mainly determined by a rapidly decaying factor $\exp\left(-\frac{(z-z')^2}{4\kappa t'}\right)$, which provides an opportunity to perform a substitution $z' \longrightarrow z$ in the remaining factor with a relatively slow dependence on z' and factor it out from under the integral sign. In this case, we can take $-\infty$ as the lower limit for this integral. This provides an opportunity to integrate in a closed form both repeated integrals in Eq. (14) and obtain the following approximate dependences:

along the beam axis at $r = 0$,

$$\delta T_{ap}(r = 0, z, t) = \frac{\alpha I_0 a_g^2 e^{-2\alpha R}}{4\kappa\rho C} \times\ln\left(\frac{8\kappa t_2 + a_g^2\left(\left(\frac{\delta z}{R}\right)^2 + \left(\frac{R}{l_d}\right)^2\right)}{8\kappa t_1 + a_g^2\left(\left(\frac{\delta z}{R}\right)^2 + \left(\frac{R}{l_d}\right)^2\right)}\right), \tag{15}$$

where $\delta z = z - R$;

in the focal plane at $z = R$ and $r > 0$,

$$\delta T_{ap}(r, z = R, t) = \frac{\alpha I_0 a_g^2 e^{-2\alpha R}}{4\kappa\rho C} \times\left[E_1\left(\frac{2r^2}{8\kappa t_2 + a_g^2R^2/l_d^2}\right) - E_1\left(\frac{2r^2}{8\kappa t_1 + a_g^2R^2/l_d^2}\right)\right], \tag{16}$$

where $E_1(z) = \int_z^{\infty}\frac{e^{-t}}{t}dt$ is the exponent integral function. The values of t_1 and t_2 are determined according

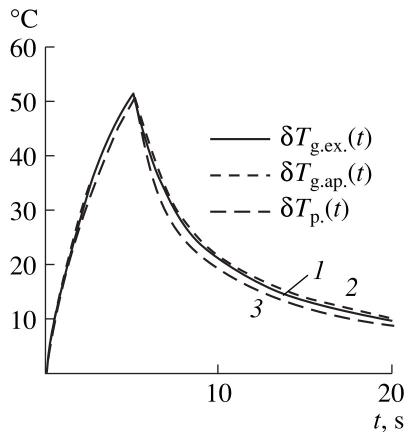

Fig. 3. Time variation of the maximal temperature increment in the beam focus for the Gaussian beam: results of the calculations by the (*1*) exact and (*2*) approximate solutions; (*3*) the same dependence for an equivalent beam from a piston-type radiator.

to Eqs. (6) and (7) and correspond to the analyzed stage of heating or cooling.

The precision of the obtained analytical approximations is demonstrated in Fig. 3, which presents the time variation of the maximal temperature calculated by the exact Eq. (14) and approximate Eq. (15) at the point $r = 0$, $z = R$ under the five-second action (the heating stage) of a Gaussian ultrasonic beam with the parameters $a_g = 5/\sqrt{2}$ cm, $R = 10$ cm, and $I_0^{(g)} = 4$ W/cm^2 and further cooling after the beam is turned off. One can see that these two results almost coincide. The approximation given by Eq. (16) provides the same high precision in the focal plane. Figure 3 also presents the analogous dependence obtained from Eqs. (12), (9), and (8) for an equivalent (in the sense of Eqs. (13)) ultrasonic beam from a focusing piston-type transducer with the corresponding parameters $a_p = 5$ cm, $R = 10$ cm, and $I_0^{(p)} = 1$ W/cm^2. The closeness of the curves obtained for the two models of ultrasonic beams demonstrates the efficiency of the introduced equivalence condition (11). We also note the useful practical conclusion following from the result shown in Fig. 3. One can see that, at the cooling stage, which is long relative to the heating time, the temperature remains sufficiently high and far exceeds the safety threshold of 43°C. Therefore, it is necessary to take into account the sufficiently long stage of cooling in analyzing the mode of multiple ultrasonic action on the biological tissue.

The approximate expressions (15) and (16) make it possible to analyze and almost instantly calculate many practically useful dependences, for example, the dynamics of the time variation of the temperature profiles along the *z* axis and far from the *r* axis in the focal plane or the time dependence and the spatial profiles of temperature as functions of the basic parameters of the radiator (R, a, f) and the medium (κ, α). A very informative dependence that can be obtained from Eq. (15) is the dynamics of the characteristic dimension along the *z* axis of the region bounded by an isotherm with the preset temperature excess δT_0, for example, the region with the boundary of the biological threshold temperature 43°C where $\delta T_0 = 43 - 37 = 6$ (°C). Expressing the dependence $\delta z(t)$ from Eq. (15) for the heating stage at a constant value of δT, we obtain

$$\delta z_{\delta T_0} \equiv z_{\delta T_0} - R = \pm\frac{R^2}{l_d}\sqrt{\frac{t}{t_{\delta T_0}} - 1},$$

where $t_{\delta T_0} = \dfrac{a^2R^2}{8\kappa l_d^2}\left[\exp\left(\dfrac{4\kappa\rho C}{\alpha I_0 a^2 e^{-2\alpha R}}\delta T_0\right) - 1\right]$ is the time for initially attaining a preset temperature in the center of the region.

Up to now, the time–space dynamics of the quantity fundamental for the theory of any thermal process, i.e., temperature, or, more precisely, the temperature increment δT relative to the equilibrium temperature equal to approximately 37°C, has been considered. However the result of a thermal action on biological tissue in the form of either its functional change, or termination of its vital functions, or a direct thermal destruction up to burning out is determined not by the absolute change in the temperature of this region of the biological tissue δT but by a certain integral characteristic of this quantity and the total time of the ultrasonic action on the tissue (the time of exposure or insonification). This characteristic is called the thermal dose, or the equivalent time of heating. The significance of such a characteristic is intuitively clear, and its analog is the radiation dose in the case of radiation damage to a live organism. In the case of heating of a biological tissue, it is necessary to proceed from the fact that there is a certain empirically determined threshold value of temperature, which is equal approximately to 43°C. Starting from this value, the temperature action lasting for a certain time leads to an impairment of the vital functions of the tissue cells. This exposure time for the indicated threshold temperature is about 100 min. It is proposed to recalculate the real exposure time t_T at another, higher value of temperature T [9] into the equivalent (with respect to the threshold temperature) exposure time $t_{eq.43}$ according to the empirical formula[3]

$$t_{eq.43}\,(\text{min}) = 2^{T-43}t_T\,(\text{min}). \tag{17}$$

This simple expression provides an opportunity, by the known effects of heating of biological tissue at the temperature 43°C during the time $t_{eq.43}$, to expect the same result (for example, termination of the vital functions of cells) in the case of a thermal action with the tempera-

---

[3] A theoretical basis for such a dependence is the comparability with the Arrhenius reactions whose rate depends exponentially on the reciprocal absolute temperature.

ture T during the time t_T. Equation (17) is easily generalized for the case of varying temperatures:

$$t_{eq.43}(r, z, t) = \int_0^t 2^{T(r, z, t') - 43} dt'. \qquad (18)$$

The integration in Eq. (18) embraces a very short initial time interval (see Fig. 3) with the temperature $T < 43°C$ ($\delta T < 6$). In this case, according to [9], it is necessary to take the base of the exponential integrand function equal to four. However, just the small duration of the indicated interval and the temperature far exceeding the threshold value almost within the whole integration interval make it possible to use Eq. (18) with a constant base in the integrand without any noticeable error. The surfaces $t_{eq.43}(r, z)$ = const determine the boundaries of the volume regions that differ in the result of the thermal ultrasonic action, including the boundary $t_{eq.43}(r, z) = 100$ that confines the region of the cells destructed by heat. Figure 4 shows the regions corresponding to different doses (equivalent times) that are calculated proceeding from Eq. (18) on the basis of Eq. (14) for the case of the propagation of a Gaussian focused ultrasonic beam with the characteristic parameters I_0 = 4 W/cm^2, $a = 5/\sqrt{2}$ cm, R = 10 cm, f = 1 MHz, and t_T = 10 s in biological tissue, the common center of the regions almost coinciding with the focus. The central dark region corresponds to the spatial scales of thermal destruction of biological tissue. The light boundary marks the focal region for the intensity where it decreases to half of its maximal value.

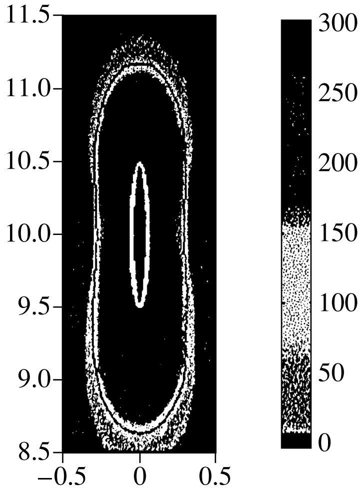

Fig. 4. Spatial distribution of thermal doses after 10 s of heating by a Gaussian focused beam. The dark central region corresponds to thermal destruction of the biological tissue.

Thus, the results of the determination of spatial boundaries of thermal doses with preset equivalent times at these boundaries and the determination of the dynamics of these boundaries are most informative and illustrative for the prediction and optimization of thermal action on biological tissues. However, the numerical determination of the temperature fields as a function of spatial and time variables from the exact solution (and, especially, their determination from the initial Eq. (1)) for further numerical integration in Eq. (18) make this procedure very laborious in the sense of both the computation time and the required computer memory. Moreover, important dependences of the characteristic times and time dynamics of the zone of thermal destruction of tissue on the beam (radiator) parameters cannot be determined from the complex and implicit Eqs. (8) and (18). Taking this into account, we can see that the obtained analytical approximations (15) and (16) are very important for the prediction estimates of these characteristics and dependences. For example, the substitution of Eq. (15) into Eq. (18) provides an opportunity to obtain an explicit dependence of thermal doses along the z axis on all possible parameters in the case of heating:

$$t_{eq.43}(z, r = 0, t) = \frac{F}{512\kappa G}\left[\left(1 + \frac{8\kappa t}{F}\right)^G - 1\right],$$

where

$$F = a^2\left[\left(\frac{\delta z}{R}\right)^2 + \left(\frac{R}{l_d}\right)^2\right], \text{ and } G = \frac{\alpha I_0 a^2 e^{-2\alpha R}}{4\rho C\kappa}\ln 2 + 1.$$

Substitution of Eq. (16) into Eq. (18) makes it possible to obtain analogous dependences along the r axis in the focal plane with the help of a single numerical integration.

Thus, the utilization of the Gaussian focused beam model taking into account the introduced concept of its equivalency and comparability with other models of amplitude distribution provides an opportunity to obtain the time–space dependences of thermal characteristics (temperature fields and thermal doses) in an explicit analytical form, which is necessary for predicting the effectiveness of the procedure of ultrasonic surgery (thermal destruction) and for optimizing this procedure depending of the basic parameters of the equipment and the biological tissue. The exact and approximate solutions obtained above for the thermal conduction equation in the axisymmetric case are also useful for analyzing other thermal processes.

ACKNOWLEDGMENTS

This work was supported by the Russian Foundation for Basic Research, the INTAS, and the program "Universities of Russia."

REFERENCES

1. C. J. Diederich and K. Hynynen, Ultrasound Med. Biol. **25**, 871 (1999).
2. A. K. Burov, Dokl. Akad. Nauk SSSR **106**, 239 (1956).
3. A. K. Burov and G. D. Andreevskaya, Dokl. Akad. Nauk SSSR **106**, 445 (1956).
4. H. H. Pennes, J. Appl. Physiol. **1**, 93 (1948).
5. P. M. Meaney, R. L. Clarke, G. R. ter Haar, and I. H. Rivens, Ultrasound Med. Biol. **24**, 1489 (1998).
6. V. I. Levin and Yu. I. Grosberg, *Differential Equations of Mathematical Physics* (GITTL, Moscow, 1951).
7. A. P. Prudnikov, Yu. A. Brychkov, and O. I. Marichev, *Integrals and Series. Special Functions* (Nauka, Moscow, 1983).
8. M. B. Vinogradova, O. V. Rudenko, and A. S. Sukhorukov, *The Theory of Waves*, 2nd ed. (Nauka, Moscow, 1990).
9. S. A. Sapareto and W. C. Dewey, Int. J. Radiat. Oncol. Biol. Phys. **10**, 787 (1984).

Translated by M. Lyamshev

Acoustical Physics, Vol. 47, No. 3, 2001, pp. 341–346. Translated from Akusticheskiĭ Zhurnal, Vol. 47, No. 3, 2001, pp. 401–406.
Original Russian Text Copyright © 2001 by Mikryukov, Popov.

Effect of the Refraction of Sound Waves in the Sediment Layer on the Sound Field Levels in the Ocean at Short Ranges

A. V. Mikryukov and O. E. Popov
Andreev Acoustics Institute, Russian Academy of Sciences, ul. Shvernika 4, Moscow, 117036 Russia
e-mail: bvp@akin.ru

Received March 1, 2000

Abstract—On the basis of the results of an acoustic experiment, which was carried out in the Indian Ocean with the use of explosive sources of sound, the effect of the refraction of sound waves in the sediment layer on the levels and the structure of the sound field formed in the water column at short ranges, namely, in the first geometric shadow zone and in the insonified zone below the channel axis, is considered. The length of the acoustic track under study is 45.0 km, and the frequency range is 10–500 Hz. © *2001 MAIK “Nauka/Interperiodica”.*

The main factor that determines the sound field levels in the geometric shadow zones of the ocean is the reflectivity of the ocean bottom. Among the variety of structures responsible for the variability of the “illumination” levels in the shadow zones, a thick layer of unconsolidated sediments underlying the water–bottom interface is of special interest. The presence of a positive vertical gradient of sound velocity in this layer causes a refraction of sound waves in the bottom. This effect substantially increases the contribution of the bottom arrivals to the total sound field levels in the water column. The numerous abyssal planes of the ocean bed are covered by thick silt layers, and the refraction of sound waves in the sediment layer must manifest itself in one or another way in the results of acoustic measurements performed in these regions [1–4]. Therefore, to calculate the sound fields in such regions, one has to choose an adequate model of the ocean bottom [5].

The phenomenon under discussion is most pronounced in the Bengal debris cone in the Indian Ocean where the thickness of the sediment layer reaches 4 to 5 km in the central part of the region (at the equator) and decreases down to 100–200 m toward the periphery (to the south of 8° S). The vertical gradient of the sound velocity in the 1-km-thick upper part of the sediment layer is within 0.86–1.87 s^{-1} [6].

Earlier, we already studied the effect of the sound wave refraction on the long-range sound propagation in this region [7]. The effect manifested itself as the partial illumination of the shadow zones at low frequencies. Below, we will consider the contribution made by the signals interacting with the sediment layer to the sound field levels at short ranges, namely, in the first shadow zone and in the insonified region below the channel axis.

The experiment was carried out on a 45-km-long acoustic track oriented along the 6° S latitude. The sound velocity profile in the region of the experiment was typical of the tropical zone of the Indian Ocean (Fig. 1a). The 30-m-thick upper layer was a mixed water layer with a sound velocity of 1541.1 m/s at the surface and with a small positive sound velocity gradient. Below, a 150-m-thick water layer with a sharp negative gradient of the sound velocity was observed. The sound velocity minimum was weakly pronounced. At the depths from 900 to 1500 m, a pseudo-isovelocity layer occurred with a mean velocity of about 1491.0 m/s. Near the bottom, at a depth of 5000 m, the sound velocity was practically equal to the sound velocity at the surface (1541.6 m/s), which resulted in a considerable effect of the bottom on the sound field formation in the ocean. The depth dependence of the sound velocity was practically the same along the entire acoustic track. The

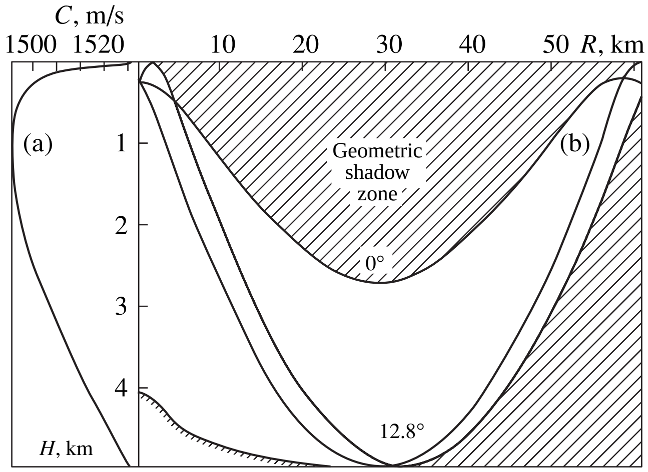

Fig. 1. (a) Depth dependence of the sound velocity and (b) the ray pattern illustrating the propagation conditions in the region of the experiment.

1063-7710/01/4703-0341$21.00 © 2001 MAIK “Nauka/Interperiodica”

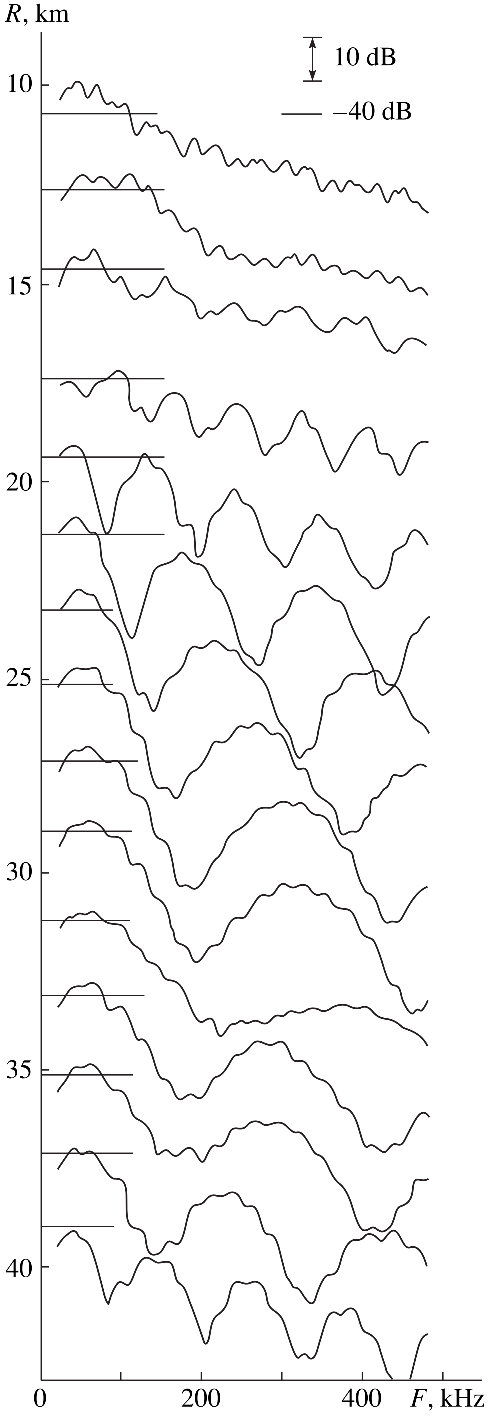

Fig. 2. Changes in the form of the smoothed spectra of two signals (a water-only signal and a surface reflected or refracted signal) with increasing distance. The reception depth is 3000 m. The segments of horizontal lines indicate the distances from which the signals are received and the spectrum level corresponding to –40 dB.

measurements were performed for the depths from 0 to 2000 m. For greater depths, the values of the sound velocity were taken from archival data and refined in the course of the experimental data processing.

According to the echo sounding data, the depth of the ocean varied along the track from 4.0 to 5.0 km. Below the water–bottom interface, the echo sounding records revealed a sediment layer 200–250 m thick.

The receiving ship, which carried isolated sound receivers lowered to the depths 250 and 3000 m, lay at the starting point of the track. The transmitting ship started its motion from the site of the receiving ship in the western direction. When moving at full speed, it dropped charges with hydrostatic detonators, the weight of each explosive charge being 2.88 kg. The charges were planned to explode at a depth of 200 m at intervals of 1.0 km along the whole path. The first charge exploded at a distance of 0.9 km and the last charge at a distance of 45.3 km from the receiving ship. The duration of the experiment was 2.5 h.

The propagation conditions for the selected transmission and reception depths were such that, for the distances under study, the lower receiver positioned below the channel axis fell in the insonified zone, whereas the upper receiver fell in the geometric shadow zone beginning from distances of about few kilometers (Fig. 1b).

The first stage of the experimental data processing was related to the refinement of both the geometry of the experiment and the parameters of the sound channel. The transmission depth measured by the period of the gas bubble fluctuation was 189 ± 5 m.

To refine the archival values of the sound velocity in the ocean at the depths exceeding 2000 m, we analyzed the variations that occurred with increasing distance in the smoothed spectrum of two water signals (a direct signal and a signal reflected from the surface and, at large distances, refracted in the upper water layer) recorded by the lower hydrophone (Fig. 2). For each of the spectra shown in Fig. 2, the distance from which the signal was received and the spectrum level corresponding to –40 dB are indicated by segments of horizontal lines. A monotone increase in the period of the spectrum oscillations with distance is caused by a decrease in the time delay between the two signals; its monotonicity is violated at a distance of about 32.0 km from the source. This means that a signal propagating along a ray leaving the source in the downward direction and having a turning point at the reception depth arrives at the lower horizon. With a further increase in distance, the ray directed downwards and reaching this horizon will have a turning point at longer distances and below the reception depth. As a result, the time delay between the signals leaving the source upwards and downwards and arriving at the reception point will increase, and, correspondingly, the period of oscillations of their spectrum will decrease, which we observe in the plots presented in Fig. 2.

The calculations showed that, to achieve a better agreement with the experimental data, the sound velocity at the depth 3000 m should be taken by 1.2 m/s less than predicted by the archival data. Therefore, we introduced some corrections in the positive gradient of the sound velocity at large depths.

In discussing the wide possibilities of the acoustical methods of monitoring the ocean medium, one should also mention that, from an analysis of the changes in the spectra shown in Fig. 2, one can derive the information on the sound velocity gradient above the transmission horizon, as well as on the position of the lower boundary of the subsurface sound channel. The estimates of these depths can be obtained from the analysis of the spectrum of the aforementioned water signals after this spectrum is extrapolated to the origin of coordinates, i.e., to 0.0 Hz. Quantitatively, this can be explained as follows. For two signals arriving at the reception point, their total intensity has the form

$$A^2 = A_1^2 + A_2^2 + 2A_1A_2\cos(\omega\Delta\tau + \Delta\varphi), \qquad (1)$$

where A_1 and A_2 are the amplitudes of the signals, ω is the circular frequency, $\Delta\tau$ is the time delay between the arrivals, and $\Delta\varphi$ is the phase shift. At the frequency 0.0 Hz, we obtain

$$A^2 = A_1^2 + A_2^2 + 2A_1A_2\cos(\Delta\varphi). \qquad (2)$$

When one signal is reflected from the surface, the phase difference $\Delta\varphi$ is close to π. In this case, the intensity $A^2 = (A_1 - A_2)^2$ will be minimal and the origin of coordinates will correspond to the minimum of the spectrum. When the signal ceases being reflected from the surface, the phase difference $\Delta\varphi$ sharply decreases and the spectrum level at the origin of coordinates will be characterized by some intermediate value.

The calculations show that, in the case under consideration, a ray leaving the source upwards and refracted at the lower boundary of the subsurface sound channel reaches the lower horizon of reception for the first time at a distance of 13.9 km. The experimental estimate based on a more detailed analysis of the spectra of the aforementioned signals yields this value for the interval between two points of the explosion: 13.15 and 14.15 km.

And finally, the last and most important refinement. Because of the considerable drift of the receiving ship in the northeasterly direction, it was necessary to take into account the changes in the bottom relief between the transmitting and receiving ships for each of the points of explosion. According to the calculations, the arrival times of the signals reflected from the bottom are highly sensitive (at a fixed reception depth) to the ocean depth. In Fig. 3, the circles show the experimental values of the time delays between the arrivals of singly bottom reflected signals received by the lower hydrophone and the arrivals of the "water-only" signals. (We note that, because the lower hydrophone is relatively far from the surface, the bottom arrival record from the lower hydrophone represents two signals arriving at the reception point with an interval of several seconds.) The dashed curves in the figure show the calculated dependences for several values of the ocean depth taken to be constant within the track. One can see that the experimental and calculated (for a constant depth) dependences noticeably differ from each other, especially at short distances. The solid curve, which agrees well with the experimental data, corresponds to the bottom relief corrected for each point of explosion (Fig. 1b). All subsequent calculations are performed with allowance for this bottom relief.

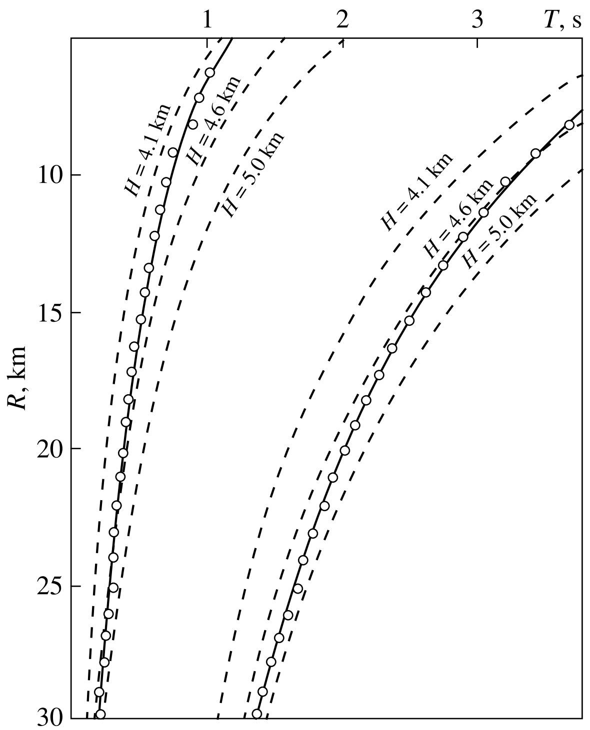

Fig. 3. Range dependence of the time delay between a singly bottom reflected and a water-only signal: the experimental data (circles) and the calculations for a sloping bottom (the solid lines) and for a constant depth *H* of the ocean (the dashed lines). The reception depth is 3000 m.

We begin the analysis of the structure of the bottom arrivals on the basis of the record obtained for the first pair of signals that experienced a single interaction with the bottom and were recorded by the lower hydrophone. For short ranges, from the records of the bottom arrivals in the case of a practically normal incidence, we can conclude that the sediment layer is a complex structure of thin layers with different thicknesses. The study of their variation with distance with the aim to obtain detailed information on the bottom structure proved to be impossible because of the large intervals between the points of transmission. No pronounced signal termination was observed in the experiment. At the same time, the records obtained for the initial third of the track reveal a signal reflected directly from the water–sediment boundary and arriving before all other signals at the point of reception from these distances. The changes observed in the amplitude of this signal with increasing distance suggest some conclusions.

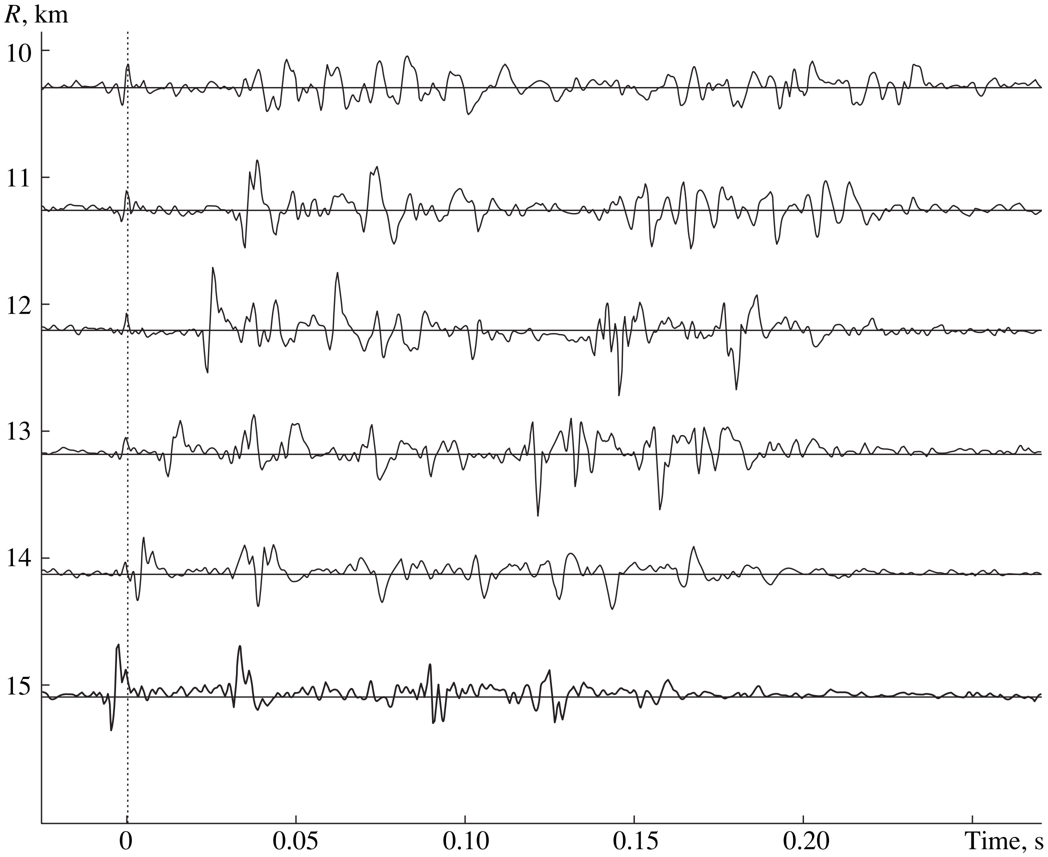

Fig. 4. Form of the bottom arrival recorded by the lower hydrophone within the distances 10–15 km. The zero on the time axis corresponds to the arrival of the signal reflected from the water–bottom boundary.

Within a distance of 11.2 km, the amplitude of the signal is practically constant and, then, it begins to decrease (Fig. 4). Starting from the distance 15.05 km, an intense arrival from the bulk of the sediment layer begins to overtake the signal that is mirror reflected from the water–bottom boundary, and the following variation of the amplitude of the latter signal cannot be observed any longer because of the arising interference effects. However, even with these limited data, we can conclude that the observed variations in the amplitude of the bottom reflected signal correspond to the case when the sound velocity in the uppermost part of the sediment layer is less than the sound velocity in water near the bottom. Beginning from the distances exceeding 30 km, the bottom arrival ceases being resolvable in time with the arrival of the water-only signals. Therefore, it is impossible to observe the sharp increase that occurs in the amplitude of the signal reflected from the water–bottom boundary at low grazing angles, this increase being typical of the situation under study. However, one can assume that the total internal reflection from the water–bottom boundary will not be observed and all sound energy incident on the ocean bottom will easily penetrate into the bottom at any grazing angles.

As was mentioned above, starting from the distance 15.05 km, the signal reflected from the water–bottom boundary begins to lag behind the intense signal arriving after the interaction of sound with the sediment bulk. From the data reported in the literature and from the results of our numerical experiments with the simplest bottom models, it follows that such a situation should occur in the presence of two factors: a sloping water–bottom boundary and a positive vertical gradient of the sound velocity in the bulk of a fairly thick sediment layer.

The presence of the slope of the water–bottom boundary was already established above. The presence of a vertical sound velocity gradient is revealed by analyzing the form of the signals that interacted with the sediment layer. The gradient of sound velocity in the sediment layer causes a refraction of sound waves in it, which results in the formation of a caustic. It is known that a signal propagating along a ray touching a caustic will acquire an additional phase shift of $\pi/2$; i.e., it will take the form of the derivative of the initial signal [4]. Figure 5 shows the forms of the shock wave of a water-only signal, its derivative, and a signal that returned into the water layer after interacting with the sediment layer. The presence of the phase shift equal to $\pi/2$ in the latter signal relative to the initial signal is evident, which testifies to the existence of a positive gradient of the sound velocity in the sediment layer and, as a consequence, to the refraction of sound waves in it.

To estimate the effect of the bottom on the sound field levels at short ranges in the ocean, we analyze the results obtained by recording the signals from the lower hydrophone, which are well resolved in time. Figure 6 presents the range dependences of the sound intensity for a central frequency of 200 Hz for water-only signals and for the first pair of signals that experienced a single interaction with the bottom. The analysis bandwidth is 50 Hz. From these dependences, one can see that, beginning from the distances 10–12 km, a considerable and steep increase in the level of the bottom arrival is observed with its maximum being reached at a distance of 13 km. For the distances that correspond to the maximal level of the bottom arrival, the intensity of the sound field formed by the bottom arrivals exceeds the intensity level of water-only signals. The superposition of the water and bottom signals leads not only to an increase in the total field, but also to flattening of the minimums of its interference pattern.

The complex oscillatory behavior of the bottom arrival level in the course of its decrease indicates that this arrival, in turn, is a superposition of signals arriving along two kinds of rays: the rays refracted by the sediment layer and the rays reflected from the water–bottom boundary.

The energy that returns to the water column after the interaction of the sound waves with the sediments penetrates into the upper layers of the ocean and causes an illumination of the shadow zone. The maximal level of the sound field at the upper reception horizon (250 m) and, after the sound reflection from the surface, again at a depth of 3000 m is observed at the distances 17 and 21 km, respectively. All three aforementioned distances, i.e., 13, 17, and 21 km, are connected by a ray that leaves the source at an angle of 31.5°. Assuming that the vertical gradient of the sound velocity in the sediment layer is about 1.0 s^{-1}, we can infer that the turning point of a ray with such an exit angle must lie 200 m below the water–bottom boundary (where the sound velocity is 1.715 km/s). This result agrees well with the data on the thickness of the sediment layer along the track.

Since the bottom in the region under study has a complex structure with a sloping boundary and, also, because of the absence of reliable information on the geological–acoustical characteristics of the bottom, we do not perform any numerical calculations of the sound field levels to compare them with the experimental data. However, it is easy to show that, in the case under study, the mean sound field level in the shadow zone proves to be fairly close to the level of the sound field formed as a result of the mirror reflection from a homogeneous liquid halfspace with the longitudinal wave velocity 1.715 km/s (in agreement with the exit angle specified above, i.e., 31.5°). Figure 7 presents the calculated range dependence of the sound intensity at the upper reception horizon for such a bottom model and the experimental data for a central frequency of 400 Hz with the analysis in a 1/3-octave band. The experimental and calculated levels of sound intensity were correlated by matching the corresponding levels for the water-only signals at the lower reception horizon at the given frequency. One can see that the mean sound field level in the shadow zone is predicted with fair accuracy. This closeness of the mean levels clearly demonstrates the substantial contribution of the bottom refracted arrivals to the levels of the sound field in the shadow zone. At the same time, the oscillatory behavior of the experimental curve indicates that the real bottom structure is much more complicated than the structure adopted in the computational model.

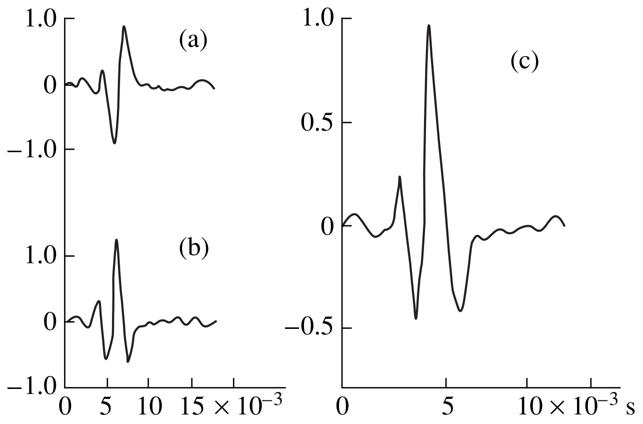

Fig. 5. Oscillograms of the signals: (a) the form of the shock wave of the initial signal (a water-only signal at a distance of 6.7 km), (b) the derivative of the shock wave, and (c) the shock wave of the signal that interacted with the bulk of the sediment layer. The reception depth is 3000 m.

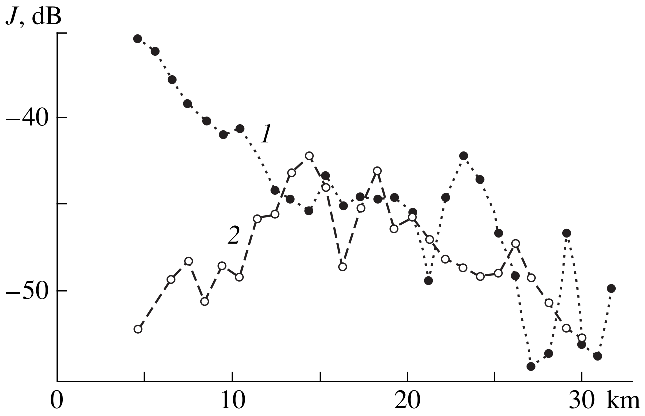

Fig. 6. Range dependence of the sound intensity at a frequency of 200 Hz in the insonified zone (*1*) for water-only signals and (*2*) for signals that experienced a single interaction with the bottom. The analysis bandwidth is 50 Hz.

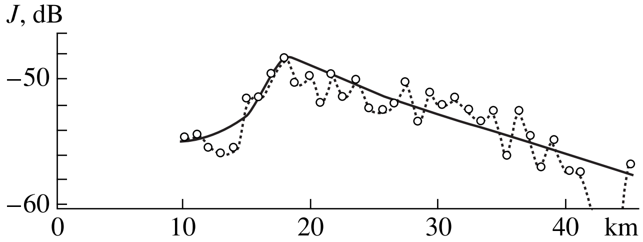

Fig. 7. Range dependence of the sound intensity in the geometric shadow zone: the experimental data (circles) and the calculation for the bottom model in the form of a liquid halfspace with a sound velocity of 1715 m/s. The central frequency is 400 Hz with the 1/3-octave bandwidth.

Summarizing the results of our study, we note that the refraction of sound waves in the sediment layer considerably affects the formation of the energy and time structure of the sound field at low frequencies. Firstly, we observe a noticeable increase in the sound field level in the insonified zone below the channel axis and a considerable illumination of the shadow zone. According to our estimates, in the insonified zone, within the distances 10–20 km, the increase in the sound field level varies from 3 dB in the frequency range 50–250 Hz to 1.5 dB at a frequency of 500 Hz. The mean sound field level in the shadow zone proves to be close to the field level produced by the mirror reflection of sound from a bottom in the form of a homogeneous halfspace with the longitudinal wave velocity far exceeding that observed in the upper layers of the real bottom. The critical angle of reflection from such a halfspace is close to the exit angle of the ray for which the refraction in the sediment layer begins 200 m below the water–bottom boundary. Secondly, the decrease in the sound field level with distance in the shadow zone has the form of an oscillatory dependence, which is a result of the interaction of two signals: the signal reflected from the water–bottom boundary and the signal refracted in the bulk of the sediment layer. Thirdly, in the insonified zone, a similar oscillatory decrease in the level of the bottom arrivals with distance leads to a transformation of the interference pattern formed by the water signal arrivals and to a flattening of the minimums of this pattern.

ACKNOWLEDGMENTS

This work was supported by the Russian Foundation for Basic Research, project no. 00-02-17694.

REFERENCES

1. R. F. Christensen, J. A. Frank, and W. H. Geddes, J. Acoust. Soc. Am. **57**, 1421 (1975).
2. S. R. Santaniello, F. R. Napoli, R. K. Dullea, and P. D. Herstein, Geophysics **44**, 1922 (1979).
3. G. V. Frisk, J. A. Doutt, and E. E. Hays, J. Acoust. Soc. Am. **80**, 591 (1986).
4. D. P. Knobles and P. J. Vidmar, J. Acoust. Soc. Am. **79**, 1760 (1986).
5. A. J. Robins, J. Acoust. Soc. Am. **103**, 1337 (1998).
6. R. E. Houtz, in *Bottom-Interacting Ocean Acoustics*, Ed. by W. Kuperman and F. Jensen (Plenum, New York, 1981; Mir, Moscow, 1984), Chap. 7.
7. A. V. Mikryukov and O. E. Popov, Akust. Zh. **42**, 672 (1996) [Acoust. Phys. **42**, 592 (1996)].

Translated by E. Golyamina

Acoustical Physics, Vol. 47, No. 3, 2001, pp. 347–352. Translated from Akusticheskiĭ Zhurnal, Vol. 47, No. 3, 2001, pp. 407–412.
Original Russian Text Copyright © 2001 by Potapov, Rodyushkin.

Experimental Study of Strain Waves in Materials with a Microstructure

A. I. Potapov and V. M. Rodyushkin

Blagonravov Institute of Mechanical Engineering, Nizni Novgorod Branch, Russian Academy of Sciences,
ul. Belinskogo 85, Nizhni Novgorod, 602024 Russia
e-mail: wvs@dynamo.nnov.ru

Received June 8, 1999

Abstract—Transmission of a pulse with a velocity different from the velocity of longitudinal waves is observed in a material with a microstructure. It is demonstrated that, in the presence of an internal structure, the wave properties of a medium acquire some particular features that cannot be described in terms of the classical theory of elasticity. *© 2001 MAIK "Nauka/Interperiodica".*

Investigation of the dynamic behavior of materials with microscopic inhomogeneities cannot be conducted in full in the framework of the classical models of continuous media, which ignore the material structure. Many real materials whose properties are determined by their supermolecular structure, i.e., by dislocations, grains, residual internal stress, and microscopic cracks [1–4], belong to such complex media, as do granular and reinforced materials [5]. Despite the difference in molecular composition, the internal space of almost all optically opaque structural materials is available for waves of a mechanical nature. Therefore, the acoustic sensing techniques with different kinds of action on the material (pulsed or continuous, monochromatic, polychromatic, or random) are often used to study the internal structure and the physical and mechanical properties of real media [6–11].

The results of acoustic sensing of a material are used as a rule to solve two problems. The first one is the evaluation of the applicability range of unconventional, newly introduced models of the medium behavior. In this case, the mathematical model of the material dynamics is assumed to be known and, hence, the law of the conversion of the action ξ to the response $\eta = \Psi \times \xi$, where Ψ is the conversion function, is also known. An experiment confirms or refutes the existence of a desired physical phenomenon, e.g., a new type of waves or some other feature, predicted in the framework of the proposed model [8–12].

The second problem is the development of a theoretical model of a medium according to the results of experimental observations. In this case, one has to solve an inverse problem: the determination of the conversion function Ψ by the acoustic response η at a preset external action ξ. Solving this problem without *a priori* information on the function Ψ is very difficult. Therefore, artificial media are used in the experimental investigation of strain waves in a material with a microstructure. Such an approach was used by different researchers [8, 9, 13, 14] who prepared a special artificial composite medium for testing the micropolar theory of elasticity.

In our experiments, to study strain waves in a material with a microstructure, we used a pulsed action ξ on the material and observed the response η of the latter to this action. Dynamic tests were conducted according to the Kol'skiĭ technique using the Hopkinson split rod (Fig. 1). The medium under investigation in the form of a cylindrical sample with the diameter 20 mm was installed between two steel cylinders. A striker (a steel cylinder with a length from 50 to 150 mm) was accelerated by a light-gas gun to the velocity 10–20 m/s and struck the end of a steel rod to excite a one-dimensional strain wave in it. A pair of strain gauges positioned on the rods at the points x_1 and x_2 symmetrically with respect to the sample detected the waves that were incident on the sample, transmitted through it, and reflected from it. The signals from the gauges were recorded by a digital oscilloscope. The digitization time was 50 ns, and the total length of the dynamic process that could be recorded was 500 μs or 1024 points. The data obtained were subjected to the necessary computer processing. A detailed description of the experimental technique can be found in [15].

In the simulation of a dynamic process, the wave propagating in the sample and the measuring cylinders was assumed to be one-dimensional and the properties of the sample and the cylinders were taken to be linear. The prediction of the dynamics is based upon the space–time theory of wave propagation [16, 17]. If we describe the pulse propagation in the coordinates x, t by taking into account the rod dimensions and the velocity of wave propagation in the material (Fig. 2), the formation of a wave pattern in the sample and cylinders becomes apparent and, therefore, it becomes clear how to obtain the information on the velocity of the wave

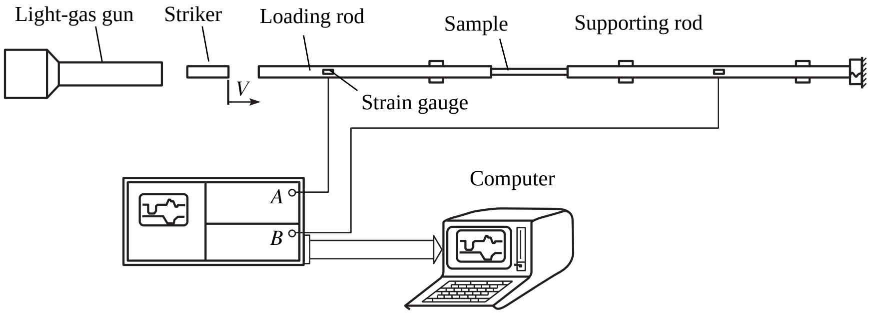

Fig. 1. Experimental setup.

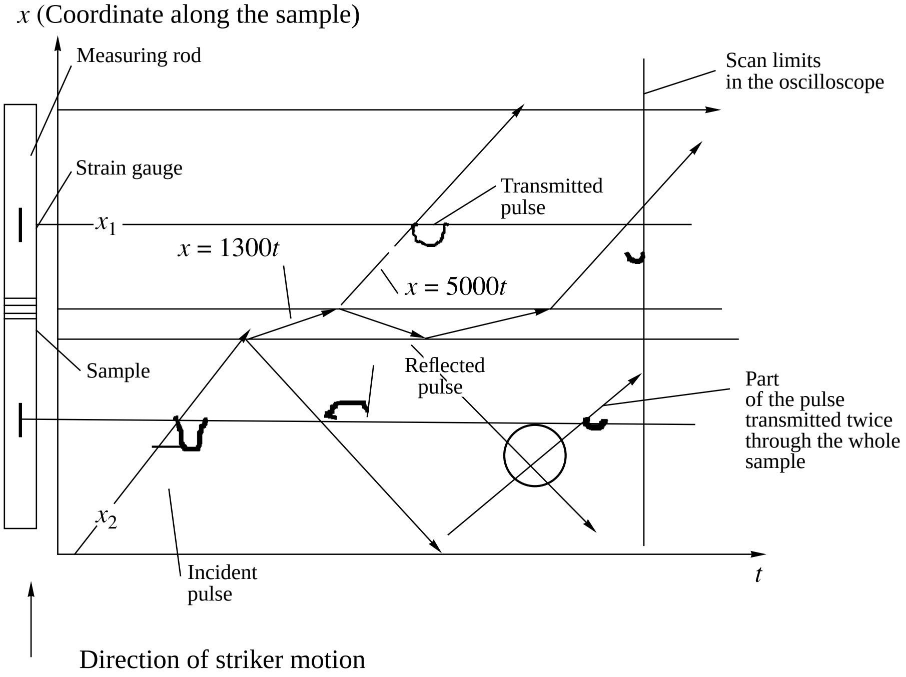

Fig. 2. Schematic representation of the space–time behavior of a signal in the sample and in the measuring rods.

motion in the sample under the effect of the pulse $\xi(x_0, t)$ from the obtained oscilloscope records. Part of the incident pulse $\xi(x_0, t)$ is reflected from the front end of the sample because of the difference in the wave impedances of the materials of the measuring rod $Z_r = \rho_r C_r$ and the sample $Z_{sp} = \rho_{sp} C_{sp}$, which in our case are equal to $Z_r = 46 \times 10^6$ kg/(m^2 s) and $Z_{sp} = 3.9 \times 10^6$ kg/(m^2 s), respectively. The coefficients of single reflection R and transmission T for a signal incident on the contact boundary are calculated according to the formulas [16]

$$R = (Z_2 - Z_1)/(Z_2 + Z_1), \quad T = 1 - R.$$

Here, Z_2 is the impedance of the medium into which the wave enters and Z_1 is the impedance of the medium from which the wave goes out. A pulse transmitted into the sample arrives at the rear end and also gets divided into the reflected and transmitted parts equal to $R(1 - R)$ and $(1 - R)^2$, respectively. We note an important fact that needs to be taken into account while interpreting the experimental oscilloscope records. A compression (or tension) pulse changes its polarity depending on the direction of its propagation, i.e., from which medium it arrives and on which medium it is incident. As the sample impedance is always smaller than the impedances of the steel rods ($Z_{sp} \leq Z_r$), the coefficient of reflection R from the front end of the sample (i.e., from a soft boundary) is negative and the reflected pulse changes its polarity. In the case of the reflection from the rear end, the reflection coefficient is $R > 1$ and the polarity of the reflected pulse does not change. It is evident that the response curve of the strain gauge positioned at the point x_1 consists of the sum of the oscilloscope records of the incident signal $\xi_1(x_1, t)$, the signal reflected from

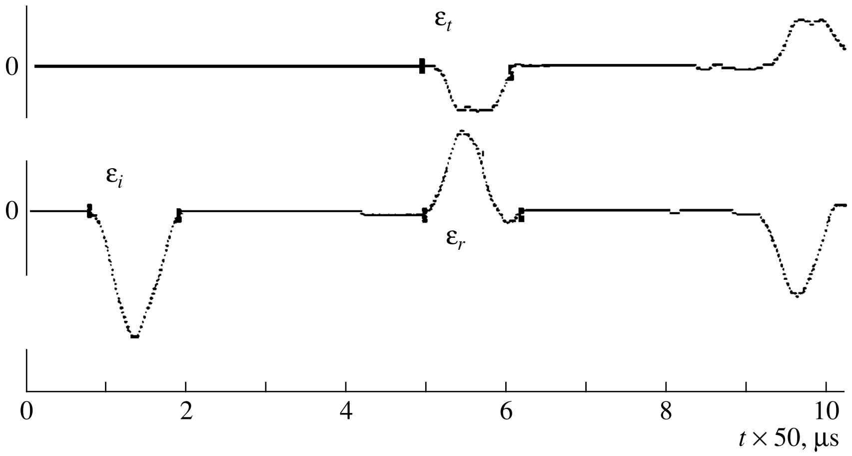

Fig. 3. Response of the reference sample made of an aluminum alloy.

the front end of the sample $\xi_2(x_1, t)$, the signal reflected from the rear end and transmitted through the front end into the measuring rod $\xi_3(x_1, t)$, and so on, as long as the process of rereflection continues (Fig. 2). If the sample length is small, the delay $\tau_0 = l_{sp}/C_{sp}$ in the arrival time of the signal $\xi_3(x_1, t)$ relative to the arrival of the signal $\xi_2(x_1, t)$ is smaller than the pulse length τ and the summed parts $\xi_n(x_1, t)$ overlap. The complex structure of the response causes problems for the interpretation of the oscilloscope records and leads to the necessity of simulating the response form by calculating several first components. For example, in [13] this procedure is performed for seven rereflections of a signal. Thus, some incorrectness in interpreting the observed wave phenomena and the appearance of errors in calculating the wave velocities in the studied material become possible. The pulse velocity in the steel rod C_r is determined experimentally according to the time interval between the peaks of the signal that traveled a calibrating distance. In the case of a small length of the sample, a direct experimental determination of the velocity C_{sp} by the indicated technique is impossible. In such a situation, C_{sp} is usually estimated indirectly according to the known or measured parameters of the material, E and ρ. In order to measure directly the velocity C_{sp}, it is necessary to use a sample where the delay time is longer than the pulse length ($\tau_0 > \tau$). Such a condition contradicts the requirements of the Kol'skiĭ technique [14]. The classical version of the Kol'skiĭ technique presumes the use of short samples (with the length smaller than the diameter) in which a homogeneous mode of deformation is realized. We used both short and long samples in our experiments. In these samples, the mode of deformation is not homogeneous and represents a combination of overlapping traveling strain waves. Such a deviation from the Kol'skiĭ technique is acceptable, because the purpose of our study is the measurement of the kinematic and dynamic characteristics of the wave process in the sample rather than the determination of quasi-static stress–strain dependence in the material. In this connection, the requirements of the equality of stress and strain at the ends of the sample are unnecessary. The values of strain amplitudes in the reflected and transmitted pulses are calculated using the reflection and transmission coefficients according to the formulas

$$R = (1 - Y)/(1 + Y), \quad T = (1 - R), \quad (n = 1),$$

$$R_n = [4Y/(1 + Y)^2][(Y - 1)/(Y + 1)]^{2n-1},$$

$$T_n = [4Y/(1 + Y)^2][(Y - 1)/(Y + 1)]^{2n-1}; \quad (n > 1).$$

Here, $Y = Z_r/Z_{sp}$ is the ratio of the impedances of the steel rod and the sample and n is the number of the pulse transmission through (reflection from) the boundary.

The tested materials were an AMTs-type aluminum alloy, which was used as the reference medium without a granular microscopic structure, and a tungsten–epoxy composite consisting of an epoxy resin and ball-shaped tungsten pellets with the diameter from 0.02 to 0.2 mm. The composite density was about 2000 kg/m^3. Acoustic measurements of the velocity of longitudinal waves with the precision 50 m/s were conducted using the pulsed technique [8, 9], which consisted of the measurement of the travel time of an ultrasonic wave pulse at a known distance. A USN-52 device of the Krautkramer company was used for this purpose. The value of the velocity in the composite at the frequencies 1–5 MHz was $c_l \cong 1950$ m/s. The attenuation at these frequencies was 4.5–5 dB/cm. The dynamic modulus of elasticity, which was measured using a sample with the thickness 10 mm under strain up to 0.02 by the technique described in [14], was 4502 MPa. The results of independent tests of the sample made of the same material were well reproduced. Typical oscilloscope records of the sample response to a dynamic action are given in Figs. 3–6. Experiments were conducted using two samples made of the tungsten–epoxy composite: the first sample had the length 10 mm and the second one, 75 mm.

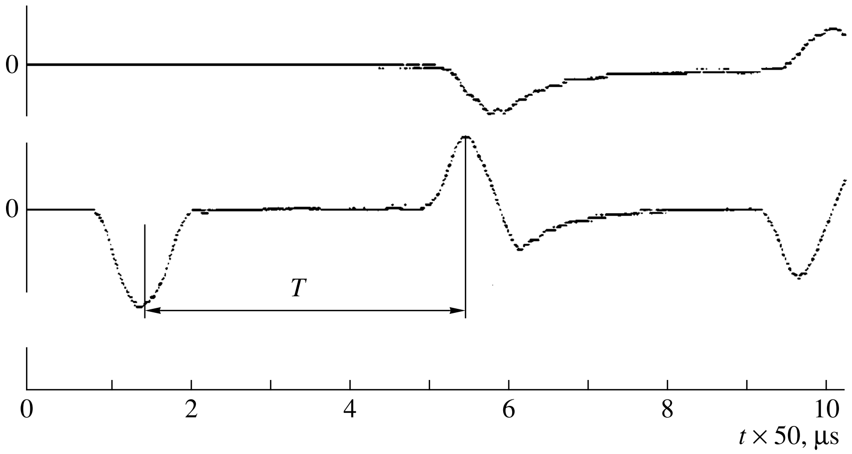

Fig. 4. Response of a sample made of a material with a microstructure; the sample length is 10 mm.

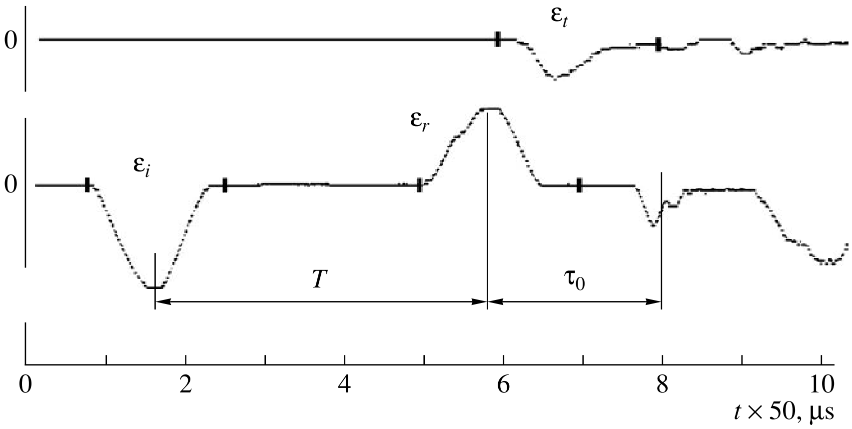

Fig. 5. Response of a sample made of a material with a microstructure; the sample length is 75 mm.

The samples were manufactured so as to satisfy the conditions $\tau_0 < \tau$ in the first case and $\tau_0 > \tau$ in the second case. The reference sample made of the aluminum alloy was used for the comparison of results. The upper oscilloscope records in the figures correspond to the signal from a resistance strain gauge installed at the point x_2, and the lower records, to the signal from the resistance strain gauge installed at the point x_1. The ordinate axis is calibrated in arbitrary units proportional to the strain, and the abscissa represents the time in μs. The measured time delay between the peaks of the incident and reflected pulses at the distance 1000 mm gives the value of the velocity in the rod $C_r = l_r/T = 5000$ m/s, which agrees well with the calculated value of $C_r = (E/\rho)^{1/2}$ for the rod material. Interference is observed in the measured signal because of the interaction of the surfaces of the rod and the sample (misalignment, roughness, nonflatness, etc.). One can see from the given figures that the dynamic response of the samples made of the tested materials (the aluminum alloy and the epoxy compound) is well predictable (Fig. 3). Small differences are caused by signal attenuation due to the dissipation in the medium. More essential differences between the predicted form of the response and the experiment arise in the case of samples made of a tungsten–epoxy composite. These differences are represented by not only the signal attenuation but also by the appearance of time misfits (Figs. 4, 5). Such effects were observed only in the samples made of the tungsten–epoxy composite and did not manifest themselves in the sample made of the aluminum alloy. This fact can be explained proceeding from the model of a micropolar medium in which the waves of microrotation can exist. Equations for a longitudinal wave u and the waves of microrotation ϕ in a centrally symmetric micropolar medium in the case of the wave propagation along the x axis have the form [7]

$$\rho\frac{\partial^2 u}{\partial t^2} - (\lambda + 2\mu)\frac{\partial^2 u}{\partial x^2} = \frac{\partial}{\partial x}(d_1 u_x^2 + d_2\phi_1^2 + d_3 u_x \phi_2),$$

$$J\frac{\partial^2 \phi_1}{\partial t^2} - (\beta + 2\gamma)\frac{\partial^2 \phi_1}{\partial x^2} + 4\alpha\phi_1 = \frac{\partial}{\partial x}(-2d_2\phi u_x), \quad (1)$$

$$J\frac{\partial^2 \phi_2}{\partial t^2} - (\gamma + \varepsilon)\frac{\partial^2 \phi_2}{\partial x^2} + 4\alpha\phi_2 = d_4 u_x \phi_2 - d_5 \phi_{1,x}\phi_2.$$

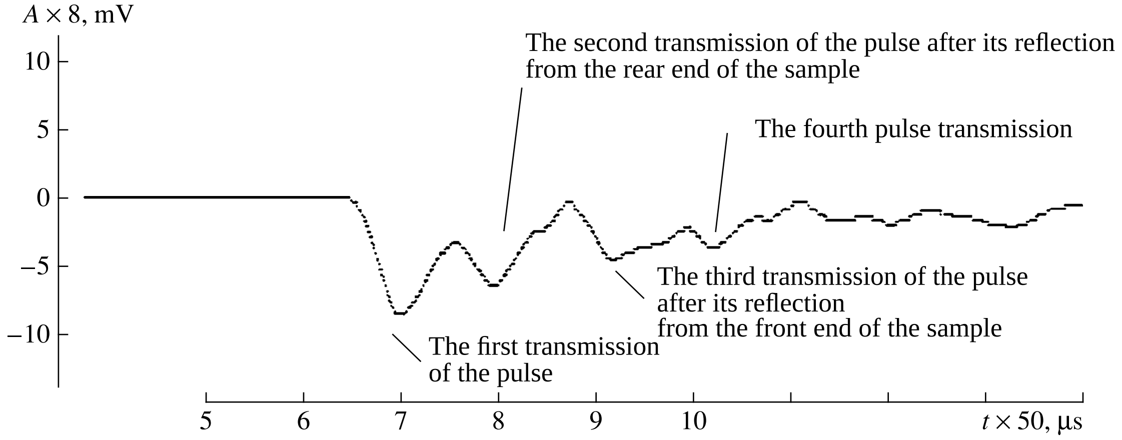

Fig. 6. Response of a sample made of a material with a microstructure. The signal is obtained from the resistance strain gauge installed on the sample in the longitudinal direction.

Here, u is the longitudinal displacement of the medium particles; ϕ_1 and ϕ_2 are the projections of the vector of particle rotation onto the x and y axes, respectively; J is the moment of inertia of a particle with respect to the axis passing through its center of gravity; λ and μ are the Lame constants; α, β, γ, and ε are the linear constants of microelasticity; and d_k are the nonlinear coefficients. It follows from Eq. (1) that the value of the propagation velocity of waves of microrotation (spin waves) depends on the direction of microrotations of particles and differs from the propagation velocity of longitudinal waves. A theoretical analysis of different cases of propagation of elastic waves in a medium with a microstructure can be found, e.g., in [7].

Since the samples were identical in design and the conditions of dynamic loading were also identical, it is natural to assume that the differences observed in the responses are caused by the particular features of the internal structure of the tested material. The differences in the responses include not only the signal absorption related to different dissipation of the oscillation energy in the material, but also the appearance of new additional oscillations in the oscilloscope record, which agrees with the experimental results [13]. The latter effect is caused by the existence of new types of oscillations predicted theoretically in a medium with an internal structure. These oscillations are excited in a sample as a result of dynamic action and propagate in it carrying the excitation energy with the velocities different from the velocity of longitudinal waves. The correctness of the interpretation of the observed distortions that is given in [13] is questionable, because it is grounded on the use of the experimental data obtained within a half-period of microrotation waves predicted in the medium. In order to demonstrate unambiguously the presence of new types of oscillations in a medium with an internal structure, it is necessary to investigate the arising distortions of a pulse by using samples of different lengths. Since part of the energy is carried along the sample with smaller velocity than the main pulse, the latter becomes spread, as can be seen in Fig. 4 (the short sample). After traveling a large distance in the medium, a part of the pulse produced by the new type of oscillations must separate from the main pulse and exist independently. In this case, the distortions observed previously must disappear from the main pulse. The experimental results confirm this assumption, as can be seen in Fig. 5.

The propagation velocity of a strain pulse in a material with a microstructure was determined using the technique described above. It follows from Fig. 5 that the velocity $C_{sp} = 2l_{sp}/\tau_0$ can be equal to 1200–1300 m/s. The spread in values is caused by the ambiguity in the determination of the reference point in measuring the propagation time of a pulse and by the influence of the pulse delay in the sample–rod transition layer on the result. The analysis of the dynamics of the pulse propagation in the sample provides an opportunity to decrease the influence of the factors mentioned above on the results of measurements. The velocity of the pulse propagation was calculated at the length $4l_{sp}$ (taking into account the multiple reflection) with the precision 50 m/s on the basis of the oscilloscope records of signals from the resistance strain gauges installed on the sample (Fig. 6). The resulting value of the velocity is equal to 1300 m/s, which does not correspond to the velocity of longitudinal waves in these materials. In addition, a separation of the action pulse into two components is observed, which is evidence of the fact that the pulse is carried by two types of oscillations that differ in velocity. The difference in velocities was equal to the value comparable with the measurement error. The nature of this effect and its detailed quantitative evaluation are the subject of further experimental studies.

Thus, we observed experimentally the propagation of an elastic pulse in a material with a microstructure. The propagation velocity of the pulse was found to differ from the velocity of longitudinal waves. It was demonstrated that the presence of an internal structure introduces particular features into the wave properties of a medium and these features cannot be described in terms of the classical theory of elasticity.

ACKNOWLEDGMENTS

This work was supported in part by the INTAS (project no. 96-2370), the Russian Foundation for Basic Research (project no. 00-02-16582), the Program of Support for the Leading Scientific Schools of Russia (grant no. 00-15-96741), and the Federal Special Program "Integratsiya."

REFERENCES

1. T. D. Shermergor, *Theory of Elasticity of Microinhomogeneous Media* (Nauka, Moscow, 1977).
2. V. N. Nikolaevskiĭ, *Geomechanics and Fluid Dynamics* (Nedra, Moscow, 1996).
3. L. D. Gik, Fiz. Mezomekh. **1** (2), 101 (1998).
4. A. L. Krylov, N. G. Mazur, V. N. Nikolaevskiĭ, and G. A. Él', Prikl. Mat. Mekh. **57** (6), 100 (1993).
5. C. S. Chang and J. Gao, J. Eng. Mech.–ASCE, No. 1, 52 (1997).
6. A. I. Potapov, I. S. Pavlov, and S. A. Potapova, *New Advances in Modal Synthesis of Large Structures*, Ed. by L. Jezequel (Balkema, Rotterdam, 1997), pp. 399–410.
7. V. I. Erofeev, *Wave Processes in Solid States with a Microstructure* (MGU, Moscow, 1999).
8. V. I. Erofeev and V. M. Rodyushkin, Akust. Zh. **38**, 1116 (1992) [Sov. Phys. Acoust. **38**, 611 (1992)].
9. V. M. Rodyushkin, Mec. Indust. Mater. **48** (5), 208 (1995).
10. P. A. Johnson and K. R. McCall, Geophys. Res. Lett. **21**, 165 (1994).
11. K. A. Naugolnykh, S. V. Egerev, I. B. Esipov, and K. A. Matveev, J. Acoust. Soc. Am. **106**, 3135 (1999).
12. T. N. Dragunov, I. S. Pavlov, and A. I. Potapov, Fiz. Tverd. Tela (St. Petersburg) **39**, 137 (1997) [Phys. Solid State **39**, 118 (1997)].
13. R. D. Gauthier, in *Mechanics of Micropolar Media* (World Sci., Singapore, 1982), pp. 395–463.
14. R. D. Gauthier and W. E. Jashman, Arch. Mech. **33**, 717 (1981).
15. A. M. Bragov, A. K. Lomunov, and E. E. Rusin, Prikl. Probl. Prochn. Plast., No. 16, 138 (1980).
16. M. A. Isakovich, *General Acoustics* (Nauka, Moscow, 1973).
17. Yu. K. Éngel'brekht and U. K. Nigul, *Nonlinear Strain Waves* (Nauka, Moscow, 1981).

Translated by M. Lyamshev

Acoustical Physics, Vol. 47, No. 3, 2001, pp. 353–360. Translated from Akusticheskiĭ Zhurnal, Vol. 47, No. 3, 2001, pp. 413–421.
Original Russian Text Copyright © 2001 by Rudnitskiĭ.

Two-Channel Processing of Signals for the Separation of Breath and Cardiac Sounds

A. G. Rudnitskiĭ
Institute of Hydromechanics, National Academy of Sciences of Ukraine,
ul. Zhelyabova 8/4, Kiev, 252057 Ukraine
e-mail: apm@ihm.kiev.ua

Received May 21, 1999

Abstract—An algorithm based on the two-channel processing and the confluence analysis techniques is proposed for obtaining the averaged spectra of additive components of a nonstationary random signal. A numerical experiment demonstrating the efficiency of the proposed algorithm is conducted. The algorithm is tested using a real signal recorded at a human thorax and including breath and cardiac sounds and a stationary background noise. *© 2001 MAIK “Nauka/Interperiodica”.*

The development of electronic devices for recording auscultative data along with the new techniques for data processing supplemented by computer analysis provides an opportunity to considerably increase the efficiency of the diagnostics of respiratory disorders.[1] This is connected not only with high sensitivity of the devices but also with the possibility of a simultaneous processing of acoustic data received through several channels and its recording in the form of power spectra, coherence functions, respiratory sonograms, etc. Today, the broad opportunities offered by the computer processing of breath sounds allow one to consider digital auscultation as an approved clinical technique for investigating the respiratory system [1–3].

However the computer analysis of auscultative data brings about several problems that are nontrivial from the point of view of the data processing. One of these problems is the separation of lung and cardiac sounds in the total signal recorded on the thorax surface.

The importance of this problem is connected with the fact that the level of the sound signals generated by one’s heart is very high (as compared to breath sounds). This leads to the masking of important auscultative diagnostic signs by the cardiac sounds, which in this case play the role of interference. This phenomenon is aggravated by the fact that, in performing the frequency analysis, one deals with averaged spectra. As a result, the respiratory diagnostic signs appearing once or twice during the total realization under analysis can become undetectable.

The problem of separating the breath and cardiac sounds is also of importance for cardiologists when the detection of a weak diastolic and systolic murmur is necessary (in this case, the respiratory sounds play the role of interference).

There are several approaches that allow one to solve this problem to a certain degree. First, one can use the signals obtained when the patient holds his breath. Taking into account the absence of correlation between breath and cardiac sounds and performing the procedure of subtraction of uncorrelated interference, it is possible to obtain the desired statistical characteristics of the signal. Unfortunately, this technique is often inadmissible, because, even for healthy people, holding one’s breath leads to a change in the character of the cardiac activity and the statistical characteristics of cardiac sounds can be changed. Moreover, in the case of children and some categories of patients, this method cannot be realized.

In connection with the aforesaid, the techniques most popular in practice are those in which the effect of cardiac sounds and sounds connected with muscle vibration are suppressed in the frequency range below 100 Hz by the filters eliminating (or reducing) the low-frequency part of the analyzed sound signal [4]. However, such a direct solution of the problem can lead to a considerable loss of diagnostically meaningful information [5, 6], because it is difficult to apply a standard approach to a human body that is characterized by a large variability in both normal and pathological states. If it is necessary to retain the low-frequency part of the spectrum, other more sophisticated methods are used: recording of breath sounds within the interval between cardiac tones [7] or utilization of adaptive filtering techniques in the digital processing [8, 9]. The advantages and shortcomings of the indicated algorithms are analyzed in more detail in the paper by Iyer, Ramamoorthy, and Ploysongsang [10], who used a modified Kalman filter to solve the problem of separating the breath and cardiac sounds.

Below, we suggest a technique for solving this problem on the basis of the two-channel processing of sig-

---

[1] Auscultation is listening to breath and cardiac sounds.

1063-7710/01/4703-0353$21.00 © 2001 MAIK “Nauka/Interperiodica”

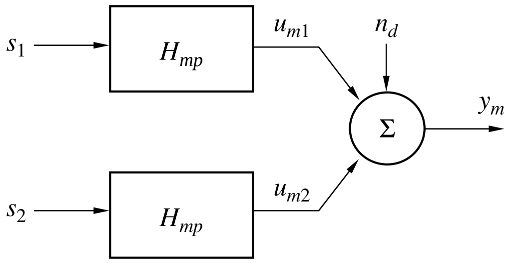

Fig. 1.

nals. The technique allows one not only to solve the main problem (the separation of additive components from the total signal), but also to calculate additional diagnostic parameters.

It is evident that the problem can be solved most effectively when the corresponding algorithm contains the maximal amount of *a priori* information on the nature of the signals to be separated. Therefore, the development of adequate models describing the formation of the signals recorded at the thorax surface is of primary importance.

Now, there is no consensus on the mechanisms that govern the formation of the breath sounds. The model suggested in [11–13] seems to be the most adequate one. In this model, it is assumed that the breath sounds detected at the thorax have a twofold nature. First, they are the sound generated in the trachea due to the turbulent airflow passing through it and then transformed in the course of its propagation through the lung and thorax tissues. The second source of breath sounds is the minor air-carrying channels with diameters of 2–3 mm. The sounds arising there have a weaker intensity. However, they are formed in the immediate vicinity of the thorax surface where the signal is recorded.

Taking the model suggested in [13] as the basis, we assume that the sound signal received by a sensor positioned at the thorax is the sum of three uncorrelated components: the cardiac sounds, the breath sounds, and the background noise. This model is schematically represented in Fig. 1.

Here, s_1 represents the lung sounds, which, according to the majority of researchers, are generated in the trachea and bronchi [11, 12]; s_2 represents the cardiac sounds; H_{mp} is the frequency characteristic depending on the properties of the lung tissue ($p = 1, 2$); u_{m1} and u_{m2} are the lung and cardiac sounds transformed in the course of their propagation through the lung and thorax tissues; n_d is the background noise; and y_m is the signal received by the mth sensor.

The frequency characteristic H_{mp} reflects the transformation of the sound signals generated in pth source in the course of their propagation to the mth sensor.

The problem is to estimate the signal $u_{m1}(t)$ from the available realization of the additive sum $y_m(t) = u_{m1}(t) + u_{m2}(t) + n_d(t)$ of the signal $\hat{u}_{m1}(t)$ and the interference $u_{m2}(t) + n_d(t)$. It is clear that the choice of what to take as a useful signal and what to consider as interference depends on whether a cardiologist or a lung doctor performs the examination of the patient.

In solving the problem, we proceed from the fact that it can be solved as soon as it will be possible to determine the spectra of the additive components of the recorded signal. This will provide an opportunity to apply the theory of optimal linear filtering and, in so doing, to solve the problem of interest.

It should be noted that each of the additive components of the signal $y_m(t)$ has a complex structure. Both breath and cardiac sounds are nonstationary random processes, which exhibit not only periodic intensity variations, but also a frequency modulation.

The point is that, even in the case of normal breath sounds, the spectrum of inhalation slightly differs from the spectrum of exhalation [14], not to mention the breath sounds in the case of lung pathology.

As for cardiac sounds, they are divided into tones and noise. Tones I and II always accompany the normal operation of the heart. Tones III and IV appear less often. The noise (systolic and diastolic murmurs) occur mainly in the case of heart defects. Each of these components has its own characteristic frequency band (30–120 Hz for tone I, 70–150 Hz for tone II, 50–600 Hz for systolic murmur, and 120–800 Hz for diastolic murmur).

In the described conditions, the process at the output of the mth sensor is described by the equation

$$y_m(t) = \sum_p \int h_{mp}(\tau) s_p(t-\tau) d\tau + n_d, \qquad (1)$$
$$p = 1, 2; \quad m = 1, N,$$

where N is the number of sensors, p corresponds to the source number, and $h_{mp}(\tau)$ is a pulsed transition function satisfying the equation

$$H_{mp}(f) = \int h_{mp}(\tau) \exp(2\pi f \tau) d\tau.$$

We solve this problem using the signals recorded by two sensors. We denote the hypothetic transition functions between the sensors for each of the sources by $\alpha(f)$ and $\beta(f)$, i.e., $\alpha = |H_{11}|/|H_{21}|$ and $\beta = |H_{12}|/|H_{22}|$. We denote the phase shift between the signals at the sensors as $\theta_1(f)$ for the first source and $\theta_2(f)$ for the second one. We note that the functions $\alpha(f)$, $\beta(f)$, $\theta_1(f)$, and $\theta_2(f)$ are time independent; i.e., it is assumed that the properties of the lung tissue through which the sound signals propagate remain constant within different phases of breath and heart cycles. We also assume that the background noise recorded by each sensor is stationary and mutually uncorrelated. Taking into account the mutual uncorrelation of the cardiac and breath sounds, which is determined by the difference in their origin, we obtain the following system of equations for the instant power spectra:

$$\begin{cases} W_1(t, f) \\ = \alpha(f)^2\mathcal{U}_1(t, f) + \beta(f)^2\mathcal{U}_2(t, f) + \mathcal{U}_3(f) \\ W_2(t, f) = \mathcal{U}_1(t, f) + \mathcal{U}_2(t, f) + \mathcal{U}_4(f) \\ W_{12}(t, f) = \alpha(f)\mathcal{U}_1(t, f)\exp(-i\theta_1(f)) \\ +\beta(f)\mathcal{U}_2(t, f)\exp(-i\theta_2(f)), \end{cases} \tag{2}$$

where W_1 and W_2 are the instant autospectra of the signals recorded in the first and second channels, respectively; W_{12} is their cross-spectrum; $\mathcal{U}_1$ and $\mathcal{U}_2$ are the instant autospectra of breath and cardiac sounds in the second channel; $\alpha^2\mathcal{U}_1$ and $\beta^2\mathcal{U}_2$ are the corresponding autospectra in the first channel; and $\mathcal{U}_3$ and $\mathcal{U}_4$ are the autospectra of the background noise in the first and second channels, respectively.

Eliminating the autospectra $\mathcal{U}_1$ and $\mathcal{U}_2$ from the system of Eqs. (2), we arrive at the expression

$$AW_1 + BW_2 + CW_{12} + D = 0, \tag{3}$$

where the stationary coefficients A, B, and C are the functions depending on α, β, θ_1, and θ_2 and the coefficient D in addition depends on the stationary spectra $\mathcal{U}_3$ and $\mathcal{U}_4$.

Let $t_1, t_2, \ldots, t_M$ be the time moments for which the values of the observed spectra W_1, W_2, W_{12} at the frequencies $f_1, f_2, \ldots, f_N$ are known. Then, from the known values of $W_1(t_j, f_i)$, $W_2(t_j, f_i)$, and $W_{12}(t_j, f_i)$, it is possible to determine the regression coefficients A_i, B_i, C_i, and D_i for each fixed frequency f_i by the least-squares method. After the determination of the regression coefficients, we can determine the values of α_i, β_i, θ_{1i}, and θ_{2i} for each i by solving the system of equations

$$\begin{cases} A(\alpha_i, \beta_i, \theta_{1i}, \theta_{2i}) = \hat{A}_i \\ B(\alpha_i, \beta_i, \theta_{1i}, \theta_{2i}) = \hat{B}_i \\ C(\alpha_i, \beta_i, \theta_{1i}, \theta_{2i}) = \hat{C}_i, \end{cases} \tag{4}$$

where $\hat{A}_i$, $\hat{B}_i$, and $\hat{C}_i$ are the estimates of the regression coefficients corresponding to each frequency band. Here, we should bear in mind that the regression coefficients have imaginary and real parts and, therefore, the system of Eqs. (4) is overdetermined.

Substituting the known values of α, β, θ_1, and θ_2 into system (2) and averaging its left-hand and right-hand sides over time, we can resolve this system with respect to the desired time-averaged spectra of breath and cardiac sounds, U_1 and U_2.

A series of numerical experiments was conducted in order to test the obtained theoretical results and to reveal the potentialities of the proposed method.

Four Gaussian uncorrelated sequences of random numbers $s_p(t_k)$ ($k = 1, K$, where K is determined by the length of realization) with unit dispersion, a zero average value, and different spectra were generated by a random-number generator. The length of each sequence was selected so as to simulate the situation when each sequence represents a random process having a duration of ≈ 20 s and digitized with the sampling rate 2560 Hz. Precisely these parameters of the studied realizations of the sound signals recorded at the thorax of a patient were used in the experiments described in our previous papers [13, 14].

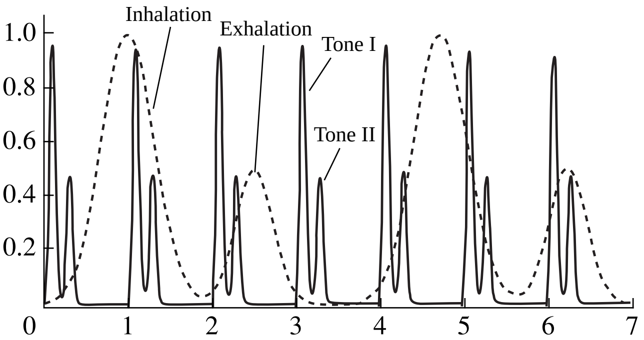

Fig. 2. Envelopes of (—) cardiac and (- - -) breath sounds set in the numerical experiment.

Then the first and second sequences were multiplied by the functions $a_p(t_k)$ ($p = 1, 2$) simulating the envelopes of breath and cardiac sounds (see Fig. 2) with the periods of breath cycle $T_1 = 3.5$ s and heart cycle $T_2 = 1$ s. The third and fourth sequences simulated the Gaussian background noise.

After that, an initial signal was formed in each channel according to Eq. (1):

$$\begin{cases} y_1(t_k) = \alpha a_1(t_k)s_1(t_k) + \beta a_2(t_k)s_2(t_k) + \gamma s_{n1}(t_k) \\ y_2(t_k) = a_1(t_k)s_1(t_k) + a_2(t_k)s_2(t_k) + \gamma s_{n2}(t_k). \end{cases} \tag{5}$$

Here, the signal in the second channel $a_2(t_k)s_2(t_k)$ ("cardiac sounds") was shifted relative to the corresponding summand in the first channel by τ_0, and the value of γ was determined by the desired level of background noise (two versions of background noise were used: "white noise" and "colored noise").

In the experiment, the values of the time shift varied within the range 0–0.05 s and the values of α and β were set equal to 1 and 2, respectively. One of the realizations of such a mixed nonstationary signal (at $\gamma = 0.1$) and its spectrum are given in Fig. 3. Curves *1*, *2*, and *3* describe the spectra of the mixed signal, "breath sounds," and "cardiac sounds," respectively.

Both signals were processed according to the algorithm described above, and the estimates $\hat{\alpha}$, $\hat{\beta}$, $\hat{\tau}_0$, $\widehat{U_1}$, and $\widehat{U_2}$ were obtained in the result.

It is well known [15] that the problem of the least-squares method is ill-posed. Therefore, the regression coefficients in Eq. (3) are calculated by two techniques:

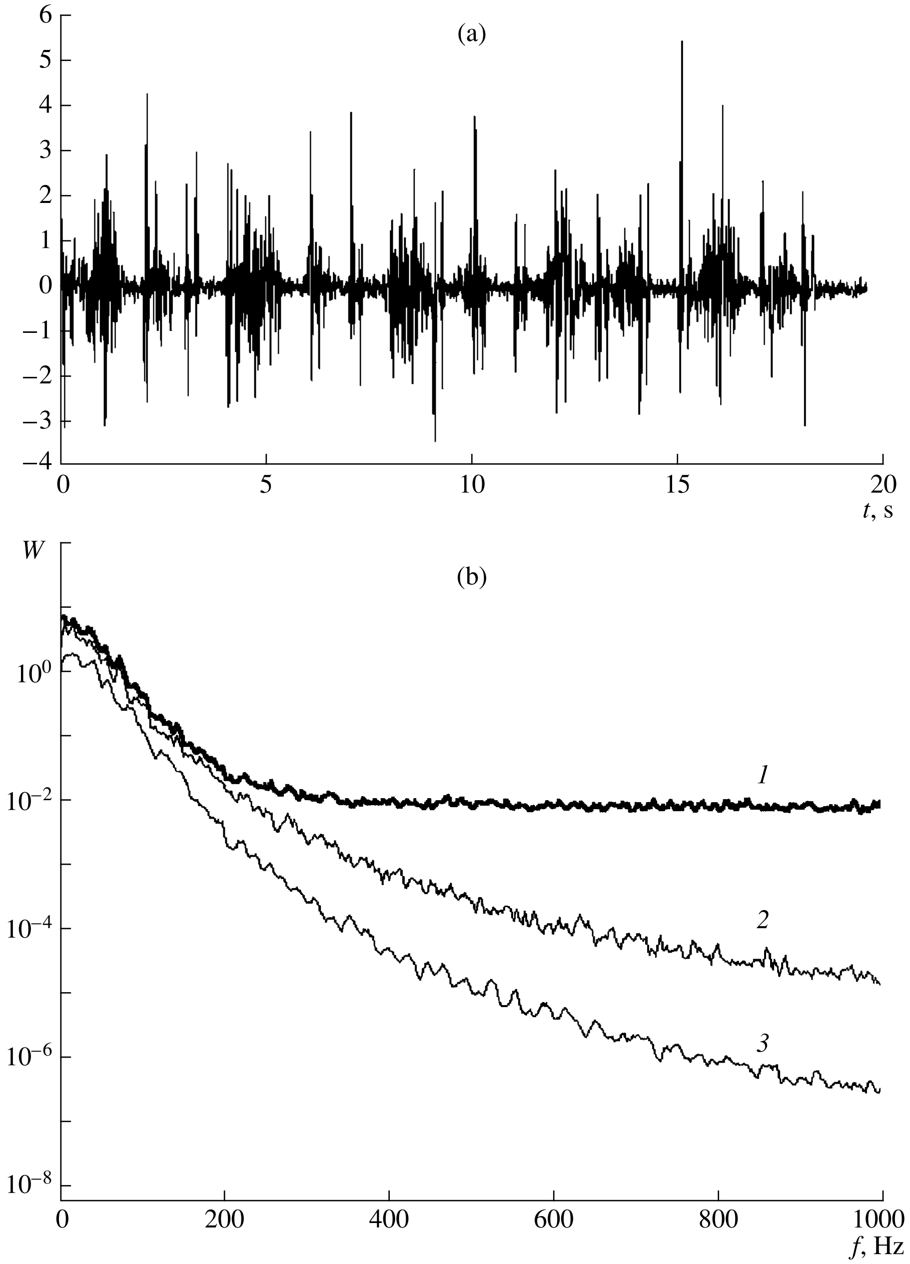

Fig. 3. (a) Realization of the preset signal and (b) the spectra of the preset signal and its additive components.

the Tikhonov regularization method and the method of confluence analysis. The numerical experiment showed that the confluence analysis gives a somewhat smaller scatter of estimates.

The estimates $\hat{\alpha}$, $\hat{\beta}$, and $\hat{\tau}_0$ were used to estimate the reconstructed spectra of "breath" and "cardiac" sounds, $\hat{U}_1$ and $\hat{U}_2$.

Figure 4a presents the plots of the preset and reconstructed power spectra of the corresponding sounds. The ratio between the levels of "cardiac" sounds and background noise was $U_2(f)/U_n(f) = \gamma$, where $U_n(f)$ is the time-averaged autospectrum of stationary background noise, which is the same for both channels. Curve *1* describes the preset spectrum of "cardiac" sounds, and curve *3* describes the preset spectrum of "breath" sounds U_1 and U_2 characterized by a wider frequency band. Their reconstructed estimates, $\widehat{U_1}$ and $\widehat{U_2}$, are represented in the figure by curves *2* and *4*, respectively.

The preset and calculated spectra of "breath" sounds coincide in the figure with graphical precision (curves *3*, *4*). As for "cardiac" sounds (curves *1*, *2*), here we also

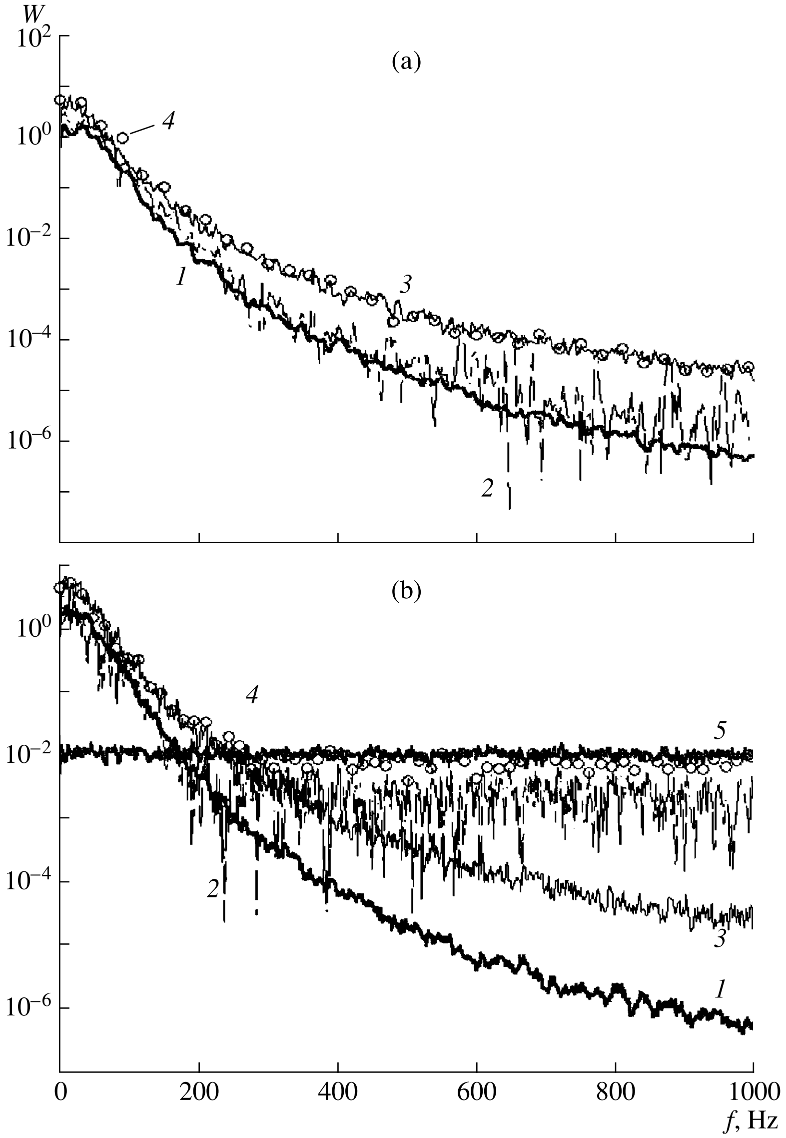

Fig. 4. (*1*) Preset spectrum of "cardiac" sounds; (*2*) reconstructed spectrum of "cardiac" sounds; (*3*) preset spectrum of "breath" sounds; (*4*) reconstructed spectrum of "breath" sounds; and (*5*) preset spectrum of background noise.

have a good agreement between the preset and calculated curves, although the dispersion of the estimate $\hat{U}_2$ tends to grow with increasing frequency.

The equivalence of the estimates of the preset and reconstructed spectra was quantitatively verified by the method suggested in [16]. According to this method, the statistics

$$X^2 = \left[\frac{1}{n_{d1}} + \frac{1}{n_{d2}}\right]^{-1} \sum_{i=0}^{N} \left[\log \frac{\hat{G}_1(f_i)}{\hat{G}_2(f_i)}\right]^2 \quad (6)$$

obeys the χ^2-distribution with N degrees of freedom. Here, $\hat{G}_1(f)$ and $\hat{G}_2(f)$ are the estimates of the averaged spectra to be compared and n_{d1} and n_{d2} are the averaging numbers for these estimates. In this case, the region of acceptance of the hypothesis that $G_1(f) = G_2(f)$ is

$$X^2 \le \chi^2_{n;\,\alpha_1}, \quad n = N, \quad (7)$$

where α_1 is the significance level of the criterion.

The results of the analysis of the realizations under investigation demonstrated that the hypothesis on the equality of the preset and reconstructed spectra can be accepted for "breath" sounds within the whole frequency band (0–1000 Hz) with the significance level $\alpha_1 = 0.05$ and for "cardiac" sounds within the frequency band 0–450 Hz with the significance level $\alpha_1 = 0.01$.

The case when the background noise is uniform within the whole frequency band ($\gamma = 0.1$, $\tau_0 = 0.01$ s) is presented in Fig. 4b. From this figure, one can see

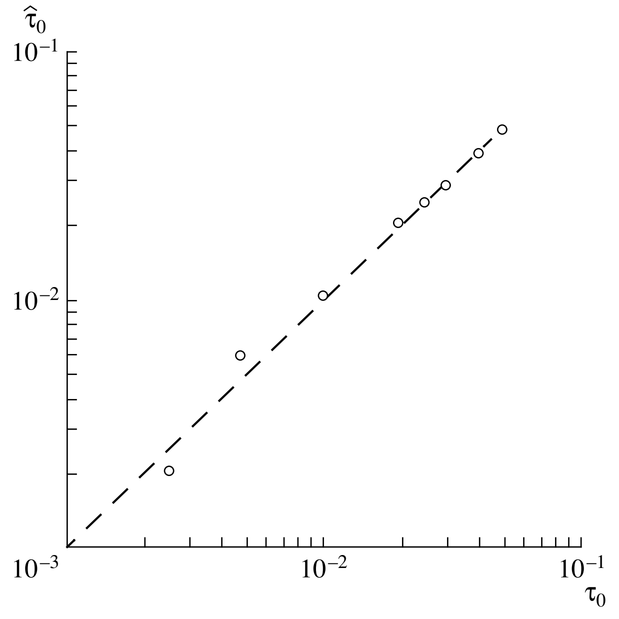

Fig. 5. Comparison of the (—) preset and (○) calculated values of τ_0.

how the signal-to-noise ratio affects the efficiency of reconstruction.

Figure 5 presents the results of the calculation of the delay time τ_0. The calculated values of $\hat{\tau}_0$ are represented by the ordinate axis, and the preset values of τ_0, by the abscissa axis. Apparently, in this case, the efficiency of the algorithm also proves to be fairly high (the correlation coefficient is $r = 0.97$).

It is clear that the conducted numerical experiment is of only illustrative character. Nevertheless, it demonstrates a very high efficiency and reliability of the suggested algorithm. Moreover, the auxiliary parameters (α, β, and θ) obtained as a result of the algorithm operation have an independent meaning for the problems of diagnostics of respiratory disorders.

In fact, almost all kinds of lung pathology lead either to changes in the spectra of breath sounds (rales and crepitations arise) or to changes in the characteristics of the channel of the sound signal propagation (the density of lung parenchyma, the sound velocity, and the amplitude–frequency characteristic change). In the last case, traditional methods of auscultation have little efficiency, and to reliably diagnose such diseases as chronic pneumonia or dust diseases, it is necessary to use X-ray examination, which is often objectionable. At the same time it is well known that the spectral characteristics of breath sounds strongly depend on the breathing intensity, which is difficult to control during real clinical tests [13, 14]. Thus, the differences between the spectra of breath sounds can be large even for healthy patients. The utilization of the two-channel (multichannel) processing of the recorded signals provides an opportunity to solve this problem to a certain degree. In this case, the use of the coherence function, which is a very sensitive instrument for the detection of dry rales against an uncorrelated noise, allows one to diagnose the first group of lung pathology [13, 14], while the use of the parameters α, β, and θ, which strongly depend on the acoustic characteristics of the lung parenchyma, makes it possible to separate the second group of disorders.

In addition, the possibility of separating the breath and cardiac sounds and the background noise provides an opportunity to reveal the particular features of the corresponding spectral characteristics that are masked in the total signal.

In conclusion, we present an example of the separation of cardiac and breath sounds in a real signal. To do this, we first consider the validity of the assumption on the time independence of the frequency transfer functions between the sensors. The signals subjected to the processing were recorded by the technique described in [13, 14], which includes the two-channel recording of signals detected by sensors fixed on the right and left sides of the patient's thorax. Figure 6a shows a respiratory sonogram of such a signal received by a sensor positioned at the level of the seventh rib, at the angle of the left shoulder-blade. It should be noted that the respiratory sonogram is a three-dimensional image of the signals recorded by the sensor in the time–frequency–intensity coordinates. The intensity is represented in the form of the constant-level contours separated from each other by 10 dB and covering the whole range of 40 dB. In the figure, one can see the differences between the spectra of inhalation and exhalation.

The isolines of the function $H(t, f) = 10\log[W_1(t, f)/W_2(t, f)]$ drawn at a step of 5 dB are presented in Fig. 6b. Here, $W_1(t, f)$ and $W_2(t, f)$ are the "instant" spectra of the signals recorded by the sensors that are fixed at the level of the seventh rib at the angles of the left and right shoulder-blades, respectively. Comparing Figs. 6a and 6b, one can see that the transition function between the right and left sensors, $H(t, f)$, strongly depends on time within the whole breath cycle. At the same time, during the phase of inhalation or exhalation, $H(t, f)$ remains almost constant along the time axis for the diagnostically meaningful frequency range (50–1000 Hz).

Thus, if we complement the algorithm proposed above with the unit separating inhalation and exhalation, the suggested model that assumes the time invariance of the frequency transition characteristic is quite acceptable within each phase of the breath cycle.

To obtain the spectrum of cardiac sounds, we have "cut out" from the initial realization those parts of the signal where tones I and II of cardiac sounds were well defined during the pause between exhalation and inhalation. The averaged spectrum of cardiac sounds calcu-

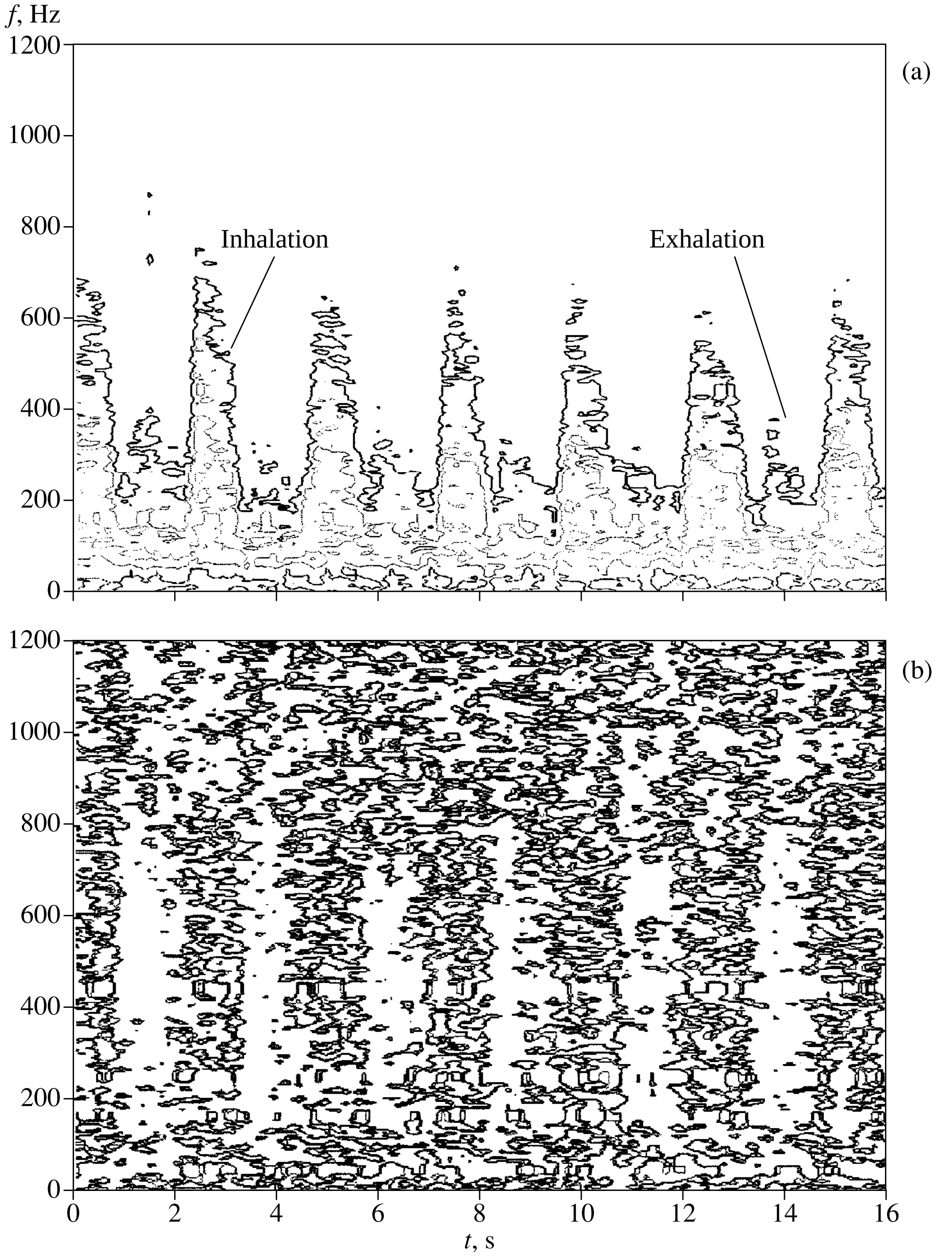

Fig. 6.

lated in such a way is given by a thin solid line in Fig. 7 (curve *2*).

Then, the same sample (17 s long) was processed according to the algorithm suggested in this paper. The spectrum obtained as a result of the algorithm application is given in Fig. 7 by a dotted line (curve *3*).

Curve *1* in Fig. 7 shows the spectrum of the initial signal including the breath and cardiac sounds and the stationary background noise (the spectral levels are in dB).

The good agreement between curves *2* and *3* proves not only the efficiency of the algorithm for separating the spectral characteristics of additive components from the total noise signal but also the adequacy of the suggested model of the sound signals recorded at a human thorax.

Evidently, the proposed algorithm can be applied not only in medical acoustics. The problem of separating the additive components from a random signal, as well as determining the delay times, is important for many fields connected with the processing of random signals. The above example of the determination of the spectral characteristics of breath and cardiac sounds and background noise, which comprise the total signal

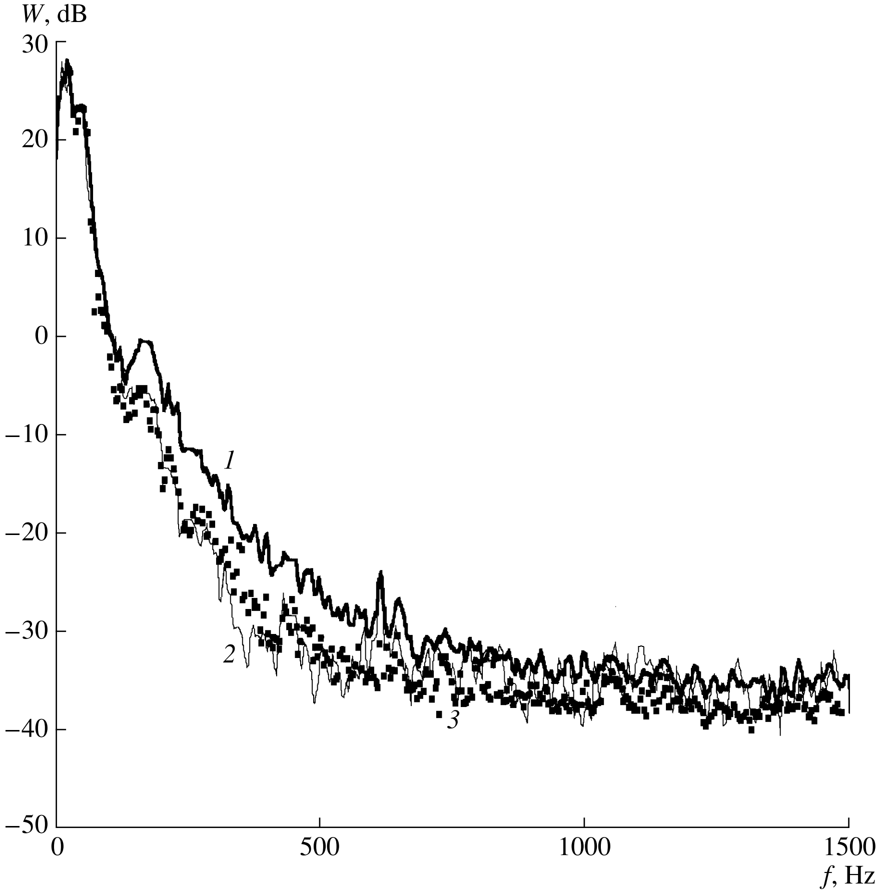

Fig. 7.

recorded at a human thorax, is very illustrative and almost classical for the problems of this type.

REFERENCES

1. H. Pasterkamp, C. Carson, D. Daien, and Y. Oh, Chest **96**, 1405 (1989).
2. N. Gavrialy and C. S. Irving, in *Proceedings of 24th International Lung Sounds Conference* (Inst. of Physiology, Marburg, 1999), p. 17.
3. *Understanding Digital Breath Sounds Technology* (Karmel Medical Acoustic Technologies LTD, Sensor Medics, Israel, 1999) (CD-ROM).
4. G. Charbonneu, J. L. Raccineux, M. Sudraud, and E. Tuchais, J. Appl. Physiol. **55**, 1120 (1983).
5. N. Gavrialy, Y. Palti, and G. Alroy, J. Appl. Physiol. **53**, 307 (1981).
6. Y. Ploysongsang, V. K. Iyer, and P. A. Ramamoorthy, Respiration **58**, 158 (1991).
7. H. Pasterkamp, R. Fenton, A. Tal, and V. Chernick, Am. Rev. Respir. Dis. **131**, 61 (1985).
8. V. K. Iyer, P. A. Ramamoorthy, and Y. Ploysongsang, IEEE Trans. Biomed. Eng. **33**, 1143 (1986).
9. V. K. Iyer, P. A. Ramamoorthy, and Y. Ploysongsang, IEEE Trans. Biomed. Eng. **36** (11) (1989).
10. S. Charleston and M. R. Azimi-Sadjadi, IEEE Trans. Biomed. Eng. **43**, 421 (1996).
11. Y. Ploysongsang, Respir. Physiol. **53**, 203 (1983).
12. Y. Ploysongsang, R. R. Martin, W. R. D. Ross, *et al.*, Am. Rev. Respir. Dis. **116**, 187 (1977).
13. V. T. Grinchenko, A. P. Makarenkov, and A. G. Rudnitskiĭ, Tekh. Akust., No. 11, 12 (1996).
14. A. P. Makarenkov and A. G. Rudnitskiĭ, Akust. Zh. **41**, 272 (1995) [Acoust. Phys. **41**, 234 (1995)].
15. A. N. Tikhonov and M. V. Ufimtsev, *Statistical Treatment of Experimental Results* (Mosk. Gos. Univ., Moscow, 1988).
16. J. S. Bendat and A. G. Piersol, *Random Data: Analysis and Measurement Procedures* (Wiley, New York, 1986; Mir, Moscow, 1989).

Translated by M. Lyamshev

Acoustical Physics, Vol. 47, No. 3, 2001, pp. 361–368. Translated from Akusticheskiĭ Zhurnal, Vol. 47, No. 3, 2001, pp. 422–430.
Original Russian Text Copyright © 2001 by Furduev.

Acoustic Monitoring of the Sea Medium Variability: Experimental Testing of New Methods

A. V. Furduev

Andreev Acoustics Institute, Russian Academy of Sciences,
ul. Shvernika 4, Moscow, 117036 Russia
e-mail: bvp@akin.ru

Received April 27, 2000

Abstract—Two new methods of acoustic monitoring of the sea medium are tested in a shelf region. One of the methods is the difference-pulse technique in which the variability of the medium is characterized by the difference in the energies of the sequences of arrivals of two multiray signals. The other method is the self-sustained oscillator technique in which the information on the changes that occur in the water temperature, the velocity of currents, and other parameters of the medium is obtained from the frequency deviation of a self-sustained oscillator that has a feedback loop closed through the underwater sound channel. *© 2001 MAIK “Nauka/Interperiodica”.*

Since the pioneering work [1] on acoustic tomography was published, intense studies of the methods and instruments for underwater acoustic monitoring have been performed to tackle the problems of climate forecasts, monitoring of the environment, and the search for fish, as well as the problems of security in economic sea zones and ports, the operation safety of oil and gas plants and pipelines, etc. [2–6]. In spite of the growing understanding of the scientific and practical significance of these methods, along with considerable progress achieved in increasing the accuracy and broadening the scope of the acoustic methods of measuring the parameters of a medium, underwater acoustic monitoring and ocean tomography are still at the stage of theoretical studies and experimental testing [3–8].

Most experiments in different ocean and sea regions were carried out with the use of the correlation method. With this technique, a resonant sound source generates a long broad-band pseudonoise signal of sufficient intensity. The signal received at the opposite end of the path to be monitored is subjected to cross-correlation processing. As a result, one obtains the correlation function that exhibits maximums determining the propagation times for individual rays (modes) [1, 6]. In this method, the accuracy of measuring the times increases with the spectral width of the emitted signal and with the signal-to-noise ratio. Therefore, one has to construct high-power broad-band sound sources and transmit long signals and assume that the medium does not change within the time of the data acquisition. The distortions of the signal spectrum, which are caused by the mode interference at the reception point, and the fluctuations of the medium during the acquisition time decrease the sharpness of the correlation peaks and lead to lower accuracy in measuring the propagation time. Thus, in the pioneer global experiment by Munk [3], which was carried out in January 1991, an acoustic power of 3500 W of the multielement projector was required with the 12-Hz band around the central frequency 57 Hz and with the 50-min signal duration. The cost of such a projector predominated in the total cost of the experiment. The analysis of other large-scale experiments [3–5] showed that it is necessary to develop alternative monitoring methods suitable for application on the scales of a strait, lake, or harbor. A goal was advanced to develop simpler methods of underwater acoustic monitoring that are self-adjustable to the constant part of the medium transfer function. With such methods, a lower acoustic power and a narrower frequency band can be used and higher sensitivity to the medium variations can be achieved. The medium variations, i.e., the movements of inhomogeneities of a hydrophysical, technogenic, or biological nature, temperature trends, and water currents, are the objects to be monitored in long-term observations in a relatively small sea region or lake. In this connection, some methods [8, 10–12] were developed, and, as the preliminary tests show, these methods are promising in the aforementioned sense, although further studies and improvements are required.

One of the methods [10, 11] is based on analyzing the difference in sequences of the signal arrivals, which are spread in time because of the multiray propagation. The method is called the difference-pulse method. It is useful in that, for eliminating the constant part of the medium transfer function and the bottom reverberation interference, only the difference in the time sequences is analyzed for each pair of the continuously transmitted pulses. The time sequences can be obtained, for instance, by the correlation analysis, with the use of the M-sequence, or another broad-band signal. However, the study of the methods shows that time-delay spectrometry [7, 8] is the most advantageous technique. S.D. Chuprov from the Acoustics Institute was the first

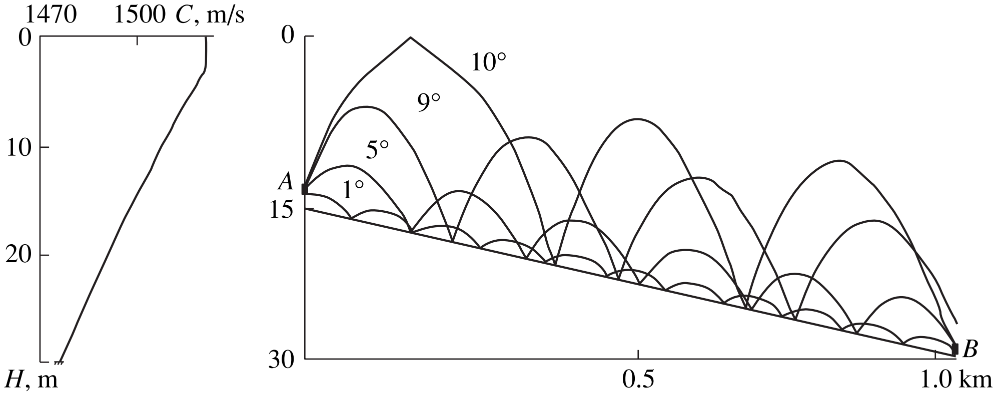

Fig. 1. Sound speed profile, ray pattern, and sea-floor relief for the path perpendicular to the coast.

to apply this technique to ocean sensing in 1985. The time-delay spectrometry was instrumentally implemented in Nizhni-Novgorod State Engineering University, under the supervision of N.I. Knyazeva. In this method, the sound source transmits linearly frequency-modulated (LFM) pulses with an optimally chosen time of the frequency sweep and adjustable repetition rate. On the opposite path end, the hydrophone receives several LFM pulses (according to the number of rays) whose instantaneous frequency difference corresponds to the time delay in the signal arrivals for different rays. By multiplying (heterodyning) the transmitted and received signals with subsequent filtering, one obtains the sequence of the arrivals. Subtracting these sequences from one another for the successive pulses reveals every change that occurs in the medium during the time separating the pulses. On the axis of the time difference, these changes manifest themselves for the rays (modes) that are most strongly affected by the medium inhomogeneities. Thus, the difference-pulse method detects the changes on the propagation path and is insensitive to the mean propagation conditions, including the reflection from the stationary bottom and the refraction by the medium inhomogeneities that remain unchanged within the interval between the pulses. To test the difference-pulse method in an experimental tank, during the interval between pulses, we placed a ball in water in the trajectory of a reflected ray. In the difference pattern, the signal appeared only in the position that corresponded to the time of this very reflection [8].

In-sea tests of the difference-pulse method were carried out at the Black Sea shelf, near Gelendzhik, at the experimental site of the Southern Branch of the Institute of Oceanology of the Russian Academy of Sciences. This experiment did not allow us to obtain such a striking and unambiguous result as in the tank. The experiment was performed in autumn when sharp northeasterly off-shore winds (the Novorossiisk “bora”) create currents, temperature drops, and internal waves. It is evident that an internal wave reconstructs the entire pattern of the sound field, whereas a separate obstacle (such as the ball in the tank) influences only certain reflections.

Figure 1 shows the ray pattern, the sound speed profile, and the sea-floor relief at the experimental site. Two reversible piezoelectric transducers were bottom-moored at points *A* and *B*; they formed a path, 1 km in length, that was oriented perpendicularly to the coast. The propagation conditions were useful in that most rays were spread near the absorptive bottom (silt-covered sand). Therefore, the intensity-predominating signal arrivals seem to be associated with the rays that leave the source at the angles close to 9° and 10° (see Fig. 1).

Figure 2 illustrates how the difference-pulse method works. The presented example corresponds to periodic variations in the first signal arrival Fig. 2a, which are probably caused by an ashore-propagating, short-period internal wave generated by the off-shore wind in the vicinity of the depth drop. The fluctuations in the arrival times were not higher than 0.2 ms and had a period of about 20 min. Figure 2b shows the sequences that were obtained by time-delay-spectrometry processing for the LFM pulses transmitted through the path in times *A*, *B*, and *C*, i.e., the ones separated by the half-period (*A*–*B*) and period (*A*–*C*) of the internal wave (see Fig. 2a).

Figure 2c presents two differences of the time-power sequences: *A*–*B* (the dotted curve) corresponding to a high difference value and *B*–*C* (the solid curve) corresponding to a low one. Note that the first two rays in Fig. 2b are actually unresolved ray pairs (that are very close in their arrival times). They cannot be resolved because both the sound source and the receiver were close to the bottom. It is also worth mentioning that the strongest effect of the medium variability is experienced by the second (later) power-dominating ray, this difference in the effects being caused by the type of density stratification and the associated type of the internal wave that influences the temperature only on the deep-water part of the path.

The second method of the acoustic monitoring of the medium variability and its integral (path-averaged) parameters is called the self-sustained oscillator method [10, 12]. The main feature that determines its efficiency and capability of self-adaptation to the medium is that the medium to be monitored is itself a part of the self-sustained oscillator and serves as the time-delaying feedback loop, with the delay being governed by the sound speed and the path length, and the feedback coefficient being frequency dependent.

A simplified layout of this method is presented in Fig. 3. The shown regenerative circuit consists of the sound source (with the sensitivity $E_R = U_R/P_R$); an electronic amplifier (with the transfer factor $K_E = U_S/U_R$) which has a nonlinear amplitude response and an adjustable transfer factor; a transmitting electroacoustic transducer (with sensitivity $E_S = P_S/U_S$); and an acoustic path that closes the loop (with frequency-dependent transfer factor $K_W = P_R/P_S$). Such a scheme presumably was first considered by Yu.M. Sukharevskiĭ in his analysis [9] of sound amplification in a hall in 1940.

It is convenient to characterize the regenerative circuit by the loop transfer factor $M = E_R K_E E_S K_W$. Obviously, the circuit cannot be self-excited until $M < 1$, and the scheme operates as a regenerator for the ambient noise in the sea. At $M \geq 1$, the scheme works as a self-sustained oscillator whose frequency is determined by the maximum in the spectrum of the ray (mode) interference at the reception point when the condition of phase matching is met.

There are two operational modes for the monitoring scheme at hand:

1. In the regenerative mode ($M < 1$), the received ambient noise is retransmitted from a distant point, this regime significantly increasing the contrast of the ray interference spectrum and allowing the interray time delays to be measured to a high accuracy. The variations of the delays in time can be used to get the information on the processes that occur on the path.

2. In the self-excitation mode ($M \geq 1$), the system emits a nearly monochromatic signal. Its frequency is determined by the maximum in the interference spectrum, and the frequency deviations and their spectrum reveal the type of the variability, e.g., the changes caused by a vessel or a fish shoal crossing the path.

To illustrate these considerations, let us apply the linear approximation to a simple case of single-ray propagation. Assume that $M < 1$, so that the system operates in the regenerative mode. Then, the hydrophone receives the noise P_N and the transmitted signal P_R (Fig. 3): $(P_N + P_R)E_R K_E E_S = P_S$. At the same time, $P_R = P_S K_W$. Hence, we obtain

$$(P_N + P_S K_W)E_R K_E E_S = P_S. \tag{1}$$

Here, $E_R K_E E_S = M/K_W$ is the transfer factor for the entire electroacoustic circuit of the system (Fig. 3).

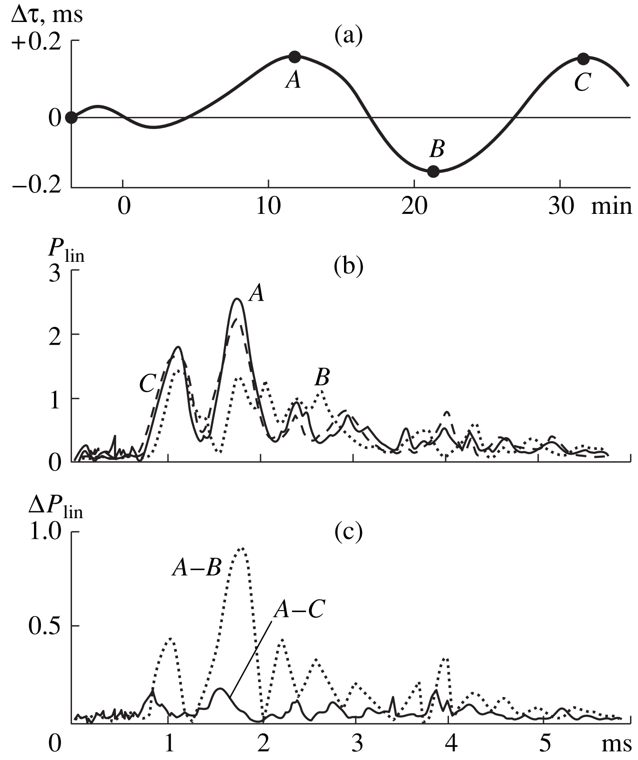

Fig. 2. Difference-pulse method of acoustic monitoring: (a) fluctuations of arrivals for the signal transmitted through the path; (b) sequences of arrivals for three pulses at the points *A*, *B*, and *C*; and (c) difference-pulse sequences (*A*–*B*) for the intervals of the medium variability and (*A*–*C*) for the inter-period variability.

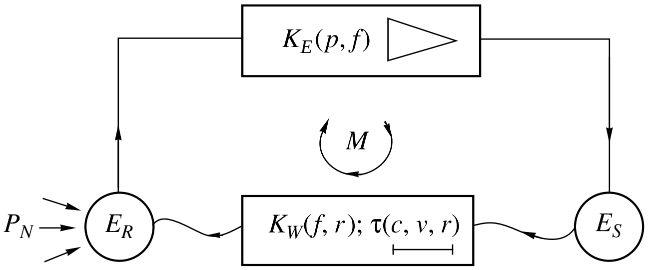

Fig. 3. Simplified layout of the regenerative system for underwater acoustic monitoring: E_R and E_S are the sensitivities of the electroacoustic transducers; K_E is the transfer factor of the amplifier; K_W is the transfer factor of the propagation path; P_N is the ambient sea noise; and $M = E_R E_S K_W K_E$ is the loop transfer factor for the whole circuit.

From Eq. (1), we can determine the acoustic pressure measured at 1 m from the source:

$$P_S = \frac{E_R K_E E_S P_N}{1 - M}. \tag{2}$$

As far as $M < 1$, the circuit is linear (the limiter does not operate) and the transfer factor *A* (see Fig. 3) can be expressed as

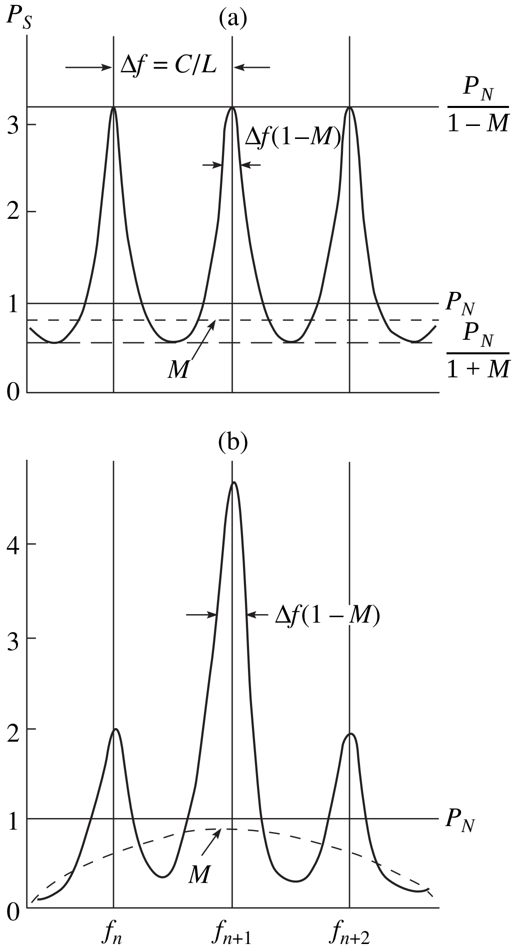

Fig. 4. Calculated frequency response for the spectrum part in the noise regeneration scheme for (a) $M = 0.7$ and (b) M varying over the frequency band; P_N is the initial noise level (treated as unity), Δf is the difference between the neighboring frequencies of positive feedback, and M is the loop transfer factor in the regenerative circuit.

$$A = \frac{P_R}{P_N} = \frac{P_S K_W}{P_N} = \frac{M}{1-M}. \tag{3}$$

Obviously, M, i.e., the loop (regenerative) transmission factor, is generally a complex quantity, which, for a monochromatic signal, can be written as $M = M_0 e^{1\varphi}$, where φ is the phase increment that consists of the phase shift $\varphi_E(\omega)$ in the electroacoustic part of the circuit (transducers, amplifier) and the phase increment $\varphi_W = \omega\tau$ due to the signal propagation along the path (path length L, propagation time τ). For arbitrary phase shifts φ_E, the path length can be treated as constant, and the phase φ_W determines the condition of a positive or negative feedback and takes all allowable values depending on the frequency ω. By taking into account the phase φ_W as the only variable that is informative in the specified monitoring scheme, we can write

$$M = M_0 e^{i\varphi_W} = M_0(\cos(\omega\tau) - j\sin(\omega\tau))$$

and obtain the following expression for the absolute value of A:

$$|A| = \frac{M_0}{(1 - 2M_0\cos\varphi_W + M_0^2)^{0.5}}. \tag{4}$$

From this expression, one can estimate the regeneration-caused modification of the noise spectrum. For the frequencies of positive feedback, $|A|$ has a maximum value and $\cos\varphi_W = 1$; i.e., the signal arrives at the hydrophone in phase. Hence,

$$|A| = \frac{M_0}{1 - M_0}. \tag{5}$$

For the negative-feedback frequencies (the noise level decreases), $|A|$ has a minimum value, $\cos\varphi_W = -1$, the signal arrives in antiphase, and we have

$$|A| = \frac{M_0}{1 + M_0}. \tag{6}$$

Obviously, the difference between the neighboring frequencies of positive feedback is constant for all rays (all propagation times τ over the ray) within the entire frequency band. This difference can be obtained from the condition $\varphi_W = 2\pi n$, where n is a positive number. Hence, we can write

$$\Delta f = \frac{1}{\tau} = \frac{c}{L}. \tag{7}$$

For positive feedback, the frequency bandwidth of the maximum in $|A|$ can be estimated as $\Delta f_{\max} = \Delta f(1 - M_0)$ at a level of 0.7.

In Fig. 4, the calculated noise spectrum is shown for the regenerative operational mode. The upper plot corresponds to $M = 0.7$ with the constant loop transfer factor M for all frequencies; the lower curve is obtained for a value of M that varies in frequency (e.g., because of the nonuniformity in the amplifier frequency response or the medium transfer function). A similar effect also takes place when M is constant within a certain frequency band, but a peak occurs in the spectrum of the regenerated noise.

The process of noise regeneration leads to a much higher contrast in variations of M or in those of the medium transfer coefficient K_W (which is the same). Thus, the maximum in the interference signal spectrum or in the frequency dependence of M can be detected to a high accuracy, if the frequencies of positive feedback are sufficiently close to each other, this being the case for a long acoustic path. For instance, for path lengths of 1.5 and 15 km, these frequencies will be separated by 1 or 0.1 Hz, respectively. When $M = 1$, the operational mode changes to the self-sustained oscillator mode. The oscillations occur at the maximal values of M (the central frequency in the lower plot of Fig. 4). In this case, the side spectrum maximums are suppressed because of the amplifier nonlinearity at high signal amplitudes.

The above considerations are valid for single-ray sound propagation. Multiray propagation makes the explicit analysis more complex: only numerical modeling leads to some results that are unfortunately far from being accurate and unambiguous. That is why we decided to experimentally solve the problem of the frequency grid of positive feedback for the multiray case, at different signal amplitudes and time delays.

Figure 5 illustrates the experiment for the path length $L = 1$ km (see Fig. 1). The upper plot presents the noise spectrum for a frequency band of 2500 Hz, with the maximum at 6509 Hz. The band of analysis was limited by nothing but the responses of the transducers. Figure 2b shows the sequence of signal arrivals. Note that the two initial predominating rays are separated by 1 ms in time, this separation being illustrated by the peaks in the interference spectrum, which are spaced by 1 kHz in frequency. Observing the time variations of the interference pattern seems to be quite informative for path monitoring. Thereby, one can separate the rays and detect the inhomogeneities on the path. Nevertheless, further methodical and theoretical developments of this method are still required. One can expect that the regenerative method will be useful in the studies of the interference spectra (for instance, such as those carried out in the Marine Physical Laboratory of the Scrips Institute of Oceanology, USA, [13]) or in monitoring the dislocations of the wave-field phase fronts (as was proposed in [14] for one of the methods of underwater acoustic tomography).

Note that, in the regenerative mode, the frequencies of the interference maximums can be measured to a high accuracy. This fact is illustrated by the middle plot in Fig. 5. Here, the regeneration spectrum is presented within the band 37 Hz, in the vicinity of the main maximum (about 6509 Hz) in the interference pattern (M = 0.9). The situation is identical to the calculations illustrated by Fig. 4. According to the experiment, the maximum can be traced to an accuracy of about 0.005 Hz at a frequency of 6500 Hz, the relative accuracy being about 10^{-6} in this case.

The following experimental conclusion is worth mentioning: All frequency separations Δf (Eq. (7)) between the positive-feedback peaks are constant. These separations proved to be equal to 1.56 Hz for the example at hand (Fig. 5), this value corresponding to the travel time for the second intensity-dominating ray (see Fig. 3), which is transmitted through the path within 0.64 s. In other words, the frequency grid of positive feedback is equidistant in the vicinity of the main maximum of the ray interference for the regeneration monitoring scheme.

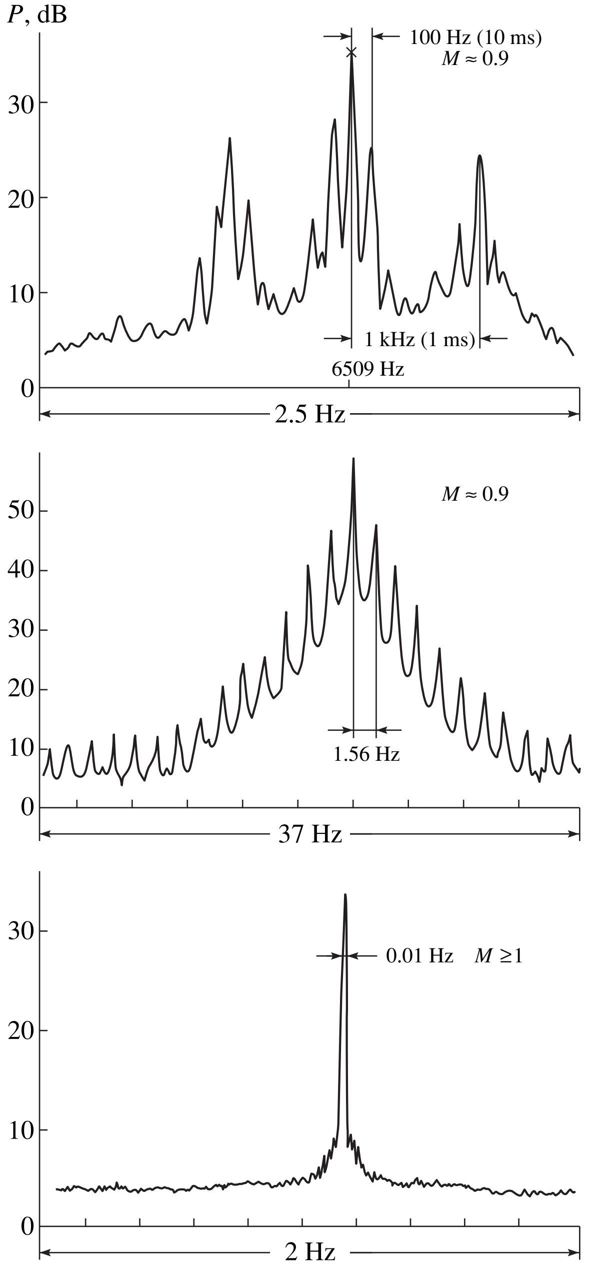

Fig. 5. Experimental testing of the regenerative monitoring system (Fig. 3) in the regime of measuring the interference spectrum (two upper plots) and in the self-excitation regime (the lower plot).

In long-term observations of the spectra (similar to the middle plot in Fig. 5), we noticed that the frequency grid of positive feedback remained unchanged and equidistant, but the interference maximum that followed the changes in the propagation conditions on the path was slowly displaced with changes in the amplitudes of the corresponding peaks (the grid step kept to be equal to 1.56 Hz). However, at a sufficiently high displacement of the maximum (by 8–10 Hz over 40–50 min), the grid abruptly changed its step to 1.58 Hz, this value corresponding to the first intensity-dominating ray. Then the situation can be repeated. Such a behavior of the regeneration spectrum near the interference maximum leads to the conclusion that the self-sustained oscillations (if $M \geq 1$) occur at a frequency close to the interference maximum that is created by a

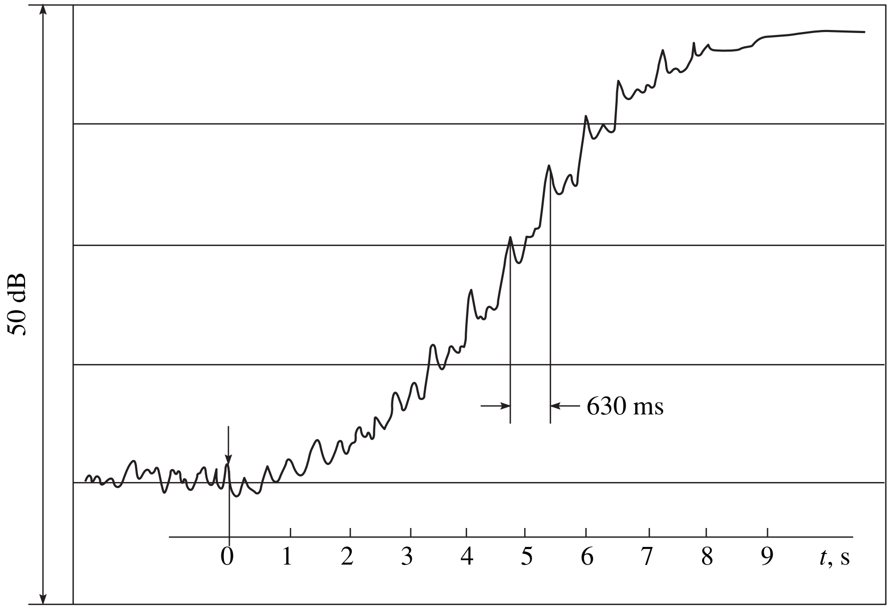

Fig. 6. Self-excitation of the self-sustained oscillator: zero time is the instant when the sound source was switched on in the circuit (as indicated by the arrow); 0.63 s is the time of the single-cycle propagation along the path.

number of ray arrivals (the amplitude condition) with the phase condition that is provided by a single power-dominating ray. However, we must confess that the changes in the frequency grid of positive feedback cannot be always unambiguously related to the travel time over a certain ray (frequency differences of 1.62 and 1.48 Hz were observed). Nevertheless, the fact that the grid remains equidistant is interesting by itself. It seems that sometimes the physical reasons for forming the grid step can be associated with an individual ray and sometimes this mechanism is governed by a vector sum of several rays. This interesting fact still needs to be theoretically explained.

By turning to Fig. 5 again, one can notice that the increase in M to $M \geq 1$ leads to the self-excitation of the oscillator. In this regime, a monochromatic signal is observed whose frequency is highly sensitive to the changes in the propagation conditions on the path, including passages of a vessel or a fish shoal, changes in the water temperature, the presence of currents or other inhomogeneities in the water bulk. If the path is sufficiently long and the time needed for the oscillator to reach a steady state is long (the time constant of the self-sustained oscillator was 8–9 s in our case), the wind-generated surface waves with periods of 2–3 s do not suppress the oscillations, though generally the waves destroy the signal coherence. The high value of the time constant of the self-sustained oscillator with a feedback through the underwater sound channel is one of the main features of this monitoring technique. The effect of the time constant on the capability to monitor the inhomogeneities of different scales in time and space is a subject of special studies. Nevertheless, we mention the fact that the self-sustained oscillator immediately responds to a sharp change in the propagation conditions (a passage of a vessel across the path, for instance). After that, the oscillator frequency recovers in accordance with its time constant, and the medium inhomogeneities with periods 20 s and over are traced by the system relatively smoothly.

Figure 6 illustrates the process of excitation of the self-sustained oscillator from the level of natural ambient noise to monochromatic oscillations on a 1-km-long path (Fig. 1). At zero time, the transmitting transducer was switched on in the operating circuit, (see Fig. 3, the time of switching on is indicated by the arrow). The excitation process took about 9–10 s, which approximately corresponded to 15 cycles of sound propagation over the path (a single cycle of 0.63 s is indicated in Fig. 6). It is worth mentioning that, on a path of about 100 m in length, it is practically impossible to obtain stable oscillations if even weak surface waves are present. With longer paths, the stability of the self-sustained oscillator becomes higher, although the instant response to a perturbation (path crossing by a vessel) still remains.

The acoustic power that is required for the self-sustained oscillator to work is low, because the oscillator is always excited at a frequency that is close to the interference maximum, and the circuit amplification must only compensate for the loss related to the sound propagation through the medium. This compensation occurs at the frequency of the interference maximum, and the emitted spectrum is narrow (the bandwidth is usually less than 0.01 Hz at a frequency of about 6000 Hz).

Let us consider several experimental examples that illustrate the self-sustained oscillator method [12] tested at the Black Sea shelf (Fig. 1). These examples do not include the measurements that were accompanied by vessel passages near the path, because, in these cases, the self-sustained oscillations were suppressed or their frequency varied with high amplitude (if the vessel passed far enough from the path). The measuring system was similar to that shown in Fig. 3 but complemented with a frequencymeter (or a periodometer for low-time-lag recording of the oscillation frequency) and a recorder of the frequency deviations. The predicted monochromatic nature of the oscillator signal (with a Q-factor of 10^6, see the lower plot in Fig. 5) allowed us to use a periodometer, thereby simplifying the circuit and making it lag-free. The electroacoustic transducers used in the experiment were reversible, so that the direction of the sound propagation could be changed to opposite without losing the spatial position of the phase. Hence, the projection of the velocity of the current onto the path could be measured. The use of separate sound sources and receivers would cause additional problems in performing the measurements.

Figure 7 is an example. Figure 7a represents a fragment of the oscillator frequency record (the record width corresponds to a frequency band of 4 Hz). After sunset at 20:00, the water began to cool down, as indicated by the upward trend in the record. Within the record fragment labeled as *R* (which corresponds to nearly a 1-hour period), the direction of sound propagation was changed to its opposite. The frequency increase in this fragment corresponds to the observed velocity of the current in the direction along the path (about 0.05 m/s). Figures 7b, 7c show the oscillator spectra that were measured at the points *B* and *C* just before and after the change in the propagation direction. The complex form of the spectra is caused by the so-called “soft” nonlinearity, which was used in this case in the amplification circuit, the transmitted power being low (just on the brink of self-sustained oscillations, $M \approx 1$).

Figure 8 (where the abscissa axis represents the local time in hours) shows another example of such a monitoring procedure, which is interesting because of the oceanographic regimes typical for a shelf. Similarly to Fig. 7, fractions of the records are presented for the self-sustained oscillator frequency. The shown fragments cover the day-time, evening, and morning of the next day. The record scale corresponds to a frequency change of 10 Hz, which can be shown to correspond to a temperature change of 1°C.

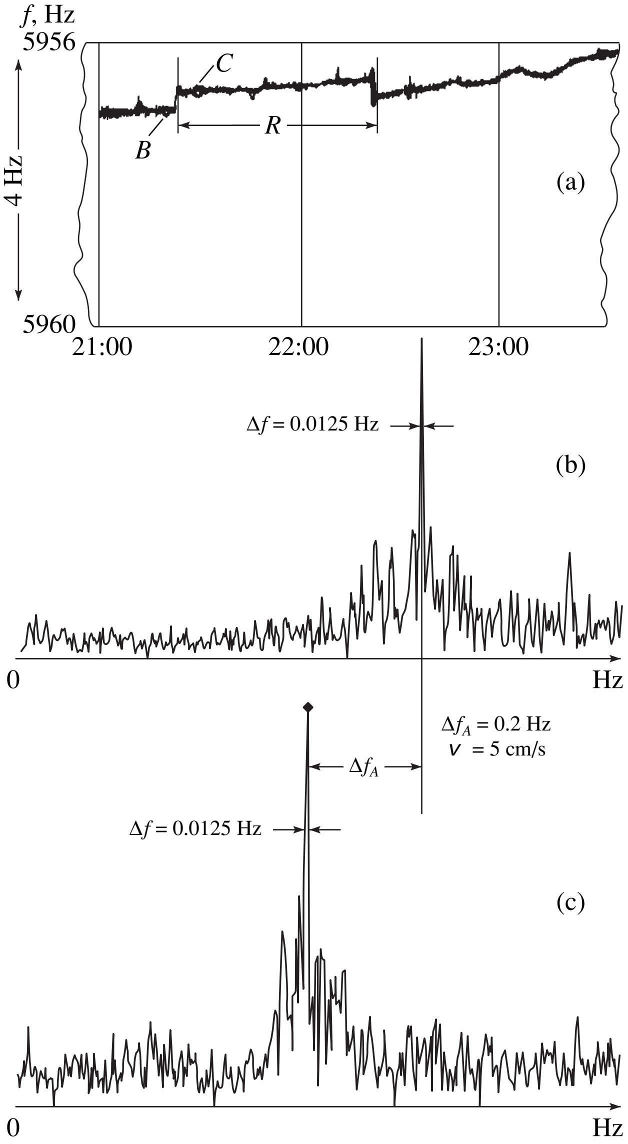

Fig. 7. Measurements of the evening-time decrease in the water temperature and of the velocity of current by using the self-sustained oscillator method on the path of Fig. 1: *R* is the zone of inverted sound propagation; (a) is the example of the frequency record for the self-sustained oscillator; (b, c) are the spectra before and after the inversion of the propagation direction. The frequency difference determines the velocity of the current.

The near-surface periodic temperature changes labeled as *S* had amplitudes of about 0.01°C and periods of 10–20 min. These temperature fluctuations seem to be governed by short-period internal waves. The fluctuations were quite pronounced in the records, this being evidence of the high sensitivity of the method. The estimates showed that temperature fluctuations ten times weaker can be detected. The subsequent behavior of the record is also quite predictable: when calm windless weather changed to a sharp off-shore wind of 10–15 m/s at 18:00. (*W* indicates the beginning of the wind), the warm water moved away from the coastal area and a temperature decrease occurred on the path. At night, the wind terminated, the sea became dead calm, and, by the morning, warm waters returned to the shelf in the form of trains of short-period internal waves (at the right of Fig. 8).

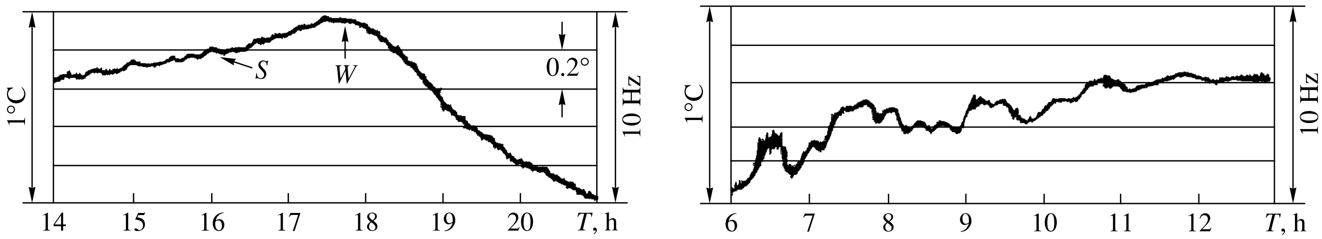

Fig. 8. Record of the self-sustained oscillator frequency with the monitoring system of Fig. 3. On the left: the process of water warming; *S* is the region of temperature variations caused by internal waves; *W* is the beginning of the strong off-shore wind that caused a decrease in the water temperature. On the right: return of warm waters by the internal-wave trains (after the termination of wind).

It is worth mentioning that a smooth record that is free from frequency drops (similar to those shown in Figs. 7, 8) was not always obtained. With high variations of the hydrological environment, sharp changes in the oscillator frequency were observed. One can assume that, in these cases, the maximums in the interference pattern abruptly changed their amplitudes, rather than smoothly "drifted" in frequency, the latter situation being typical of computer simulations that imply slow changes in the mean water temperature.

The conclusion can be drawn that the primary tests of the new methods for underwater acoustic monitoring confirmed their feasibility and showed ways for further theoretical and experimental studies required for the methods to be practically implemented. In particular, the tests revealed high sensitivity of the methods to the variability of the medium, including the inhomogeneities of a hydrophysical, technogenic, or biological origin that occur on the propagation path. The experiments also confirmed that the self-sustained oscillator method of monitoring automatically adjusts itself to the propagation conditions by closely tracing the frequency of the interference maximum. Thereby, the possibility is shown for narrow-band sound sources of comparatively low power to be used in acoustic systems for monitoring the water medium in straits, lakes, harbors, etc.

ACKNOWLEDGMENTS

The in-sea experiments were possible thanks to the assistance of the Southern Branch of the Institute of Oceanology of the Russian Academy of Sciences and the active participation of the following researchers from the Andreev Acoustics Institute: N.N. Okhrimenko, V.N. Reshetov, V.N. Chekaĭda, M.A. Lesov, and S.S. Naumov.

This work was supported by the Russian Foundation for Basic Research (project nos. 00-05-64226 and 00-05-79072).

REFERENCES

1. W. H. Munk and C. Wunsch, J. Deep Sea Res. **26**, 123 (1979).
2. W. H. Munk and A. M. Forbes, J. Phys. Oceanogr. **19**, 1765 (1989).
3. W. Munk and A. Baggeroer, J. Acoust. Soc. Am. **96**, 2327 (1994).
4. P. N. Mikhalevsky, A. N. Gavrilov, and A. B. Baggeroer, IEEE J. Ocean Eng. **24**, 183 (1999).
5. J. L. Spiesberger and K. M. Metsger, J. Geophys. Res. **96**, 4869 (1991).
6. P. F. Worcestor, B. D. Cornuelle, and R. C. Spindel, Rev. Geophys. Suppl., 557 (1991).
7. E. A. Zenyutich, N. N. Knyazeva, and S. S. Naumov, in *Radio Engineering Means and Systems* (NGTU, Nizhni Novgorod, 1997), pp. 106–111.
8. S. V. Burenkov, N. A. Dubrovskiĭ, K. D. Sabinin, and A. V. Furduev, in *Acoustic Monitoring of Media* (Andreev Acoustics Inst., Russ. Acad. Sci., Moscow, 1993), pp. 3–8.
9. Yu. M. Sukharevskiĭ, Dokl. Akad. Nauk SSSR **24** (5), 437 (1940).
10. A. V. Furduev, in *Acoustics at Threshold of the 21st Century* (Mosk. Gorn. Univ., Moscow, 1997), pp. 169–175.
11. A. V. Furduev and A. V. Agranovskiĭ, Patent of the Russian Federation No. 2,127,890 (20 March 1999).
12. A. V. Furduev and A. V. Agranovskiĭ, Patent of the Russian Federation No. 2,134,432 (10 August 1999).
13. G. L. D'Spain and W. A. Kuperman, J. Acoust. Soc. Am. **106**, 2454 (1999).
14. V. A. Zhuravlev, I. K. Kobozev, and Yu. A. Kravtsov, Zh. Tekh. Fiz. **104** (5), 3769 (1993) [Tech. Phys. (5) (1993)].

Translated by E. Kopyl

Acoustical Physics, Vol. 47, No. 3, 2001, pp. 369–370. Translated from Akusticheskiĭ Zhurnal, Vol. 47, No. 3, 2001, pp. 431–432.
Original Russian Text Copyright © 2001 by the Editorial Board.

CHRONICLE

Immanuil Lazarevich Fabelinskiĭ
(On His 90th Birthday)

January 27, 2001, marked the ninetieth birthday of the outstanding physicist, Corresponding Member of the Russian Academy of Sciences, Immanuil Lazarevich Fabelinskiĭ.

Fabelinskiĭ was born to the family of a medical doctor in Garaevo, Belostok province, of the Russian Empire. There, he studied at school and then worked as a turner in a factory for two years. Then, he left Garaevo for Moscow where he entered the Physics faculty of Moscow State University. After graduating from the university in 1936, he started his career as a researcher under the supervision of G.S. Landsberg. In 1942, Fabelinskiĭ defended his candidate dissertation, and later, as a staff member of the optical laboratory headed by G.S. Landsberg at the Lebedev Physical Institute of the Academy of Sciences of the USSR, he defended his doctoral dissertation. The entire scientific career of Fabelinskiĭ is connected with the Lebedev Physical Institute where he continues working today.

Most of the scientific works by Fabelinskiĭ are devoted to molecular scattering of light. The spectra of molecular scattering of light carry ample information on the processes that occur in a material, on its structure, on the character of fluctuations, and on the waves propagating in it. However, the extraction of this information is not a simple problem. It is the unique talent for experimentation, the fundamental understanding of physical phenomena, and the tireless energy in the development and improvement of experimental equipment that allow Fabelinskiĭ to obtain reliable information from his experiments.

The study of molecular scattering of light was especially difficult before the appearance of lasers, because all measurements required not only special lamps, but also long exposure times. The invention of lasers gave new life to this field of physics.

For many liquids and gases, the spectrum of molecular scattering of light is mainly determined by the fluctuations of density. These fluctuations give rise to a doublet (the Brillouin doublet). The distance between the doublet components determines the velocity of hypersound (sound with the frequency 10^9–10^{10} Hz), and the width of these components determines the hypersound attenuation coefficient. Fabelinskiĭ obtained the velocity and the attenuation coefficient of hypersound in many liquids. The comparison of these values with the corresponding values obtained for ultrasound revealed the dispersion of the velocity of sound and the dependence of the attenuation coefficient on frequency in a variety of liquids. Owing to these studies, acoustic spectroscopy has become possible in a very wide frequency range: from 10^{10} Hz to several hertz. This has made it possible to test the validity of the relaxation theory in many liquids, to determine the relaxation times, to find new relaxation regions, and in some cases to determine the process responsible for this relaxation. These studies largely contributed to the progress of physical acoustics.

In the course of these investigations, Fabelinskiĭ together with his colleagues arrived at the conclusion that the relaxation theory is not valid for high-viscosity liquids. They observed characteristic half-integer dependences on frequency, which did not fit the relaxation theory, and formulated the requirements for a new theory that could describe sound propagation in such liquids. This gave impetus to the development of such a theory.

In addition to the Brillouin doublet, molecular scattering of light produces a continuous spectrum whose maximum coincides with the unbiased line and the intensity monotonically decreases on both sides of this maximum to a distance of 100–150 cm^{-1}. This continuous spectrum is called the Rayleigh line wing. It is strongly depolarized. This spectrum is believed to be related to the fluctuations of the anisotropy tensor (to the rotation of anisotropic molecules). Fabelinskiĭ and his colleagues showed that this spectrum can be described by two relaxation times. These times were determined for a variety of liquids. In studying the wing, Fabelinskiĭ and his colleagues observed a fine structure (a doublet) for a number of low-viscosity liquids. It was shown that this doublet is caused by shear waves, and the distance between the components of the doublet yields the propagation velocity of shear waves. The novelty of this discovery becomes evident if one remembers that, at that time, the shear modulus of such liquids was believed to be zero.

An important part of the investigations carried out by Fabelinskiĭ is related to the molecular scattering of light near the critical layering point of binary solutions and near the double critical layering point. These studies stimulated the development of the theory of critical phenomena and, in particular, the theory of sound propagation near the critical layering point.

The investigations mentioned above were performed by using lamps and low-power lasers whose light did not affect the thermal fluctuations in the medium. Using high-power solid-state lasers, Fabelinskiĭ discovered and studied the stimulated Rayleigh-wing scattering and the stimulated thermal (entropy) scattering of light, both these phenomena being related to the effect of light on the fluctuations of anisotropy and entropy. He also observed the stimulated Brillouin scattering in amorphous solids and compressed gases. These phenomena have become an integral part of modern nonlinear optics.

Fabelinskiĭ is the author of more than 150 scientific works and the well-known monograph “Molecular Scattering of Light” published in 1965. In 1968, a revised and expanded version of this book appeared in English. This monograph serves as a manual for many researchers working with the molecular scattering of light in Russia and in other countries. For his outstanding contribution to science, Fabelinskiĭ received the Lomonosov prize (1966), the Mandel’shtam prize (1991), and the Beruni Uzbekistan State Award (1993). In 2000, Fabelinskiĭ was awarded the Vavilov Gold Medal.

Fabelinskiĭ is the founder of a school of physicists who now are working in many cities of Russia and the Commonwealth of Independent States. He is the center of attraction for researchers whose interests lie in molecular scattering of light and in adjacent areas. All who have worked with Fabelinskiĭ, as well as all who know him, are happy that they have the possibility to communicate with such a wise and kind person.

The Editorial Board of *Acoustical Physics* and the friends and colleagues of Immanuil Lazarevich Fabelinskiĭ sincerely congratulate him and wish him health and further success in his scientific activity.

Translated by E. Golyamina